Title: Characterization of Pliocene and Miocene Formations in the Wilmington Graben, Offshore Los Angeles, for Large-Scale Geologic Storage of CO2

PI: Dr. Michael Bruno Final Report

DOE Grant No: DE-NT0001922

PIR-10-062

Characterization of Pliocene and Miocene Formations in the Wilmington Graben, Offshore Los Angeles, for Large-Scale Geologic Storage of CO_2

Final Report

For Period
2010 to 2014

Dr. Michael S. Bruno (PI)
GeoMechanics Technologies
103 E. Lemon Ave.,
Monrovia, CA 91016
Phone: 626 305-8460
Fax: 626 305-8462

In Collaboration With:

City of Los Angeles, Dept. of Public Works

March 2015

Title: Characterization of Pliocene and Miocene Formations in the Wilmington Graben, Offshore Los Angeles, for Large-Scale Geologic Storage of CO_2

PI: Dr. Michael Bruno Final Report

Disclaimer:

This report was prepared as an account of work sponsored by an agency of the United States Government. Neither the United States Government nor any agency thereof, nor any of their employees, makes any warranty, express or implied, or assumes any legal liability or responsibility for the accuracy, completeness, or usefulness of any information, apparatus, product, or process disclosed, or represents that its use would not infringe privately owned rights. Reference herein to any specific commercial product, process, or service by trade name, trademark, manufacturer, or otherwise does not necessary constitute or imply its enforcement, recommendation, or favoring by the United States Government or any agency thereof. The views and opinions of authors expressed herein does not necessarily state or reflect those of the United States Government or any agency thereof.

This material is based upon work supported by the U.S. Department of Energy (DOE) National Energy Technology Laboratory (NETL) under Grant Number DE-NT0001922. This project is managed and administered by the Geomechanics Technologies and funded by DOE/NETL and cost-sharing partners.

Title: Characterization of Pliocene and Miocene Formations in the Wilmington Graben, Offshore Los Angeles, for Large-Scale Geologic Storage of CO_2

PI: Dr. Michael Bruno Final Report

1 Abstract

Geomechanics Technologies has completed a detailed characterization study of the Wilmington Graben offshore Southern California area for large-scale CO_2 storage. This effort has included: an evaluation of existing wells in both State and Federal waters, field acquisition of about 175 km (109 mi) of new seismic data, new well drilling, development of integrated 3D geologic, geomechanics, and fluid flow models for the area. The geologic analysis indicates that more than 796 MMt of storage capacity is available within the Pliocene and Miocene formations in the Graben for midrange geologic estimates (P50). Geomechanical analyses indicate that injection can be conducted without significant risk for surface deformation, induced stresses or fault activation. Numerical analysis of fluid migration indicates that injection into the Pliocene Formation at depths of 1525 m (5000 ft) would lead to undesirable vertical migration of the CO_2 plume. Recent well drilling however, indicates that deeper sand is present at depths exceeding 2135 m (7000 ft), which could be viable for large volume storage. For vertical containment, injection would need to be limited to about 250,000 metric tons per year per well, would need to be placed at depths greater than 7000ft, and would need to be placed in new wells located at least 1 mile from any existing offset wells. As a practical matter, this would likely limit storage operations in the Wilmington Graben to about 1 million tons per year or less. A quantitative risk analysis for the Wilmington Graben indicate that such large scale CO_2 storage in the area would represent higher risk than other similar size projects in the US and overseas.

Title: Characterization of Pliocene and Miocene Formations in the Wilmington Graben, Offshore Los Angeles, for Large-Scale Geologic Storage of CO_2

PI: Dr. Michael Bruno Final Report

Table of Contents

List of Figures

Title: Characterization of Pliocene and Miocene Formations in the Wilmington Graben, Offshore Los Angeles, for Large-Scale Geologic Storage of CO_2

PI: Dr. Michael Bruno Final Report

List of Tables

2 Introduction

The Los Angeles Basin (Figure 1) presents a unique and special combination of great need and great opportunity for the large-scale geologic storage of CO_2. Los Angeles is home to more than a dozen major power plants and oil refineries which produce greater than 5 MMt (5.5 Mtn) of fossil fuel related CO_2 emissions each year. Pliocene and Miocene sediments in the Los Angeles Basin (massive interbedded sand and shale sequences) are known to provide excellent and secure traps for oil and gas. The Wilmington Graben is adjacent to the giant Wilmington Field in Long Beach (more than two billion barrels produced to date). These formations have been used by the Southern California Gas Company for the very large-scale underground storage of natural gas at half a dozen locations throughout the Los Angeles basin for more than fifty years. This demonstrates both the storage potential and security of these formations for CO_2 sequestration.

Title: Characterization of Pliocene and Miocene Formations in the Wilmington Graben, Offshore Los Angeles, for Large-Scale Geologic Storage of CO_2

PI: Dr. Michael Bruno Final Report

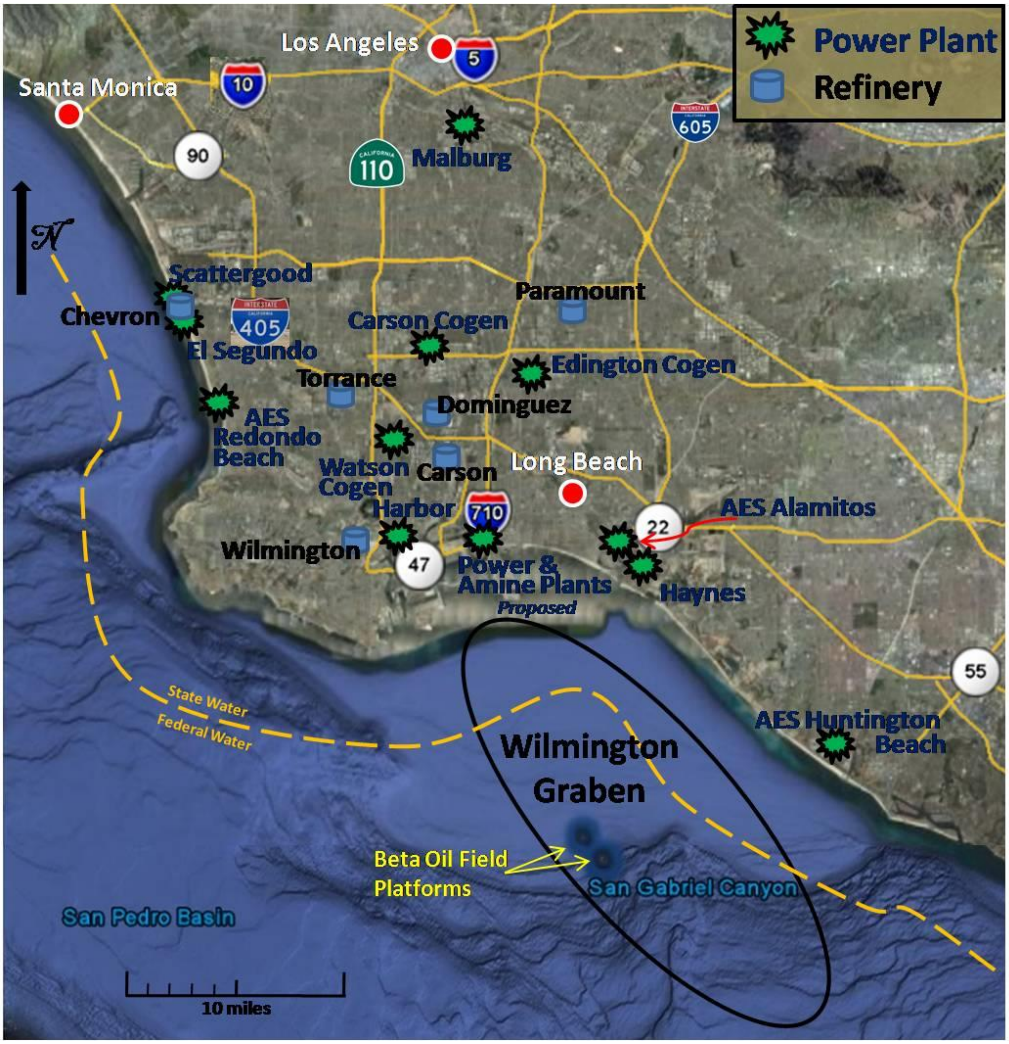

Figure 1: Wilmington Graben location, power plants, and refineries within the geologic Los Angeles basin

GeoMechanics Technologies, working in cooperation with the Department of Energy through DOE Grant No: DE-NT0001922, California Energy Commission Grant No: PIR-10-062, the City of Los Angeles, US Environmental Protection Agency Region 9, DOGGR, USGS, California State University, Long Beach, and University of California, Irvine, has conducted a five year research project to evaluate and quantify the Pliocene and Miocene Formations in the Wilmington Graben, offshore Los Angeles, for the large-scale geologic storage of CO_2. The research project has included the following efforts:

- Provided improved evaluations and interpretations of existing and newly acquired seismic data within the Wilmington Graben;
- Provided detailed log evaluations of previously drilled exploration wells in the area and tied existing seismic data to them for a better understanding of the geology throughout the graben;
- Drilled and core two new evaluation wells, and deepen an existing well in the Wilmington Graben to test for Miocene sand continuity;
- Developed 3D geologic models, geomechanical models, and CO_2 injection and migration models for the region;
- Provided risk assessment and characterization of the Wilmington Graben for large-scale CO_2 storage;
- Detailed review, quantification and documentation of the top 20 industrial sources of CO_2 emission in the area;
- Detailed engineering review and analysis of existing and new, potential pipeline and gas storage systems in the LA Basin.

3 Seismic data analysis and interpretation

Geophysical investigations provide a large component of the data necessary to produce the geological representation of the subsurface. Extensive seismic reflection data existing in the public domain were used to map the Palos Verdes fault and other important structures in San Pedro Bay including the Wilmington Graben (Figure 2). Most of these data are located in the offshore area, especially south of the breakwater and beyond the 3-mile limit of California State Lands. There is sparse data coverage at the nearshore area between the breakwater and the 3D survey grid ("Data Gap Area" in Figure 2). The newly acquired lines were integrated into the existing industry, government, academic and commercial seismic sources to produce 4 stratigraphic horizons for mapping the Wilmington Graben.

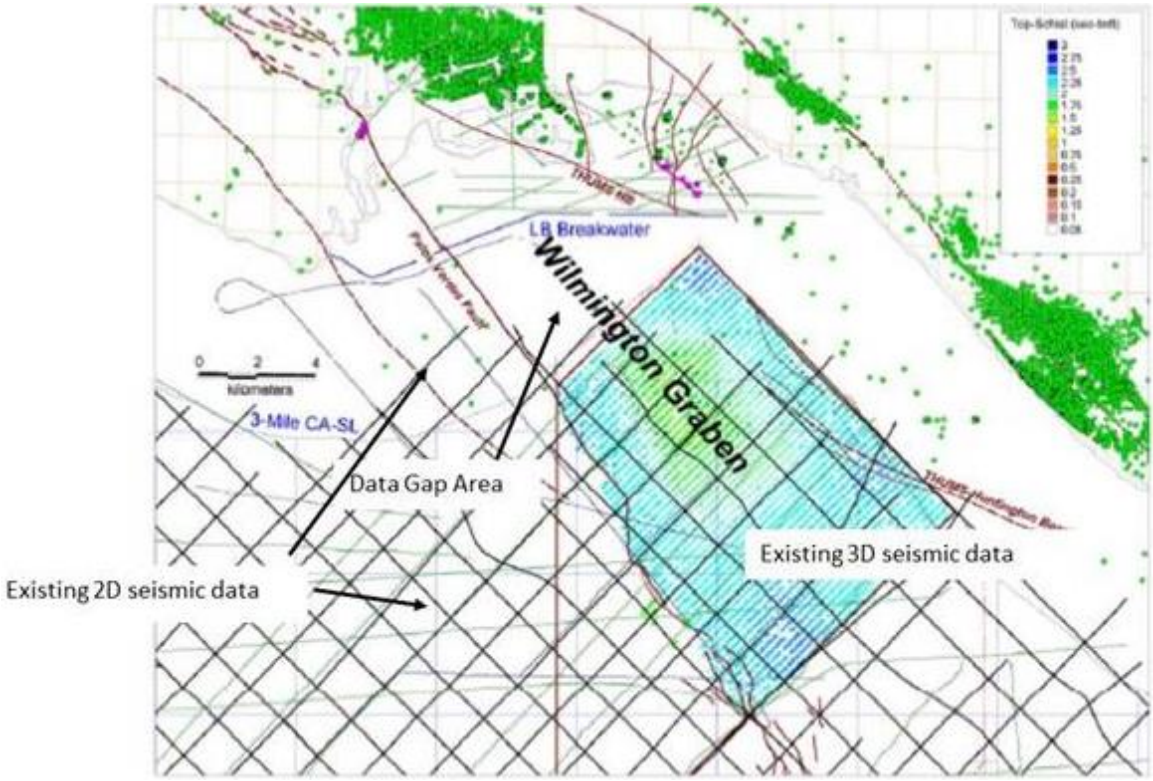

Figure 2: Seismic lines already available

3.1 New data acquisition

Nineteen new lines totaling 175 km (109 mi) in the "Data Gap Area" were acquired April 5 to 9, 2010 (Figure 3). The seismic data were acquired using shipborne seismic arrays provided

by Cal State Long Beach, managed by Legg Geophysical. Lines outside the breakwater were acquired with the full 72 channel GeoEel streamer; inside the channel, only 24 channels were deployed due to tight maneuvering and boat traffic. The new seismic data were processed through stack with RMS velocity analysis and Finite Difference migration at 90% of the RMS stacking velocity. Excellent data quality was achieved, and sub-surface penetration to 1.3 to 1.4 sec twtt inside the breakwater, 1.5 to 2.0 sec twtt outside (with 72 channels) was observed.

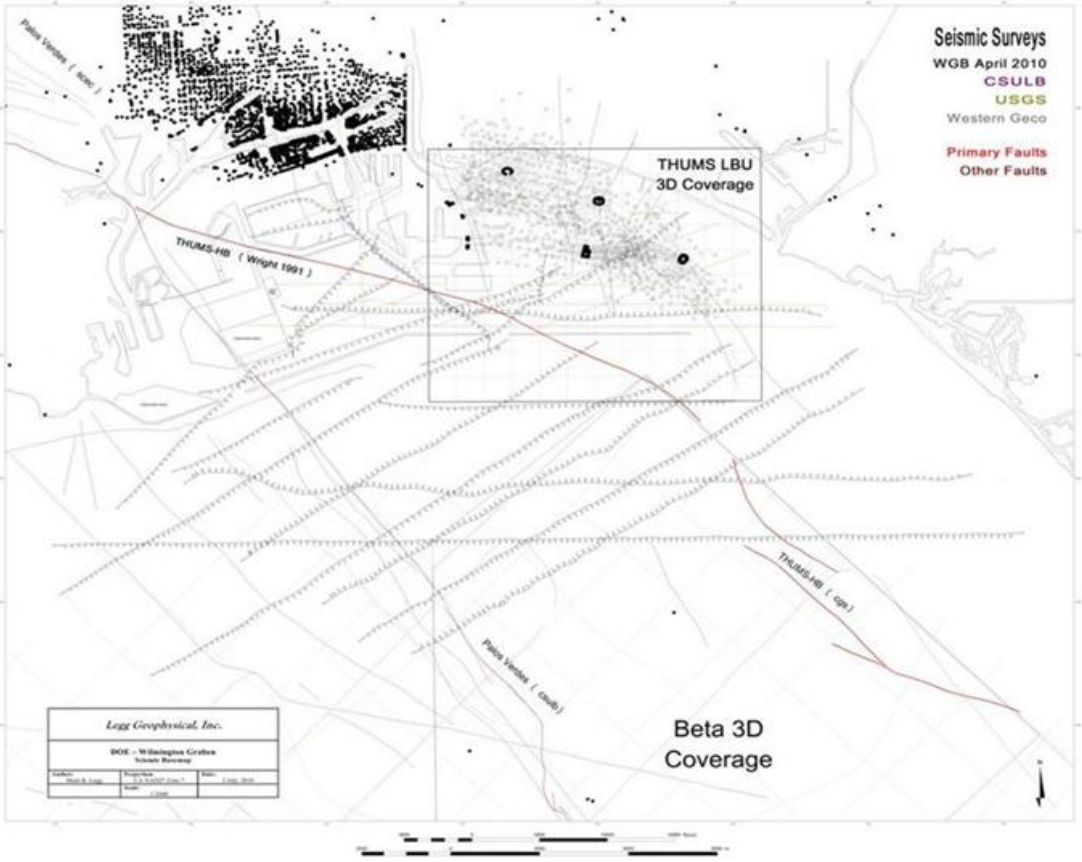

Figure 3: Shot point map for the new seismic lines

3.2 Analysis and Interpretation

Structural interpretation relied upon a combination of 3D exploration industry seismic surveys, 2D high-resolution seismic profile data available from government, academic and commercial sources and the newly acquired 2D seismic data in the northern area. Prior Beta 3D seismic data provide structural imaging on basement but the new high resolution 2D seismic

survey is too shallow for imaging basement at depths exceeding 3000 m (10,000 ft). Two major fault zones were mapped; the Palos Verdes and the THUMS-Huntington Beach fault zones that define the major structural boundaries of the Wilmington Graben. Four major seismic horizons were refined and calibrated with well logs, and are presented in figures below. Also mapped is basement using well data and published literature information. The stratigraphic column for Wilmington Graben is shown in Figure 4.The seismic horizons are:

- *Tmp* which represents the top of an unconformity below a prominent transgressive deltaic sequence. This horizon appears to correlate with the base of Pleistocene (Figure 5).
- *Tr* which represents an unconformity at the top of the Repetto (Upper Repetto Unconformity), base of the Pico Formations. This horizon denotes the top of CO_2 sequestration potential within the Pliocene strata.
- *Td4* which correlates with the base of a massive sand sequence, and is considered to be a horizon in the lower part of the Repetto Formation.
- *Tmd* is interpreted to be about 76 m (250 ft) above the top of the Miocene Puente Formation. This horizon denotes the basal portion of the Repetto Formation of Pliocene age (Figure 6).
- *Basement* reflection is poorly defined from the seismic data; well data is used to augment the basement structure map for the Wilmington Graben. Only 12 wells penetrated the studied area, and 4 wells penetrate basement, hence Figure 7 is rough at best.

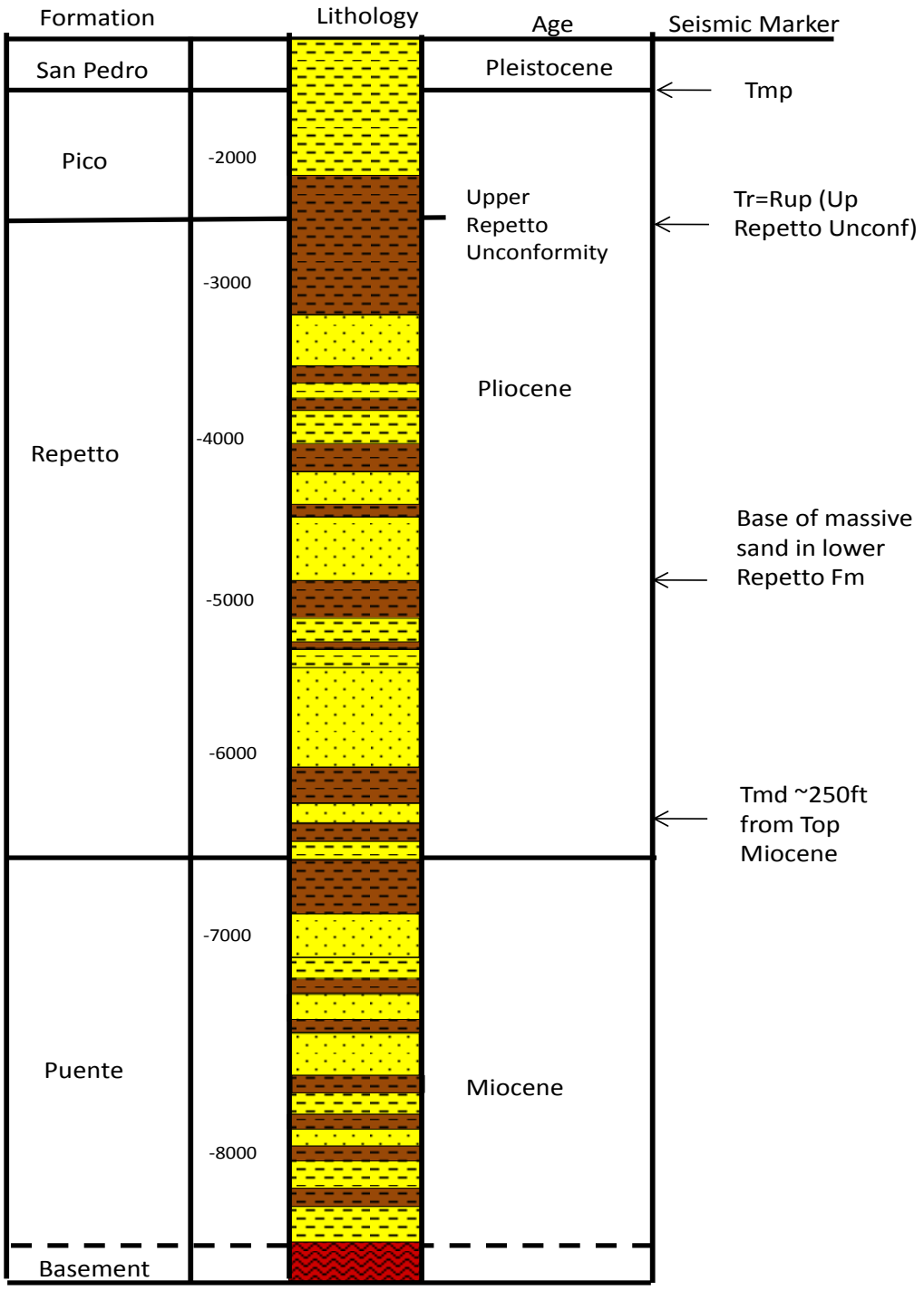

Figure 4: Stratigraphic Column for north Wilmington Graben

Title: Characterization of Pliocene and Miocene Formations in the Wilmington Graben, Offshore Los Angeles, for Large-Scale Geologic Storage of CO_2

PI: Dr. Michael Bruno Final Report

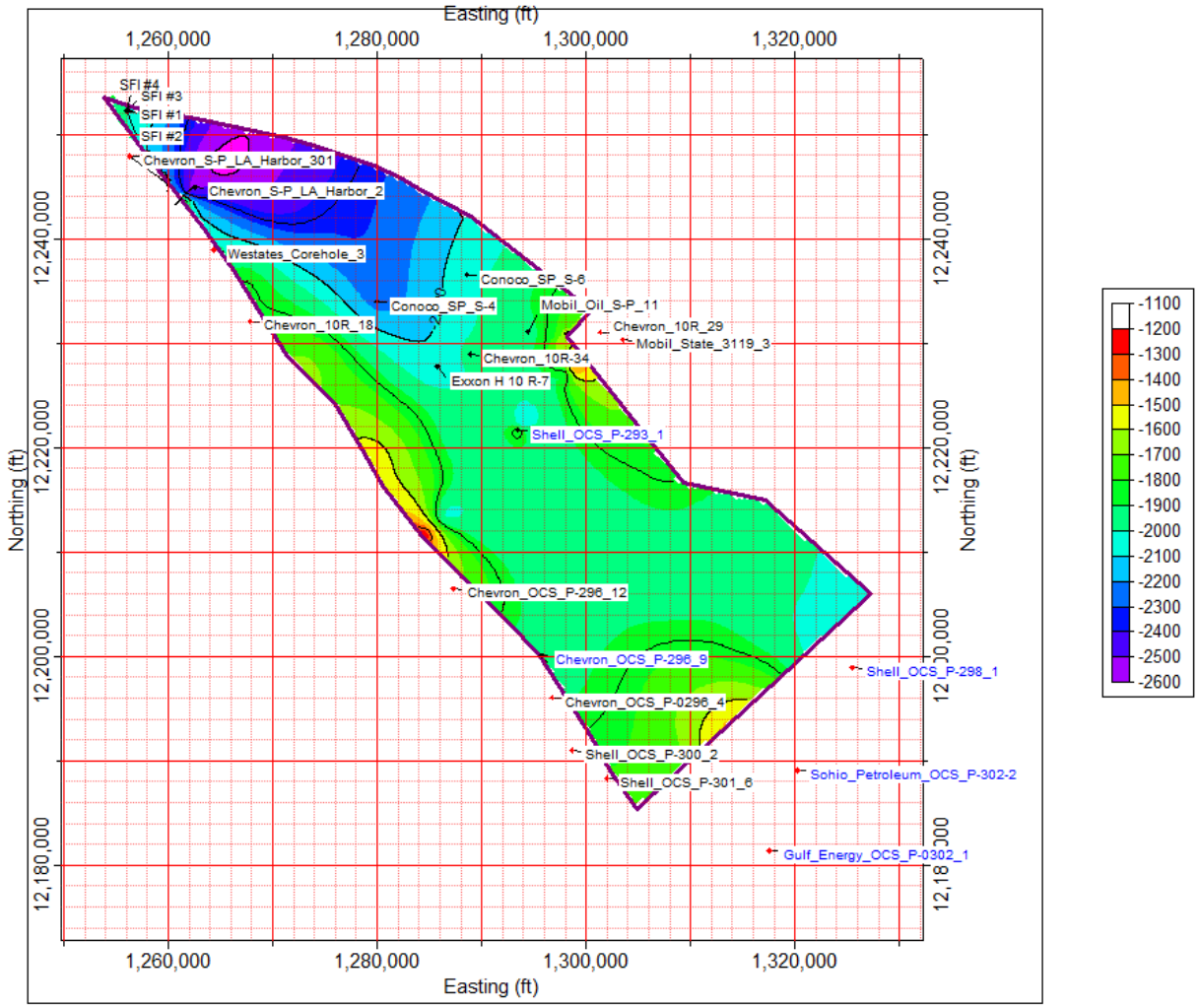

Figure 5: Pico (Top Pliocene) Structure Map

Title: Characterization of Pliocene and Miocene Formations in the Wilmington Graben, Offshore Los Angeles, for Large-Scale Geologic Storage of CO_2

PI: Dr. Michael Bruno Final Report

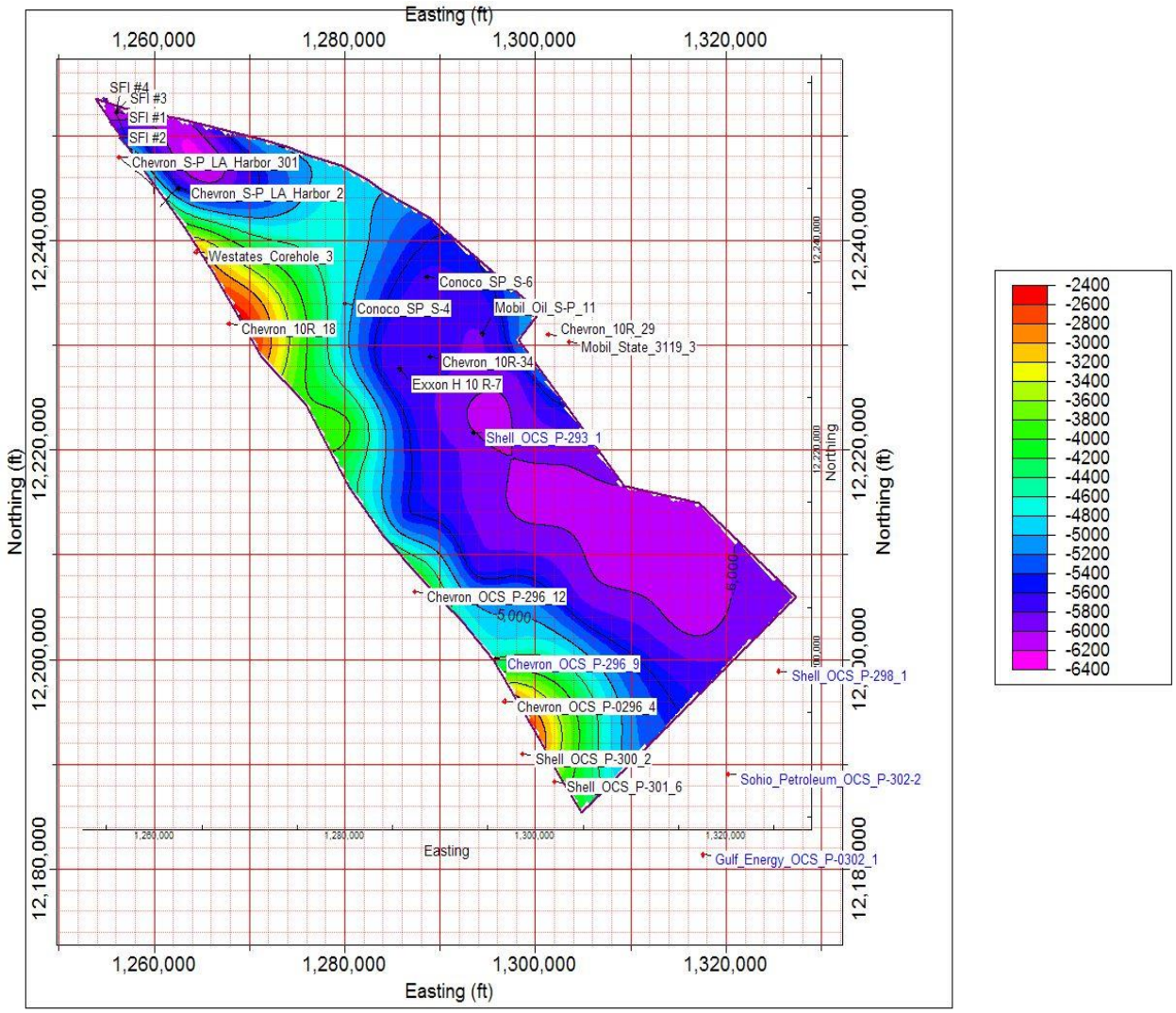

Figure 6: Top Miocene Structure Map

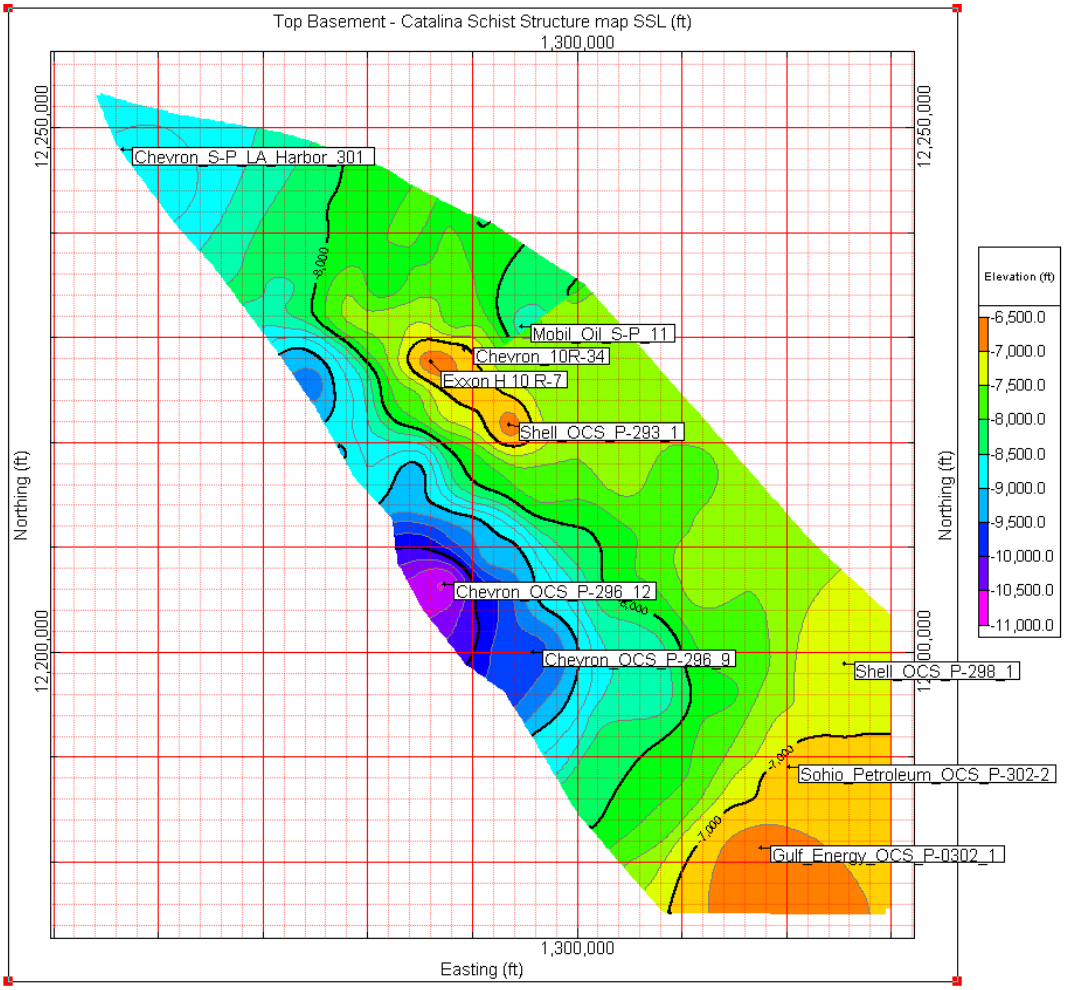

Figure 7: Top Basement Structure Map

4 Well data review and formation evaluation

Geomechanics Technologies in collaboration with Professor Dan Francis associated with the California State University, Long Beach, home of an extensive well data repository, and Don Clarke, who has over 30 years' experience in the Wilmington area, collected all the well data available in the public domain for the Wilmington Graben. We also obtained all publicly available information from USGS and DOGGR for evaluation.

The geologic characterization effort included assembly and analysis of log data from a dozen existing wells located within both State and Federal waters (Figure 8), and combination of this information into a common database. Several key geologic horizon markers were identified at each well location. Lithology versus depth was also identified for each well, separated into four categories for sand, shale, sand-shale interbed, and silt.

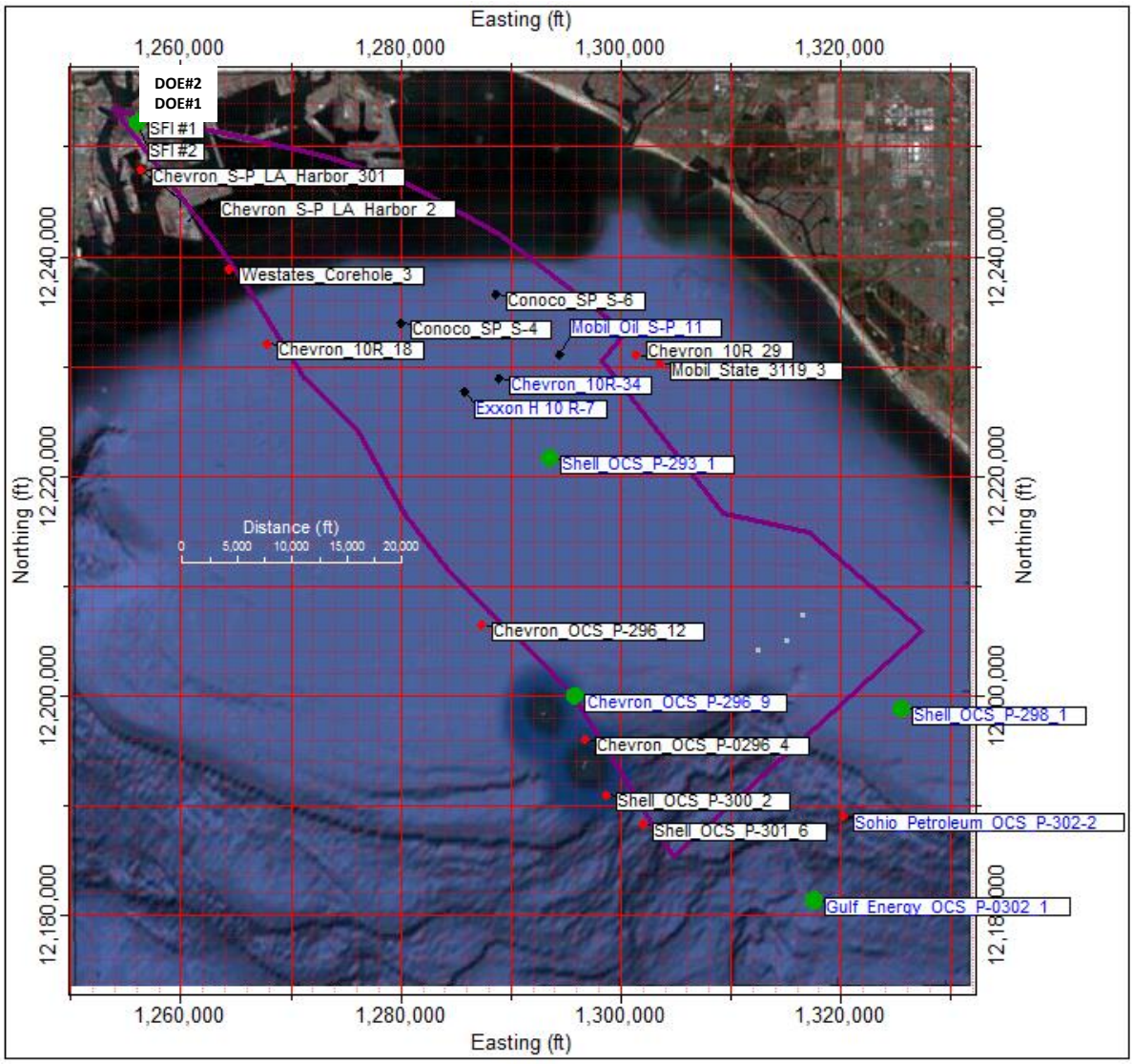

Figure 8: Well locations in the Wilmington Graben

4.1 Well log data

Geologic interpretation of the DOE wells drilled in the northern Wilmington Graben suggests that the northern portion is a fault enclosed block formed by compression. The Palos Verdes Peninsula block has pushed against and thrust up the enclosed block along the Palos Verdes Fault. There are three major dip domains: the first is separated from the lower two by the THUMS-Huntington Beach (THB) Fault; and the lower two are separated by a hinge line that

defines a chevron fold (Figure 9). There is no sign of lateral movement observed. The Palos Verdes and THUMS Huntington Beach Faults may converge to the west.

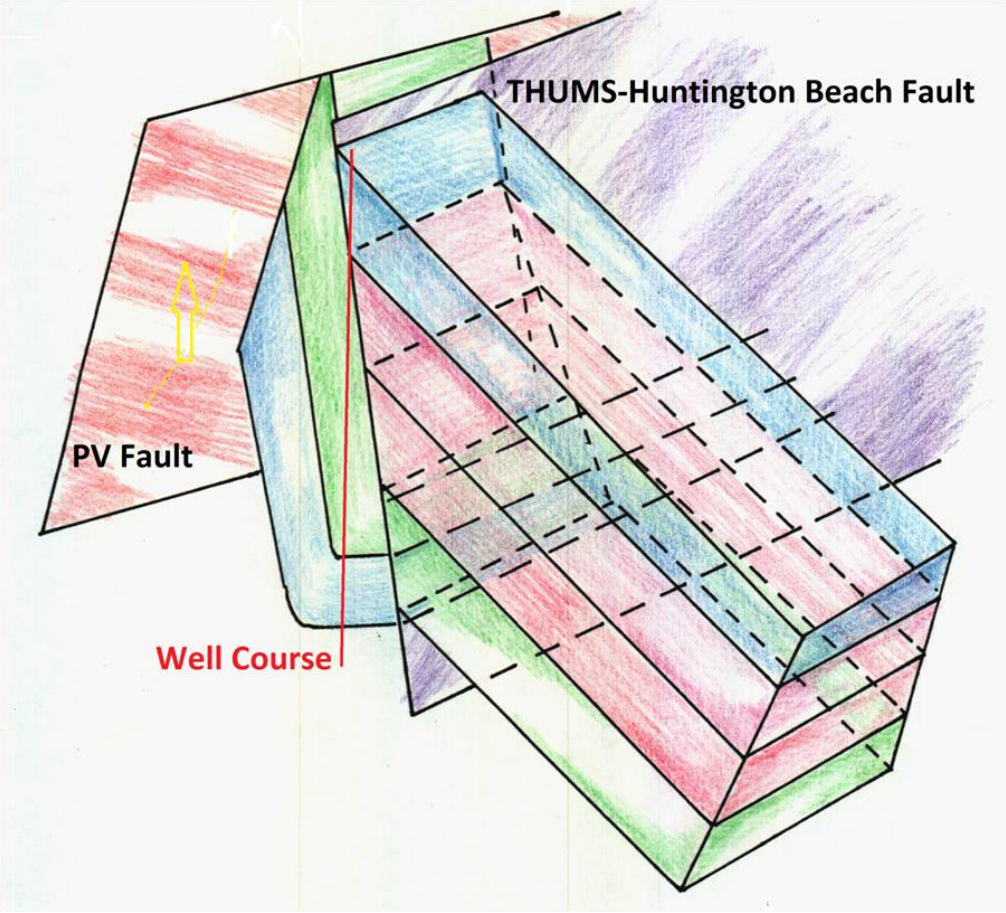

Figure 9: 3D cartoon showing the relationship between the chevron folds and the THUMS Huntington Beach Fault

The Palos Verdes (PV) Fault splits at the southern end of the Wilmington Graben (see Figure 12). In fact, the Beta Oil Field is found within the PV Fault splay zones. Wells within the fault splay zones and outside the bounding PV and THB Faults were excluded from the studied area. The remaining 12 wells have been analyzed, and key stratigraphic horizons from log and paleo picks have been tied to seismic data (Task 2). The lithology from each well was input into Rockworks software for generation of the geologic model. Figure 10 and Figure 11, are 3D

stratigraphic and lithologic models generated by Rockworks (RW). The structure maps are included in *Seismic data analysis and interpretation* section above.

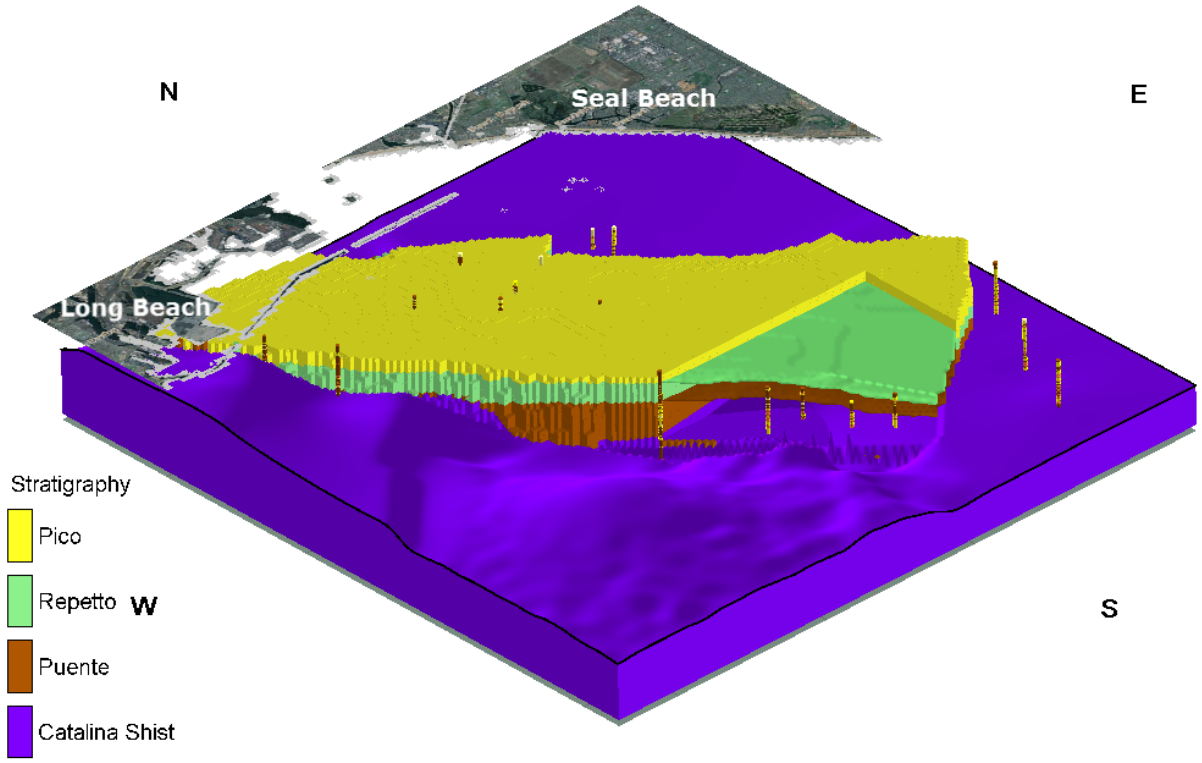

Figure 10: 3D stratigraphic model of the Wilmington Graben, showing wells and horizon markers

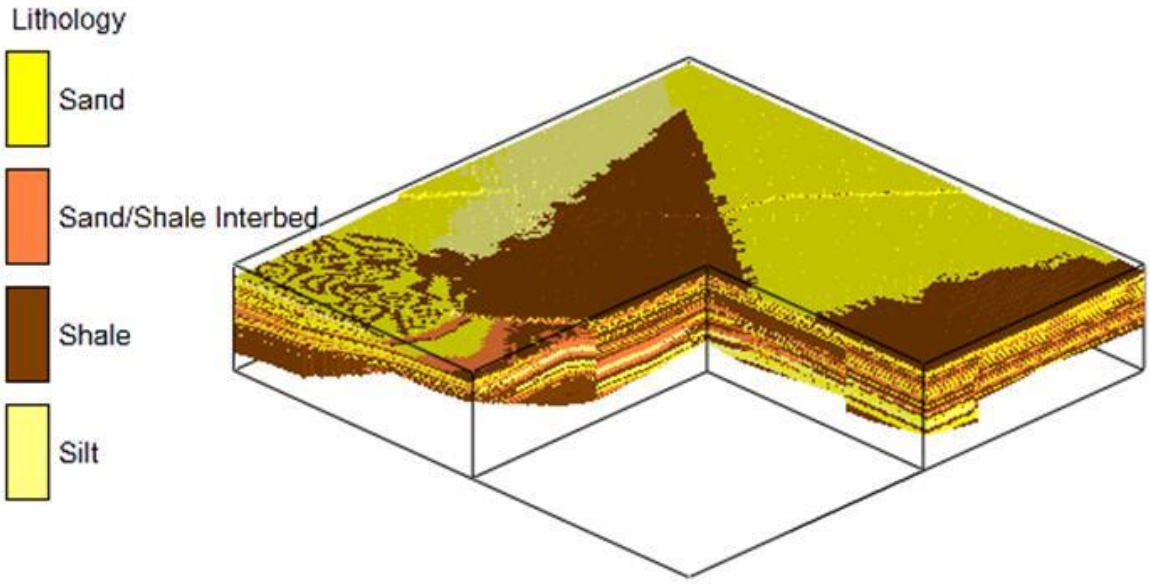

Figure 11: 3D lithology model of the Wilmington Graben, with a cut-away view

4.2 Porosity and Permeability Data

Porosity data are available in the northern graben, but lacking in the south. To have a better coverage, four federal offshore logs (three in the southern graben and one in the central graben) were digitized and their respective neutron and density porosities analyzed. The core and log porosities data from SFI#1, #2 and #3 wells (aka DOE#1) were analyzed and compared. There is no significant porosity difference between core and log porosity. Figure 12 shows the location of the wells used for statistical porosity distribution.

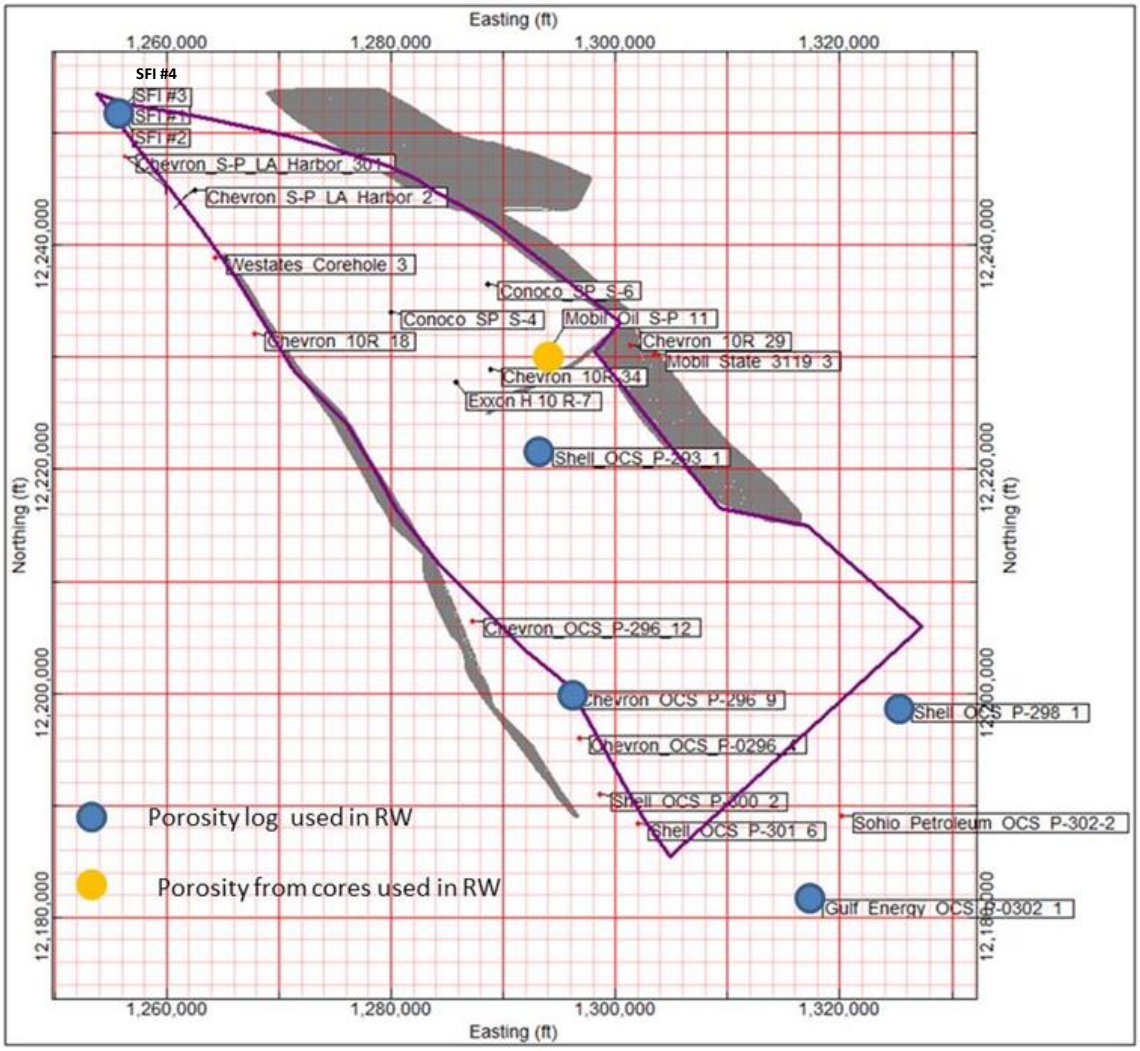

Figure 12: Location map for wells used for log modeling analysis

The porosity histograms were generated individually for the northern, central, southern graben and compared to the whole graben. The SFI and DOE wells are grouped into the northern graben, while the SP-11 and OCS P293-1 are located in the central graben, and the OCS P-296-1, OCS P-298-1 and OCS P-302-1 are grouped in the southern graben. We analyzed porosity distribution from 8 porosity logs and one well core (containing 38 sidewall cores) data using histograms to evaluate statistical distribution. Based on the statistical distribution, we present in Table 1 the statistical porosity distribution for the north, central, south and the whole Wilmington graben basin.

Title: Characterization of Pliocene and Miocene Formations in the Wilmington Graben, Offshore Los Angeles, for Large-Scale Geologic Storage of CO_2

PI: Dr. Michael Bruno Final Report

Table 1: Porosity for different lithologies and formations for the Wilmington Graben

North graben

Mean Porosity	Sand	shale	sand/shale	Silt
Pico	0.489	0.396	0.000	0.338
Repetto	0.286	0.360	0.318	0.360
Puente	0.276	0.358	0.314	0.312

Central graben

Mean Porosity	Sand	shale	sand/shale	Silt
Pico	0.31	0.29	0.29	0.35
Repetto	0.28	0.29	0.23	0.00
Puente	0.00	0.24	0.22	0.00

South graben

Mean Porosity	Sand	shale	sand/shale	Silt
Pico	0.326	0.376	0.382	0.000
Repetto	0.299	0.394	0.352	0.343
Puente	0.236	0.312	0.247	0.316

Whole graben

Mean Porosity	Sand	shale	sand/shale	Silt
Pico	0.31	0.34	0.29	0.34
Repetto	0.29	0.36	0.30	0.39
Puente	0.22	0.25	0.23	0.32

A correlation between porosity and permeability for different lithology types has been developed. Different empirical equations based on the Kozeny-Carman (Carman, 1997 & Taylor, 1948) equations were evaluated. Best fitting equation for each lithology is then used to calculate average permeability from average porosity estimated earlier. As can be seen from Figure 13, the correlation is reasonable.

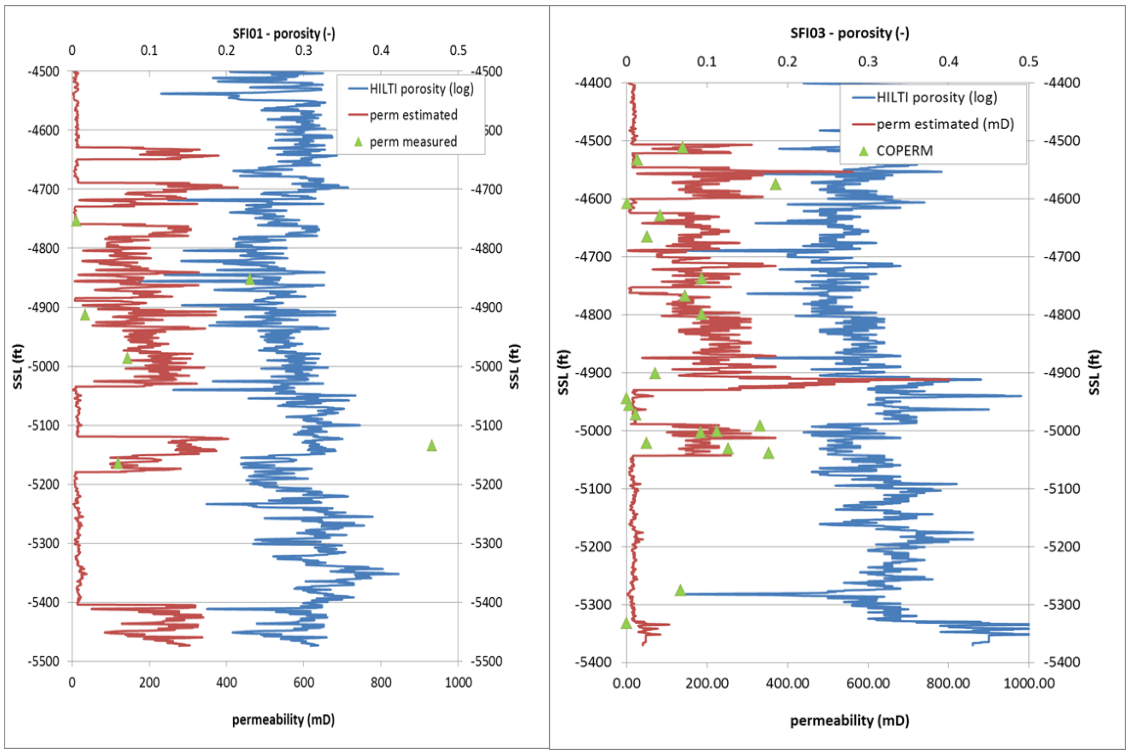

Figure 13: Correlation of measured and estimated permeability for SFI#1 (right) and SFI#3 (left)

Table 2 presents the permeabilities used for the different lithologies within the central graben gas migration modeling and is summarized below (md):

- Sand perm: 9408*n^3
- Shale perm: 71.044*n^2/(1-n)^2
- Sand/shale interbed perm: 367*n^2/(1-n)^2
- Silt perm: 71.044*n^2/(1-n)^2

Table 2: Average permeability obtained using porosity to permeability correlation for the central graben

Av perm (md)	sand	shale	sand/shale	silt
Pico	282.99	11.97	60.05	16.82
Repetto	204.32	11.97	31.83	16.82
Puente	123.66	7.01	31.83	16.82

After drilling the DOE#2 (aka SFI#4) well, we re-evaluated the correlation between porosity and permeability and the equation has been updated (below) and Table 3 presents the permeabilities used for the different lithologies in the northern graben. Since we do not believe the porosity of the northern graben is reasonable, we average the porosity for the northern graben based on north and whole graben results.

- Sand perm = 453.8 * n
- Shale perm = 62.26*n^2/(1-n)^2
- Sand/shale interbeds perm = 178.2 * n
- Silt perm = 62.26*n^2/(1-n)^2

Table 3: Average permeability obtained using porosity to permeability correlation for the northern graben

Av Perm (md)	Sand	Shale	sand/shale	silt
Pico	141.81	21.47		
Repetto				
Puente	122.53	15.10	51.68	17.53

The DOE#2 (aka SFI#4) well encountered over 120 m (400 ft) of Pliocene and 45 m (150 ft) of upper Miocene sand in the northern graben. SFI#1 well deepening also encountered Miocene sands. SFI#1 was drilled to 2145 m (7039 ft), when we encountered stuck pipe, and the well was only logged to 1777 m (5832 ft). (For details, see *New well drilling, logging, and core analysis* below). The sands shown in the mud log may be connected to those found in DOE#2 well. Figure 14 is a schematic cross section interpolated between SFI#1 and DOE#2 well.

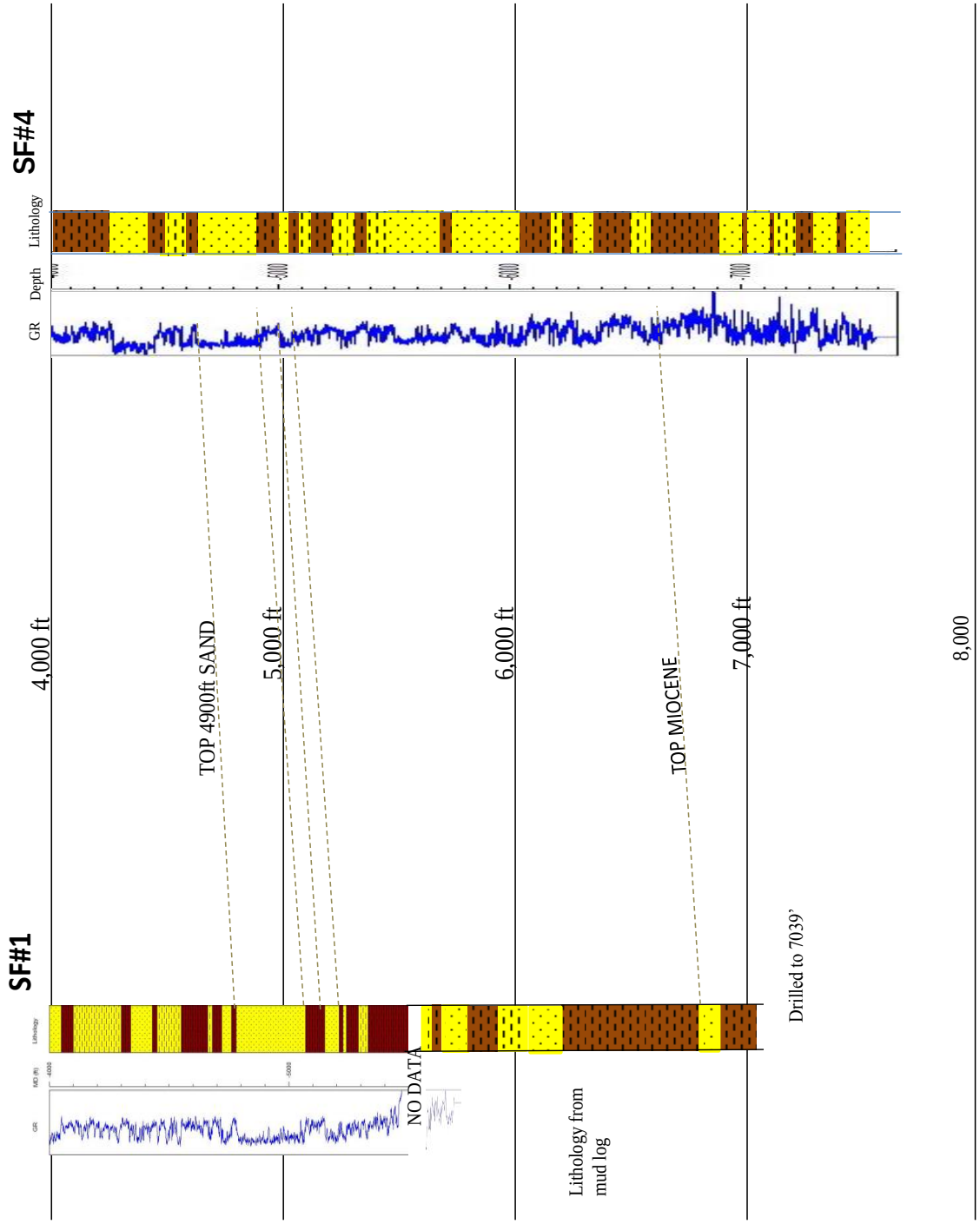

Figure 14: Correlation between SFI#1 and SFI# 4 (aka DOE#2) wells

4.3 Conclusions

The geologic characterization for the Wilmington Graben included assembly and analysis of 12 log data from existing wells located within both State and Federal waters, and combining this information into a common database. Several key geologic horizon markers were identified at each well location. Lithology versus depth was also identified for each well, separated into four categories for sand, shale, sand-shale interbed, and silt. All available data were used to create a porosity distribution for the graben and in turn correlate to permeability. The data is then fed into the geologic model for calculation of CO_2 storage capacity.

The DOE#2 (aka SFI#4) well encountered over 120 m (400 ft) of Pliocene and 45 m (150 ft) of upper Miocene sand in the northern graben increasing the potential storage capacity for the northern graben. Deepening the SFI#1 well to test for the continuity of these Miocene sands proved successful.

5 New well drilling, logging, and core analysis

The sediments within the Wilmington Graben span more than 1500 m (5000 ft) of vertical interval. We drilled 2 wells and deepened an existing well to obtain data for assessing the sand thickness, rock properties and injectivity of these sands. The data obtained have been used to validate and improve upon the initial geologic model developed from seismic and well log data in building a realistic geologic model.

5.1 DOE#1 well

Well DOE#1 was designed to test the Pliocene formation in the northern Wilmington Graben. The DOE#1 (also known as SFI#3) deviated well spud on April 28, 2010 and finished May 28, 2010 to MD 1655 m (5432 ft), TVD 1640 m (5382 ft). A suite of well logs (including Spontaneous Potential, Gamma Ray, Density, Neutron, Dipmeter, Cement bond and Mud log) were acquired. Twenty nine sidewall cores and 2.89 m (9.5 ft) of conventional core were recovered and analyzed. The well was completed during December 2010, and the Pliocene section between 1550 m to 1556 m (5086 ft to 5106 ft) was perforated, in situ fluid samples taken and analyzed. Figure 15 is the well schematic for DOE#1.

The microbiology performed on the conventional core reviewed a diverse microbial populations existed in the deep subsurface environment. In addition, formation fluid samples were collected on Dec. 14, 2010 after completing the DOE#1 well, again on Nov. 29, 2011 and April 16, 2012. The results were:

- The majority of these microbes belong to previously unknown species.
- Thermophilic, halophilic and anaerobic microorganisms were found in the core sample and formation fluid samples.
- The formation fluid sample contained 100 times fewer bacteria than the surface sludge sample (baseline). The diversity difference may indicate that the microbial is reduced after periods of storage in the deep surface environment.
- The composition of methanogens community remains similar in the formation fluid sample and the surface sludge sample, suggesting the methanogens originated in the sludge persist in the subsurface.
- The formation samples contained only cocci shaped microbes while the sludge contained many other shapes (rod, comma and coccus) and sizes implying either only cocci bacteria can survived the deep subsurface environment or the deep surface condition triggered physiological responses in the microbial community that caused the morphological change from rod and comma to coccus shape.
- A small fraction of the microbes were identified as obligated aerobic organisms (oxygen required). These bacteria either are capable of growth using previously unknown metabolic pathways or were the result of contamination of core samples during drilling

and sample retrieval. The presence of these microbes in the deep subsurface environment requires further investigation.

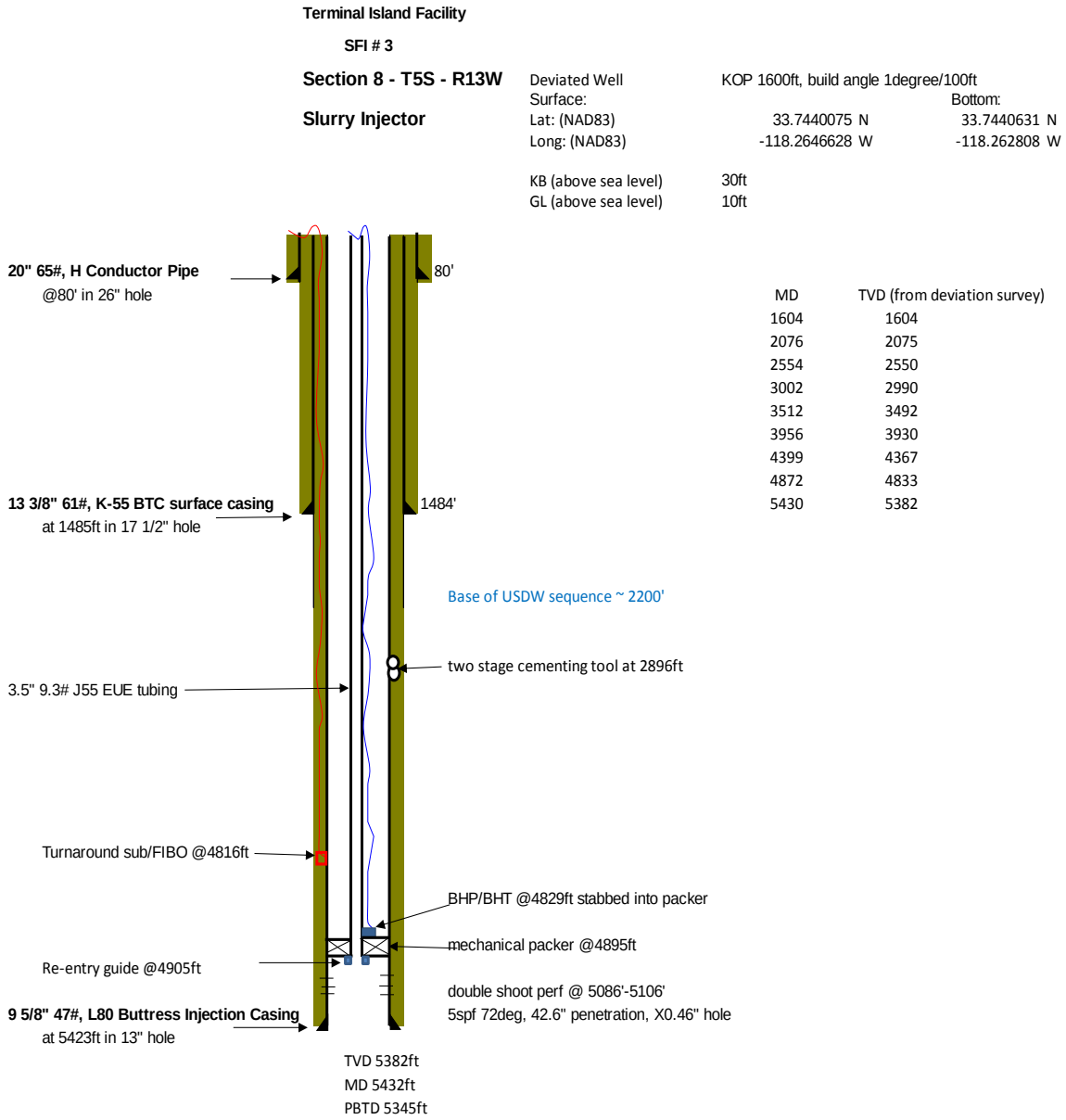

Figure 15: DOE#1 (aka SFI#3) Well Schematic

The in situ pressurized fluid samples obtained at 1550 m (5078 ft) show the formation fluid contained 0.19 - 0.32 mole % of CO_2 and 94.57 to 96.11 mole % CH_4, salinity recorded at 20,000 to 22,000 ppm and reservoir pressure at 14.35 MPa (2081 psi). We retested the fluid formation on April 16, 2012, and the analysis showed 0.92 – 1.28 mole % of CO_2 and 98.16 to 98.63 mole % CH_4, salinity recorded at 28,000 to 29,500 ppm with the reservoir pressure same at 14.35 MPa (2081 psi). The increase of CO_2 and salinity may be due to the nearby biosolids and brine injection operations. Table 4 below compares the fluid samples results.

Table 4: Geochemical analysis of in situ pressurized formation fluid sample from DOE#1

	Formula	Mole wt	SFI#3		SFI#3	
			sample 1	sample 2	sample 1	sample 2
			12/9/2010	12/9/2010	4/16/2012	4/16/2012
Depth (ft)			5078	5078	5078	5078
Sample captured (cc)			600	600	580	590
Salinity (ppm)			22000	20000	29500	28000
GLR (scf/stb)			6	4	8	8
density (g/cc)			1.025	1.025	1.032	1.032
Reservoir Pressure (psi)			2080	2080	2080	2080
Temperature (F)			170	170	170	170
pH @25C (or specified)			7.82@35C	7.85@45C	7.45	7.49
UNIT			mole%	mole%	mole%	mole%
CO2	CO2	44.1	0.32	0.19	1.28	0.92
H2S	H2S	34.06	0	0	0	0
N2	N2	28.01	3.31	4.98	0.44	0.29
CH4	CH4	16.04	96.11	94.57	98.16	98.63

We ordered 30 sidewall cores and 9.1 m (30 ft) of conventional core. However, we recovered 29 sidewall cores between 1347 m to 1468 m (4420 ft to 5409 ft) and 2.89 m (9.5 ft) of convention core between 1655 m to 1657.9 m (5430 ft to 5439.5 ft) from the turbidites sand and shale section. Table 5 summarizes the porosity and permeability of the core samples.

Table 5: Reservoir properties from DOE#1 sidewall and conventional cores

Zones	Porosity (%)	Permeability (md)
Shale between 4465-4570ft	28 to 29	2 to 4
Sand at 4640ft	32	371
Shale above 4900ft sand	27	<1
4900ft sand @ 4690-4975ft	24 to 30	51 to 187
Shale above Injection Zone	28 to 29	<1 to 2
Injection Zone (5055-5115ft)	26 to 31	50 to 353
Sand at 5351ft	29	135
Conventional Core shale (5431-5439.5ft)	23 to 24	<1

Figure 16 is a photo taken during the drilling of the DOE#1 well.

Figure 16: Well DOE#1 drilled in April, 2010, to characterize the Pliocene formation

5.1.1 Injectivity Test (Step Rate Test)

Step Rate Tests were performed on August 1, 2014 in DOE# 1 (aka SFI#3). The initial step rate test on the well did not seem to initiate fracturing. The pressures reached were below the regional fracture gradient of about 0.80 psi/ft.

We present in Figure 17 and Figure 18 plot of pressure versus time for the testing conducted in Well DOE#1. Injection proceeded in seven incremental steps, each one hour in length. Table 6 below presents the flow rates and the final pressure at the end of each step. The pressure sensor for this test was placed at a measured depth of 1556 m (5107 ft). As can be seen in Figure 18, at the conclusion of the step-rate test pressure declined rapidly to original reservoir conditions within about two days. Data was recorded for 10 days total.

Table 6: Injection rate and bottom hole pressure for DOE#1 SRT

Injection Rate (bpm)	Bottom Hole Pressure (psi)
0.00	2018
0.60	2227
1.11	2237
2.04	2338
3.06	2440
5.10	2753
7.06	3110
9.05	3424

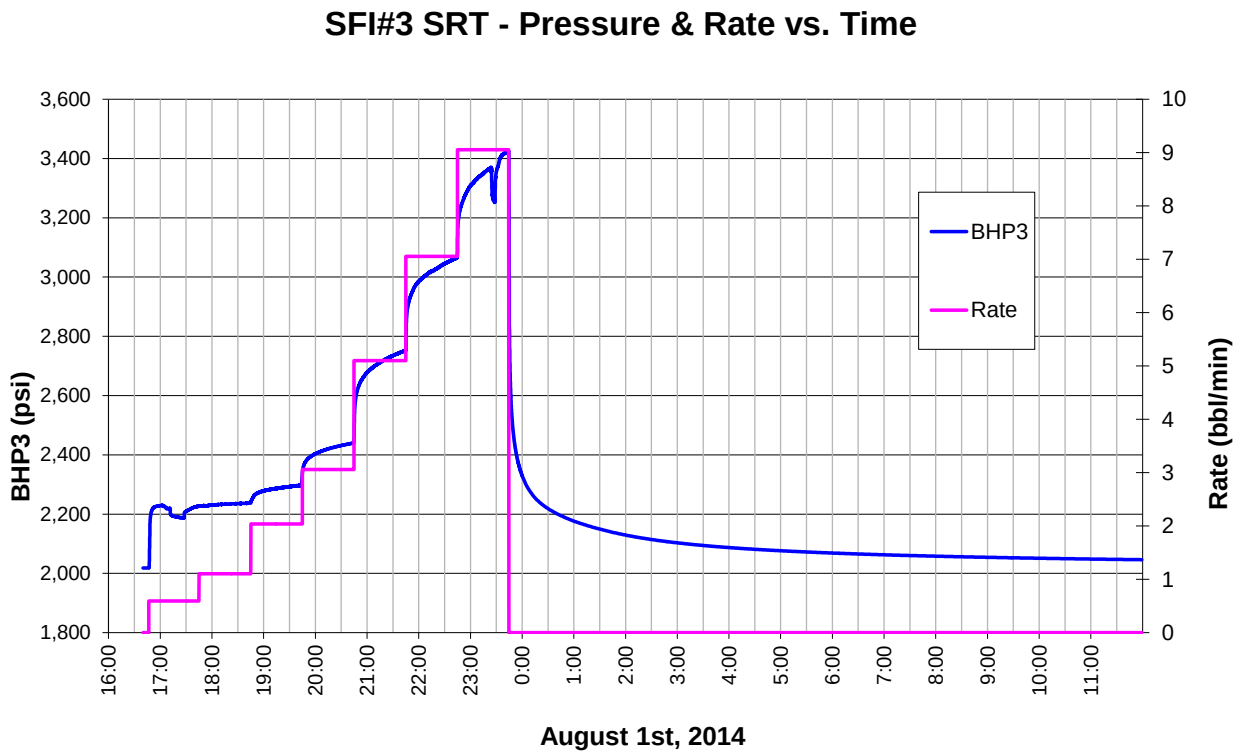

Figure 17: Injection rate and bottom hole pressure recorded during well DOE#1 step rate test.

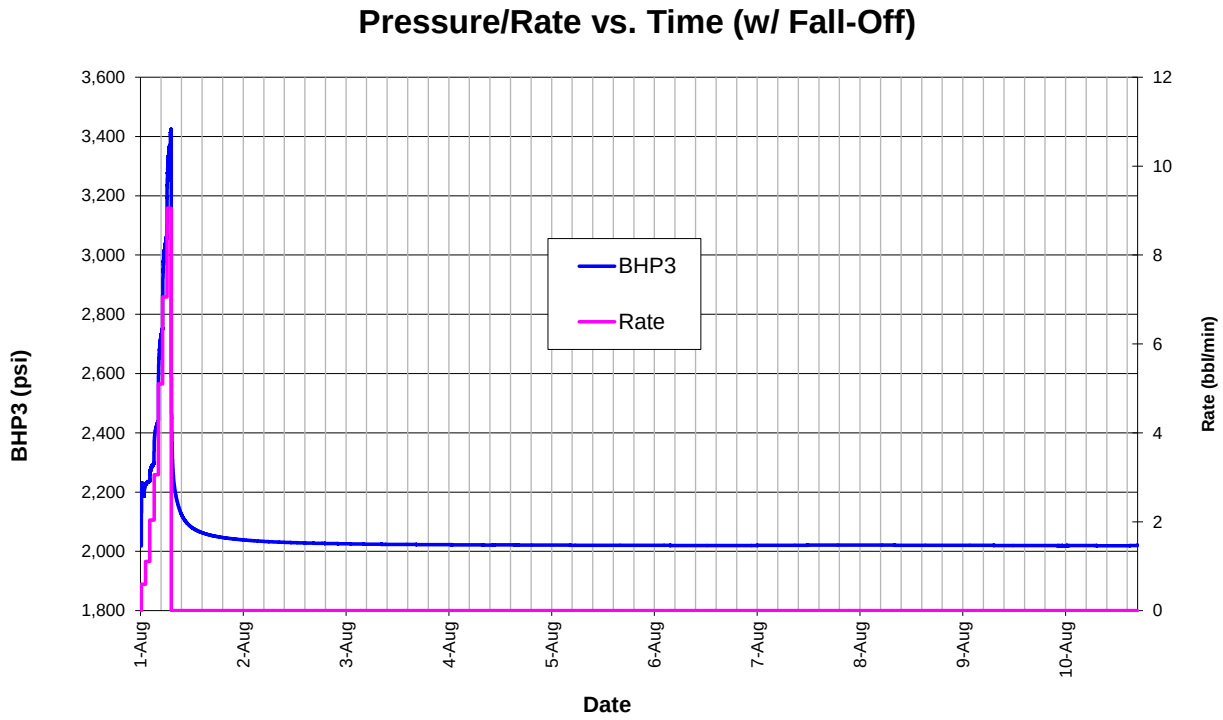

Figure 18: 10 days of fall-off data recorded after DOE#1 step rate test

We present in Figure 19 plot of pressure versus rate for the testing conducted in DOE#1. After initial breakdown of perforations in Step 1, the remaining data of pressure versus rate is a linear trend, indicating no change in flow regime. Further transient analyses described below indicate that the flow is radial in nature.

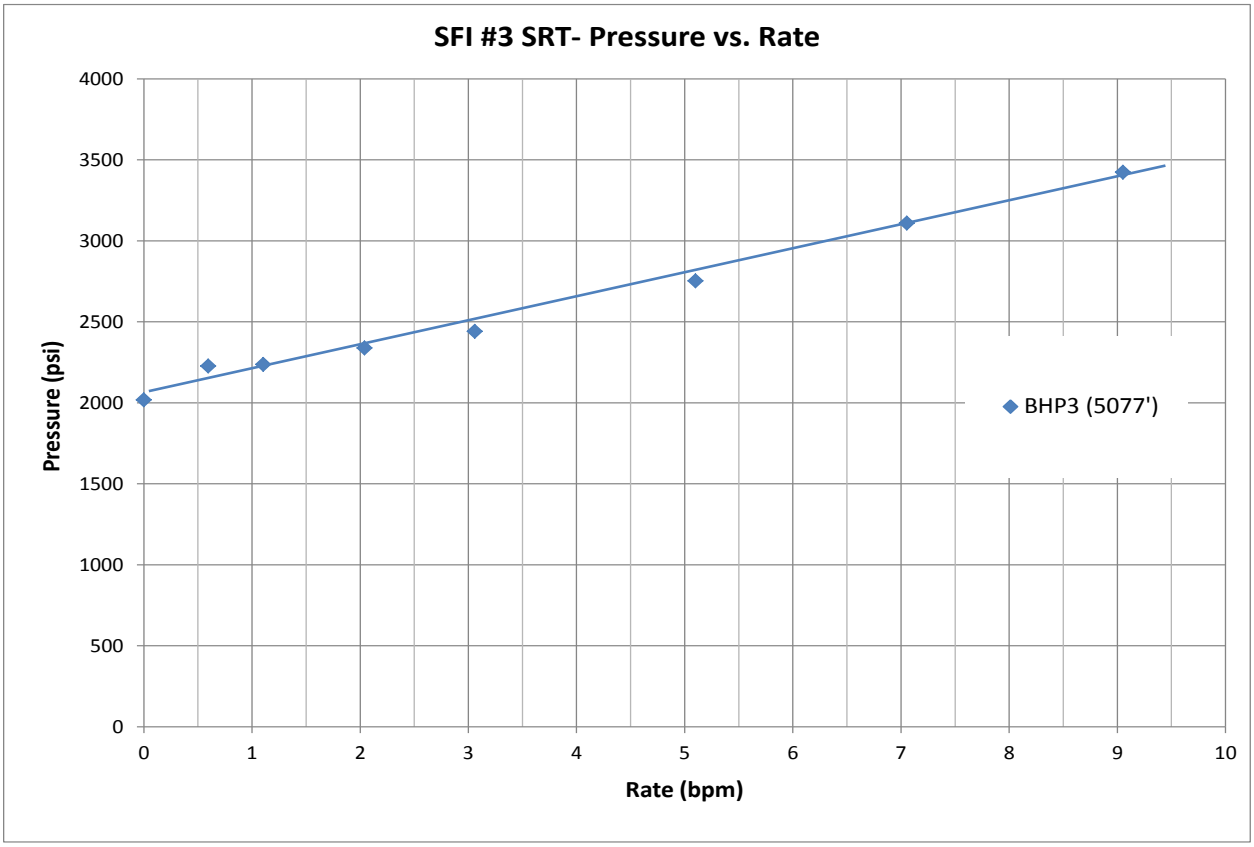

Figure 19: DOE#1 step rate test pressure vs. rate data

We next apply pressure transient analysis techniques to analyze the pressure-fall-off after SRT, using the industry standard FEKETE well test analysis software. In pressure transient analysis, an attempt is made to match both the observed pressure versus time and the pressure derivative versus time, while varying the flow model (radial for matrix flow or linear for fracture flow). As indicated in Figure 21, the pressure-fall-off analysis indicates radial flow behavior very clearly.

Odeh and Jones method for multi-rate analysis:

Next we also apply the Odeh and Jones multi-rate analysis technique as described in Singh et al. (1987). A plot of

$$\frac{p_i - p_{wf}}{q_n} \; vs \sum_{j=1}^{n} \frac{(q_j - q_{j-1})}{q_n} \log(t_n - t_{j-1})$$

is made for DOE#1's SRT data and illustrated in Figure 20.

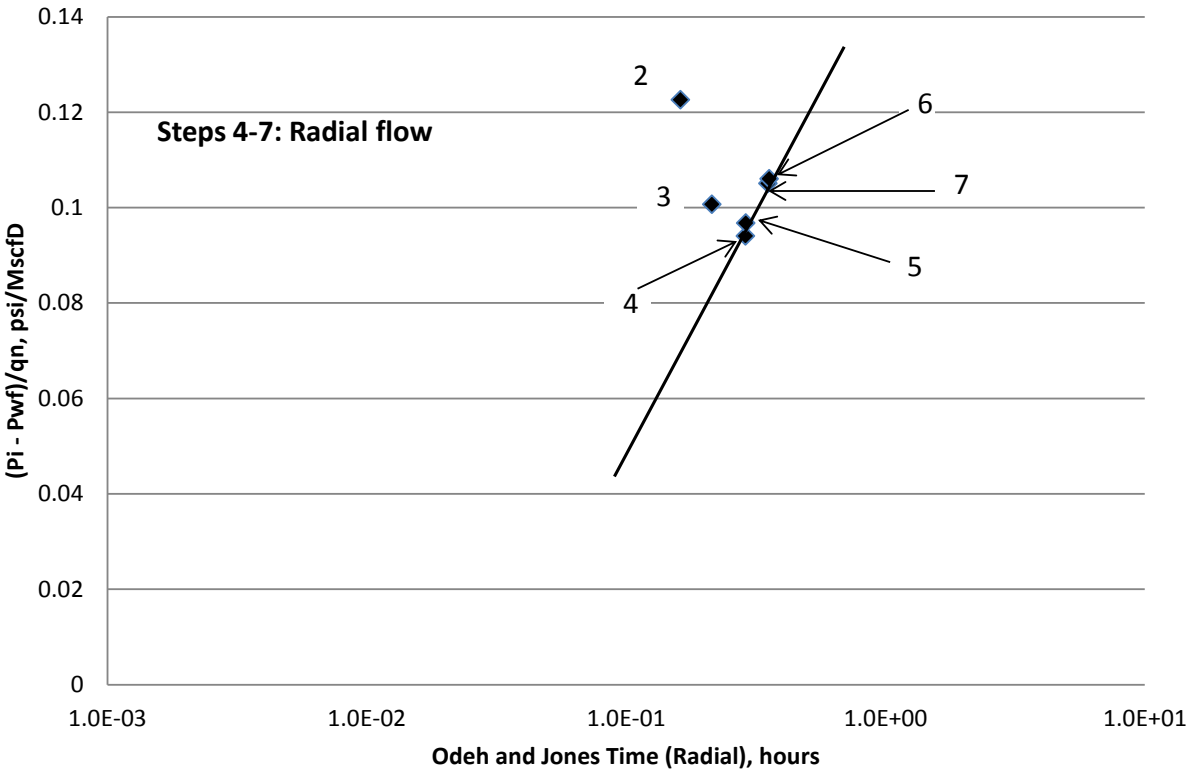

Figure 20: Odeh and Jones multirate analysis of DOE#1 SRT data

For comparison we present in Figure 22 the Odeh and Jones analysis plot from Singh et al. (1987), where all the radial flow steps fall on a single straight line (step 1,2,3), and a downward shift of data points is observed when the fracture is propagating (step 4,5,6).

Comparing Figure 20 and Figure 22, steps 4 to 7 fall on a straight line, which indicates radial flow behavior. Steps 1 through 3 are affected by initial wellbore fill-up and perforation breakdown during the early injection. This analysis is also consistent with the analysis results by FEKETE.

Title: Characterization of Pliocene and Miocene Formations in the Wilmington Graben, Offshore Los Angeles, for Large-Scale Geologic Storage of CO_2

PI: Dr. Michael Bruno Final Report

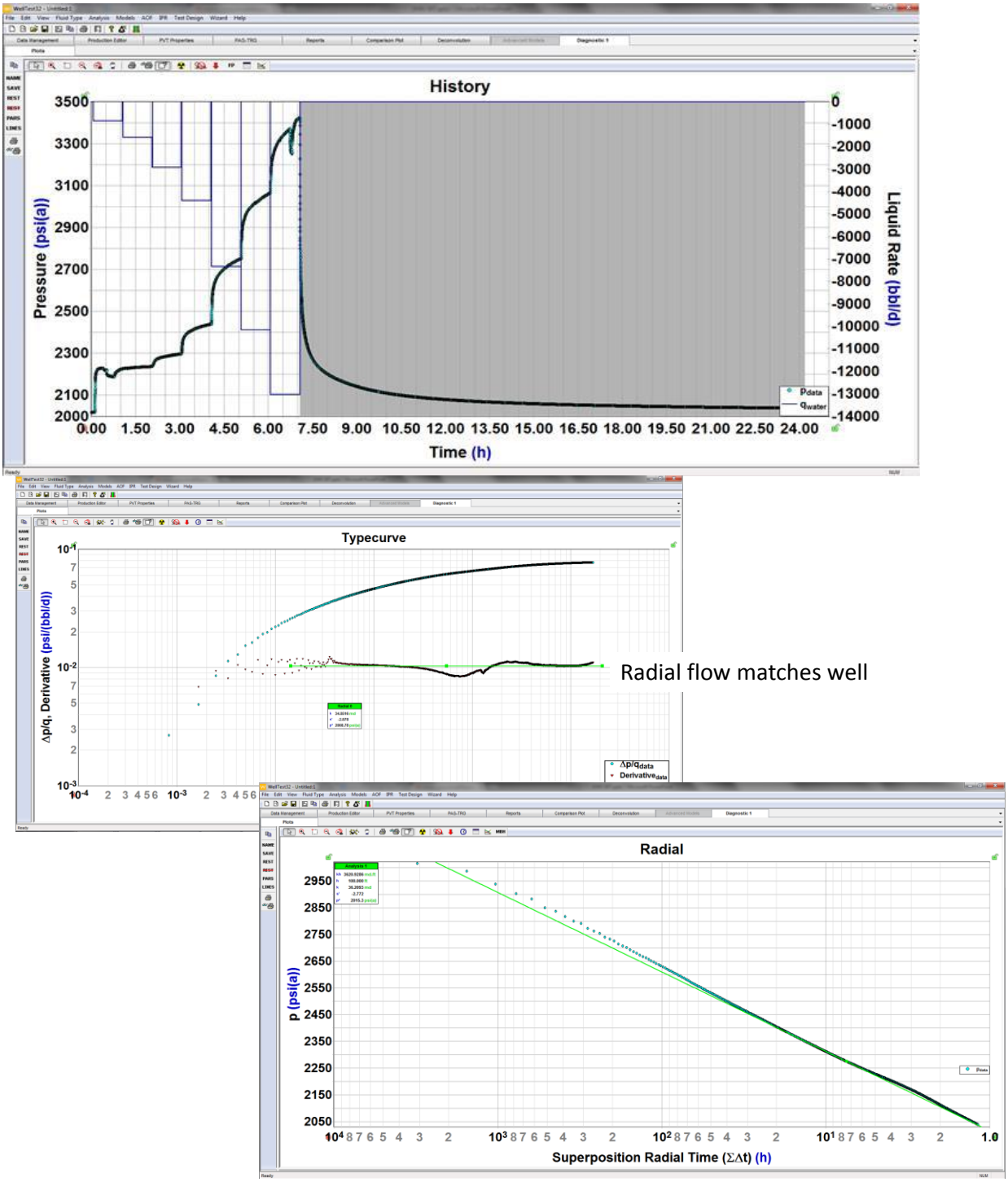

Figure 21: Pressure transient analysis indicates Radial flow during pressure-fall-off in well DOE#1

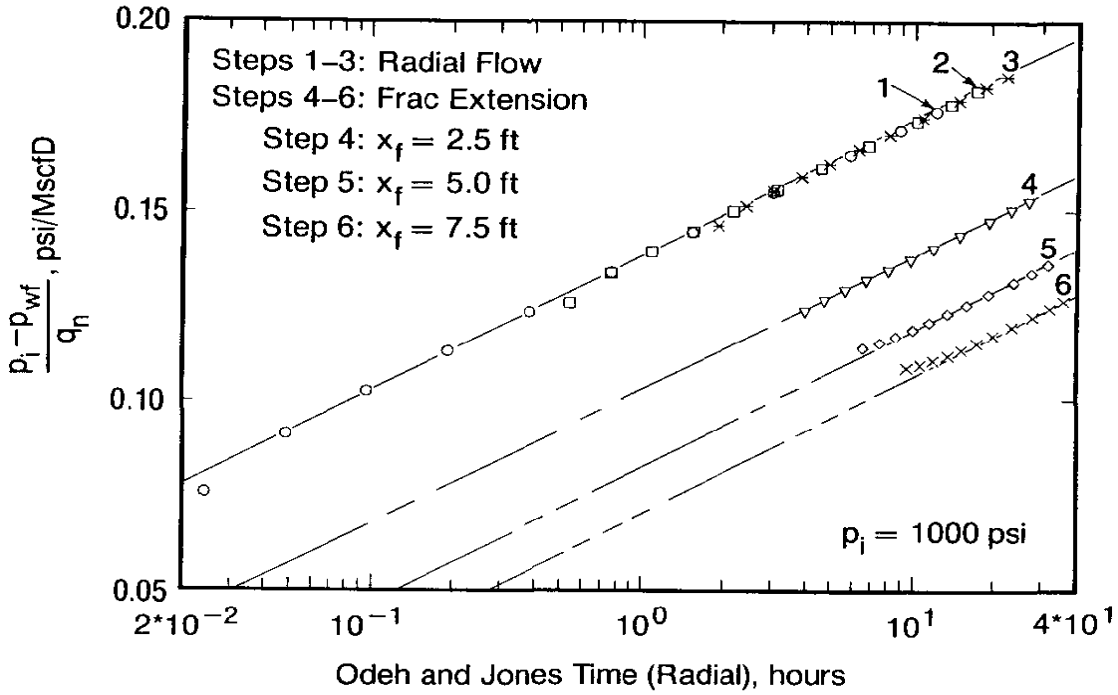

Figure 22: Odeh and Jones multirate analysis of simulated data, from Singh et al. (1987) figure 3

We repeated the step rate test on September 22, 2014 and similar radial flow behavior was observed. A plot of the ending step pressure (after 60 minutes) versus rate for August 1 and September 22 is presented in Figure 23.

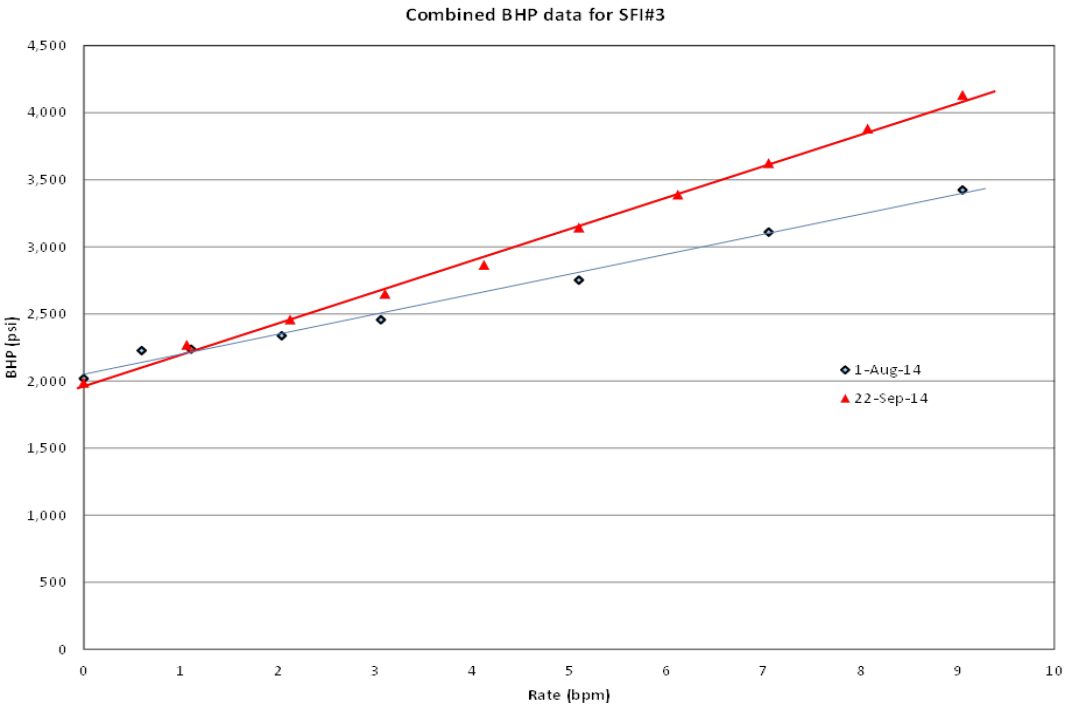

Figure 23: Step rate pressure versus rate for well DOE#1

5.1.2 Wellbore stability analysis for DOE#1 (aka SFI#3)

Once DOE#1 (aka SFI#3) well was drilled, a wellbore stability analysis was performed to optimize the mud weight window based on wells SFI#1, SFI#2 and SFI#3. Drilling experiences, lesson learned and the geomechanics conditions were taken into account to estimate the collapse pressure and define the operational mud density.

5.1.2.1 Drilling Operation Analysis

A statistical analysis from daily reports and multi-arm caliper logs was performed to identify the major incidents and borehole condition related to wellbore instability (Figure 24).

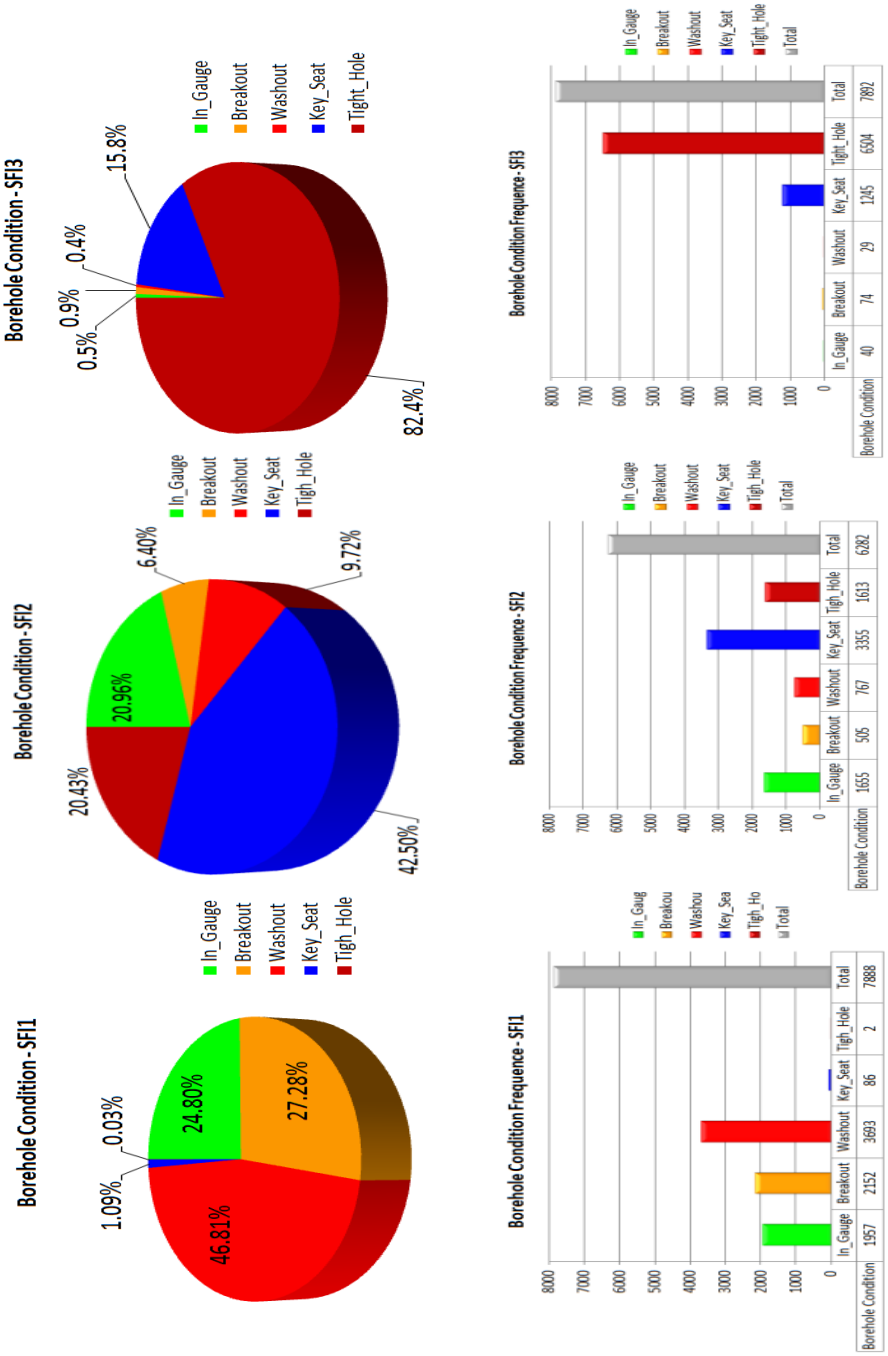

Figure 24: Statistical analysis for borehole condition

As seen in Figure 24, different borehole conditions were identified and the number of frequencies for wells SFI#1, SFI#2 and SFI#3. These figures mainly show wellbore instability in all wells as a consequence of breakout failure, washout, key seat and tight hole. Around 25% was reported as a good borehole condition (In-gauge) and the other 75% represent mainly breakout failure and washout. Furthermore, an algorithm was developed to identify these conditions from 4-arm caliper and to develop a borehole condition map code (Figure 25).

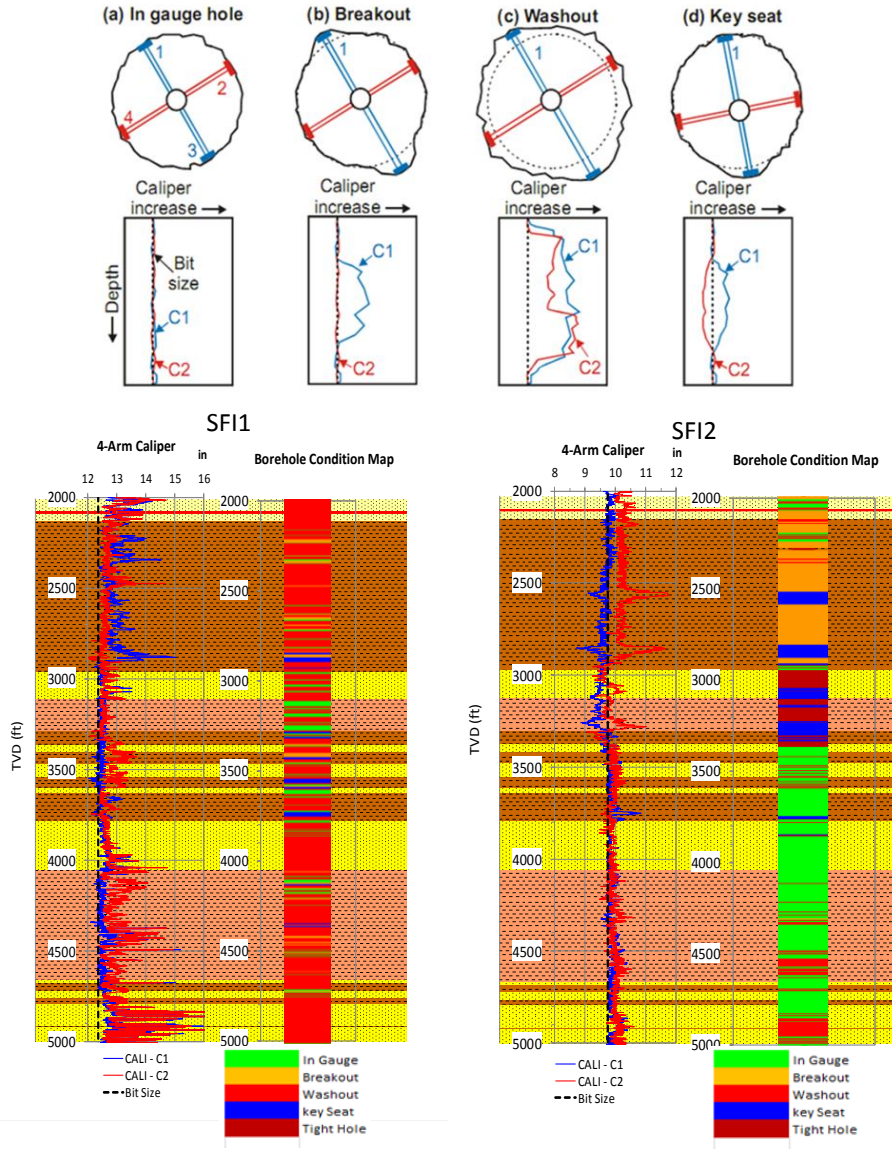

Figure 25: 4-arm caliper and borehole condition map

Based upon these results, a hydraulic and drilling fluid analysis was suggested to improve the borehole cleaning and rock mechanical stability. Drilling fluid and bit parameters such as yield point, plastic viscosity, carrying capacity index, flow rate, annular velocity, total flow area (TFA) and jet velocity were considered. Figure 26 illustrates some rules of thumb that were taken into account to evaluate the hydraulic parameters. Figure 27 shows the plastic viscosity and yield point impacted on carrying capacity index which is related to borehole cleaning. Thus, when it is less than 1, a poor hole cleaning takes place and conversely, when it is higher than 1, a good hole cleaning is obtained. In general, a good hole cleaning were performed, except from well SFI#3 that shows a poor hole cleaning at 1524 m (5000 ft) due to higher plastic viscosity and yield point.

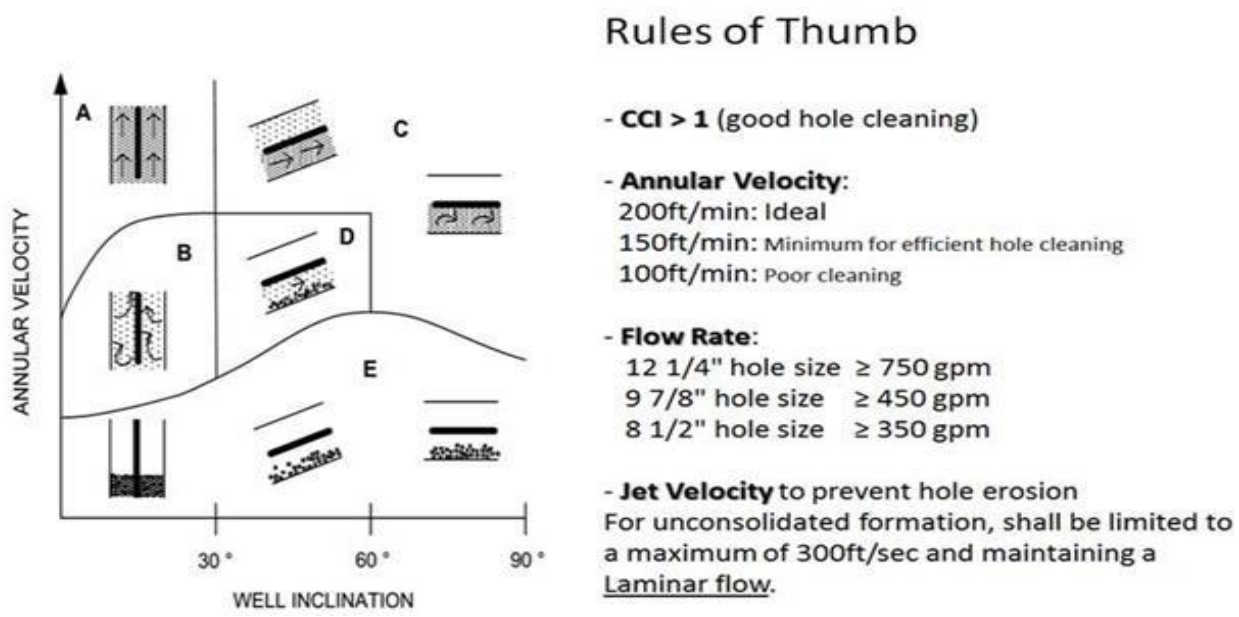

Figure 26: Optimum hydraulic parameters. (from API, 2010)

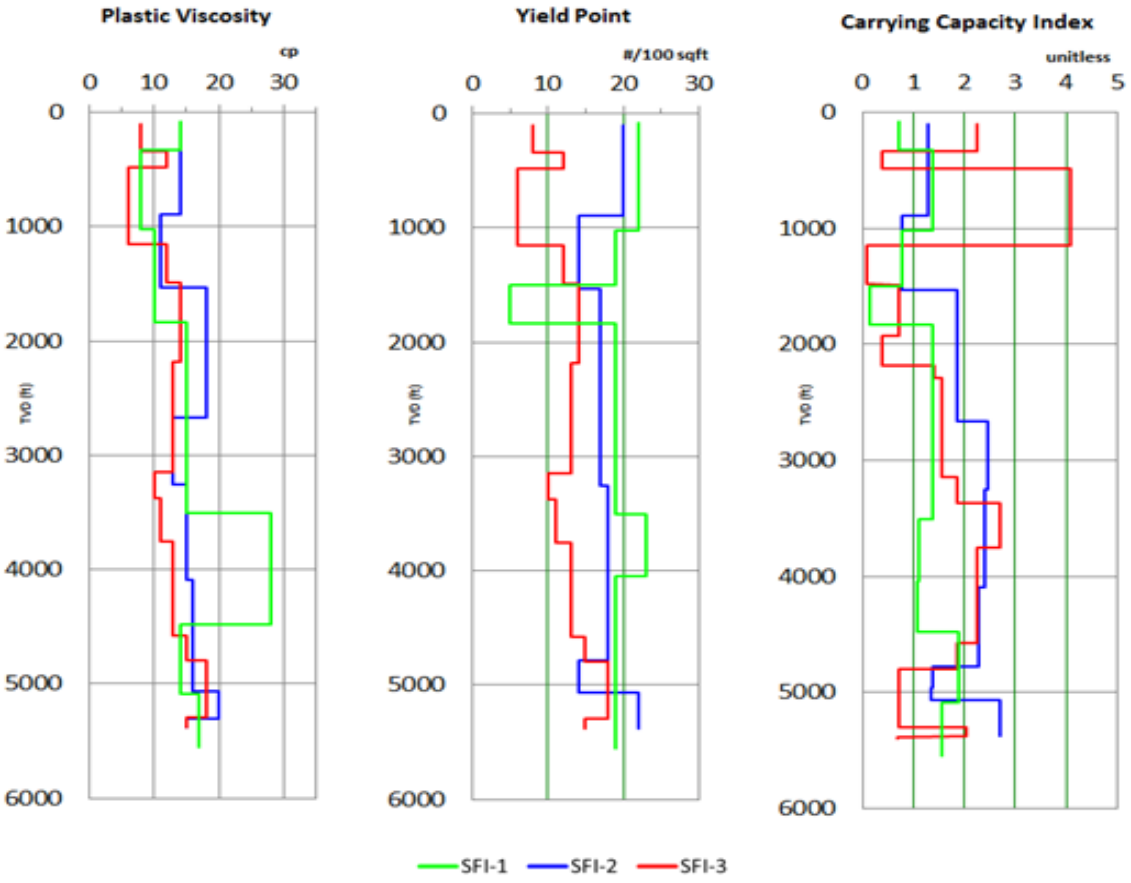

Figure 27: Plastic viscosity, yield point and carrying capacity index

On the other hand, Figure 28 represents borehole configuration, bit and nozzle sizes that impact borehole cleaning. Changes on bit nozzle sizes resulted in an optimum jet velocity between 45.72 m/s (150 ft/s) and 91.44 m/s (300 ft/s) for all wells (Figure 29), reducing the risk of erosion.

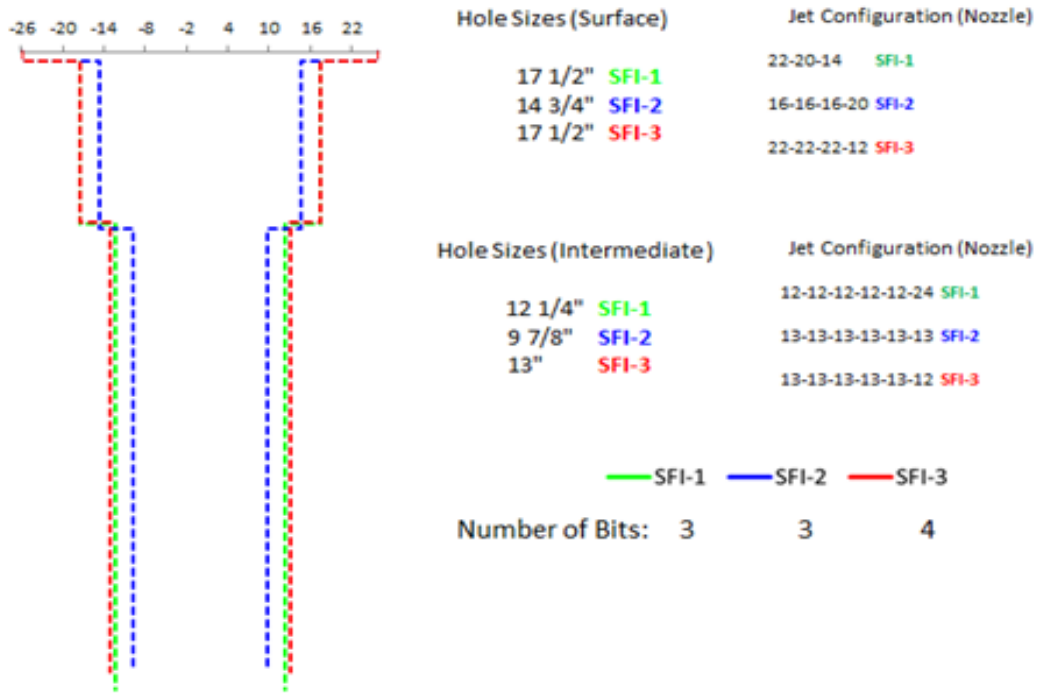

Figure 28: Borehole configuration, bit and nozzle sizes

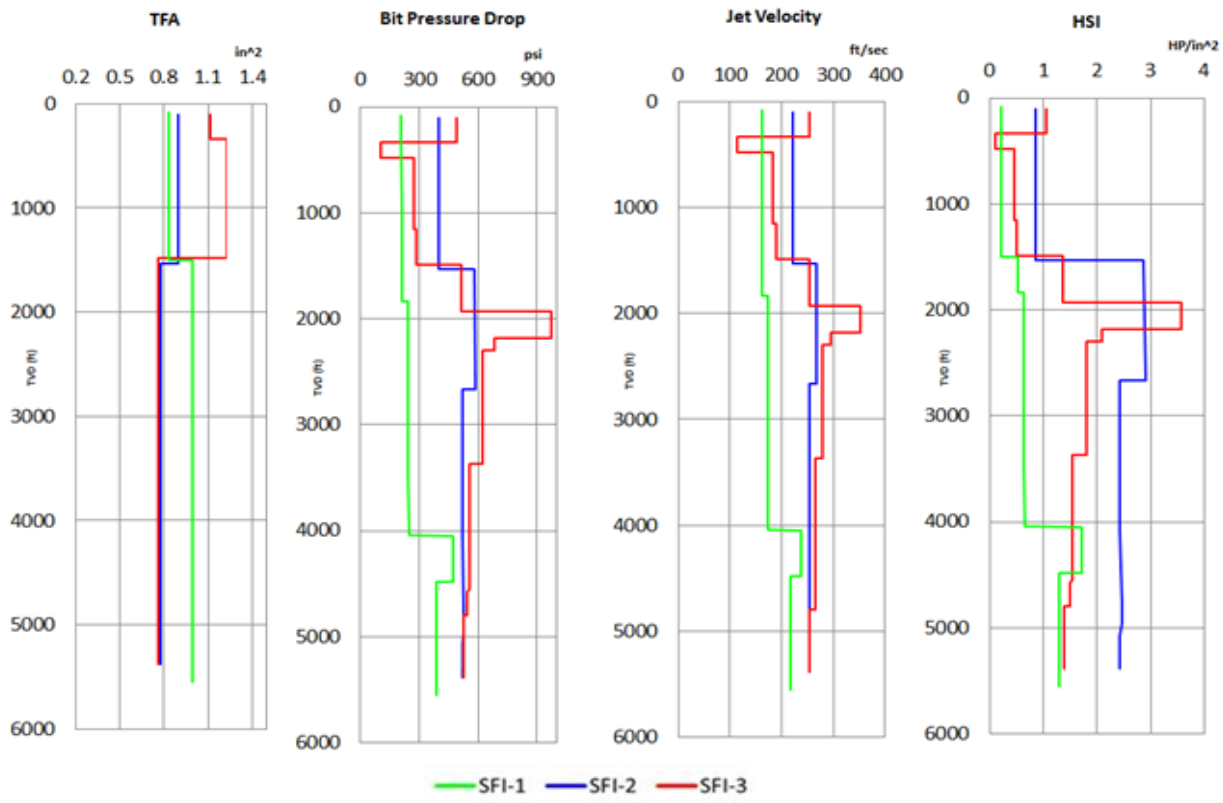

Figure 29: Hydraulic parameters

5.1.2.2 Collapse pressure and mud window

Once the drilling operation was analyzed, collapse pressure was estimated to define the mud window. It was determined by Modified Lade criterion, which is a three dimensional and less conservative failure criterion comparing with Mohr Coulomb that neglects the effect of the intermediate stress. This can be expressed as:

$$\frac{(I_1')^3}{(I_3')} = 27 + \eta$$

$$I_1' = (\sigma_1 + S - P_p) + (\sigma_2 + S - P_p) + (\sigma_3 + S - P_p)$$

$$I_3' = (\sigma_1 + S - P_p) \cdot (\sigma_2 + S - P_p) \cdot (\sigma_3 + S - P_p)$$

$$S = S_o / \tan\phi$$

$$\eta = 4\left(\tan^2 \phi\right).\left(9 - 7\sin\phi\right)/\left(1 - \sin\phi\right)$$

Where η and S are material constant and are related to the cohesion and the internal friction angle (ϕ), respectively.

Figure 30 shows an example of collapse pressure for well SFI#1. Similar analysis was performed for well SFI#2. As noted, the actual mud weight (light blue curve) is lower than collapse pressure (green curve), resulting in wellbore instability (Figure 30a). Sensibility analysis with different breakouts sizes (0°, 30°, 60° and 90°) was done for collapse pressure. As breakout sizes increase, collapse pressure decrease (Figure 30b). Based on the actual mud weight of 1.08 s.g. (9 ppg), shear failure of 90° breakout size took place.

In addition, other issue was identified in this stratigraphy/lithology column related to borehole instability. The fact that there is shale/sand interbeds with changes on collapse pressure represent a challenge for drilling operations. Therefore, drilling fluid density should be designed to keep the wellbore as stable as possible, reducing the risk of either higher overbalance that can lead to loss circulation or lower underbalance that can result in shear failure and influx.

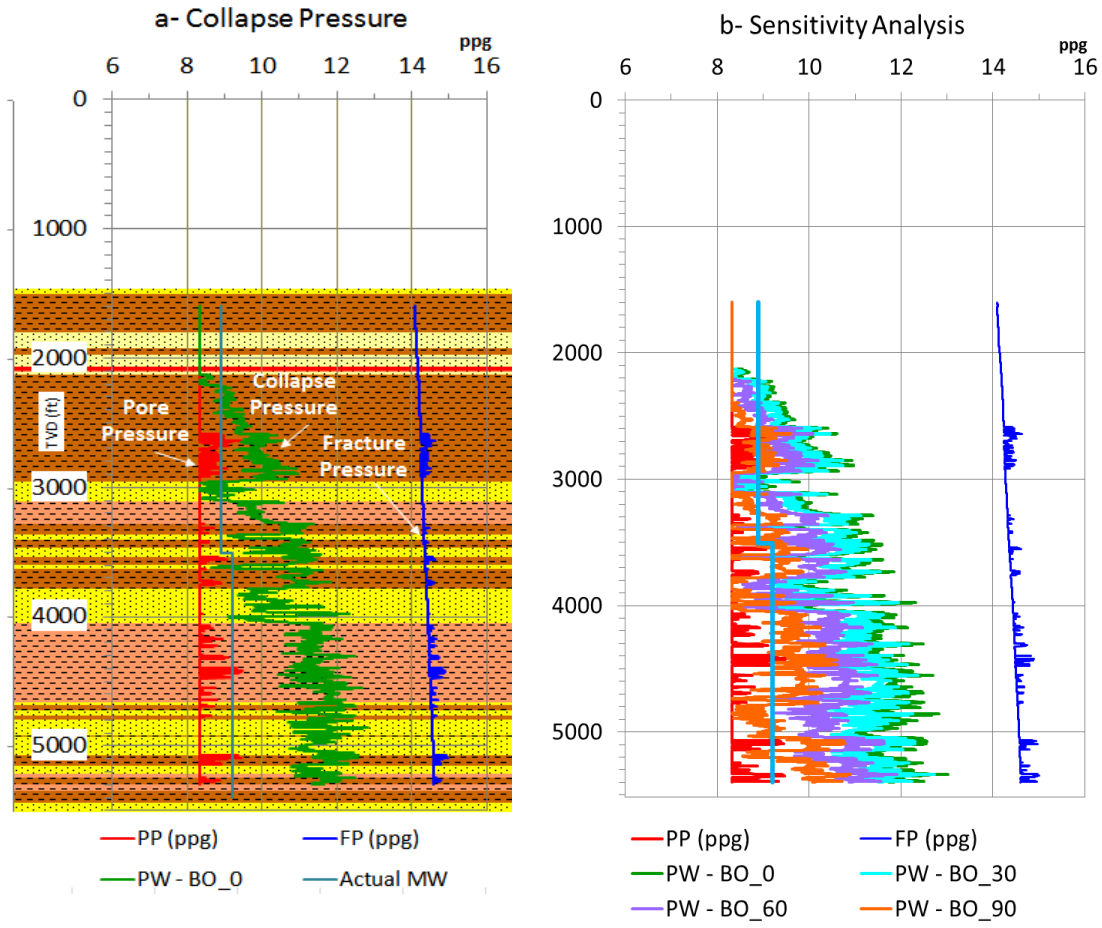

Figure 30: Collapse pressure (a) and sensibility analysis (b) for well SFI#1

Based on the wellbore stability result, 4 zones were identified for performing the mud window (Figure 31). As seen, an actual mud weight of 1.08 s.g. (9 ppg) was identified on the shear failure zone, leading to wellbore failure. Thus, an increase in drilling fluid density from 1.08 s.g. (9 ppg) for the shear failure zone to 1.32 s.g. (11 ppg) for the safe zone is suggested to mitigate this issue. Figure 32 shows a mud window in accordance with the shear failure risk level.

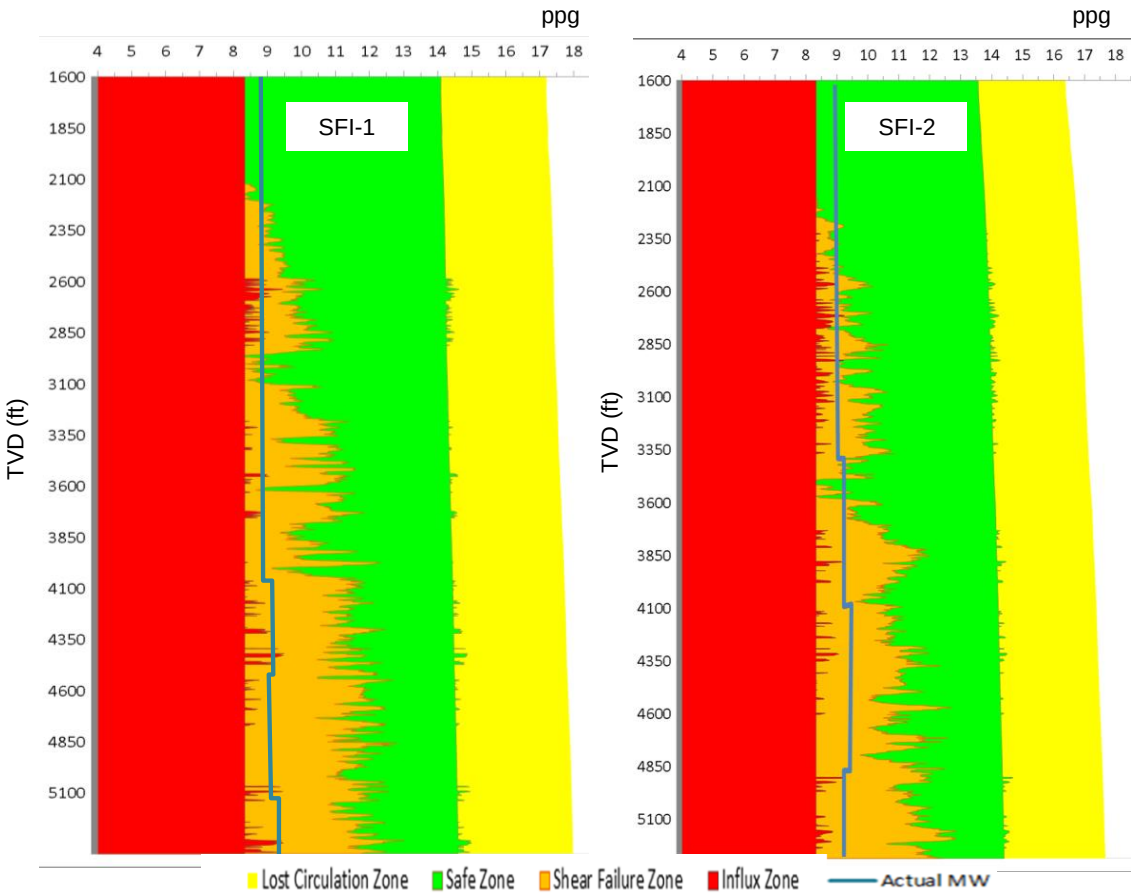

Figure 31: Mud window for wells SFI#1 and SFI#2

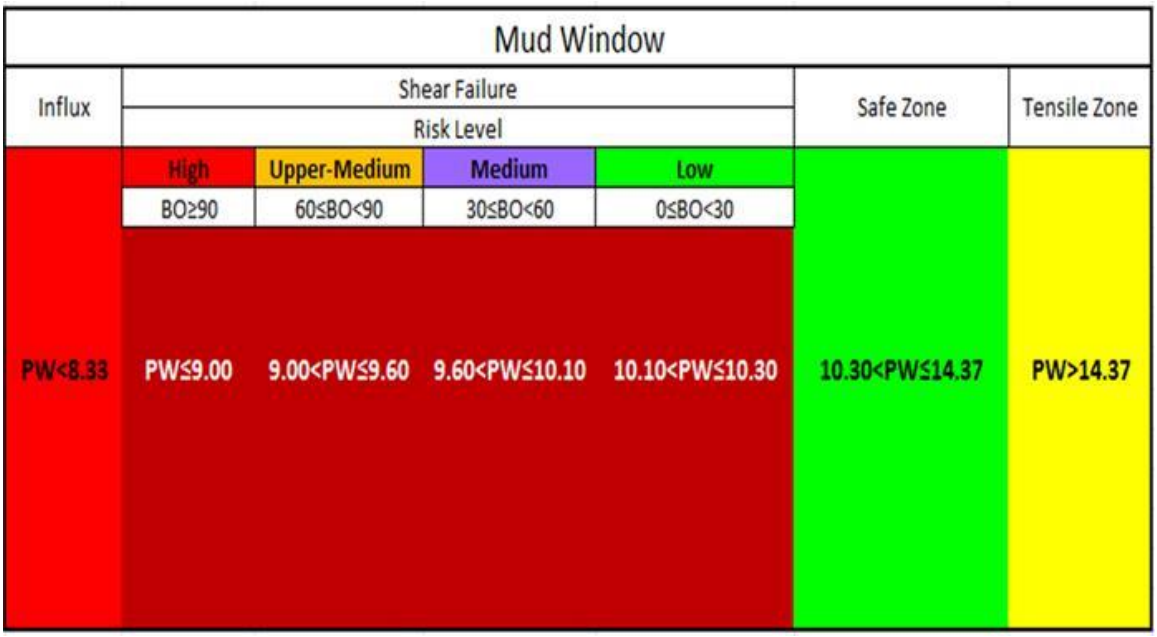

Figure 32: Mud window based on shear failure risk level for well SFI#3

5.2 DOE# 2 well

Well DOE#2 was designed to test the Miocene formation in the northern Wilmington Graben. DOE#2 (also known as SFI#4) deviated well commenced drilling on Feb. 27, 2014 and finished March 18, 2014. This well drilled to MD 2331 m (7650 ft) , TVD 2290 m (7516 ft) and hit Miocene top at MD 1981 m (6500 ft) from paleontologic correlation. Additional lower Pliocene and upper Miocene sands were found. Drill cutting samples were collected and analyzed for mud log and paleontologic identification. Again a complete suite of logs were ordered (including Spontaneous Potential, Gamma Ray, Density, Neutron, Dipmeter, and Cement bond). The well schematic for DOE#2 is shown in Figure 33.

The well was completed during July, 2014 and we recovered 38 out of 45 sidewall cores ordered. This well was perforated between 1418 m to 1431 m (4655 ft to 4695 ft) into the Pliocene turbidites sands and shales. Table 7 summarizes the porosity and permeability on the DOE#2 well. Approximately 120 m (400 ft) of additional lower Pliocene and 45 m (150 ft) of upper Miocene sands were recorded in DOE#2 well logs that can be used for CO_2 storage. The amount of sand interval discovered within the lower Pliocene - upper Miocene exceeded initial baseline estimates.

Table 7: Permeability and porosity summary for DOE#2 well

Repetto Formation Pliocene	Permeability md	Porosity Percent	**Puente Formation** Miocene	Permeability md	Porosity Percent
sand	28.6-300	28.4-37.1	sand	4-<100	26.3-28.9
shale	2	28.9	shale	<5	29.2
shale include/visible fracture(s)	2-27.5	28.9-38.5	shale include/visible fracture(s)	<5-255.5	23.1-33.3

In situ pressurized samples collected from 1414 m (4640 ft) and analyzed show the formation fluid contained 0.51 - 0.77 mole % of CO_2 and 91.96 to 94.9 mole % CH_4, salinity recorded at 17,200 to 17,300 ppm and reservoir pressure at 14.11 MPa (2047 psi).

Table 8 summarizes the fluid analysis and is the well schematic for DOE#2.

Table 8: Geochemical analysis of in situ pressurized formation fluid sample from DOE#2

	Formula	**Mole wt**	**SFI#4**	
			sample 1	sample 2
			7/26/2014	7/26/2014
Depth (ft)			4640	4640
Sample captured (cc)			580	580
Salinity (ppm)			17300	17200
GLR (scf/stb)			6	6
density (g/cc)			1.021	1.02
Reservoir Pressure (psi)			2047	2047
Temperature (F)			170	170
pH @25C (or specified)			7.21@22C	7.32@22C
UNIT			mole%	mole%
CO2	CO2	44.1	0.51	0.77
H2S	H2S	34.06	0	0
N2	N2	28.01	7.42	4.21
CH4	CH4	16.04	91.96	94.9

Title: Characterization of Pliocene and Miocene Formations in the Wilmington Graben, Offshore Los Angeles, for Large-Scale Geologic Storage of CO_2

PI: Dr. Michael Bruno Final Report

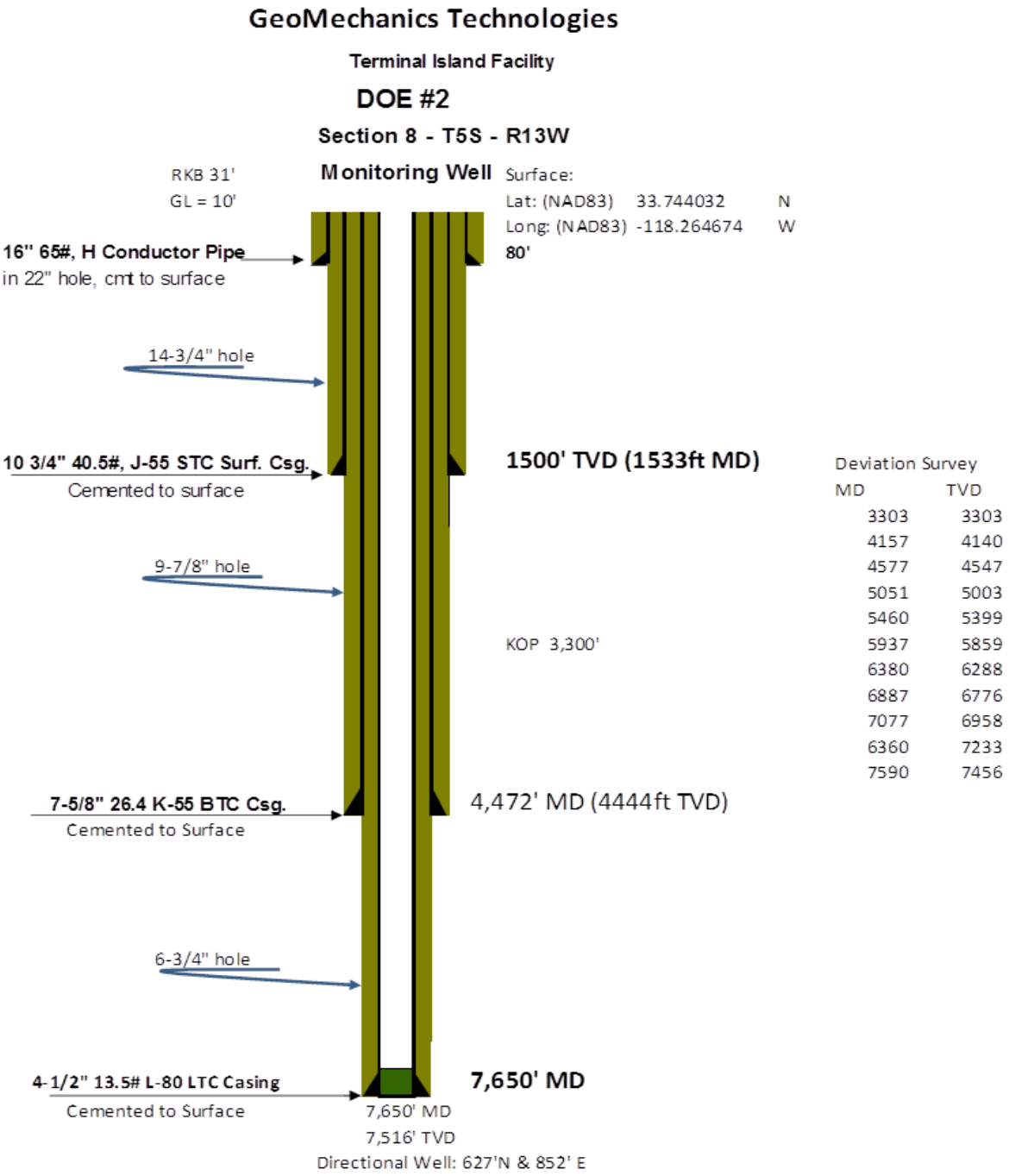

Figure 33: DOE#2 well schematic December 2014

Figure 34 is a picture of the DOE#2 well while drilling.

Figure 34: Well DOE#2 drilled in February, 2014, to further characterize the Miocene formation

5.2.1 Injectivity Test (Step Rate Test)

Similar step rate test was performed for DOE#2 (aka SFI#4) well on August 4, 2014. The pressure sensor was placed at MD 1416 m (4646 ft). We present in Figure 35 and Figure 36 a plot of pressure versus time for the testing conducted in Well DOE#2. Injection proceeded in seven incremental steps, each one hour in length. Table 9 below presents the flow rates and the final pressure at the end of each step. The pressure sensor for this test was placed at a measured depth of 1416 m (4646 ft). As can be seen in Figure 36, at the conclusion of the step-rate test pressure declined rapidly to original reservoir conditions within about two days. Data was recorded for 10 days total.

Table 9: Injection rate and bottom hole pressure for DOE#2 SRT

Injection Rate (bpm)	Bottom Hole Pressure (psi)
0.00	1854
0.60	2025
1.11	2015
2.04	2181
3.06	2419
5.10	2925
7.06	3402
9.05	3894

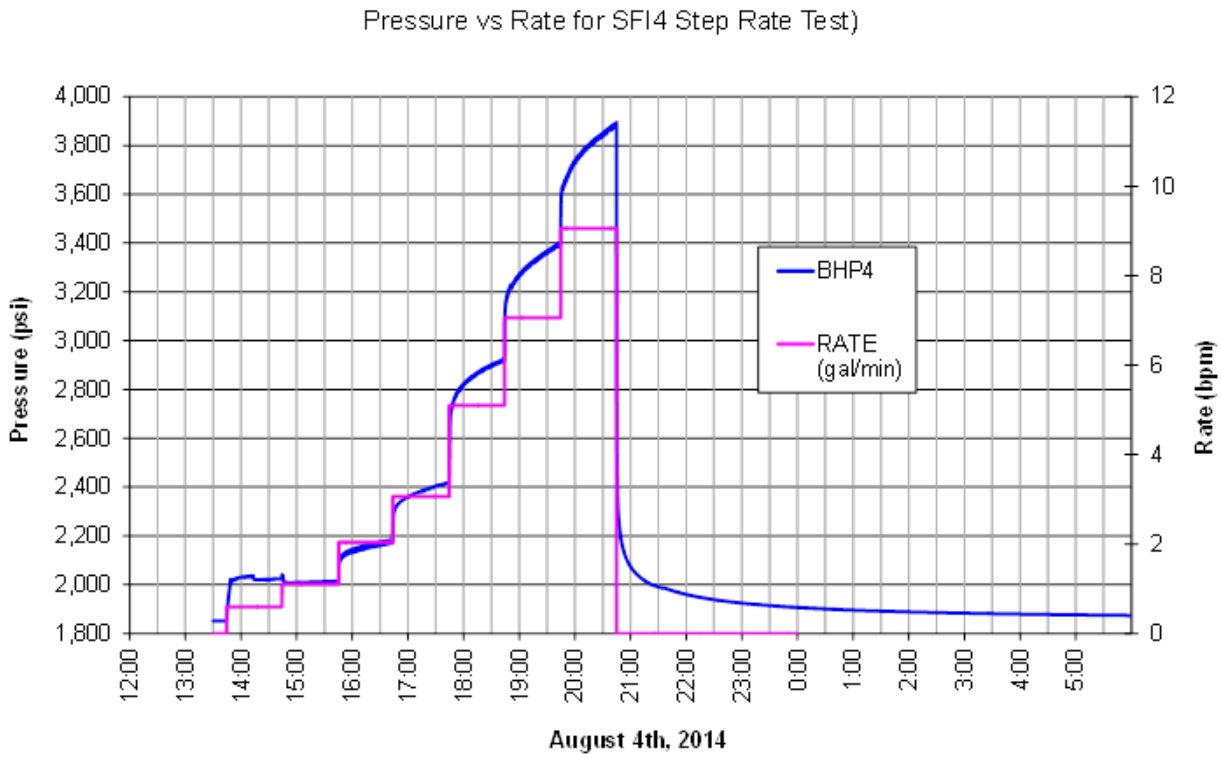

Figure 35: Injection rate and bottom hole pressure recorded during well DOE#2 step rate test.

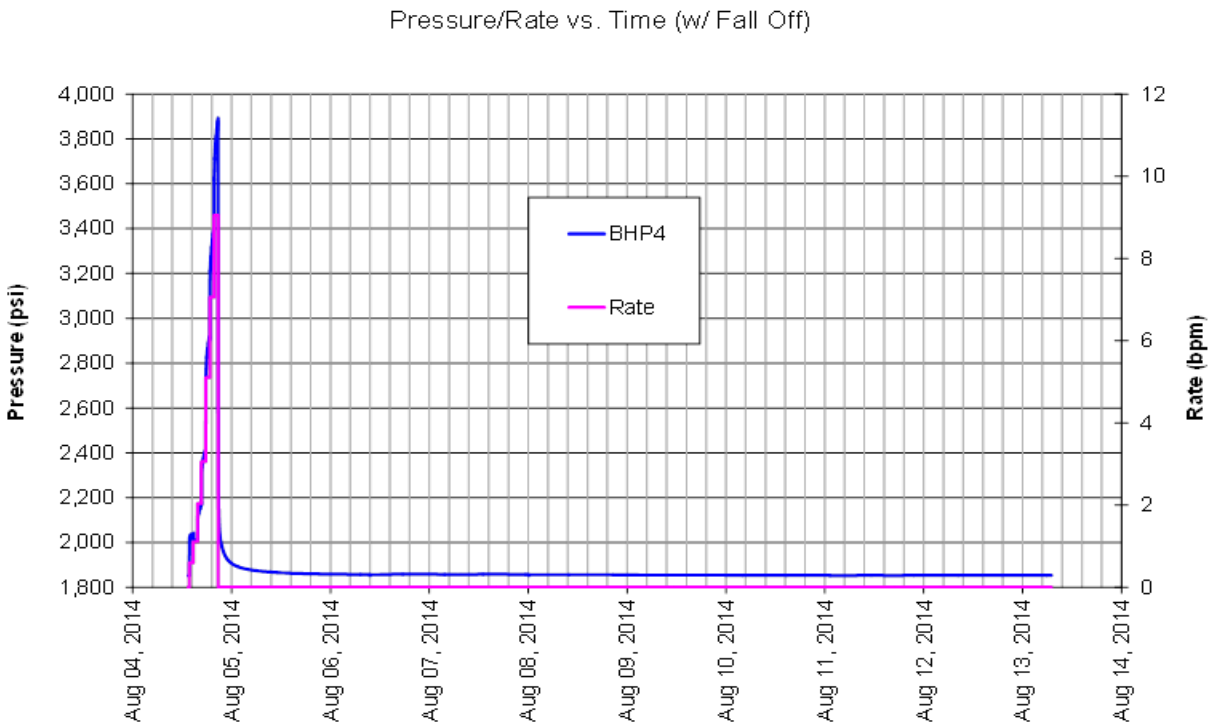

Figure 36: 10 days of fall-off data recorded after DOE#2 step rate test.

We present in Figure 37 a plot of pressure versus rate for the testing conducted in Well DOE#2. After initial breakdown of perforations in Step 1, the remaining data of pressure versus rate is a very linear trend, indicating no change in flow regime. Further transient analyses described below indicate that the flow is radial in nature.

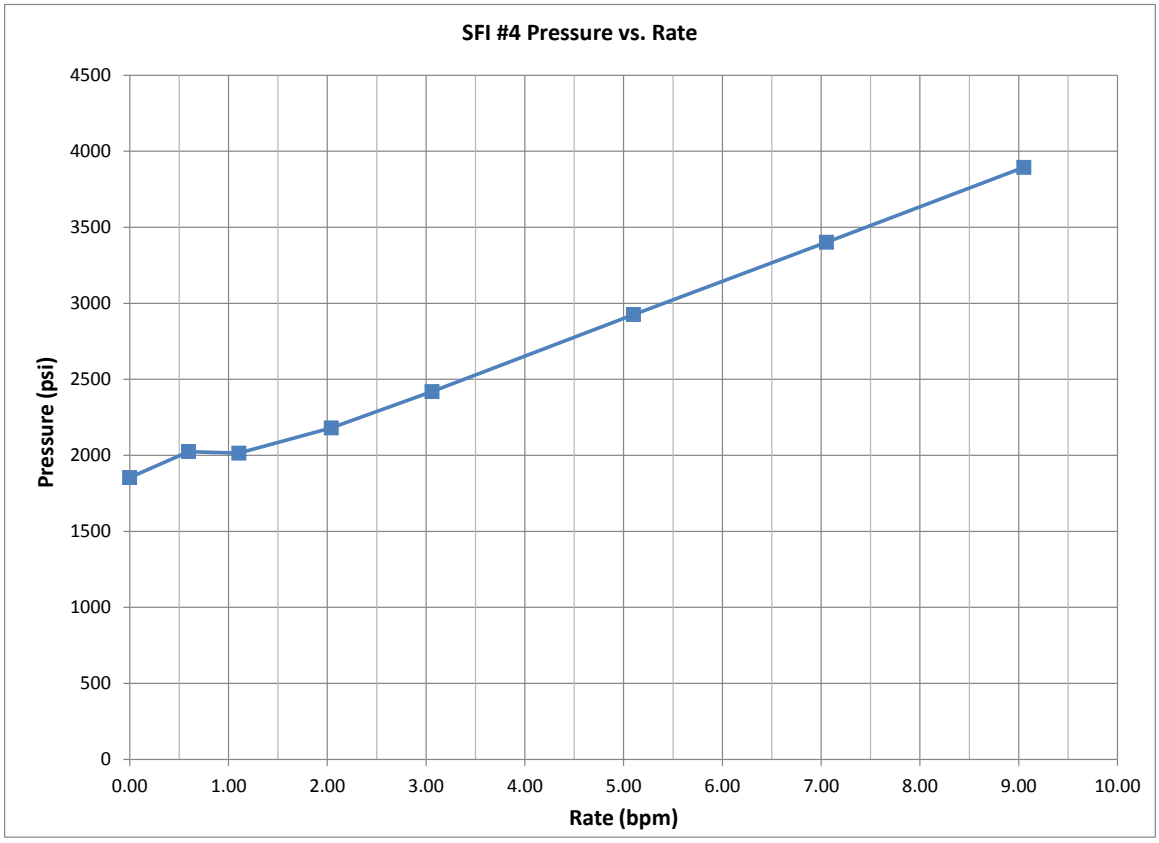

Figure 37: DOE#2 step rate test pressure vs rate data

We next apply pressure transient analysis techniques to analyze the pressure-fall-off after SRT, using the industry standard FEKETE well test analysis software. In pressure transient analysis, an attempt is made to match both the observed pressure versus time and the pressure derivative versus time, while varying the flow model (radial for matrix flow or linear for fracture flow). As indicated in Figure 38, the pressure-fall-off analysis clearly indicates radial flow behavior.

Title: Characterization of Pliocene and Miocene Formations in the Wilmington Graben, Offshore Los Angeles, for Large-Scale Geologic Storage of CO_2

PI: Dr. Michael Bruno Final Report

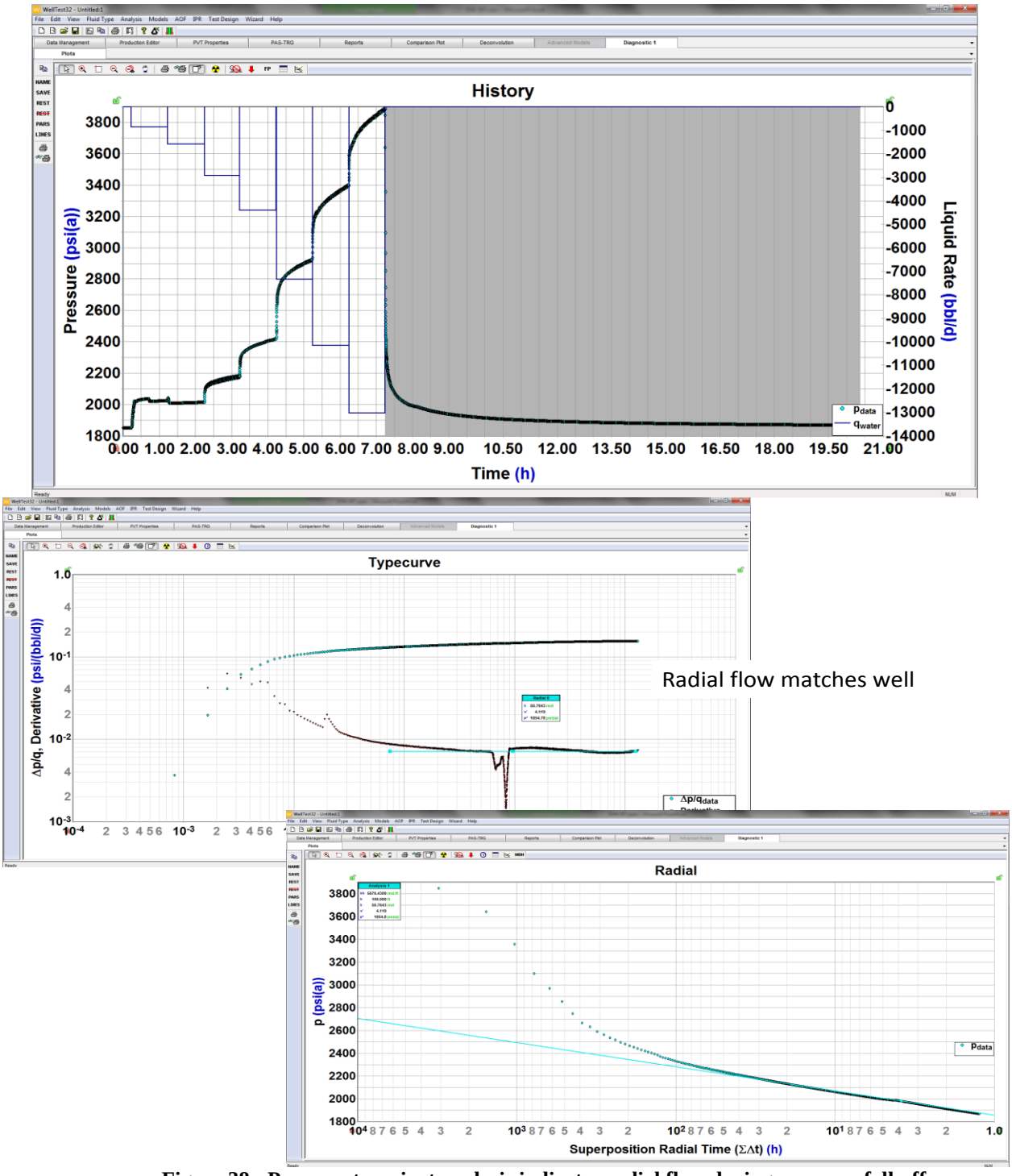

Figure 38: Pressure transient analysis indicates radial flow during pressure-fall-off

Odeh and Jones method for multi-rate analysis:

Next we again apply the Odeh and Jones multi-rate analysis technique as described in Singh et al. (1987). SFI#3's SRT data was plotted and illustrated in Figure 39.

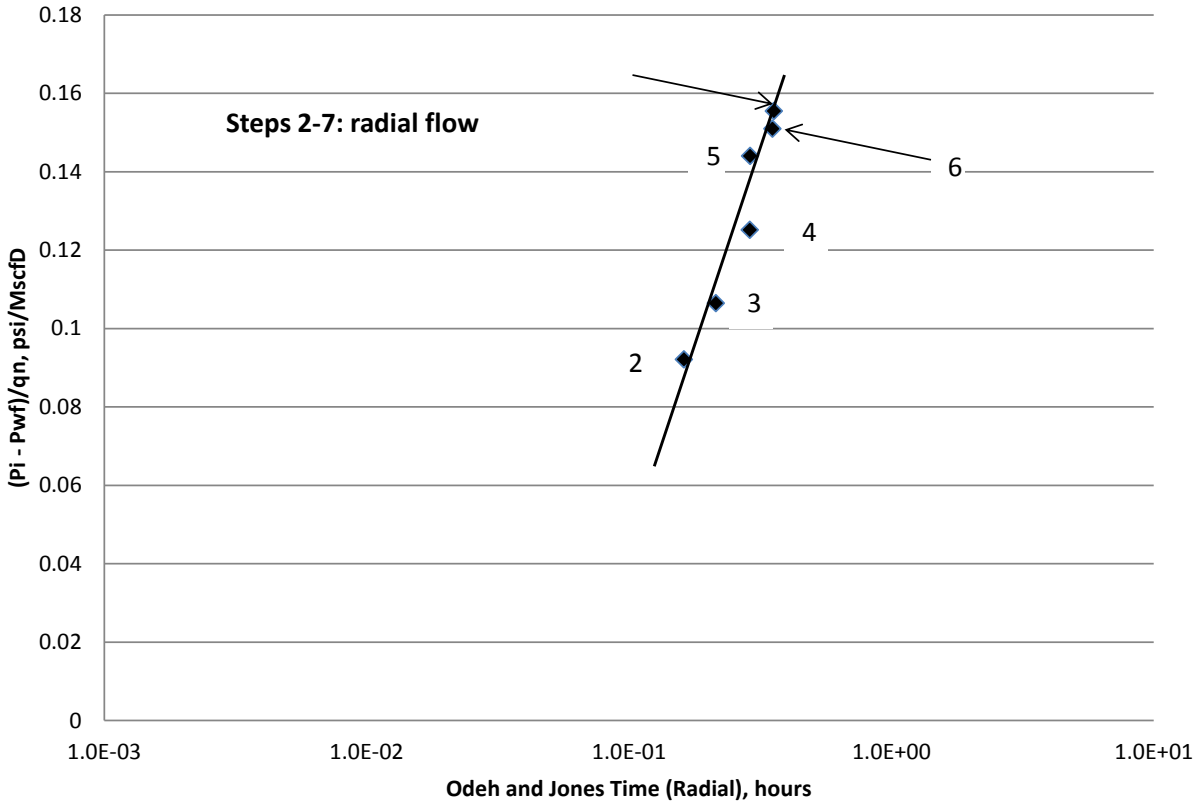

Figure 39: Odeh and Jones multirate analysis of DOE#2 SRT data

This data may also be compared to the Odeh and Jones analysis plot from Singh et al. (1987), where all the radial flow steps fall on a single straight line (step 1,2,3), and a downward shift of data points is observed when the fracture is propagating (step 4,5,6).

Comparing Figure 39 and Figure 22, steps 2 to 7 fall on a straight line, which indicates radial flow behavior. Step 1 is affected by initial wellbore fill-up and perforation breakdown. This analysis is also consistent with the analysis results of FEKETE.

5.2.2 Wellbore stability study

As part of the wellbore collapse model, a statistical analysis was performed to identify drilling events related to borehole condition. Figure 40 shows the results for DOE#2 (aka SFI#4), with a favorable condition in-gauge of 60%. Comparing with SFI#1, SFI#2 and SFI#3 wells, there was a 35% significant optimization.

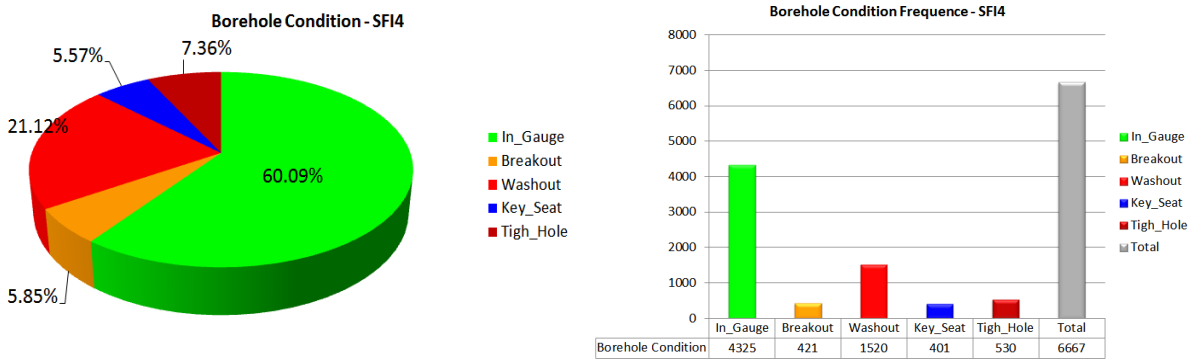

Figure 40: Borehole condition statistic for well SFI#4

In addition, a 4-arm caliper and borehole condition map can validate the fact mentioned above as illustrated in Figure 41. Note that both arm calipers (C1-C2) are almost closed to the bit size in most of the borehole sections.

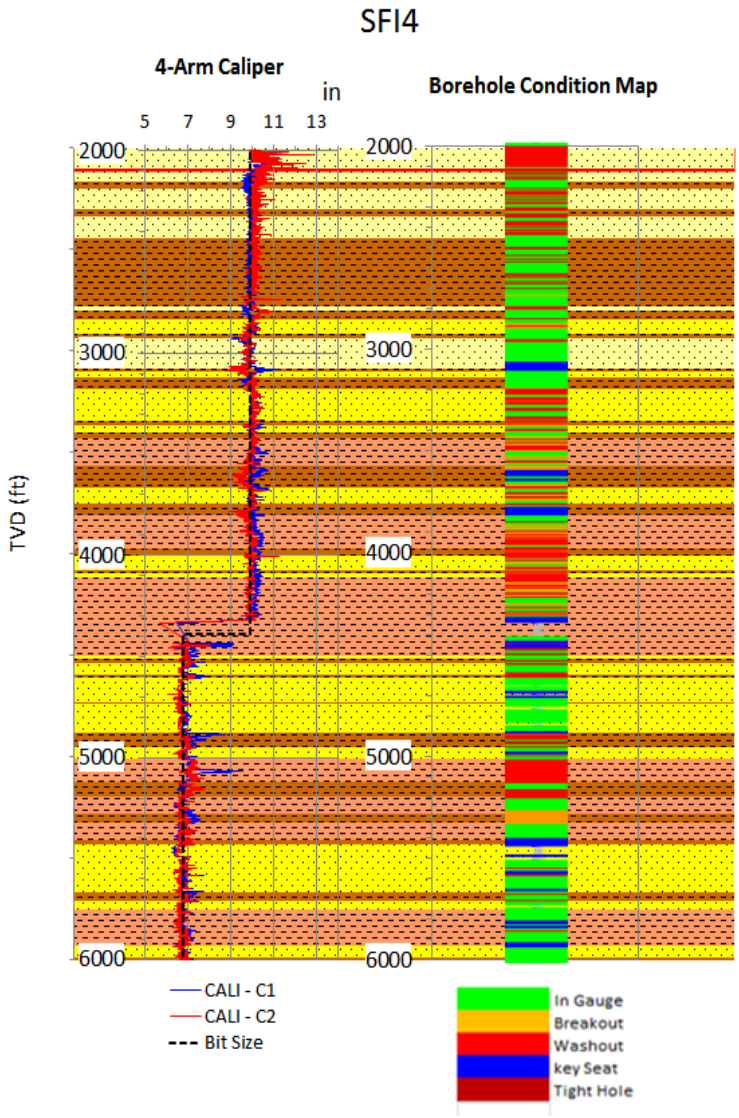

Figure 41: 4-Arm caliper and borehole condition map well SFI#4

After a geomechanics model was run and the drilling experience analyzed, we estimated the collapse pressure. A sensibility analysis was taken into account varying breakout size for 0°, 30°, 60° and 90° (Figure 42). As is well known, breakout failure is one type of shear failure that commonly takes place on borehole when rock strength is exceed by the maximum tangential

stress around wellbore. To mitigate this issue, an optimum mud density should be designed to reduce the wellbore collapse.

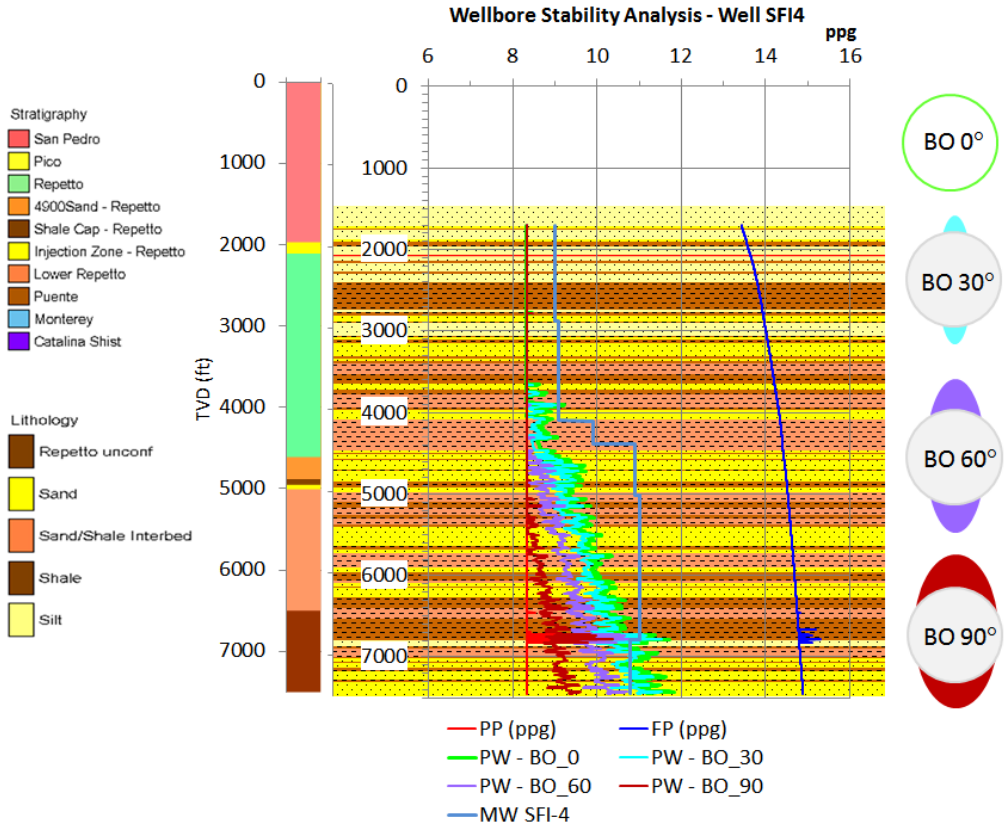

Figure 42: Wellbore collapse for well SFI#4

Note that in most of the cases the actual mud weight is higher than the breakout 0° curve, leading to a safe condition. However, at 2011.68 m (6600 ft) it reaches the breakout 30° curve, which represents a low risk of collapse. Figure 43 shows the mud window and the safe condition.

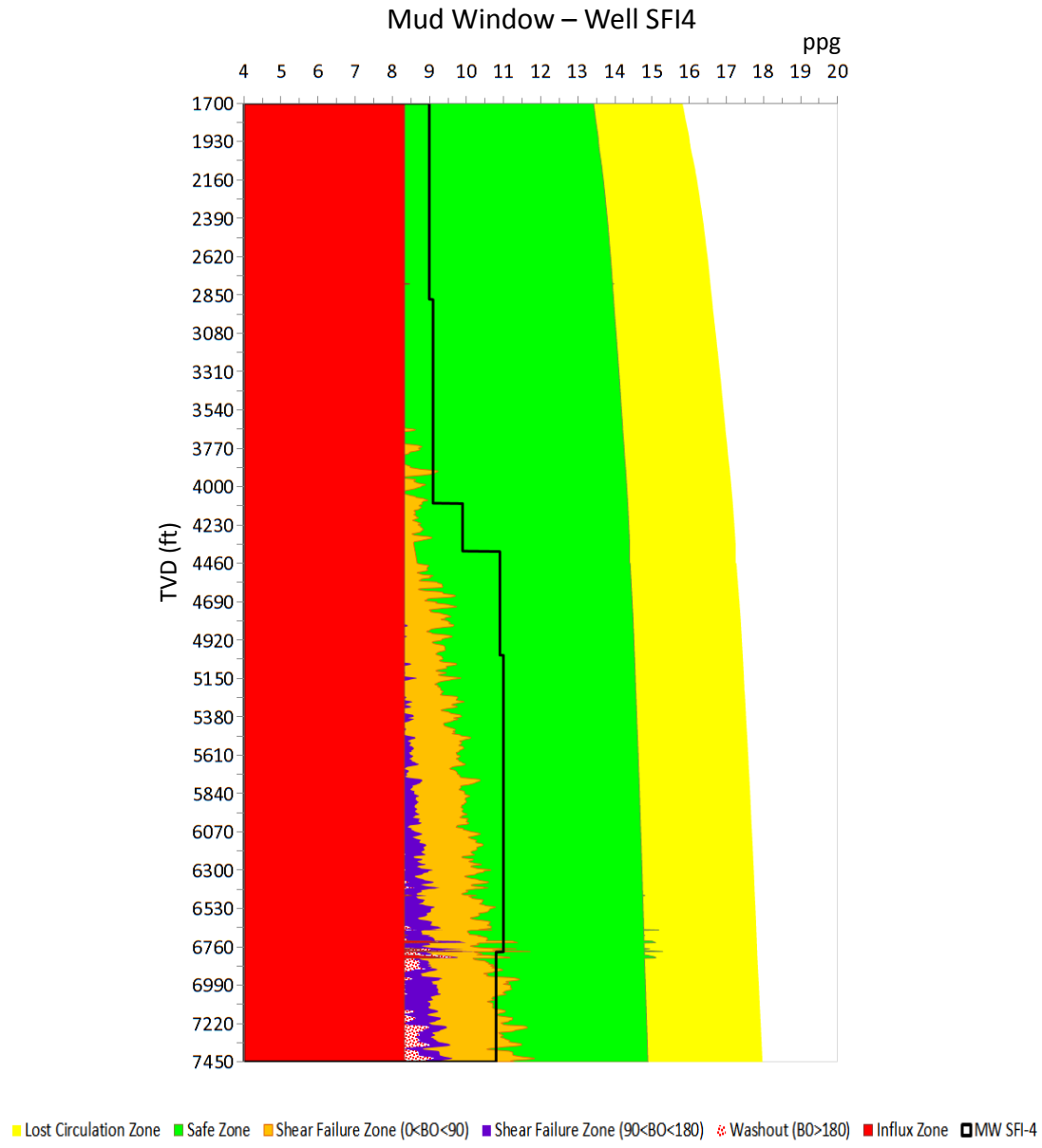

Figure 43: Mud window for well SFI#4

5.3 DOE# 3 well (Deepening of SFI#1 well)

The drilling of DOE#3 which is the deepening of the existing SFI#1 well commenced on Nov. 5, 2014. For safety reason, EPA requested that the existing perforations be squeezed-off

before deepening. While completing the cement squeeze job, the coil tubing got stuck at 1568 m (5146 ft) when pulling out of the hole. Attempts to free the stuck coil tubing were unsuccessful. The coil tubing was cut at 1471 m (4829 ft); however we were unable to release the packer. The cut coil tubing was retrieved during the fishing job performed on Nov. 11, 2014. The 3 ½" casing was subsequently chemically cut at 1566 m (5140 ft). We managed to unseat and retrieve the packer, 103 m (340 ft) of 3 ½" casing (Nov. 22, 2014), and 95 m (311 ft) of the coil tubing (Nov 24, 2014). We continued to mill and drilled through the casing shoe and coil tubing check valve from 1584 m to 1600 m (5188 ft to 5250 ft), and then rotary drilled to 2145 m (7039 ft). While pulling out of hole (Nov. 29, 2014), the drill collars and bit became stuck at 1828 m (6000 ft). Numerous attempts to free stuck drill pipe (including increasing mud weight, decreasing mud weight, use of LVT oil to soak formation etc. – see *Stuck Pipe Analysis* below) were unsuccessful. The top of fish was spotted at 1778 m (5835 ft). On Dec. 2, 2014, string shots were ordered to promote circulation. We managed to run electric logs from 1778 m to 1690 m (5835 ft to 5545 ft) to the casing shoe. We have a mud log and paleo analysis to TD 2145 m (7039 ft). Top of Miocene was picked at TVD 2075 m (6810 ft) by paleo. Analysis of the mud log shows at least 3 extensive sands in the lower Pliocene and one potential sand bed in the Miocene section; however no electric log was available to confirm the thickness. While cementing the 5 ½" liner from 1630 m to 1776 m (5381 ft to 5830 ft), a 4.5 m (15 ft) cement tool was stuck in the cement plug.

The lower part of the well was abandoned. The project ended on December 8, 2014, all field activities ceased. The current well schematic is shown in Figure 44.

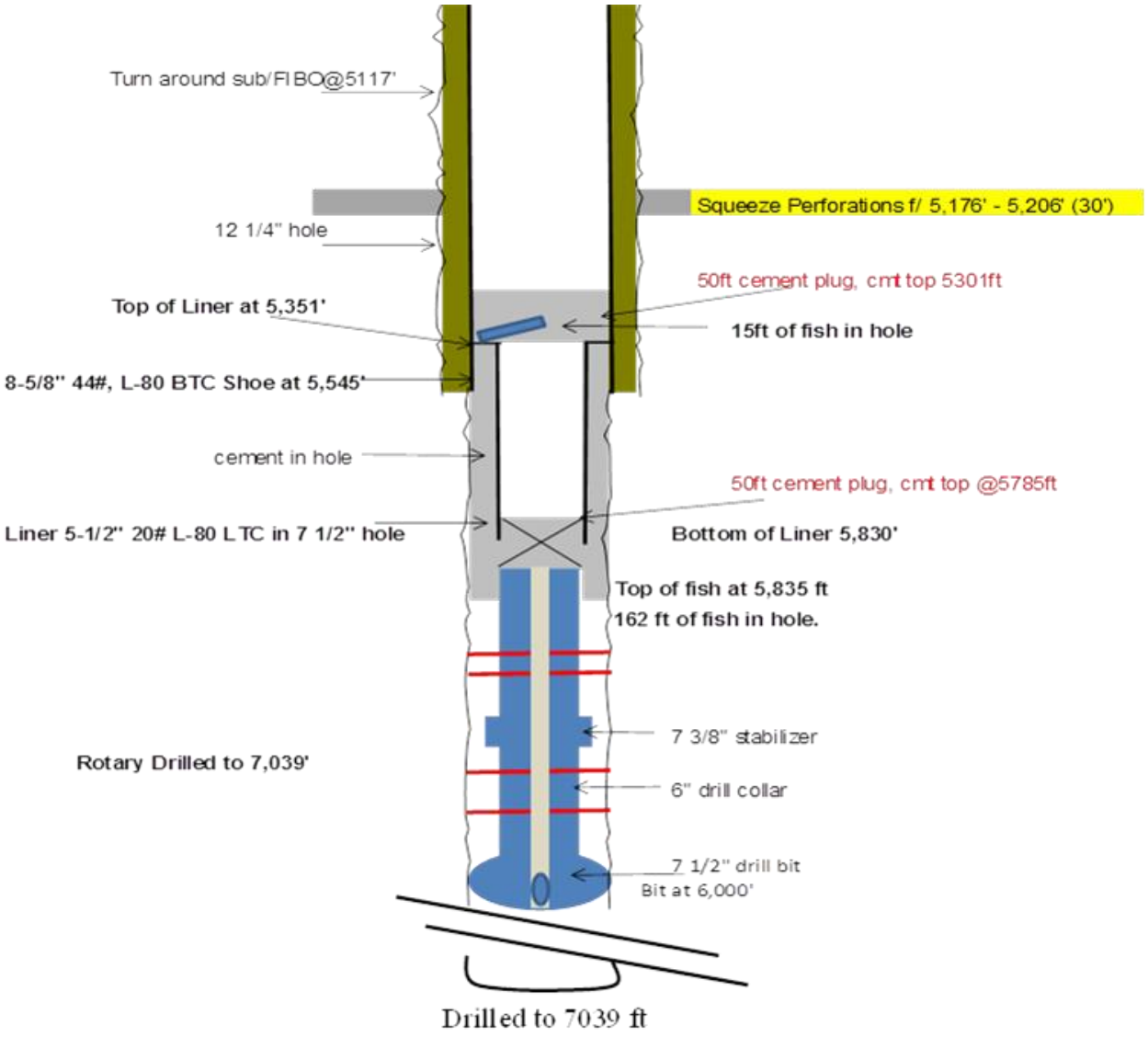

Figure 44: SFI#1 well schematic December 8, 2014

Figure 45 is a picture of the deepening activity during November 2014.

Figure 45: Well DOE#3 (SFI#1 deepening) drilled in November, 2014, to further test the continuity of the Miocene sand

5.3.1 Stuck Pipe Analysis

The main objective for deepening well SFI#1 was based on the experience of well SFI#4, to increase the CO_2 injection storage capability on potential sandstones located in the Miocene section. The original plan involved a new 7 ½" hole to be cased and cemented with a 5 ½" liner seated at 2286 m (7500 ft) (Figure 46a). However, after drilling to 2145.48 m (7039 ft), a

sticking problem emerged when the drill string was tripping out (moving up) at 1828.8 m (6000 ft) as seen in Figure 46b. The hole started to be tight but still full return and circulation was possible after the string got stuck. To mitigate the issue, back reaming was applied and the mud system was conditioned, adding lubricant to reduce the friction. Drilling jars were activated without success. Uncertainty about the stuck pipe mechanism (mechanical or differential sticking) responsible for this issue led to increasing the mud density from 1.32 s.g. to 1.39 s.g. (11 ppg to 11.6 ppg) without successful result. The mud system was then conditioned from 1.39 s.g. to 1.22 s.g. (11.6 ppg to 10.2 ppg). In spite of all efforts, the drill string remained stuck. A fishing operation was conducted and 49.37 m (162 ft) of fish was left in the hole as indicated in Figure 46b.

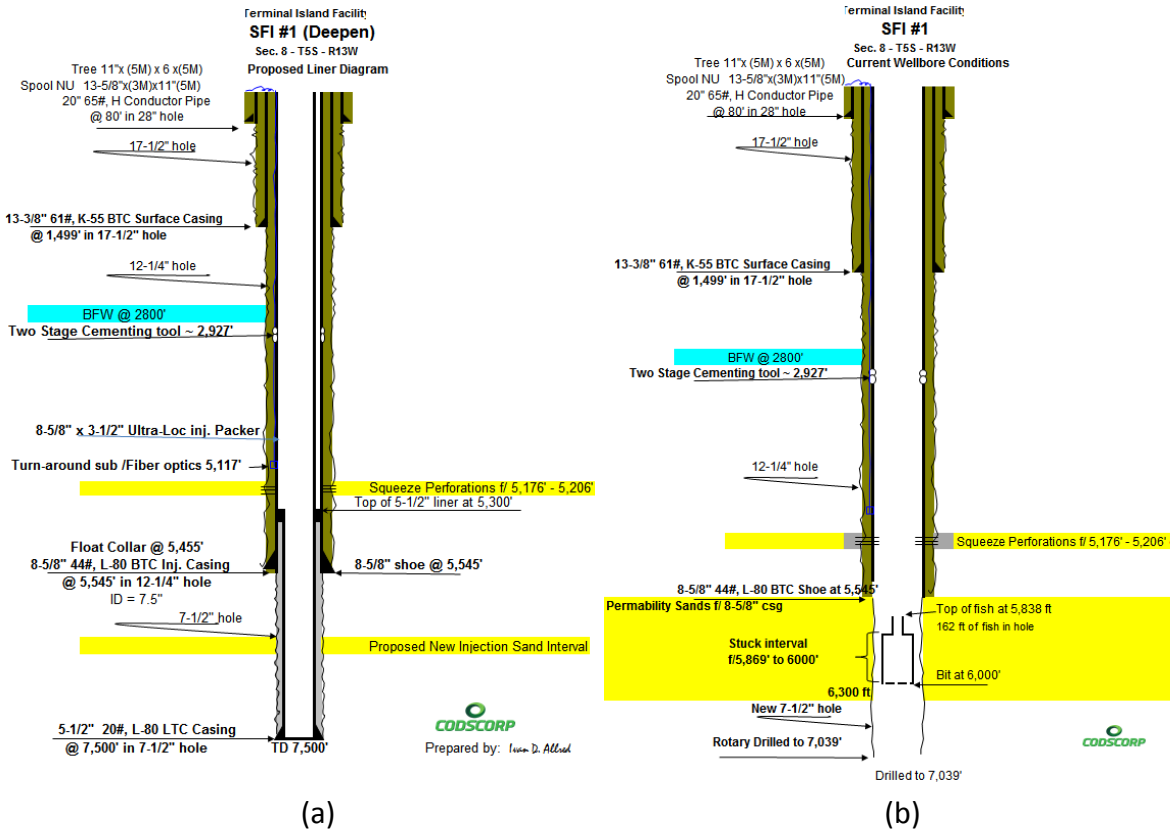

Figure 46: Well scheme plan for deepening well SFI#1 (a) and current wellbore condition after stuck pipe (b)

The main objectives of this analysis is to assess the actions that were applied to mitigate this issue, analyze the borehole condition before and after the stuck pipe, identify the principal stuck pipe mechanism (causes and consequences) and summarize the lesson learned and conclusions.

5.3.1.1 Review of drilling operation before the drill string stuck

Based on the daily drilling report, the most critical intervals before the drill string sticking are as follows:

Interval 1604.46 m – 1729.74 m (5264 ft – 5675 ft):

During rotary drill 7 ½" hole from 1604.46 m to 1693.16 m (5264 ft to 5555 ft), mud was severely contaminated with cement. Low rate of penetration was reported between 9.14 m/hr and 12.19 m/hr (30 ft/hr and 40 ft/hr) from 1693.16 m to 1729.74 m (5555 ft to 5675 ft). One hour of circulation and condition mud was performed for clean out. A minimum of two hours of circulation should be done to guarantee an effective hole cleaning. It could lead to pack-offs and bridges for cement blocks, one of the main causes of mechanical sticking.

Interval 1690.11 m – 1793.44 m (5545 ft – 5884 ft):

Due to the bit shanks worn down (out of gauge) caused by the continuous existence of cement, a new drill string with a different configuration was run in the hole. Reaming down from 1690.11 m to 1793.44 m (5545 ft to 5884 ft) was done because the hole was a little out of gauge for a worn bit. A 7 ½" stabilizer was added in the new Bottom Hole Assembly (BHA). Figure 47 shows the two BHAs that were used from 1604.46 m to 2145.48 m (5264 ft to 7039 ft). In this section, wellbore geometry was affected by low performance on the bit due to cement. Moreover, the 7 ½" stabilizer after the two drill collars (Figure 47b) could have resulted in lower drilling performance with poor borehole geometry.

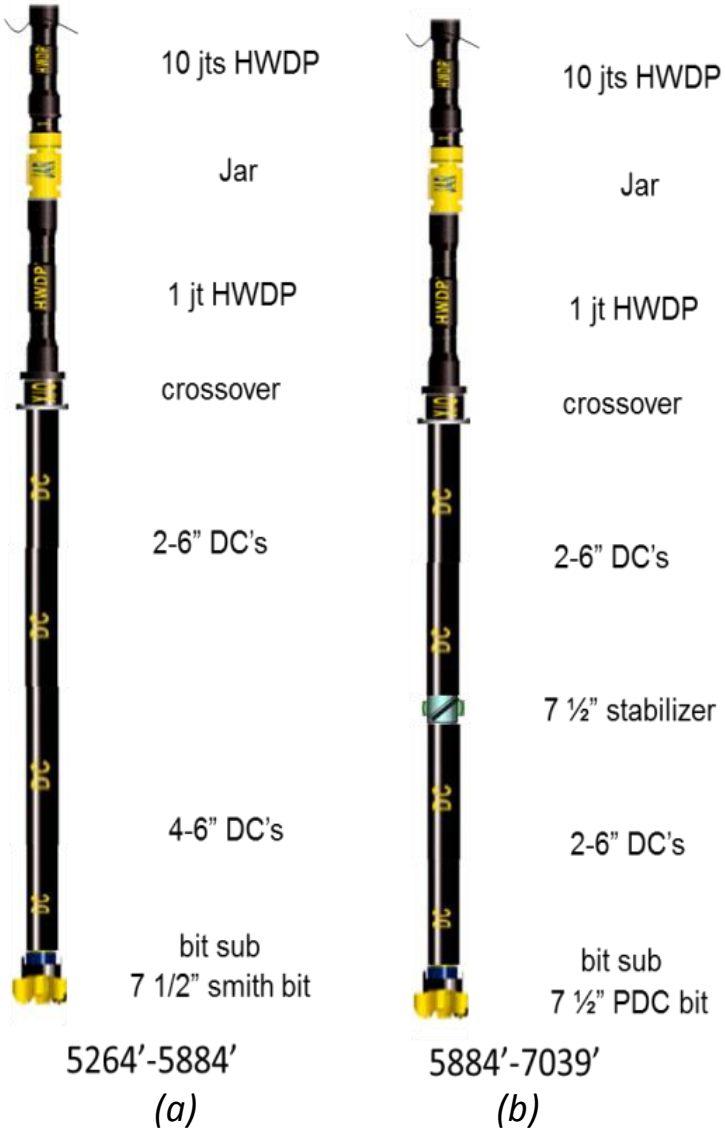

Figure 47: Bottom hole assembly without stabilizer (a) and with stabilizer (b)

Interval 1793.44 m – 1905 m (5884 ft – 6250 ft):

In this section, instantaneous Rate of Penetration (ROP) around 24.38 m/hr (80 ft/hr) was performed followed by one reduction from 15.24 m/hr to 18.28 m/hr (50 ft/hr to 60 ft/hr) as presented in Figure 48. In spite of this wellbore was planned as a vertical well, high instantaneous ROP in sand interval without directional control can affect the wellbore geometry.

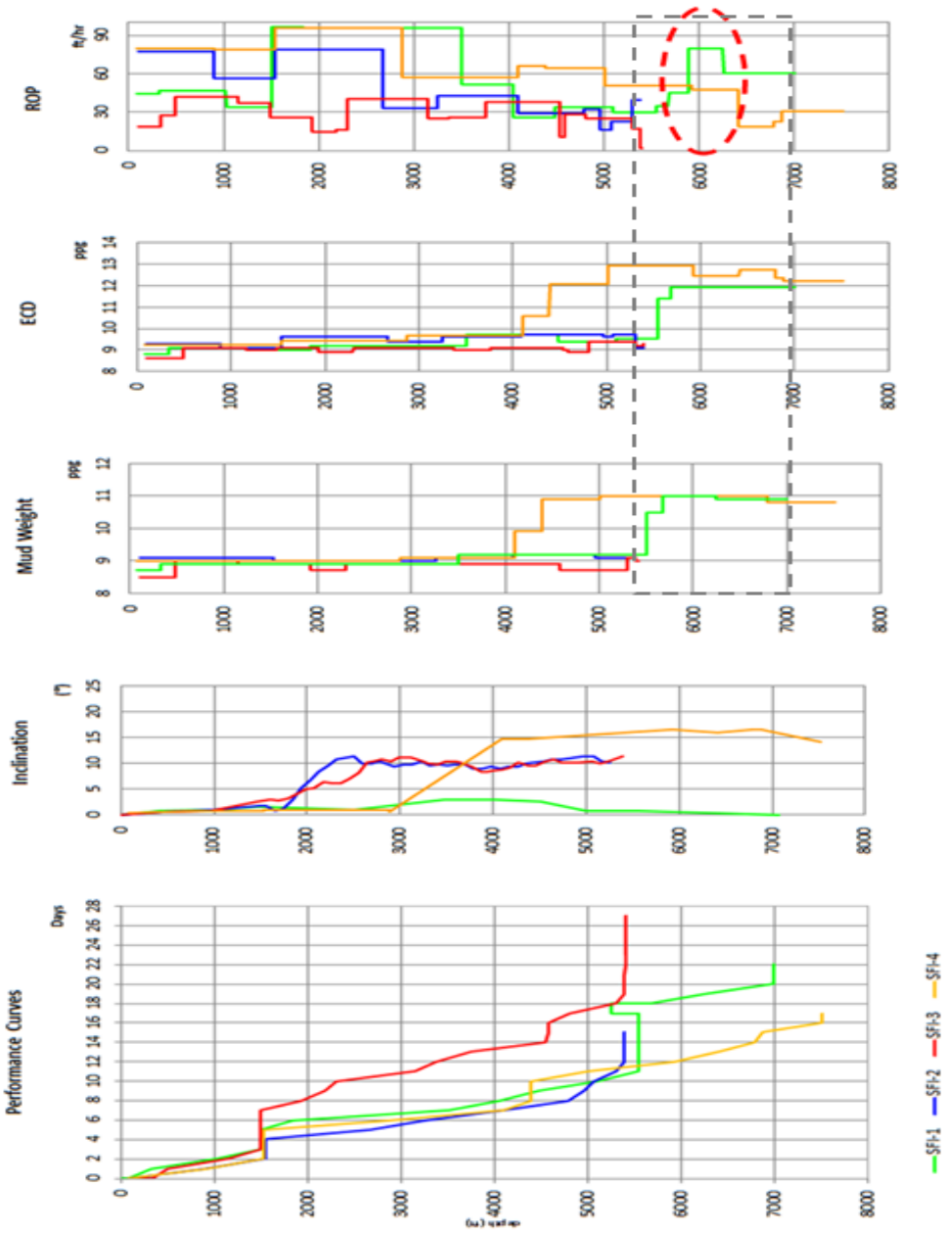

Figure 48: Performance curve, inclination, mud density and rate of penetration for SFI wells

5.3.1.2 Hole cleaning

To ensure efficient hole cleaning, the mud system should be conditioned to guarantee all cutting removal from the bottom of the borehole. Not only the main rheology properties (plastic viscosity and yield point) of the mud system play an essential role to achieve a good Carrying Capacity Index (CCI), but also an effective flow rate and jet configuration on the bit. Figure 26 illustrates some rules of thumb that were taken into account to evaluate the hydraulic parameters used in deepening SFI#1 well. Note that to obtain a good hole cleaning the CCI should be more than 1, an ideal annular velocity around 60.96 m/min (200 ft/min), flow rate more than 350 gpm for small hole size, and jet velocity shall be limited to 91.44 m/min (300 ft/sec) to prevent hole erosion for unconsolidated formation. Figure 49 and Figure 50 show the drilling fluid and hydraulic parameters, respectively, for SFI wells, including the deepened section for well SFI#1. As can be seen, optimum parameters were obtained for a CCI between 2 and 3, annular velocity around 73.15 m/min (240 ft/min) and jet velocity around 54.86 m/s (180 ft/s). Based on these numbers, a good hole cleaning was guaranteed.

Title: Characterization of Pliocene and Miocene Formations in the Wilmington Graben, Offshore Los Angeles, for Large-Scale Geologic Storage of CO_2

PI: Dr. Michael Bruno Final Report

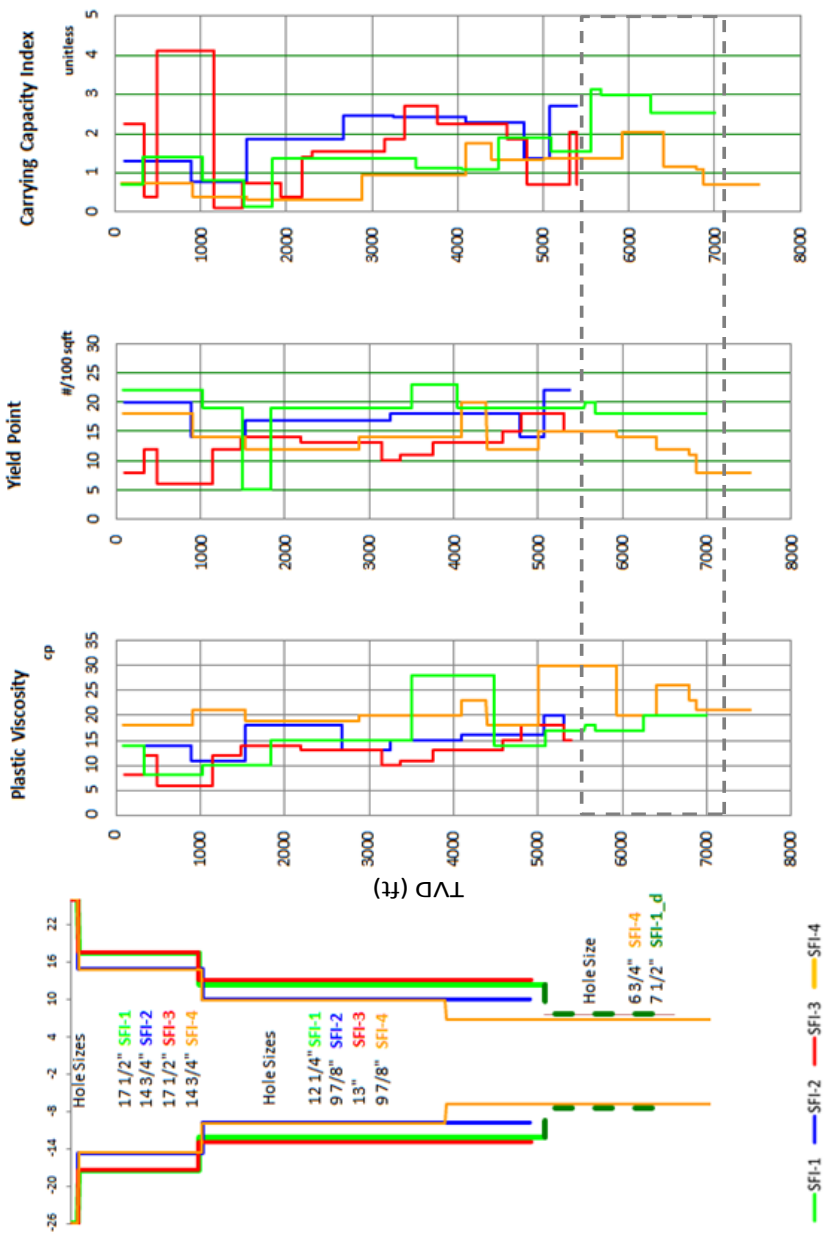

Figure 49: Drilling fluid parameters for SFI wells

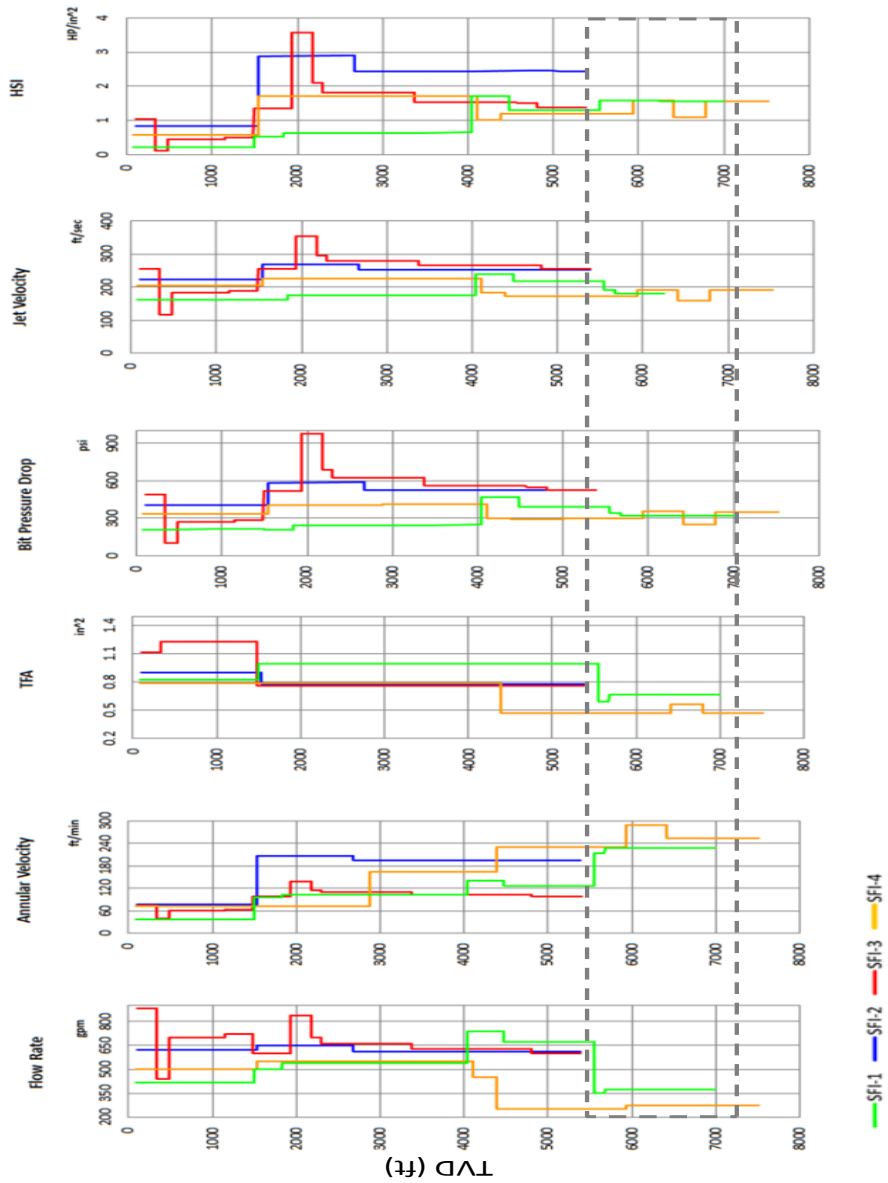

Figure 50: **Hydraulic parameters for SFI wells**

5.3.1.3 Remedial actions after the pipe stuck

Once the drill string became stuck at 1828.8 m (6000 ft), a series of remedial actions and efforts were performed for freeing the string as follows:

1. A back reaming was applied from 1920.24 m to 1828.8 m (6300 ft to 6000 ft). Circulation was carried out with full returns.
2. The pipe was worked up and down. Unable to rotate and move up and down more than 2.43 m (8 ft).
3. The mud system was conditioned with mud-adding lubricant "Torque-ease" to reduce the friction.
4. Sawdust sweeps were run in the hole.
5. The pipe was worked pulling 100 klb over string weight, drilling jars going off at 75 klb over string weight hitting hard but still unable to free stuck drill pipe at 1828.8 m (6000 ft).
6. Mud density was increased from 1.32 s.g. to 1.39 s.g. (11 ppg to 11.6 ppg) assuming a possible tight hole for induced stresses but the drill pipe remained stuck.
7. Mud density was decreased from 1.39 s.g. to 1.22 s.g. (11.6 ppg to 10.2 ppg) assuming a possible differential sticking in a permeable zone. No lost circulation was identified in this section.
8. Continuance of working stuck pipe pulling 75 klb to 100 klb over string weight but still unable to free drill string.
9. After these efforts, a free point was run to identify the stuck point and the fishing operation took place. A fish of 49.37 m (162 ft) was left on the hole, including the bit, bit sub, drill collars and stabilizer.

5.3.1.4 Stuck pipe mechanism and possible causes

After reviewing the borehole condition for well SFI#1 (deepening) before and after the drill string sticking, an analysis of the stuck pipe mechanism and possible causes was conducted. As is known, there are two sticking mechanism: mechanical and differential sticking. The former is related to pack-offs, bridges and wellbore geometry interference; and the latter is related to high overbalance pressures between wellbore pressure and formation pressure in permeable formations.

Table 10 summarizes the sticking mechanisms. Both mechanisms were evaluated based on the borehole condition.

Table 10: **Classification of stuck pipe.**

Sticking Mechanism		
Mechanical		**Differential**
Pack-offs and Bridges	Settled cutting Shale instability Unconsolidated formations Cement blocks/junk in the hole Cement flash set	High overbalance pressures Thick spongy filter cakes High solids muds High density muds Permeable formations
Wellbore Geometry	Key seats Under gauge hole Stiff drilling BHA's Mobile formations Ledges and dog legs Casing failures	

From Bowes et al. (1997)

5.3.1.5 Differential Sticking

Differential sticking occurs when one part of drill string becomes embedded in a mudcake (an impermeable film of fine solids) that forms on the wall of a permeable formation during drilling (Bourgoyne et al., 1986). If the mud pressure (*pm*), which acts on the outside wall of the pipe is greater than the formation fluid pressure (*pff*), which generally is the case with the exception of underbalanced drilling, then the drillstring cannot be moved (rotated or reciprocated) along the axis of the wellbore (Figure 51).

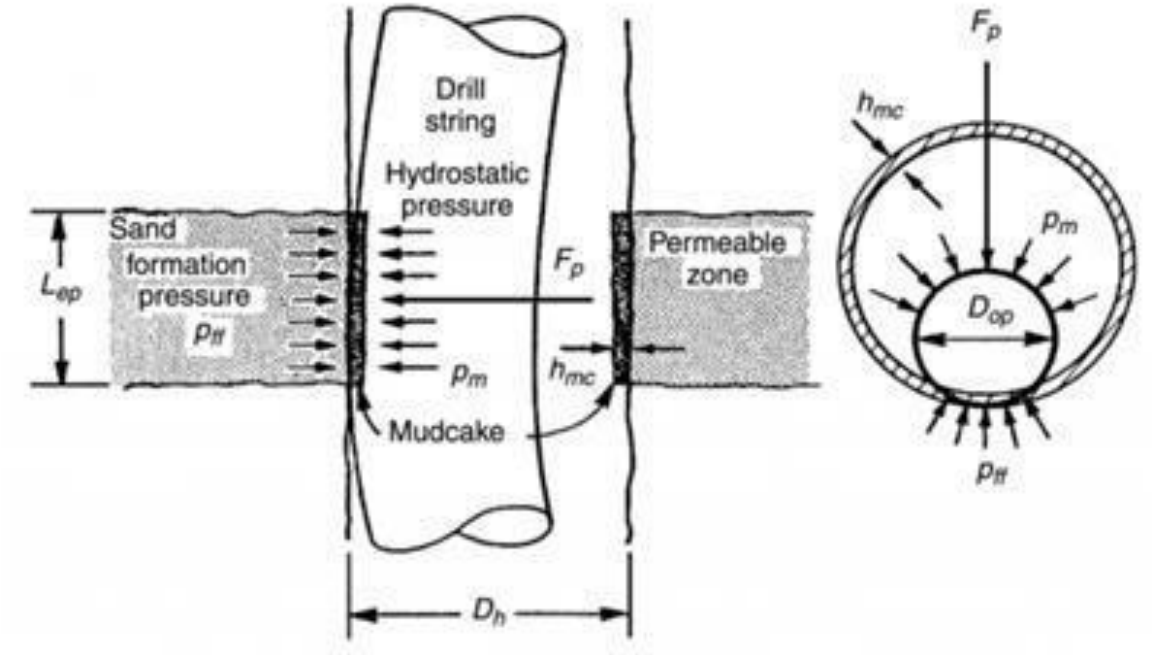

Figure 51: **Differential pressure sticking.**
From Bourgoyne et al. (1997)

The differential pressure acting on the portion of the drill pipe that is embedded in the mudcake can be expressed as (Bourgoyne et al., 1986):

$$\Delta p = p_m - p_{ff}$$

The pull force, F_p, required to free the stuck pipe is a function of the differential pressure, Δp; the coefficient of friction, f; and the area of contact, A_c, between the pipe and mudcake surfaces:

$$F_p = f * \Delta_p * A_c$$

$$A_c = 2 * L_{ep}\left\{\left(\frac{D_h}{2} - h_{mc}\right)^2 - \left[\frac{D_h}{2} - h_{mc}(D_h - h_{mc})/(D_h - D_{op})\right]^2\right\}^{0.5}$$

In this formula, L_{ep} is the length of the permeable zone, D_{op} is the outside diameter of the pipe, D_h is the diameter of the hole, and h_{mc} is the mudcake thickness. The dimensionless coefficient of friction, *f*, can vary from less than 0.04 for oil-based mud to as much as 0.35 for weighted water based mud with no added lubricants.

A differential sticking was estimated to compare the pull force to free the stuck pipe with the overpull applied of 100 klb over the string weight. These calculations can be summarized in Table 11. Note that the differential pressure is 40.20 bar (583 psi) lower than 68.94 bar (1000 psi) as a critical overbalance and the pull force (Fp) is lower than the overpull applied (pull force < overpull applied). In addition, there is no evidence of permeable sand or depleted formation that can cause high overbalance. Hence, there is a low probability of differential sticking.

Table 11: **Differential sticking calculations for well SFI#1 (deepen)**

Differential Sticking Calculations	
Stuck Depth (ft)	6000
MW @ 6000' (ppg)	10.2
Formation Pressure (ppg)	8.33
Formation Pressure (psi)	2599
Wellbore Pressure (psi)	3182.4
Differential Pressure (psi)	**583.44**
Length of Permeable Zone (ft)	20
Length of Permeable Zone (in)	240
Hole Diameter (in)	7.5
Mudcake thickness (in)	0.1
Outside Pipe Diameter (in)	6.25
Cross Section Area (in^2)	878
Coefficient of friction after lubricant	0.15
Pull Force to free the stuck pipe (Klb)	**77**
Overpull applied (Klb)	**100**

5.3.1.6 Mechanical sticking

According to the evidences shown on the daily drilling report, there were some signs that can help to identify the main mechanical sticking mechanism in the interval 1690.11 m – 1905 m (5545 ft – 6250 ft). Some of these signs are as follows:

- Presence of solid (cement) that caused a bit shanks worn.
- Low circulation time (1 hr) during the cement removal in spite of reported full return.
- Tight hole with reaming.
- Change of BHA with one stabilizer that can lead to under gauge hole, mainly over poor consolidate sandstone.
- High instantaneous ROP around 24.38 m/hr (80 ft/hr) that can result in poor wellbore geometry. Drilling between soft and hard formations.

Table 12 summarizes the mechanical sticking identified and possible causes. Basically, five kinds of mechanical sticking were identified for pack-off/bridges and wellbore geometry. Figure 52 and Figure 53 show the mechanical sticking mechanism.

Table 12: **Mechanical sticking mechanism identified for well SFI#1 (deepen)**

Mechanical Sticking		Causes	Warning Signs
Pack-off and Bridges	Cement block	Cement cutting from side track hole and low circulation time	Bit shanks worn
	Unconsolidated formation	Changes of rock strength	High instantaneous ROP
Wellbore geometry	Key seat	Change in BHA and poor vertical control	Reaming tight hole
	Under gauge hole	Running a new bit and one stabilizer on the BHA	Reaming tight hole
	Ledges and Doglegs	Drilling from soft to hard rock	Reaming tight hole

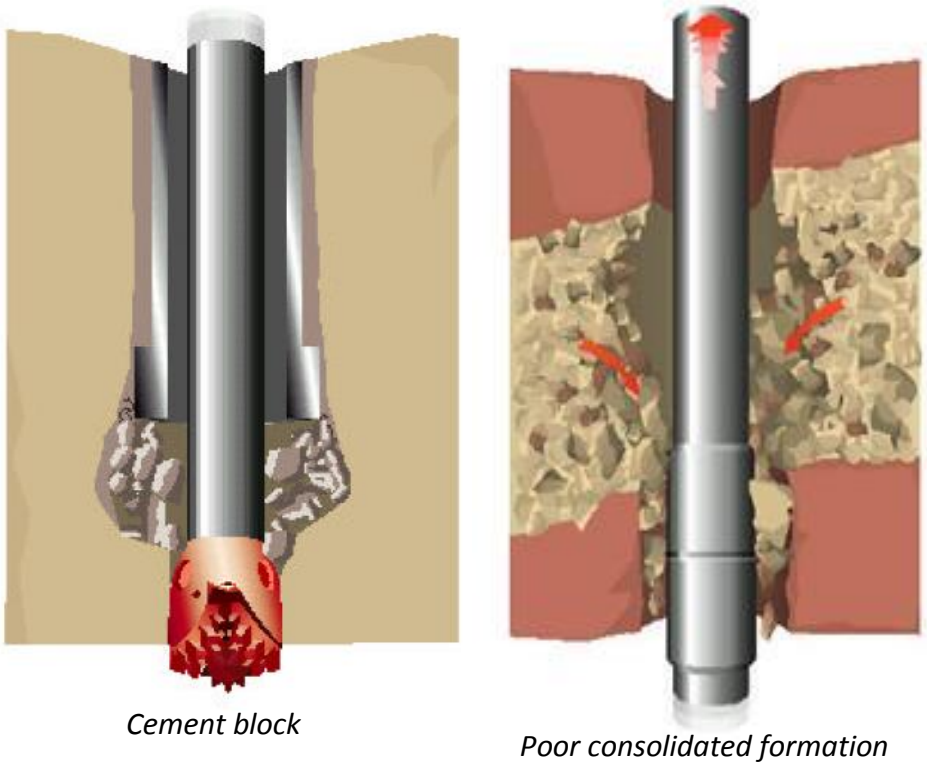

Figure 52: Mechanical sticking mechanism related to pack-offs and Bridges. (from Bowes & Procter, 1997 and Fjar et at., 2008)

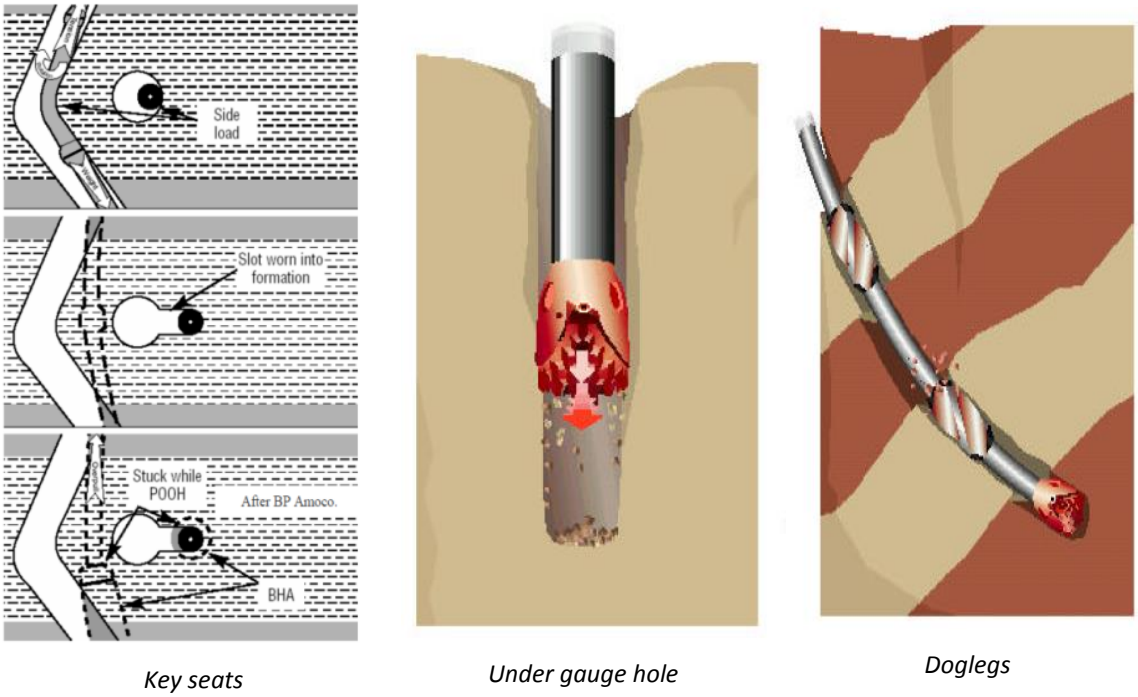

Figure 53: **Mechanical sticking mechanism related to wellbore geometry. (from Bowes & Procter, 1997 and Fjar et at., 2008)**

5.3.1.7 Qualitative analysis for stuck pipe mechanism

Once the main sticking mechanism was identified, a stuck pipe freeing worksheet (Mitchell, 2009) was applied to predict the most probable stuck pipe mechanism based on four questions associated with the activities before and after sticking. The individual probability scale range is as follows: 0-Low probability, 1-Medium probability and 2-High probability. Once all 4 items have been addressed, the column with the highest score shows the sticking mechanism (Figure 54). In this case, the main mechanism is the wellbore geometry, follow by Pack-off/Bridge and with a lower probability of differential sticking. Comparing with the previous analysis, it is clear that mechanical sticking was the main cause of the stuck pipe.

Direction of pipe movement just prior to sticking	Packoff or Bridge	Differential Sticking	Wellbore Geometry
Moving up	2	0	2
Moving down	1	0	2
Static	2	2	0
Downward motion of pipe after sticking			
Down free	0	0	1
Down restricted	1	0	1
Down impossible	0	0	0
Pipe rotation after sticking			
Rotate free	0	0	1
Rotate restricted	1	0	1
Rotate impossible	0	0	0
Circulation pressure after sticking			
Circulation free	0	2	2
Circulation restricted	2	0	0
Circulation impossible	2	0	0
Totals	**4**	**2**	**6**

Figure 54: Stuck pipe freeing worksheets for well SFI#1 (deepen). (from Mitchell, 2009)

5.3.1.8 Summary

These conclusions are based on the daily drilling report and the conditions under which this wellbore was drilled:

- Efficient hydraulic parameters (Carrying Capacity index, annular velocity and jet velocity) were performed. However, low circulation time and evidence cement solids could be one of the causes of pack-off and bridges.
- Change in Bottom Hole Assembly and poor evidence of controlled wellbore orientation could be one of the causes of wellbore geometry issues.
- High instantaneous ROP of 24.38 m/hr (80 ft/h) followed by lower ROP of 12.19 m/hr (40ft/h) could be one of the reason for wellbore tortuosity or high dog leg severity.
- No risk of differential sticking was identified.
- Based on the wellbore conditions and the qualitative analysis, wellbore geometry and pack-off/bridges are the most probable stuck pipe mechanism.

5.4 Conclusions

Three wells were drilled; DOE#1 in April, 2010, DOE#2 in February 2014 and DOE#3 (SFI#1 deepening) in November, 2014. Cores, log data, formation fluid and paleo data were all incorporated into the geologic model which was then used by the gas migration model. The results can be summarized:

- Drilled and characterized DOE#1 and DOE#2 wells, and deepened an existing SFI#1 well.
- Over 120 m (400 ft) of additional lower Pliocene sands and 45 m (150 ft) of upper Miocene sands have been encountered.
- DOE#3 deepening (though not drilled to anticipated total depth) verified the continuity of the upper Miocene sand.
- Porosities and permeabilities are recapped here:

	Pliocene		Miocene
	DOE#1	***DOE#2***	***DOE#2***
Sand Porosity (%)	24-31	28-37	26-29
Sand Permability (md)	50-353	29-300	4-<100
Shale Porosity (%)	23-29	29	29
Shale Permeability (md)	<2	<2	<5

- Based on the wellbore conditions and the qualitative analysis, wellbore geometry and pack-off/bridges are the most probable stuck pipe mechanism on SFI#1 well deepening.

6 Geologic model development

The offshore Wilmington Graben lies within a turbidite depositional environment. Lithology is known to vary often, both vertically and laterally. A simple interpolation between sparsely distributed wells (12 wells total for an area over 150 km^2 (60 mi^2)) would create an overly simplified lithologic model. Seismic horizon data can inform the general stratigraphic trends, but cannot completely resolve uncertainty in the lateral variation in lithology. To account for such variation and uncertainty, therefore, we introduced strategic phantom wells to force the Rockworks software to create a heterogeneous lithology, honoring the general stratigraphic trend and turbidity environment.

6.1 Populate grid with lithology estimates

Lithology from 14 existing wells and 18 phantom wells (FW01 to 12, FWnearH10R7 and 5 along BB' cross section) were used to create the 3D geologic model (see Figure 56). Basement depths for some areas are based on seismic sections found in Shaw (1999 & 2007) and Fisher et al. (2004) reports. The phantom wells' lithologies and depths honored the general stratigraphic trend and turbidite environment requirements. Figure 55 shows probable lithology distribution for the studied area. Figure 57 and Figure 58 are NW –SE and NE-SW, respectively, cross sections showing the heterogeneous geologic model created.

Title: Characterization of Pliocene and Miocene Formations in the Wilmington Graben, Offshore Los Angeles, for Large-Scale Geologic Storage of CO_2

PI: Dr. Michael Bruno Final Report

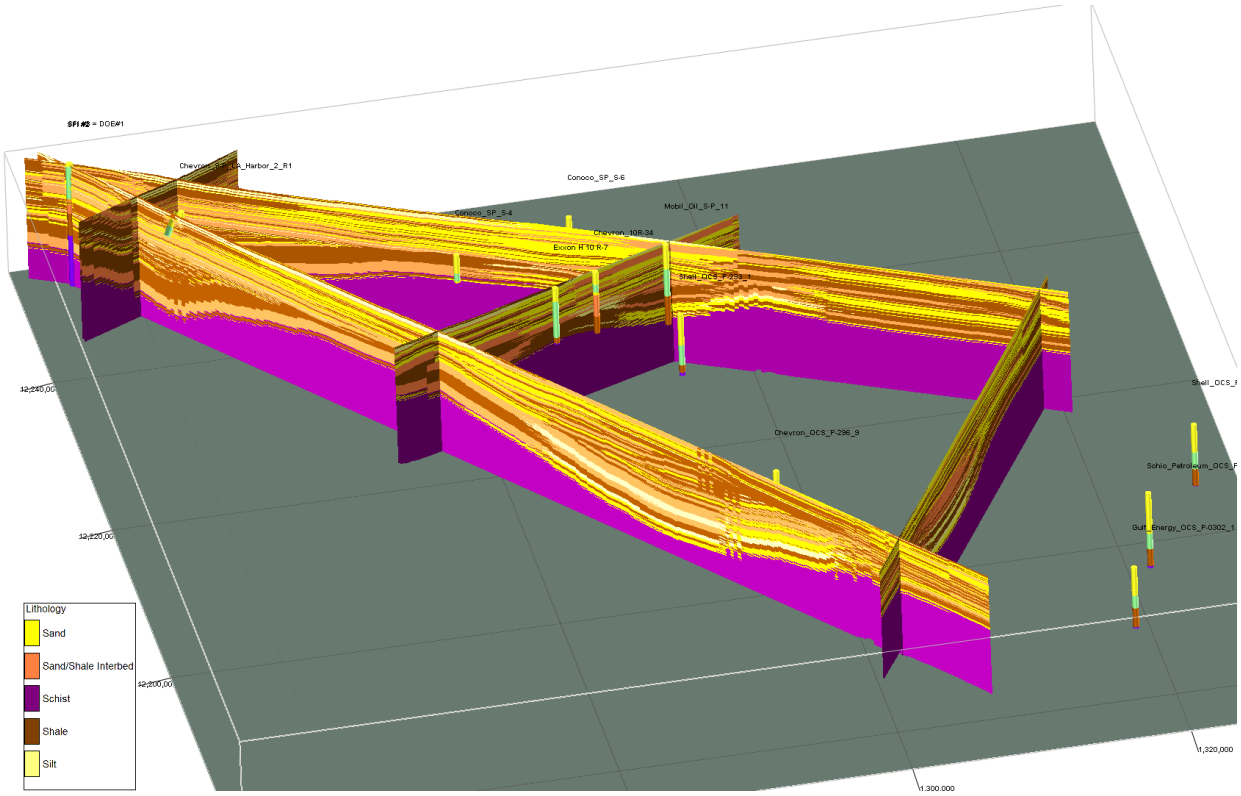

Figure 55: Wilmington Graben Fence diagram with probable lithologies fill-in between known wells

Title: Characterization of Pliocene and Miocene Formations in the Wilmington Graben, Offshore Los Angeles, for Large-Scale Geologic Storage of CO_2

PI: Dr. Michael Bruno Final Report

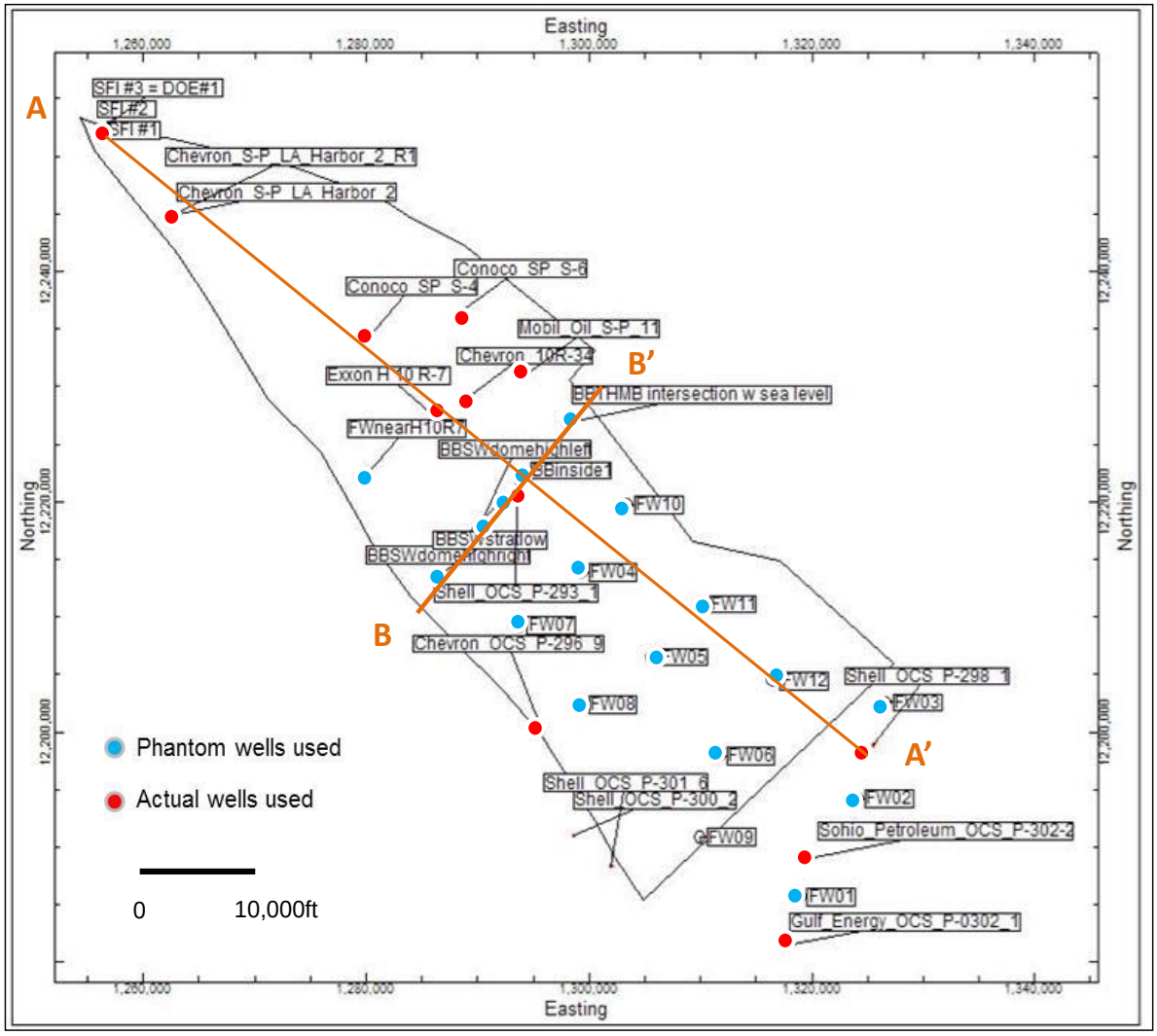

Figure 56: Map of wellbore location including phantom wells

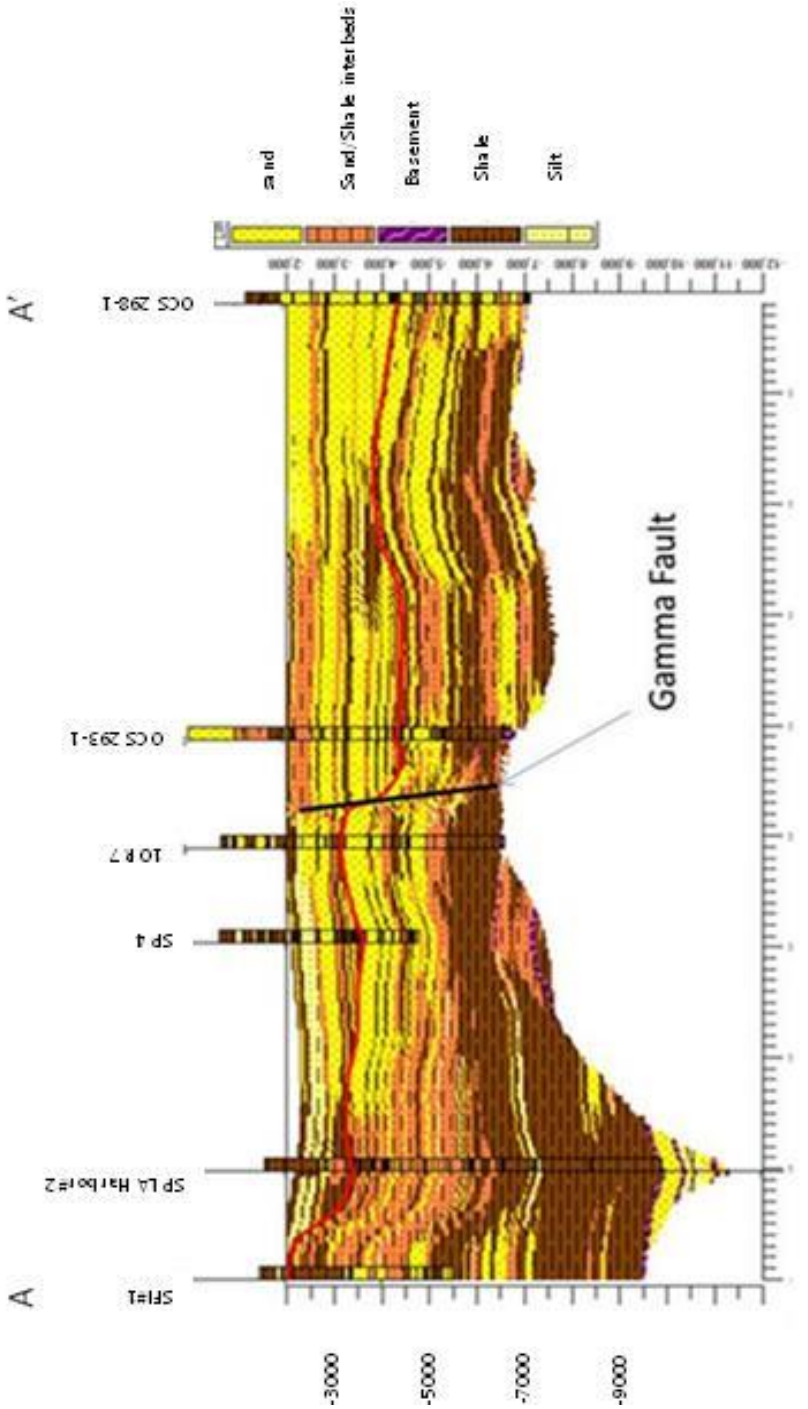

Figure 57: NW-SE cross section with updated heterogeneous model
Red line: Top Repetto Unconformity

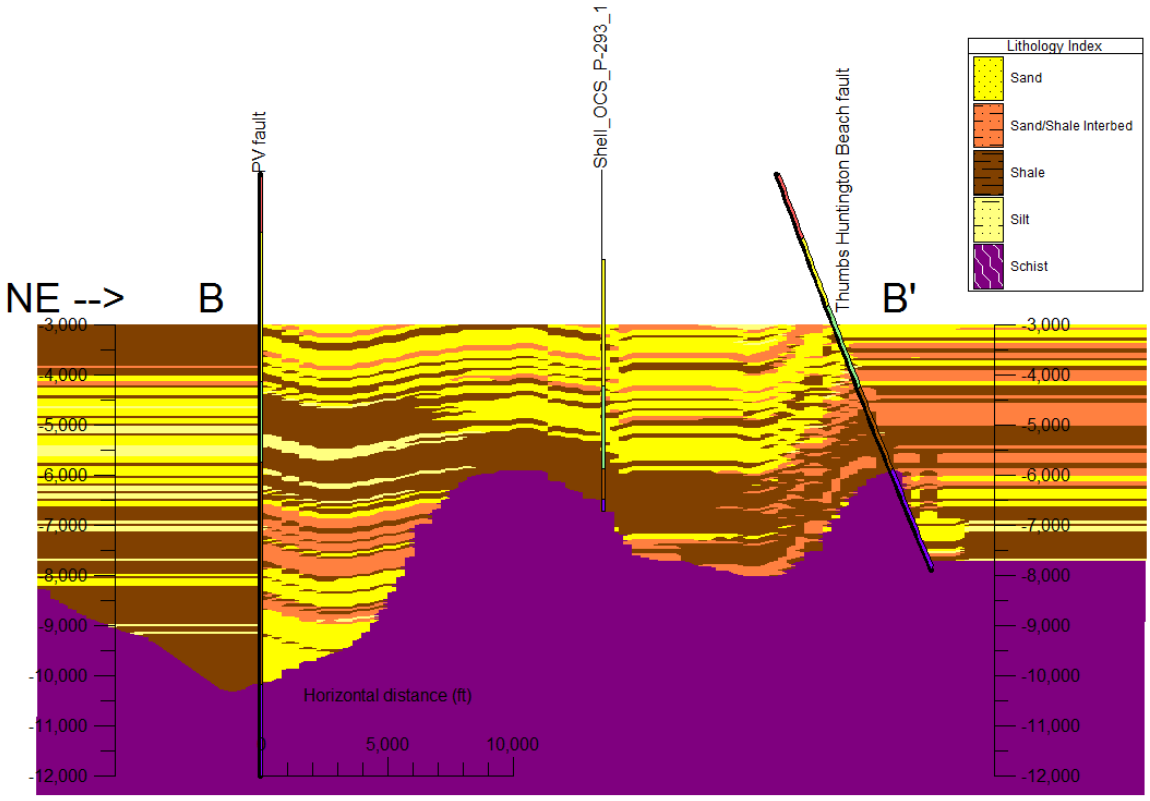

Figure 58: NE-SW cross section along B-B'

Stratigraphy models of the Pico, Repetto and Puente formations were created in Rockworks. The mean porosity, volume and percentage of each lithology type were calculated for each formation. The lithologic models of the three formations were then merged to represent a heterogeneous geologic model for the whole Wilmington Graben. The entire geologic model spans from the basement to the Pico Formation. The distribution of the four main lithology types within each stratigraphy is shown in

Table 13. With the drilling of DOE#2, over 45 m (150 ft) of Miocene sands were encountered in the northern graben, potentially increasing the Puente (Miocene) sand storage capacity in the northern graben.

Table 13: Lithologic distribution from heterogeneous geologic model

% Distribution	Sand	Shale	Sd/Sh	Silt
Pico	58%	17%	20%	5%
Repetto	34%	32%	32%	2%
Puente	10%	17%	63%	10%

6.2 CO_2 storage capacity estimates

Mean porosities of the different lithologies and formations derived from statistic distribution discussed in detailed in *Well data review and formation evaluation* above were used to estimate storage capacity. Our geologic model is composed of 6704 columnar rectangular cuboids, or cells, encompassing reservoir thicknesses of 15 m to 1175 m (50 ft to 3850 ft), with an average thickness of 355 m (1165 ft). In the model, porosities and CO_2 densities have been averaged. The average porosity of the sand reservoir is 0.27 (average of sand porosities from Table 1) and the average density of CO_2 would be 0.61 gm/cm^3 (37.76 lbs/ft$^{3)}$ (with a minimum of 0.50 gm/cm^3 (31.14 lbs/ft^3) and a maximum of 0.70gm/cm^3 (43.56 lbs/ft^3)). Rockworks also calculated the volume for each stratigraphic unit based on the 3D geologic model developed (Table 14) (Version 12, heterogeneous lithology with phantom wells).

Table 14: Volumetric numbers generated for different lithologies and formations (after drilling DOE#2 well)

Volume ft3	sand	shale	sand/shal	silt
Pico	1.82E+12	6.12E+11	5.42E+11	1.47E+11
Repetto	6.10E+12	8.07E+12	2.24E+12	5.21E+11
Puente	2.54E+12	4.58E+12	2.38E+12	5.88E+11

These values, together with the DOE recommended efficiency factors (NETL, 2010) have been used to calculate the CO_2 storage estimate for the Wilmington Graben using the following equation:

$$G_{CO2} = A_t\, h_g\, \phi_{tot}\, \rho E_{saline}$$

Where:

A_t is the reservoir area,
h_g the reservoir thickness,
ϕ_{tot} the porosity,
ρ the density of CO_2 at depth, and
E_{saline} the efficiency factor.

The DOE efficiency factors are, from low to high (i.e., P10, P50, and P90, respectively): 0.0051, 0.02, and 0.054 (DOE, 2010). Additionally, to convert pounds to metric tons we have used a factor of 0.0004536 MT/lb.

<u>LOW/P10:</u>
Repetto Storage:
6.10e12*0.268*37.76*0.0051*0.0004536 = 1.43e9

Puente Storage:
2.54e12*0.268*37.76*0.0051*0.0004536 = 5.97e7
TOTAL: 2.034e8

<u>MEDIUM/P50</u>:
Repetto Storage:
6.10e12*0.268*37.76*0.02*0.0004536 = 5.62e8
Puente Storage:
2.54e12*0.268*37.76*0.02*0.0004536 = 2.34e8
TOTAL: 7.96e8

<u>HIGH/P90</u>:
Repetto Storage:
6.10e12*0.268*37.76*0.054*0.0004536 = 1.52e9
Puente Storage:
2.54e12*0.268*37.76*0.054*0.0004536 = 6.32e8
TOTAL: 2.15e9

Figure 59 is a graphic representation of the total CO_2 storage volume for the Wilmington Graben, assuming a heterogeneous model generated by Rockworks simulation using 14 wells' data and 18 phantom wells. The storage volume increases after finding the 120 m (400 ft) of additional lower Pliocene sands and 45 m (150 ft) of upper Miocene sands.

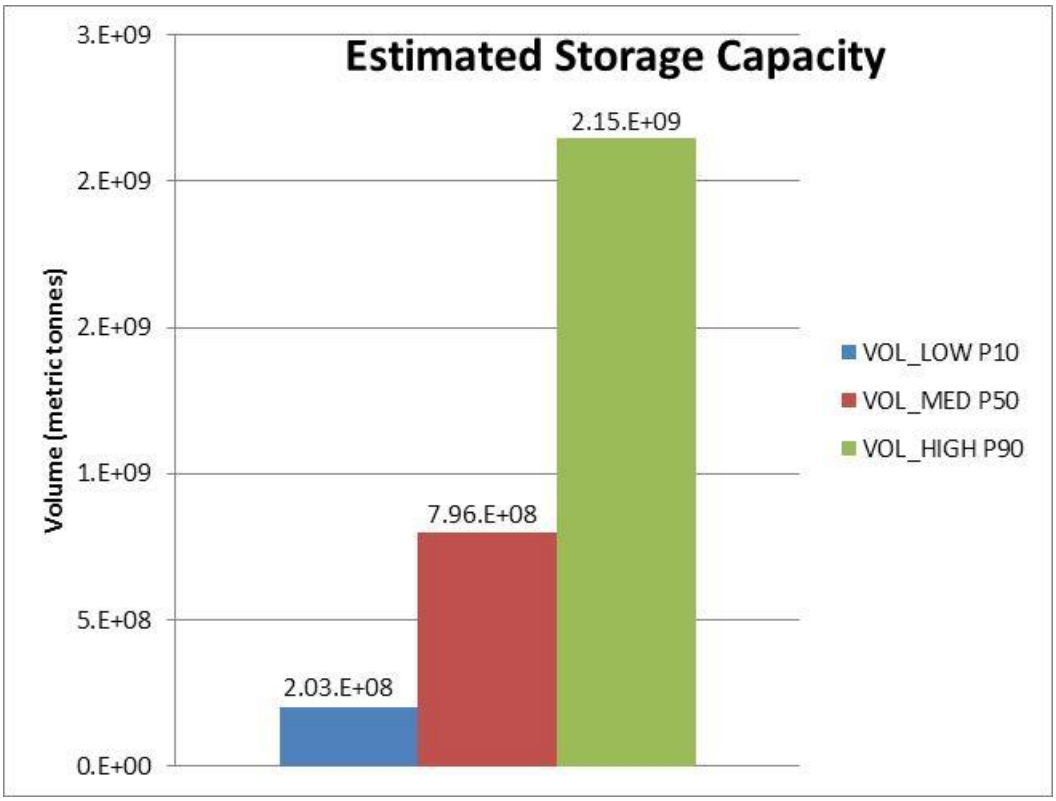

Figure 59: Total estimated storage capacity for CO_2 in Wilmington Graben sands and silts.

6.3 Conclusions

A simple interpolation between sparsely distributed wells (12 wells total for an area over 150 km2 (60 mi2)) would create an overly simplified lithologic model. A heterogeneous geologic model was created using 14 well logs and core data, seismic horizon data and the introduction of 18 strategically placed phantom wells to force the Rockworks software to create a heterogeneous lithology, honoring the general stratigraphic trend and turbidite environment.

The porosity data, together with the volumetric numbers and DOE recommended efficiency factors (NETL, 2010) and equation have been used to calculate the CO_2 storage estimate for the Wilmington Graben. The storage capacity using the Rockworks simulation is:

- Pliocene
  - P10= 1.43e8
  - P50= 5.62e8
  - P90= 1.52e9

- Miocene
  - P10= 5.97e7
  - P50= 2.34e8
  - P90= 6.32e8

7 CO_2 injection and migration modeling

7.1 Experimental methods

In order to demonstrate storage and sealing capacity of the Wilmington Graben geology we set up fluid flow models at two areas of interest in the Graben, as indicated in Figure 60. Simulating injection at potential well locations at constant pressure – below fracture pressure – over a period of 30 years, with an additional 30 years of observation of plume migration, we endeavor to determine:

1. How much CO_2 can we inject at a single well location?
2. Will the CO_2 migrate/leak into shallow layers above Upper Repetto unconformity, which is a potential cap rock?
3. Does the plume stabilize after 60 years?

Tough2/ECO_2N (http://esd.lbl.gov/research/projects/tough/) modeling software was used to simulate CO_2 migration and fluid flow during and after CO_2 injection. ECO_2N equations of state can model the three component system of water, CO_2, salt in liquid, gaseous, or solid states, but it lacks the ability to model the transition from gaseous to liquid CO_2. Thus if CO_2 migrates up to shallower depths this software could not model this scenario appropriately. Pressure and temperature conditions under which such a phase change could occur are found in the Graben above the potential cap rock, the Upper Repetto Unconformity. Since we assume any CO_2 migrating above this layer is leakage, indicating failed containment, using ECO_2N is considered reasonable for testing containment. Petrasim (http://www.thunderheadeng.com/petrasim/) is pre- and post-processor software used. This section will discuss the model set-up and scenarios simulated.

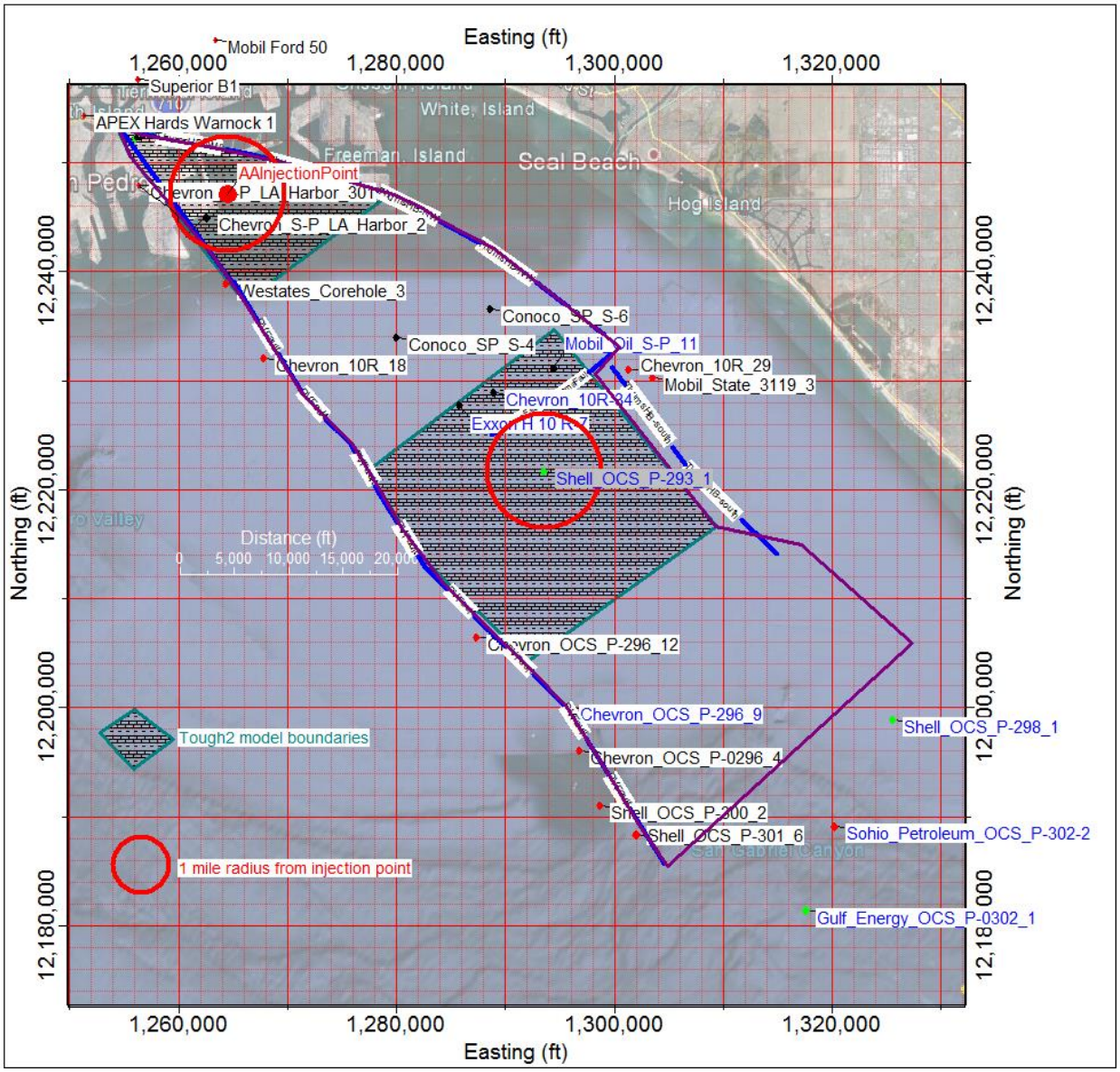

Figure 60: Integrated fluid flow models (hatched area)

7.1.1 Design and Assembly CO_2 injection model

Models are set up using the Petrasim pre-processor, with the injection well as the origin of the coordinate system. One mesh border is also aligned with the PV fault, since this fault is assumed to be a no flow barrier.

7.1.1.1 Mapping RW to Petrasim

Using the heterogeneous lithology model prepared in *Geologic model development* as a starting point, material properties were mapped from the geology model grid onto the flow simulation model grid. For example, Figure 61 presents a cross section illustration of the mapping process for the central Graben area. The following steps turned out to be most efficient for mapping from the RW to Petrasim/Tough2 grids:

- Export mesh data (ID, X,Y,Z) from PetraSim/Tough2 into csv file;
- Transform data points from local to global coordinate system using ParaView (http://www.paraview.org/);
- Use "Residuals" command in RW to find closest cell in geological model for each data point to receive lithology value from that cell; and
- Assign retrieved lithology values via "Set Cell data…" command in Petrasim.

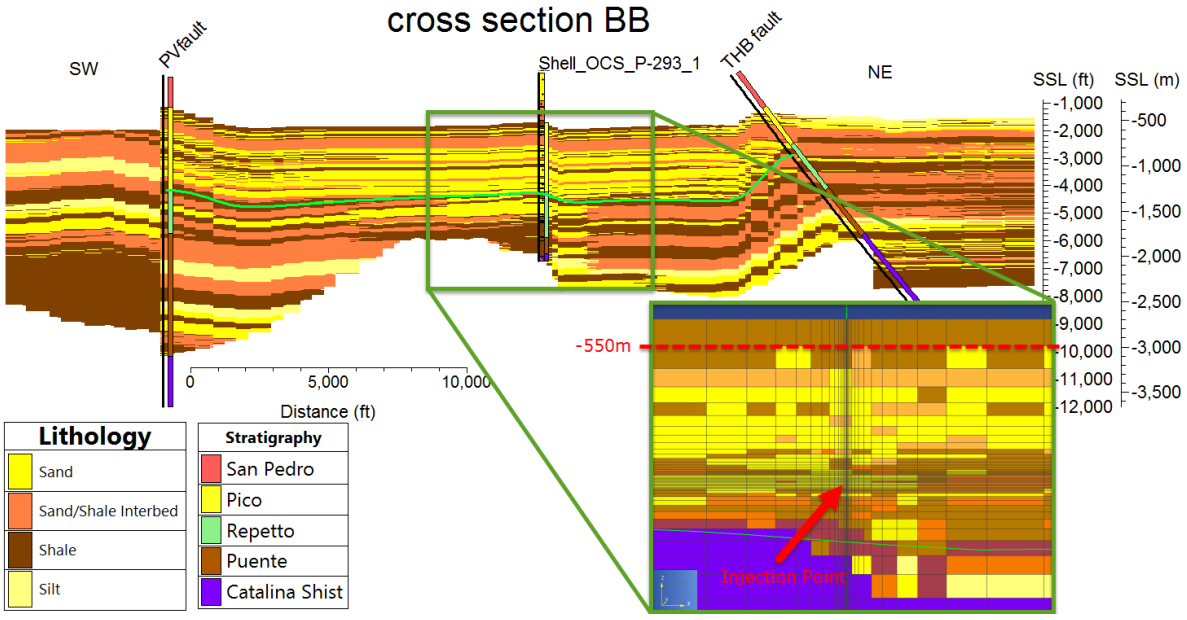

Figure 61: Mapping of lithology and flow properties from geologic to flow model

7.1.1.2 Model size and grid refinement

Initial plans to model only half of the volume of the Graben in each zone of interest and assign a symmetry plane were discarded, as the complexity and heterogeneity of the Graben argued against the accuracy of this approach. Final models for northern and central Graben areas were developed in full 3D and cover an area of 22 km^2 (8.5 mi^2) and 47 km^2 (18 mi^2),

respectively. 3D views of the baseline models showing mapped lithology types and extensions are presented below in Figure 62 and Figure 63.

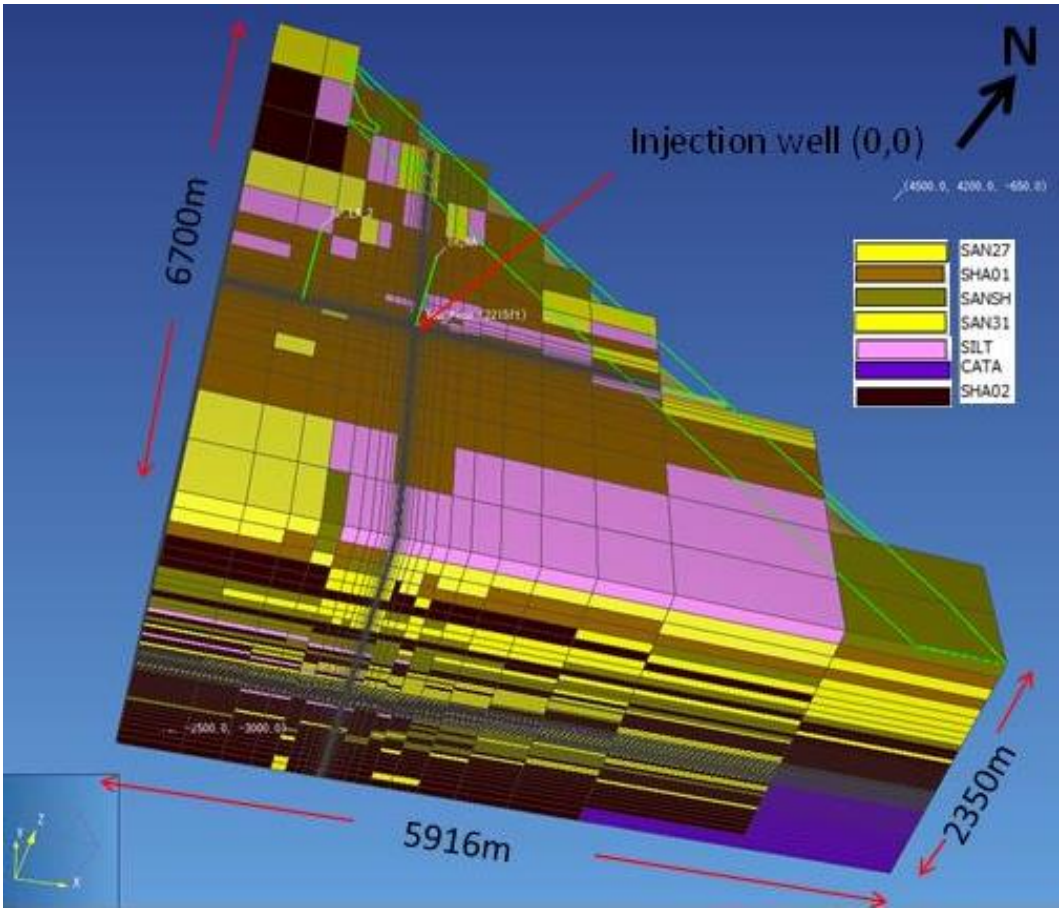

Figure 62: 3D view of northern Graben model with dimensions

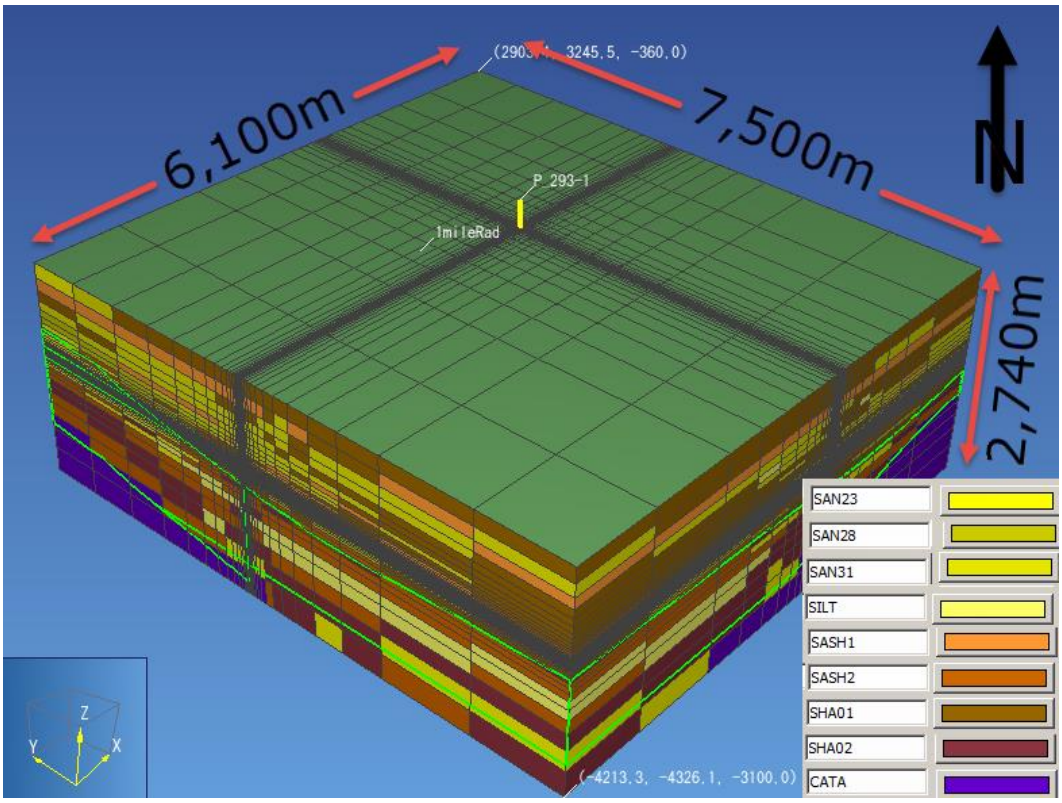

Figure 63: 3D view of central Graben model with dimensions

Summaries of the models' spatial ranges are given in Table 15 and Table 16. Note that for the northern Graben the dimensions for the entire cuboid are listed, but cells NE of the THB fault are deactivated during modeling (since we assume THB also to be a sealing fault), and thus not seen in Figure 62.

Table 15: Model dimensions Northern Graben

	x (m)	y (m)	z (m)	x(ft)	y (ft)	z (ft)
Min	-1,416	-2,500	-650	-4,646	-8,202	-2,133
Max	4,500	4,200	-3,000	14,764	13,779	-9,842
Delta	**5,916**	**6,700**	**2,350**	19,409	21,982	7,710

Table 16: Model dimensions Center Graben

	x (m)	y (m)	z (m)	x(ft)	y (ft)	z (ft)
Min	-4,213	-4,326	-360	-13,822	-14,193	-1,181
Max	2,903	3,245	-3,100	9,524	10,646	-10,171
Delta	**7,116**	**7,571**	**2,740**	23,346	24,839	8,989

The grid is refined around the injection interval in both horizontal and vertical directions. Model refinement at the injection location is 5x5 m in the horizontal direction with cell width increasing away from the well. Since plume migration in some of the simulation results suggested there is a strong gridding effect we evaluated this refinement around the injection well. A discussion is included in *Appendix 3: Gridding Effect on Plume Migration*.

7.1.1.3 Conceptual model

Figure 64 and Figure 65 illustrate the boundary conditions applied. Boundaries along the Palos Verdes and Thums Huntington Beach faults are assumed to be sealing, thus these boundaries were set with no-flow conditions, same as bottom of the model. Boundaries open to the rest of the Graben area, were defined as constant pressure conditions (depth dependent). Top of the model was set to no flow for the northern Graben and to constant pressure for the center graben – studies showed no significant change in plume migration if top of model was set to no flow or constant pressure.

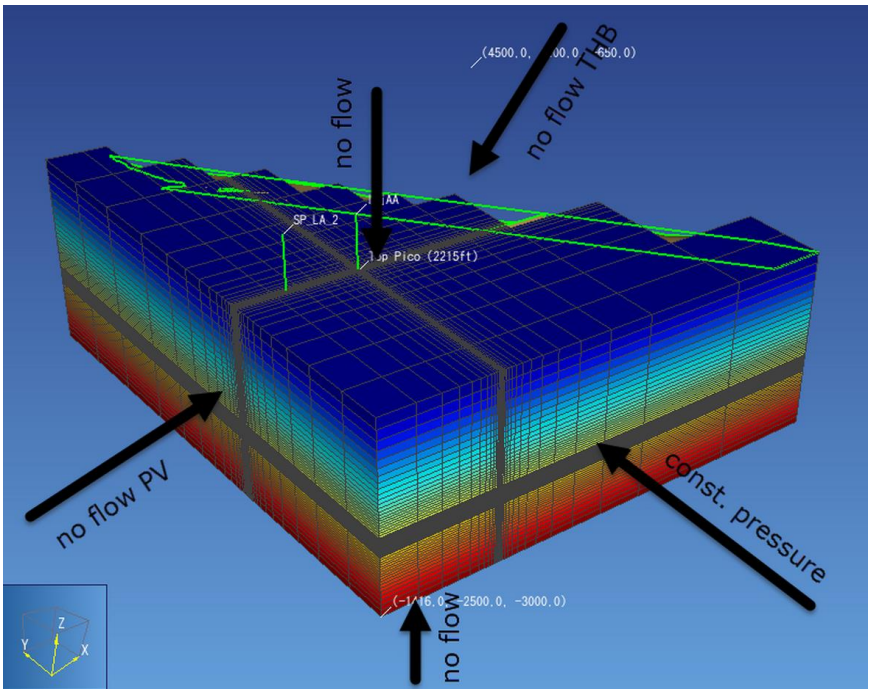

Figure 64: Conceptual fluid flow model for northern Graben area (Figure 60 for location)

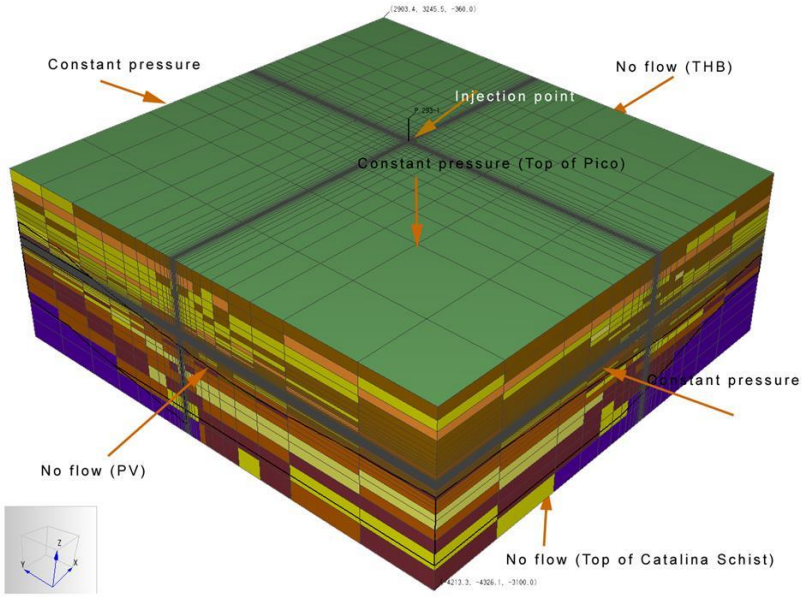

Figure 65: Conceptual fluid flow model for central Graben area (Figure 60 for location)

After establishing natural state for a model, CO_2 injection for 30 years plus an observation phase of an additional 30 years are simulated (latter only in cases where the injection did not already leak into shallow layers). An initial setup of rate-dependent injection was changed to constant pressure injection pursuant upon peer review. Pressure was set to a constant value of about 1% above initial pressure. Saturation with supercritical CO_2 was set to a maximum of 100%/80% (Northern/Central graben) in those cells, assuming that the near wellbore area would be saturated quickly after the onset of injection.

7.1.1.4 Initial conditions

The following conditions were used in each area to set the natural state. Initial equilibrium is run for a minimum of 1000 years.

Northern Graben

Initial pressure: the surface pressure is air pressure (1.01E5 Pa or 14.7 psi), thus assuming a 9790 Pa/m (0.43 psi/ft) hydrostatic pressure gradient, pore pressure is about 2.14E7 Pa (3109 psi) in the injection zone.

Initial temperature: the surface temperature is 25 °Celsius (77 °Fahrenheit), thus with a 0.026 ^{o}C/m (0.0143 ^{o}F/ft) temperature gradient, the temperature is about 81.68 ^{o}C (179 ^{o}F) in the injection zone.

Salt mass fraction: 2.14% based on fluid sample measurements in DOE#01.

Central Graben

Initial pressure: Pore pressure gradient is estimated at 11,300 Pa/m (0.5 psi/ft)

Initial temperature: With a temperature gradient of 0.0346 ^{o}C /m (0.019 F/ft), based on log data from Shell OCS P-293-1, the temperature is about 60 ^{o}C (140 ^{o}F)

Salt mass fraction: 2.14% salt mass fraction is applied.

CO_2 *mass fraction*: Though there is some CO_2 measured in the fluid sample mentioned above, we discarded the small amount (5E-6 mass fraction) of in situ CO_2, to better be able to observe the plume migration for both modeling areas.

7.1.1.5 Material properties

Initial models were set up with material properties based on one or two wells for each area (Chevron SP LA Harbor-2 and DOE#1 for northern Graben and Shell OCS P-293-1 for the central Graben). Final values presented here take into account logging and core analysis performed in *New well drilling, logging, and core analysis* above for porosity and permeability. Pore compressibility is taken as derived in *Geomechanical modeling* below. Thermal properties

are based on the literature (Incropera & DeWitt, 1996). Analytical and numerical analyses showed that the temperature effect can be neglected in these simulations (see 3rd Quarter 2012 and 4th Quarter 2013 progress reports). Thus different simulation scenarios presented in this report are all run under isothermal conditions. Detailed discussions of derivations for capillary pressure and relative permeability curves have been documented in 4th Quarter 2013 progress report.

The tables below (Table 17 and Table 18) list the material properties used for the baseline simulations in each area.

Table 17: Summary of baseline simulation – northern Graben

formation used for		PI	RE/PU	PI	RE/PU	PI/RE/PU	PI/RE/PU
Material name		SAN31	SAN27	SHA01	SHA02	SASH1	SILT
density [kg/m³]		2242	2491	2379	2379	2492	2366
wet heat conductivity [W/mC]		2.51		2.51		2.51	2.51
specific heat [J/kg-C]		920		920		920	920
pore compressibility [1/Pa]		1.39E-09	1.30E-09	1.55E-09	1.06E-09	1.36E-09	1.41E-09
total porosity [-]		0.31	0.27	0.37	0.33	0.29	35
effective porosity (-)		0.31	0.27	0.037	0.033	0.145	3.5
x permeability [mD]		141	123	21	15	52	66
y permeability [mD]		141	123	21	15	52	66
z permeability [mD]		70	61	11	8	26	33
Reference		Berea sandstone		Kimberlina shale		Berea sandstone	Berea
rel. perm. /van Genuchten	λ			0.9170			
	S_{lr}			0.30			
	S_{ls}			1.00			
	S_{gr}			0.29			
rel. perm. /Corey	S_{lr}	0.20				0.20	0.20
	S_{gr}	0.00				0.00	0.00
cap pressure /van Genuchten	λ	0.6700		0.412		0.67	0.67
	S_{lr}	0.11		0.3		0.11	0.11
	$1/P_0$ (1/Pa)	4.00E-04		1.19E-06		4.00E-04	4.00E-04
	P_{max}(Pa)	1.00E+07		1.00E+09		1.00E+07	1.00E+07
	S_{ls}	1.00		1.00		1.00	1.00

PI…..Pico
PU…Puente
RE….Repetto

Table 18: Summary of baseline simulation – central Graben

base		RW model V08							
formation used for		PI	RE	PU	PI/RE	PU	PI	RE/PU	PI/RE/PU
Material name		SAN31	SAN28	SAN23	SHA01	SHA02	SASH1	SASH2	SILT
density [kg/m³]		2200	2300	2600	2350		2200		2190
wet heat conductivity [W/mC]		2.51			2.51		2.51		2.51
specific heat [J/kg-C]		920			920		920		920
pore compressibility [1/Pa]		7.83E-10	6.21E-10	3.16E-10	5.70E-10		1.06E-09		1.39E-09
total porosity [-]		0.31	0.28	0.23	0.29	0.24	0.29	0.23	0.33
effective porosity (-)		0.31	0.28	0.23	0.029	0.024	0.145	0.115	0.033
x permeability [mD]		280	207	114	12	7	61	33	17
y permeability [mD]		280	207	114	12	7	61	33	17
z permeability [mD]		140	103	57	6	4	31	16	9
Reference		Berea sandstone			Kimberlina shale		Berea sandstone		Berea
rel. perm. /van Genuchten	λ				0.9170				
	S_{lr}				0.30				
	S_{ls}				1.00				
	S_{gr}				0.29				
rel. perm. /Corey	S_{lr}	0.20					0.20		0.20
	S_{gr}	0.00					0.00		0.00
cap pressure /van Genuchten	λ	0.6700			0.412		0.67		0.67
	S_{lr}	0.11			0.3		0.11		0.11
	$1/P_0$ (1/Pa)	4.00E-04			1.19E-06		4.00E-04		4.00E-04
	P_{max}(Pa)	1.00E+07			1.00E+09		1.00E+07		1.00E+07
	S_{ls}	1.00			1.00		1.00		1.00

7.1.1.6 Injection of CO_2

Initially we started injection at a constant rate, but that did not allow us to inject a sufficiently economical volume over the 30 years of injection simulation. Due to this and recommendations from peer review we switched to constant pressure injection. This is done by setting the injection cells to a pressure slightly higher than reservoir pressure (~ +1%) and fully saturate them with CO_2.

The proposed injection well is represented halfway between the PV and THB faults a virtual well at position 1264501.7 UTM ft Easting, 12247112.6 UTM ft Northing (Datum WGS-84 1984, Zone11) for the northern graben and at well Shell OCS P-293-1 in the central graben. The injection interval is located at a depth of -2162 to -2197 m (-7093 to -7208 ft) in the Miocene sands for the northern Graben and at about -1555 m (-5100 ft) in a sand interval approximately 50 m (165 ft) thick in the central Graben. If during the simulation of injection CO_2 does not leak into shallower layers above the potential Upper Repetto Unconformity caprock, we continue the simulation for another 30 years of monitoring the plume migration.

7.1.2 Simulating varying injection scenarios

Because a turbidite environment is by nature lithologically heterogeneous, several models were constructed to capture geologic variation, with varying proportions of shales and sands as previously discussed. Cross sections of several different models for the northern and central Graben are shown in Figure 66 - Figure 71. Baseline models (Figure 66 and Figure 69) are direct mappings of lithology type from geologic models – using the closest point method. For the high shale content models, we assumed all sand/shale interbeds to be pure shale (Figure 67 & Figure 70). In another variation we assumed lower vertical permeability for the same shale material of the baseline model. The last variation is a refinement of the vertical mesh at the depth of the Upper Repetto Unconformity, which could potentially serve as a sealing caprock, the idea being to better represent the thin shale layer during the mapping process from geologic to fluid flow model (Figure 68 and Figure 71). These variations have been applied to both models – northern and central graben – a summary of variations is listed in Table 19 and Table 20.

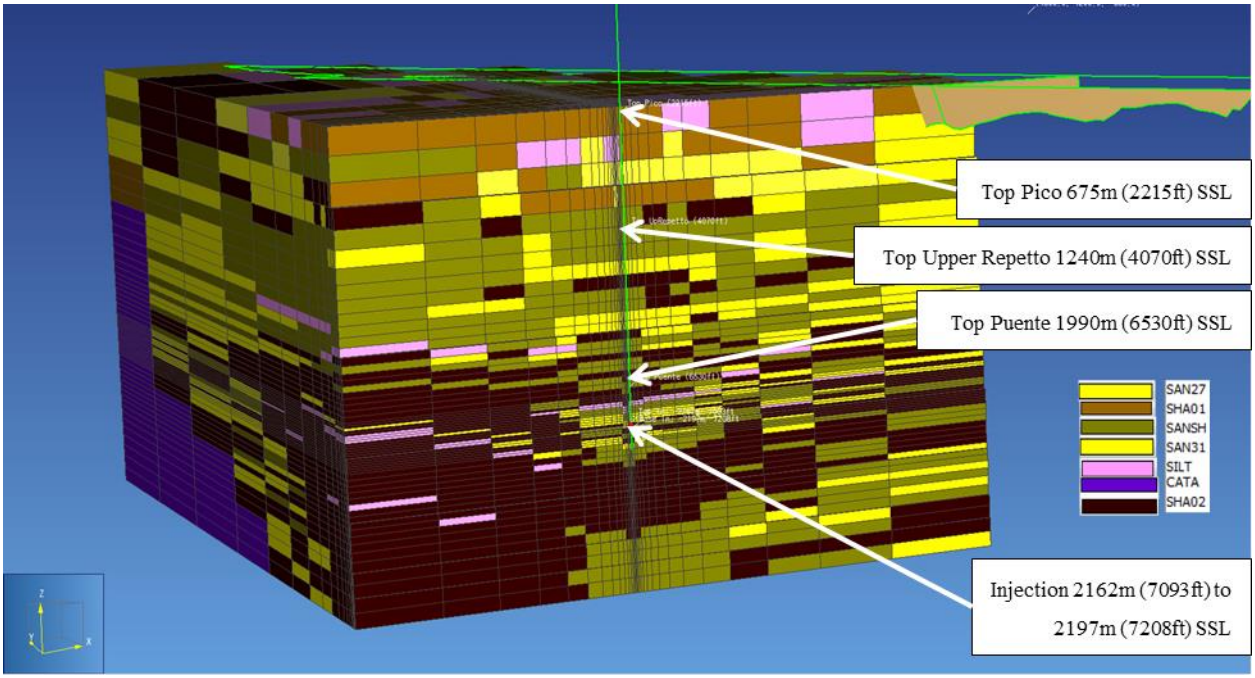

Figure 66: Northern Graben – base line cross section (SW-NE)

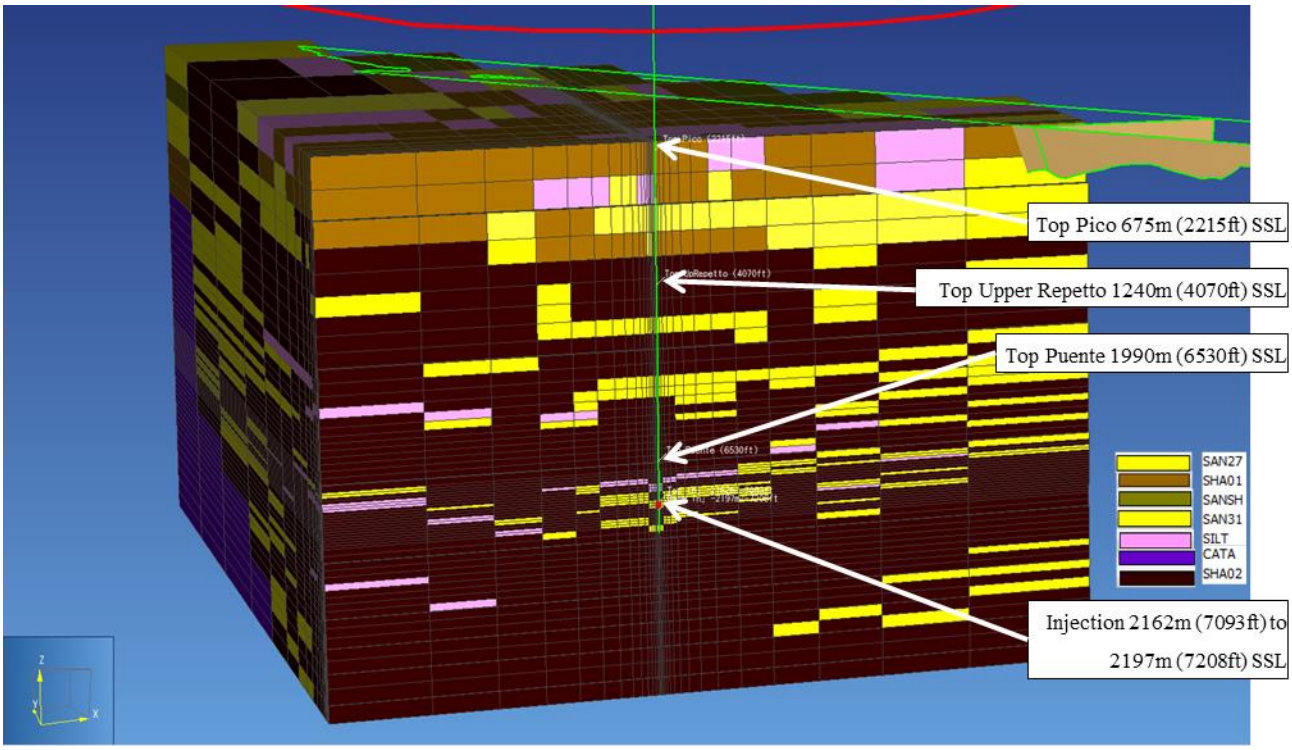

Figure 67: Northern Graben – Var1 model cross section (SW-NE)

Title: Characterization of Pliocene and Miocene Formations in the Wilmington Graben, Offshore Los Angeles, for Large-Scale Geologic Storage of CO_2

PI: Dr. Michael Bruno Final Report

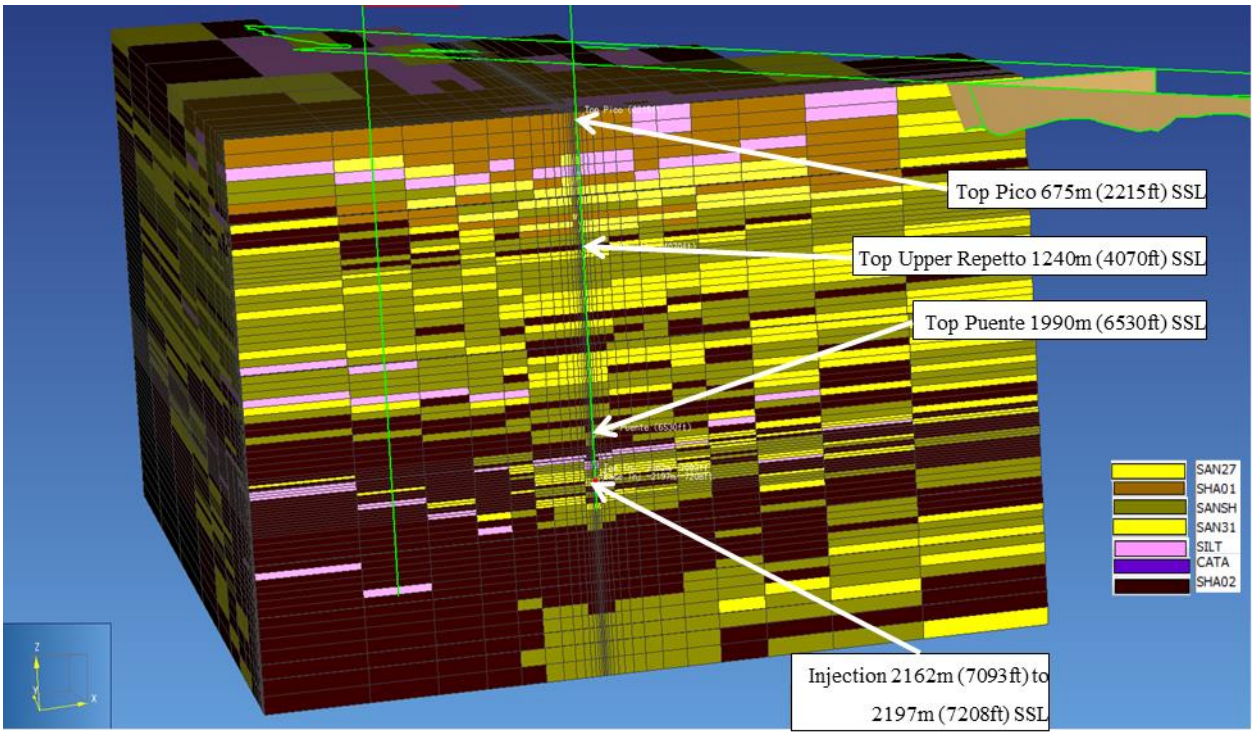

Figure 68: Var3 model cross section (SW-NE)

Title: Characterization of Pliocene and Miocene Formations in the Wilmington Graben, Offshore Los Angeles, for Large-Scale Geologic Storage of CO_2

PI: Dr. Michael Bruno Final Report

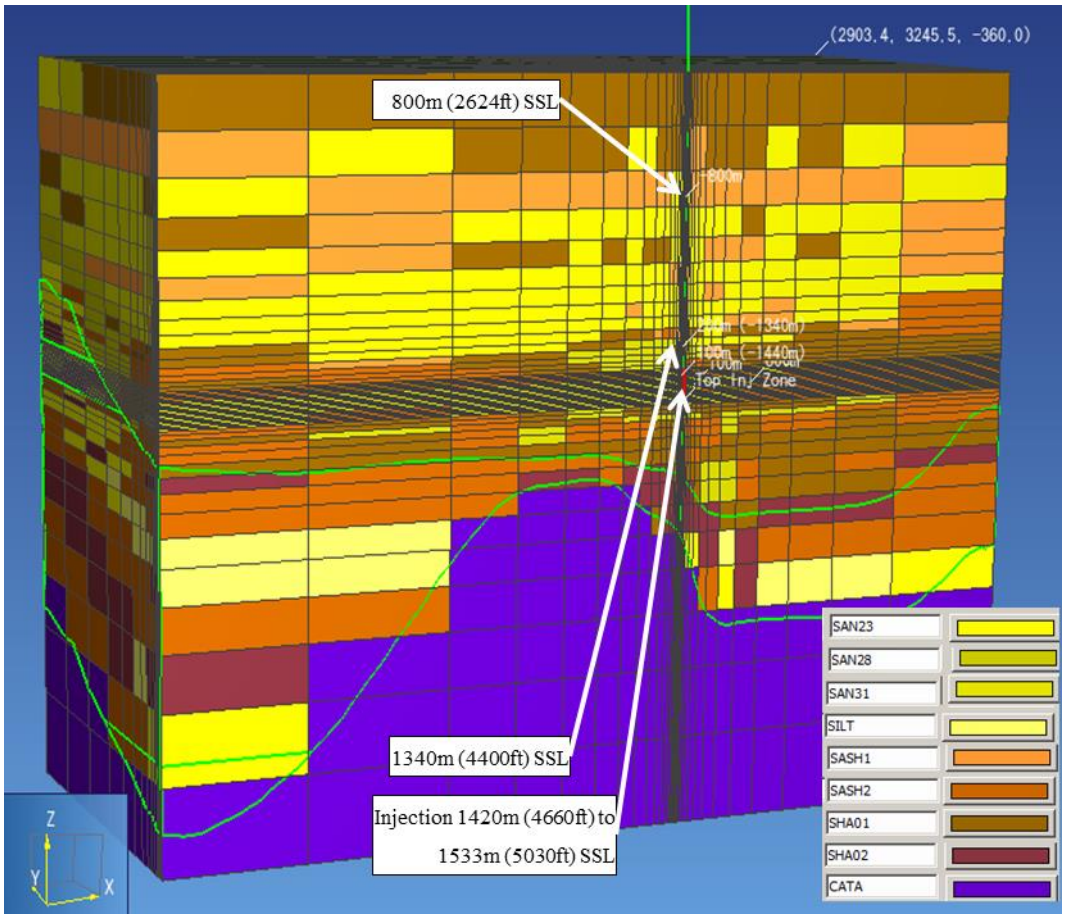

Figure 69: Central Graben - Baseline cross section (SW-NE) (2xVE)

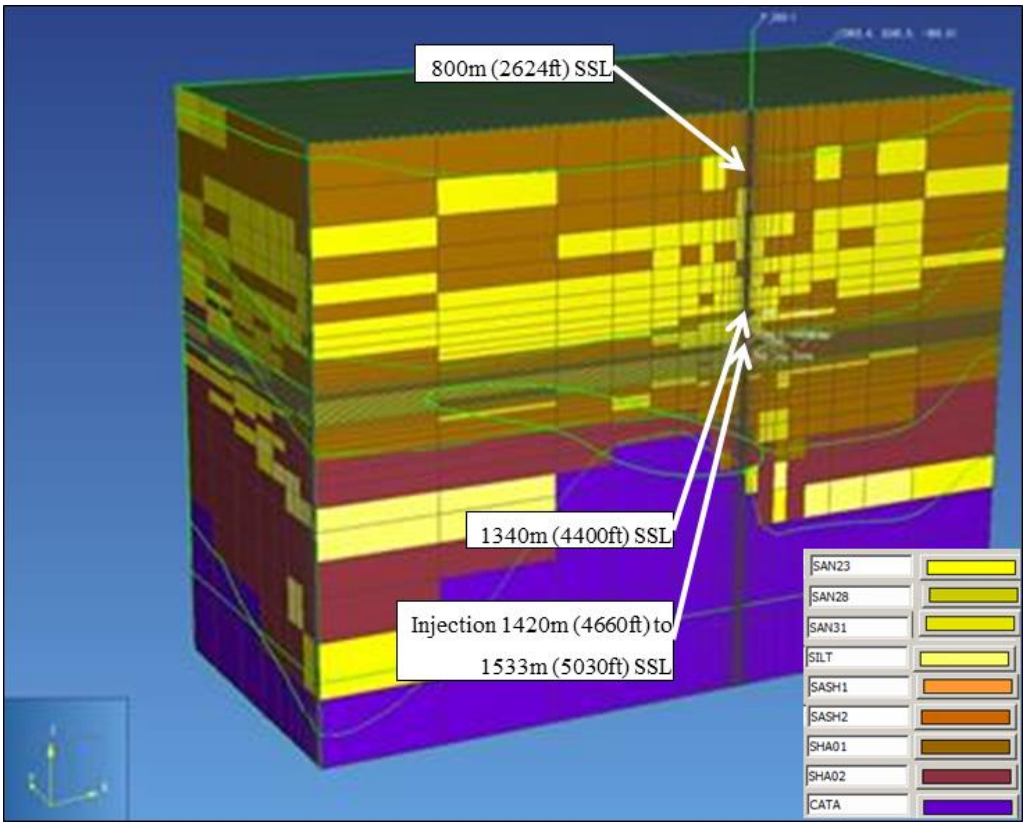

Figure 70: Central Graben - High shale model cross section (SW-NE) (2xVE)

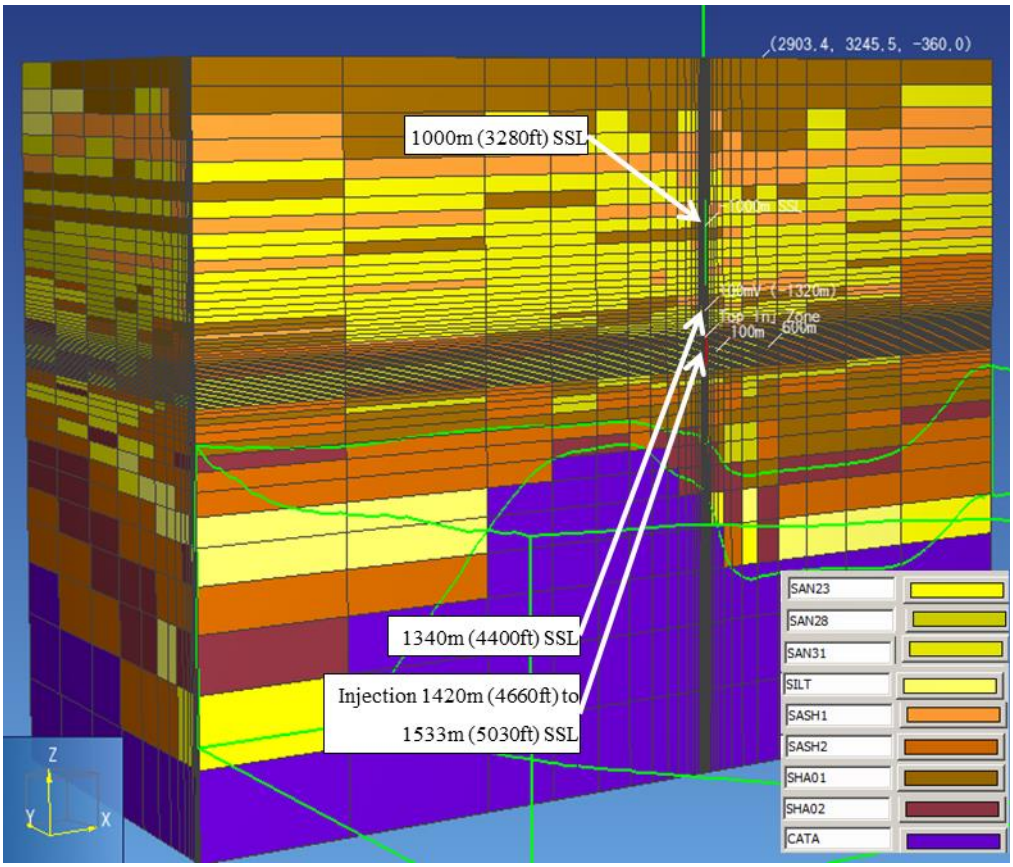

Figure 71: Central Graben - Vertical refinement of mesh at Upper Repetto unconformity (SW-NE) (2xVE)

Table 19: List of various scenarios modeled in Northern Graben

	Lithology type variation		Vertical shale perm. (mD)		# of active
CASE	Vol. % shale	Vol. % Interbeds	SHA01	SHA02	cells
Baseline	39	25	11	8	61,244
High Shale model (**Var1**)	64	0	11	8	61,244
Low Vertical shale perm model (**Var2**)	39	25	1.1	0.8	61,244
Refined Upper Repetto model (**Var3**)	41	24	1	1	80,320
SHA01... shale type 1					
SHA02... shale type 2					

Table 20: List of various scenarios modeled in Central Graben

	Lithology type variation		Vertical shale perm. (mD)		# of active
CASE	**Vol. % shale**	**Vol. % Interbeds**	**SHA01**	**SHA02**	**cells**
Baseline	29	20	6	4	60,690
High Shale model (**Var1**)	49	0	6	4	60,690
Low Vertical shale perm model (**Var2**)	29	20	0.0006	0.0004	60,690
Refined Upper Repetto model (**Var3**)	28	20	6	4	78,540

7.2 Results and discussion

This section discusses the results of the two modeling areas in detail. Pressure and gas saturation over time are shown for the different scenarios at different locations relative to the injection point. Volumes stored are summarized.

7.2.1 Northern Graben area

Baseline model results:

Approximately 15.75 MMt of CO_2 are injected after 30 years (0.525 MMt/year). Figure 72 shows the CO_2 plume after 30 years of injection. It shows that the gas migrates to upper formations close to the top of the model.

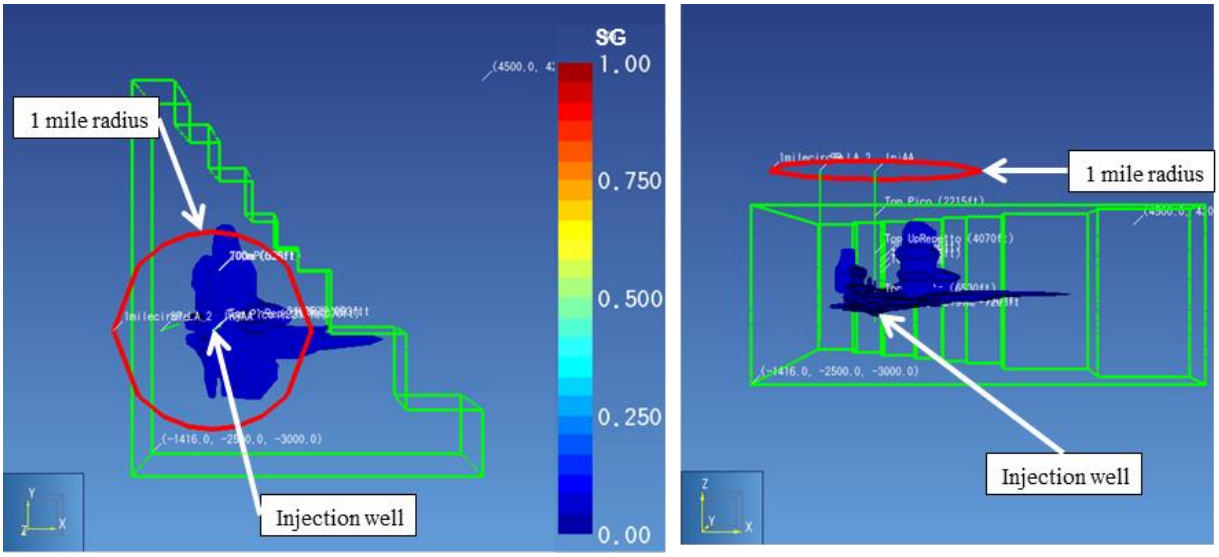

Figure 72: CO_2 gaseous plume after 30 years of injection, top view (left) and side view (right), with 1 mile red circle around injection well

The pressure ranges from 7.10E6 Pa to 2.91E7 Pa after 30 years injection. Figure 73 shows the supercritical CO_2 saturation contours. Figure 74 takes a closer look at supercritical CO_2 saturation in NE-SW direction at the cutting planes y=0 m (through the injection well) and y=120 m (120 m NW of injection well).

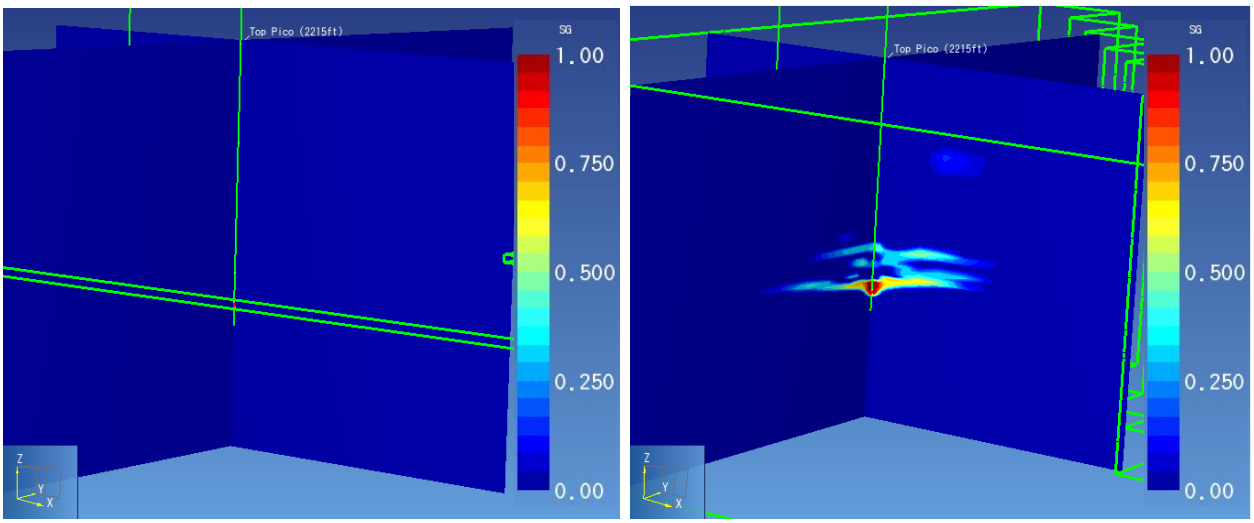

t = 0 t = 30 years

Figure 73: Supercritical CO_2 saturation contour across injection well in NE-SW and NW-SE directions

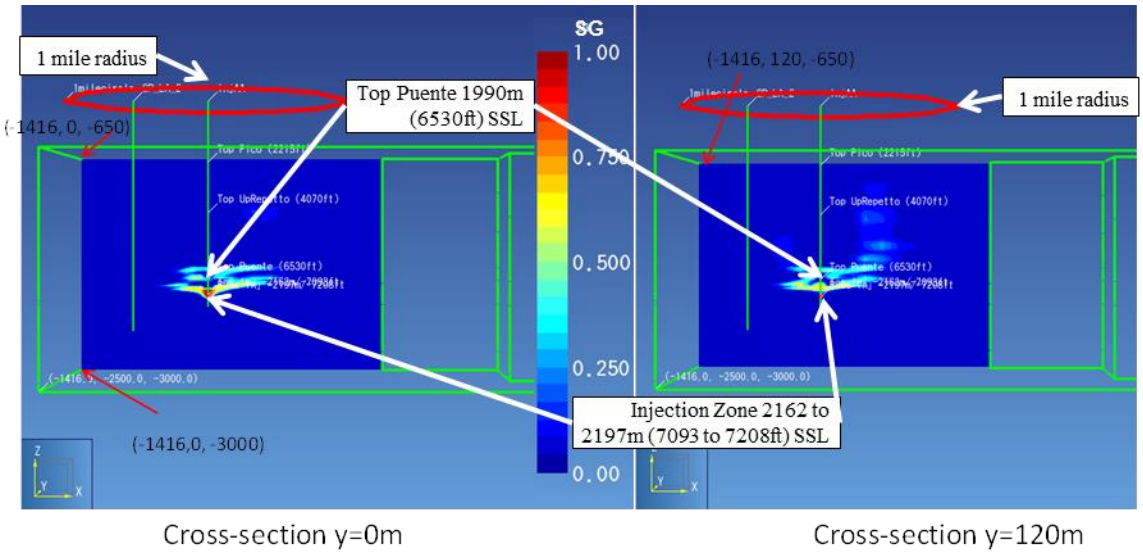

Figure 74: Closer look at supercritical CO_2 saturation in NE-SW direction

High shale model (Var1) Results:

With a constant injection pressure of 2.17E7 Pa (3150 psi), approximately 5.28 MMt of CO_2 would be injected into the formation after 30 years (0.176 MMt/ year). Figure 75 shows the CO_2 plume after 30 years injection. It shows that the gas stays within the injection zone.

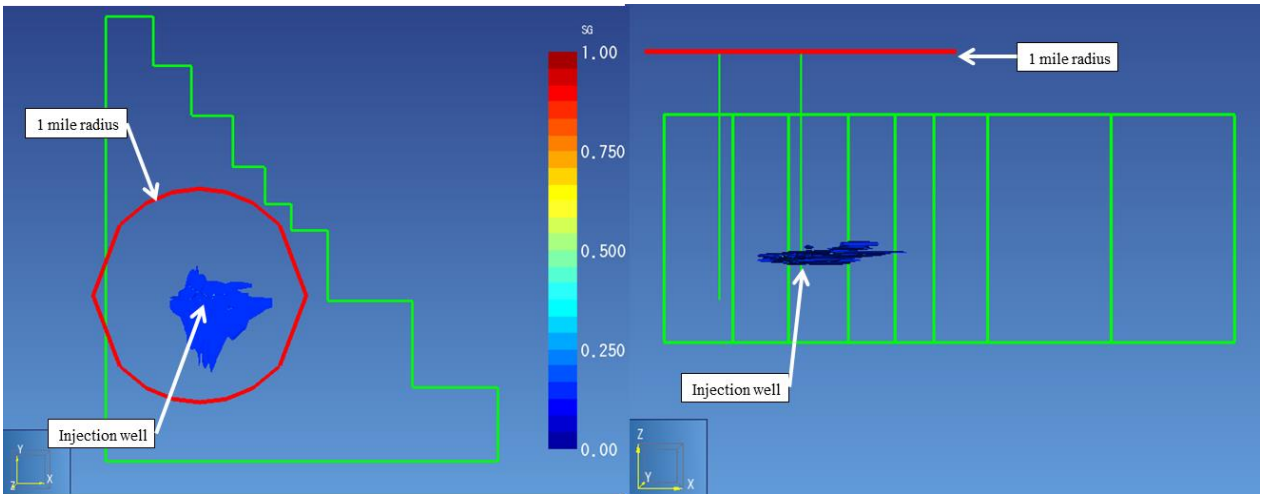

Figure 75: CO_2 gaseous plume after 30 years of injection, top view (left) and side view (right), with 1 mile red circle around injection well

The pressure ranges from 7.10E6 Pa to 2.91E7 Pa after 30 years injection. Figure 76 shows the supercritical CO_2 saturation contours.

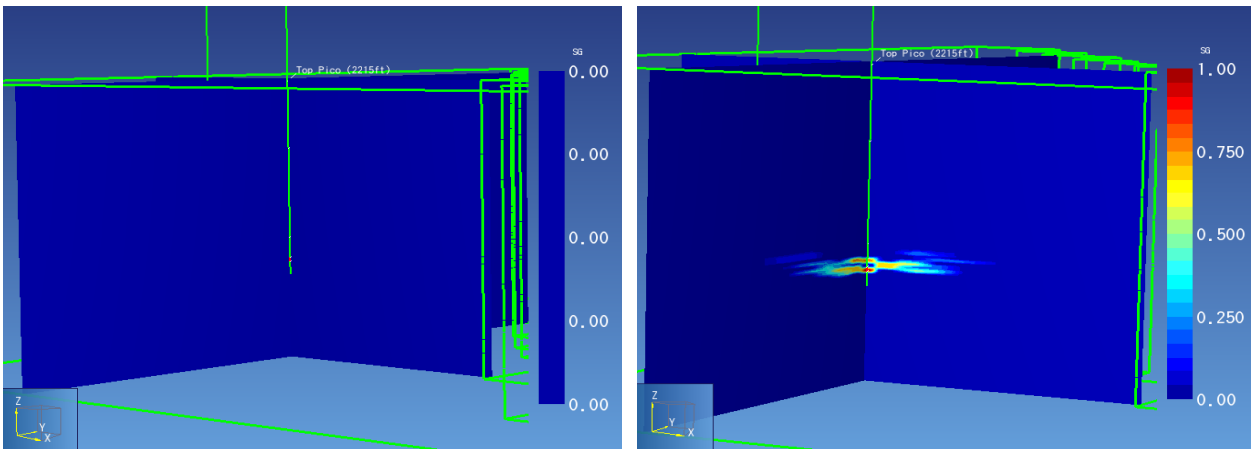

t = 0 t = 30 years

Figure 76: Supercritical CO_2 saturation contour across injection well in NE-SW and NW-SE directions

Figure 77 depicts the supercritical CO_2 saturation contour during the observation phase. The CO_2 migration continues wholly within the injection zone, thus no containment issue is predicted. Note that the CO_2 migrating to the local southern boundary along the y-axis (because of the constant pressure boundary condition) is most likely due to a gridding effect. Gridding effect occurs because of the type of mesh used in constructing the model. Thus the plume extension is not only driven by the numerical solution, but also by the aspect ratio and size of mesh cells. As demonstrated in *Appendix 3: Gridding Effect on Plume Migration* the plume extension will not look much different with a different grid refinement. Also we check CO_2 mass at the beginning and end of this simulation: 5.28 and 5.22 MMt, respectively, meaning about 0.06 MMt (=1.1% of total injected CO_2) have migrated into the SE area of the Graben.

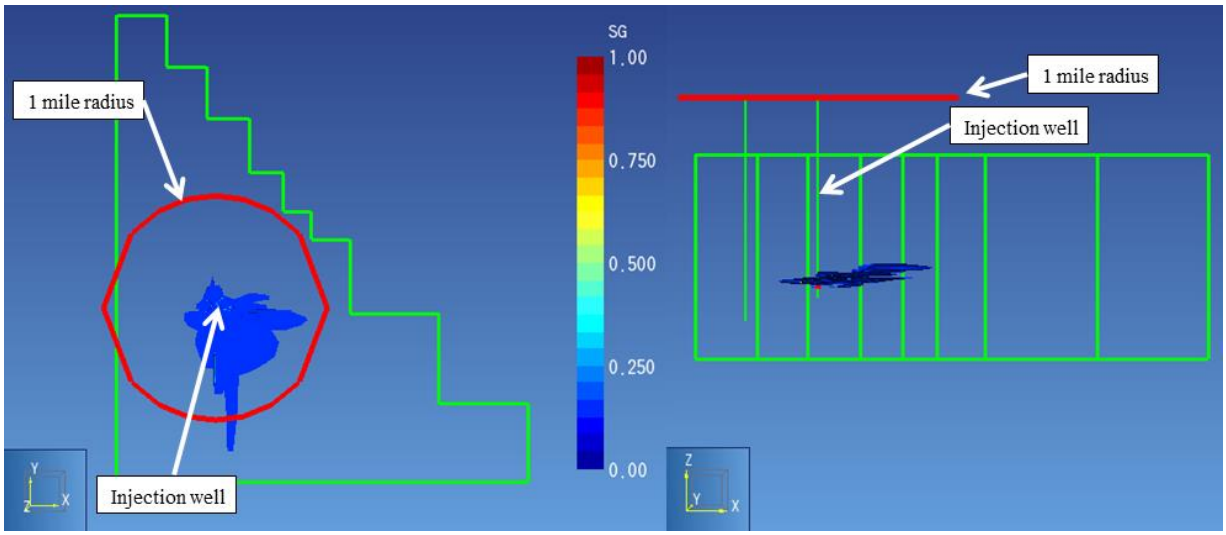

Figure 77: CO_2 gaseous plume after 30 years of observation, top view (left) and side view (right), with 1 mile red circle around injection well

Low shale permeability (Var2) Model Results:

With constant injection pressure of 2.17E7 Pa (3150 psi), approximately 14.45 MMt of CO_2 will be injected after 30 years (0.48 MMt/year). Figure 78 shows the CO_2 plume after 30 years of injection. Note the gas migrates 1330 m (4365 ft) from the injection layer to the upper formation, very close the top of the model; and the CO_2 migrates to THB fault along the x-axis due to the gridding effect.

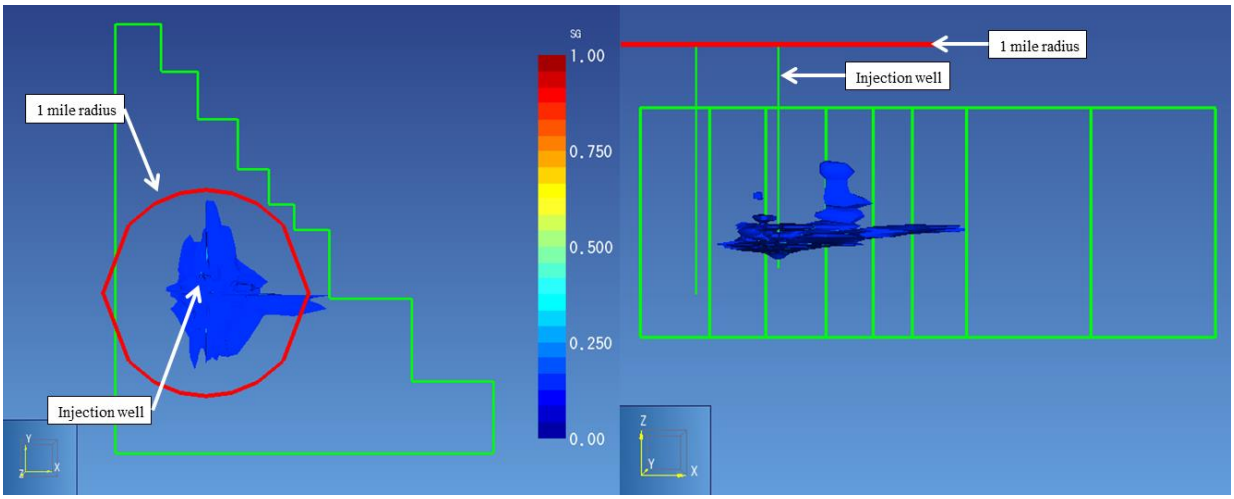

Figure 78: CO_2 gaseous plume after 30 years of injection, top view (left) and side view (right), with 1 mile red circle around injection well

The pressure ranges from 7.10E6 Pa to 2.91E7 Pa after 30 years injection.

Figure 79 shows the corresponding supercritical CO_2 saturation contours. Figure 80 takes a closer look at supercritical CO_2 saturation in NE-SW direction at the cutting planes y=0 m (through the injection well) and y=120 m (120 m NW of injection well).

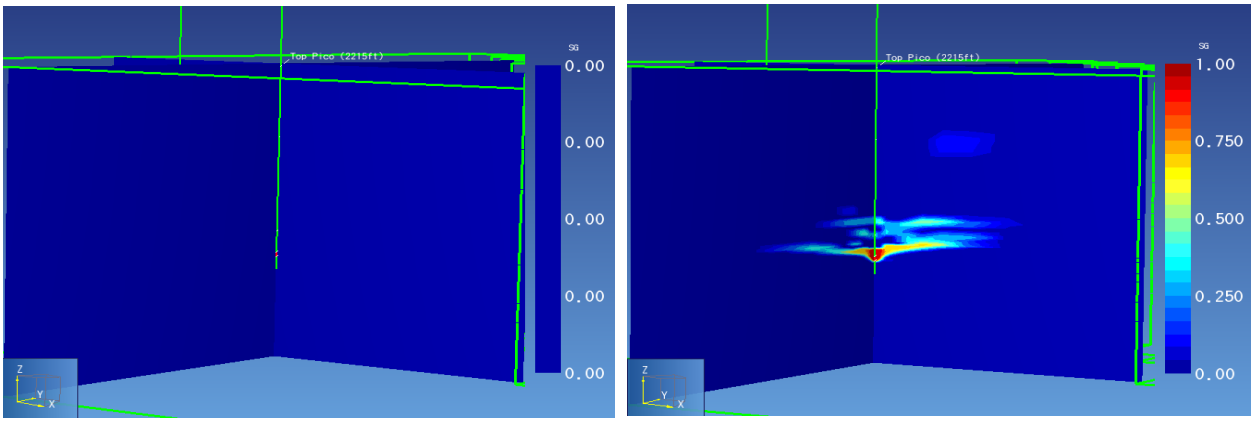

t = 0 t = 30 years

Figure 79: Supercritical CO_2 saturation contour across injection well in NE-SW and NW-SE directions

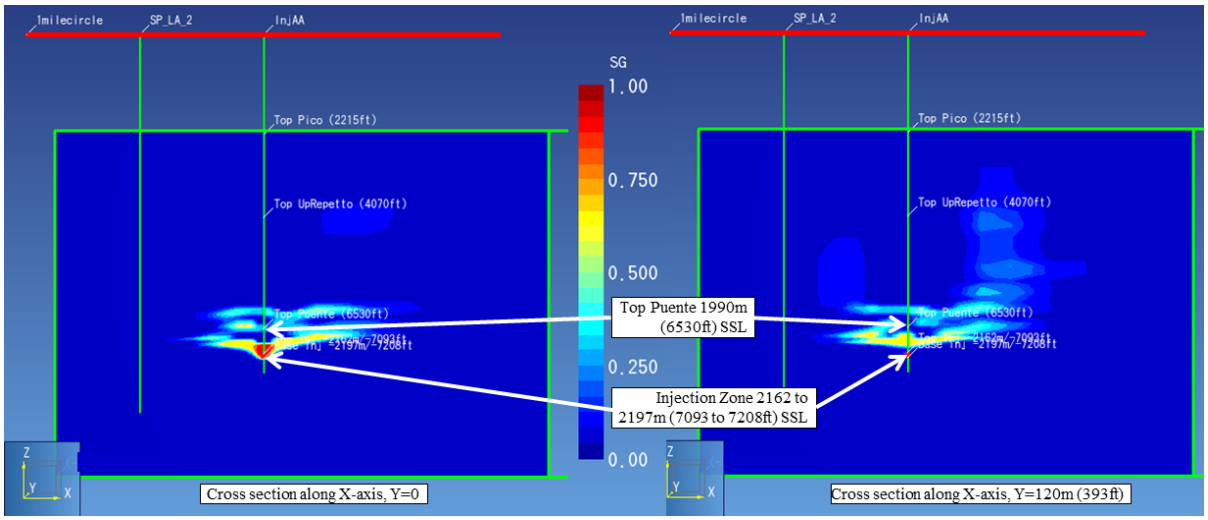

Figure 80: Closer look at supercritical CO_2 saturation in NE-SW direction

Refined Upper Repetto (Var3) Model Results:

With constant injection pressure 2.17E7 Pa (3150 psi); approximately 12.74 MMt of CO_2 will be injected after 30 years (0.42 MMt/year). Figure 81 shows the CO_2 plume after 30 years of injection. It indicates that the CO_2 gas plume migrates 750 m from the injection layer into an upper formation, in which it is arrested by an impermeable shale layer.

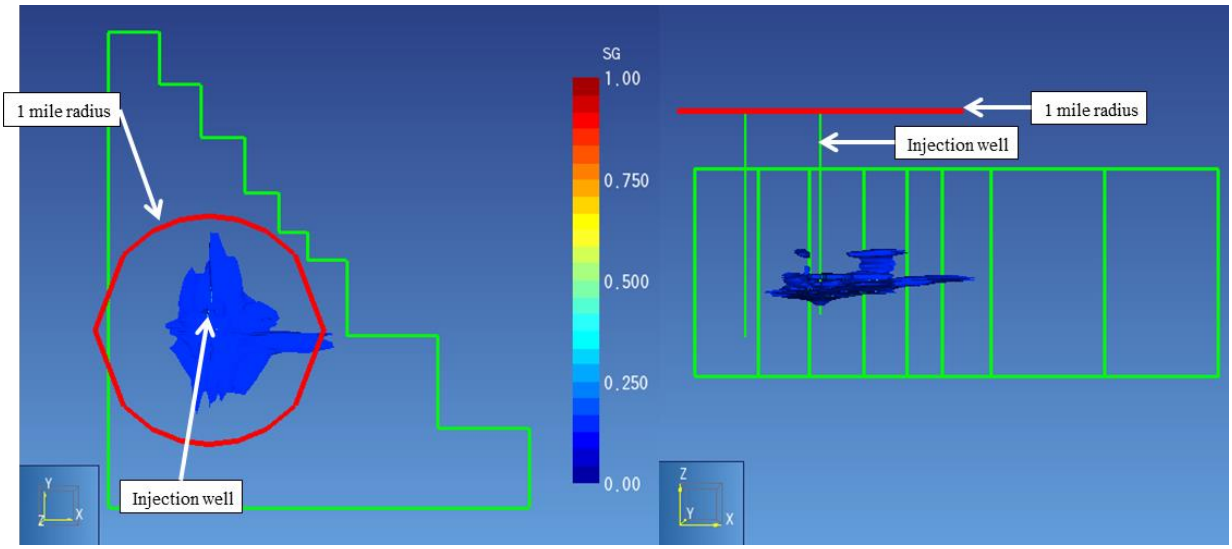

Figure 81: CO_2 gaseous plume after 30 years of injection, top view (left) and side view (right), with 1 mile red circle around injection well

The pressure ranges from 7.10E6 Pa to 2.91E7 Pa after 30 years injection. Figure 82 shows the corresponding supercritical CO_2 saturation contours.

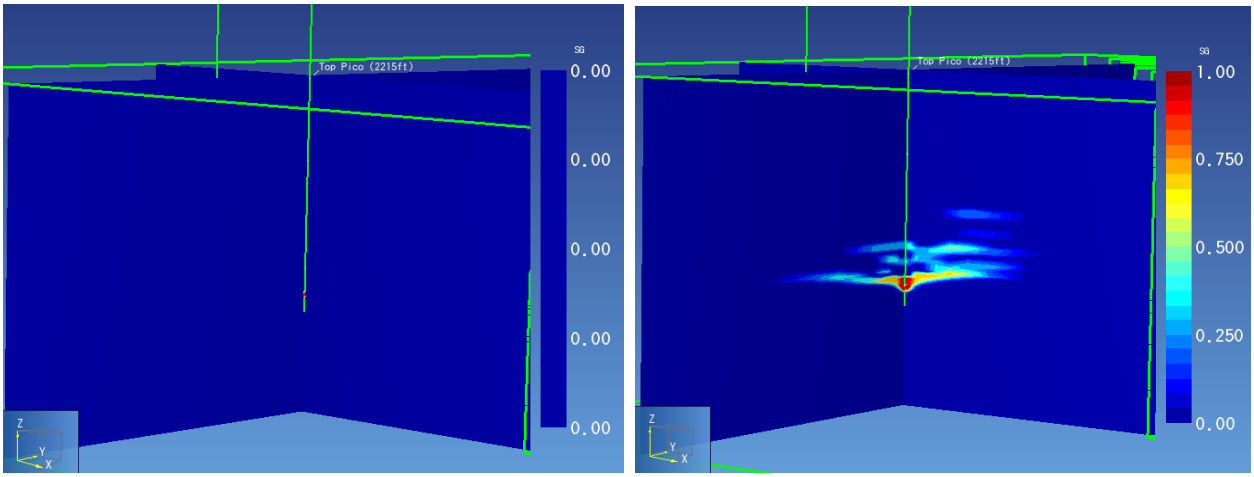

t = 0 t = 30 years

Figure 82: Supercritical CO_2 saturation contour across injection well in NE-SW and NW-SE directions

Figure 83 shows the supercritical CO_2 saturation contour during the observation phase. The CO_2 migrates close to the model's surface through the sand path, at around 400 m (1310 ft) away from injection well along the x-axis. The CO_2 migrates along the x-axis reaching the THB fault due to gridding effect.

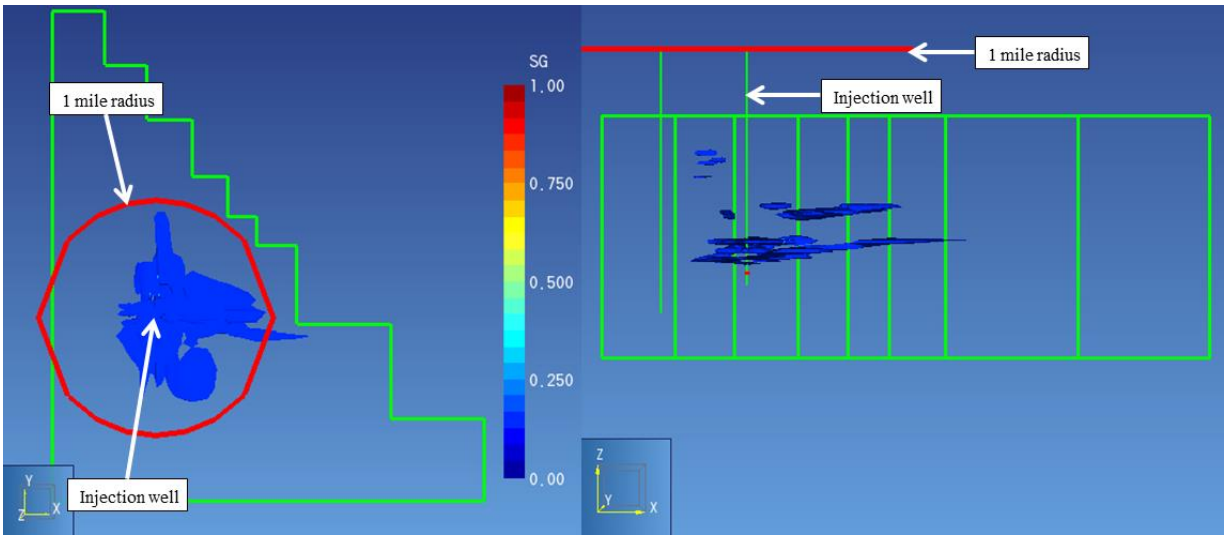

Figure 83: CO_2 gaseous plume after 30 years of observation, top view (left) and side view (right), with 1 mile red circle around injection well

Based on Tough2 modeling results for 30 years of constant pressure (21.7 MPa), supercritical CO_2 injection, a brief summary is shown in Figure 84 and Table 21. Var1 injected 5.28 million tons totally (0.176 million tons per year), and Var3 injected 12.74 million tons totally (0.425 million tons per year). CO_2 migrates 1330 m (4365 ft) vertically from the injection layer for baseline and Var2 scenarios, which could pose containment issues. In Var1 and Var3 scenarios, CO_2 migrates 280 m (920 ft) and 750 m (2460 ft) vertically, respectively, from the injection layer, which is conservative for 30 years' injection.

Var1 contains the most shale (over 60%), and the least sand (7%; Table 19). The shale blocks the CO_2 injection migration. Var2 uses the same lithology as baseline simulation except the vertical permeability of shale is reduced 10 times relative to baseline shale vertical permeability. However, the lower permeability shale did not arrest CO_2 migration through the sand path. Var3 has a finer mesh than the baseline in the Upper Repetto Unconformity. The finer mesh captures more shale lithology (Table 19), which stops the CO_2 migration and reduces leakage, though a small amount of CO_2 leakage was observed during the 30 years observation phase in Var3.

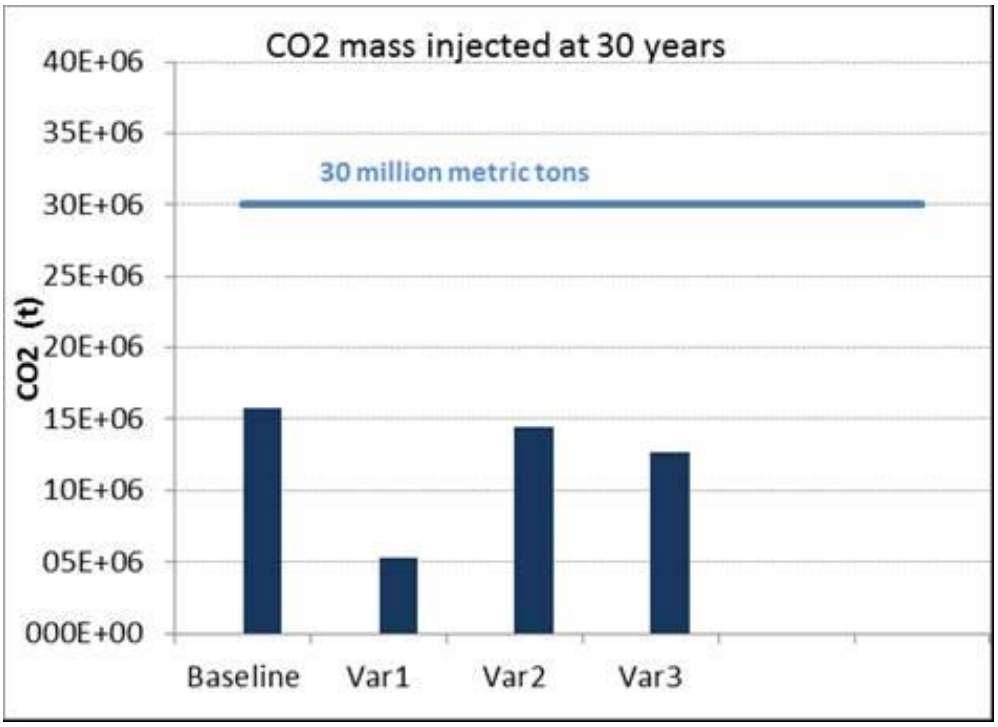

Figure 84: The depth of CO_2 migration to upper formation and total injection volume after 30 years constant pressure injection

Table 21: Results after 30 years of injection in Northern Graben area

CASE	Shallowest CO_2 (m SSL)	Leaking?
Baseline	-850	Y
High Shale model (**Var1**)	-1,901	N
Low Vertical shale perm model (**Var2**)	-850	Y
Refined Upper Repetto model (**Var3**)	-1,428	N

7.2.2 Central Graben area

Injected volumes for the different scenarios discussed in section 7.1.2 range from 36 to 52 MMt of CO_2, into one well as shown in Figure 85.

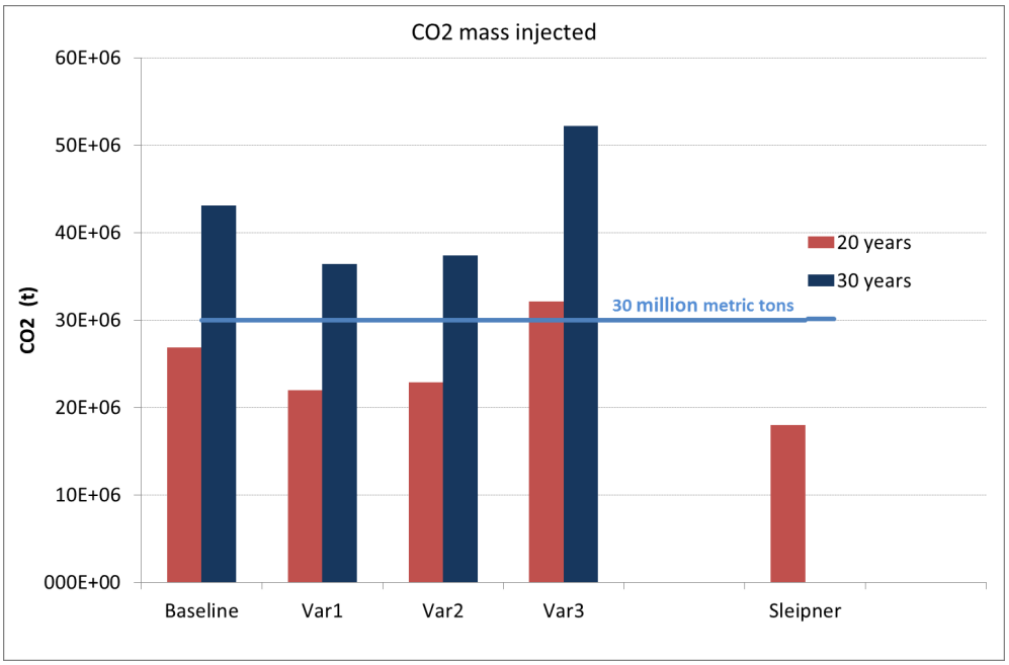

Figure 85: CO_2 amount injected into Central Graben

During the following discussion and comparison of the simulation results we will refer to different locations in the model as monitoring points. These are cells specified throughout the model for which we show different parameters over time for all time steps. Figure 86 shows the position of these.

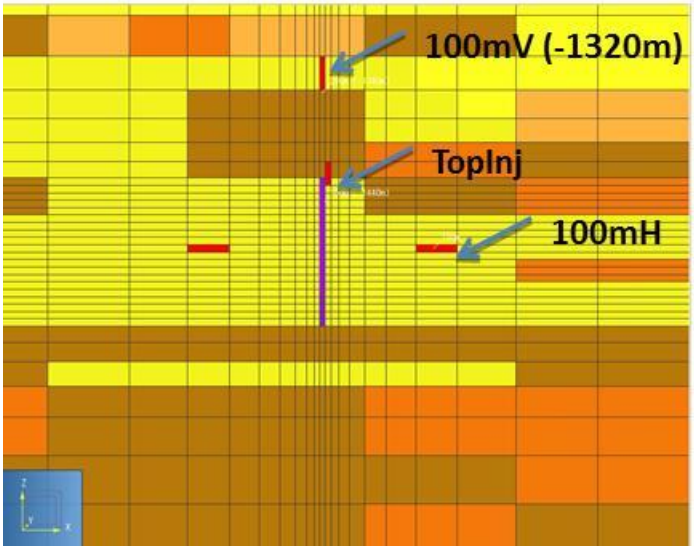

Figure 86: Monitoring cells (red) close to injection cells (purple)

Comparing pressure at different monitoring points

Since the injection gradient is the same for all simulations the pressure over time at the top of the perforations (Figure 87) evolves similarly, with a maximum of 1% higher than the initial pressure. Pressure increase at a distance of 100 m (330 ft) in horizontal NE-direction from the injection interval (Figure 88) is about 1% for the low shale permeability run (Var2) also; all other pressure curves show lower increase. Moving up the well a distance of 420 m (1377 ft) we see a slightly higher pressure increase in the order of 1.4% for all simulation variations (see Figure 90), which can be explained by the accumulation of CO_2 below the impermeable layers.

One third of the way to the PV fault in the horizontal direction from the injection point the maximum pressure increase is observed in the model with high shale content (Var1, Figure 89), but still below 1% of the initial pressure.

Title: Characterization of Pliocene and Miocene Formations in the Wilmington Graben, Offshore Los Angeles, for Large-Scale Geologic Storage of CO_2

PI: Dr. Michael Bruno Final Report

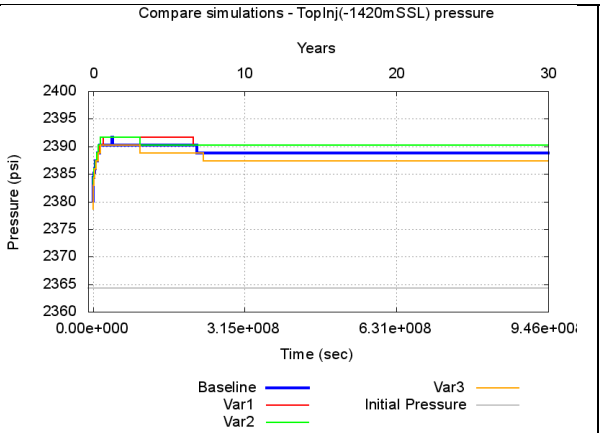

Figure 87: Top injection pressure

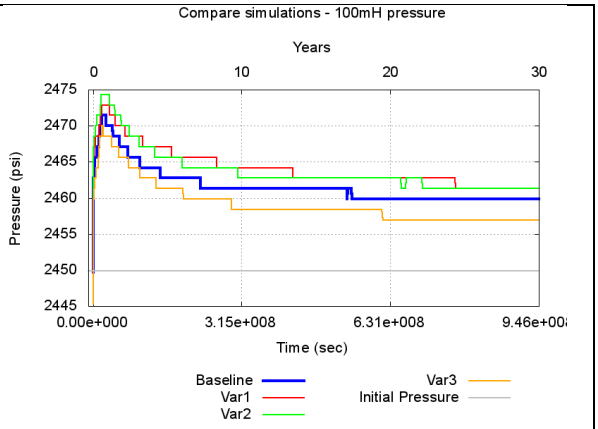

Figure 88: 100 m horizontal from injection

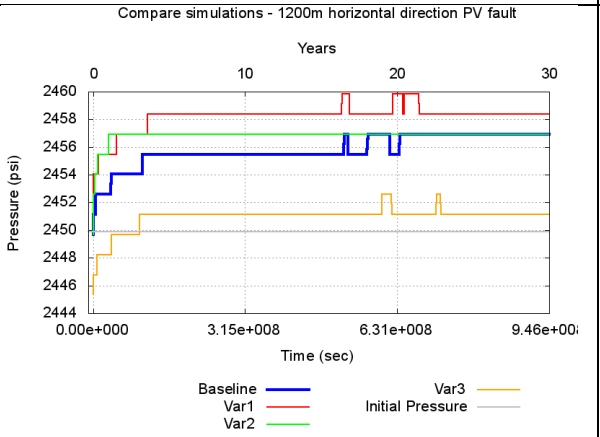

Figure 89: 1200 m horizontal from injection

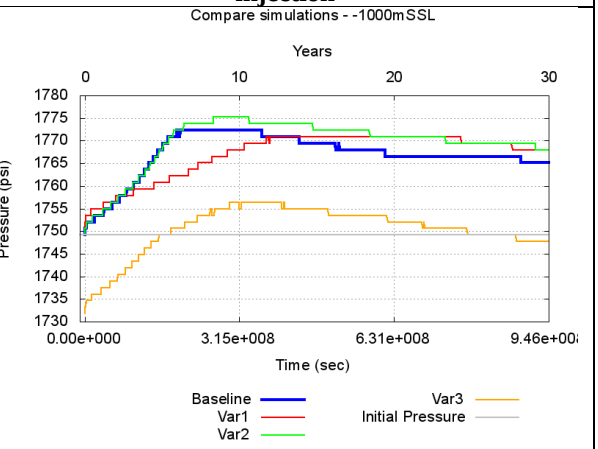

Figure 90: 420 m above injection (-1000 m SSL)

Compare gas saturation and CO_2 mass fraction at monitoring points

The following graphs show the gas saturation (thick lines) and the mass fraction of dissolved CO_2 in aqueous phase (dashed thin lines) over time at selected monitoring points. After two to three years CO_2 has migrated 100 m (330ft) in vertical direction (Figure 91) in the shaly model (Var1) and the mesh refined model (Var3), and the amount of CO_2 reaching there has exceeded saturation in liquid phase and appears in the supercritical gaseous phase. Baseline and low permeability shale models seem to allow CO_2 migration further, thus it has not yet accumulated at this point in order to evolve as gaseous phase. Looking at Figure 92, CO_2 starts accumulating at a shallower depth for the baseline and low vertical permeability (Var2) model , as gas phase evolves after 12 to 13 years about 420 m (1375 ft) above the injection point.

Title: Characterization of Pliocene and Miocene Formations in the Wilmington Graben, Offshore Los Angeles, for Large-Scale Geologic Storage of CO_2

PI: Dr. Michael Bruno Final Report

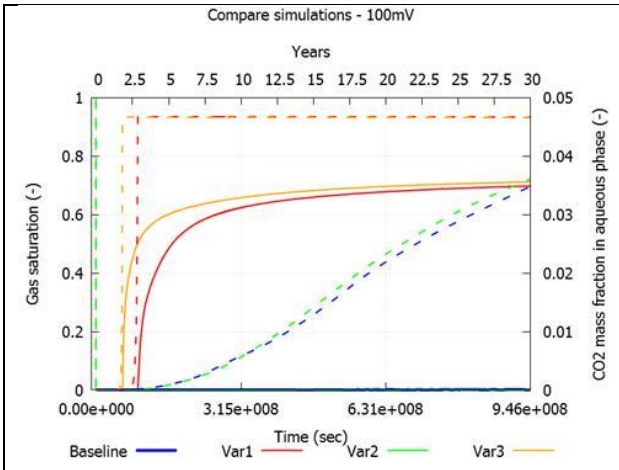

Figure 91: 100 m above injection (-1320mSSL)

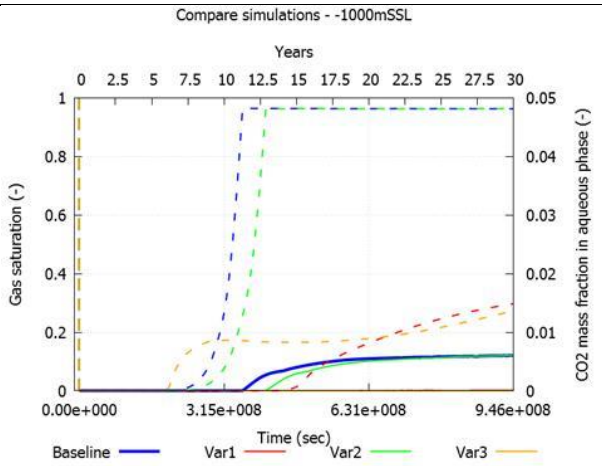

Figure 92: 420 m above injection(-1000mSSL)

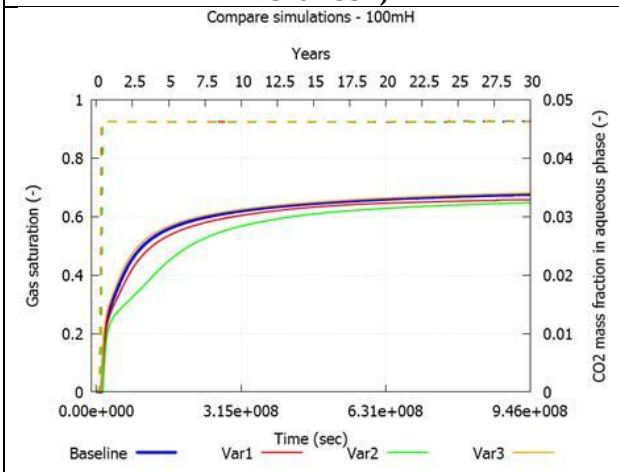

Figure 93: 100 m horizontal from injection

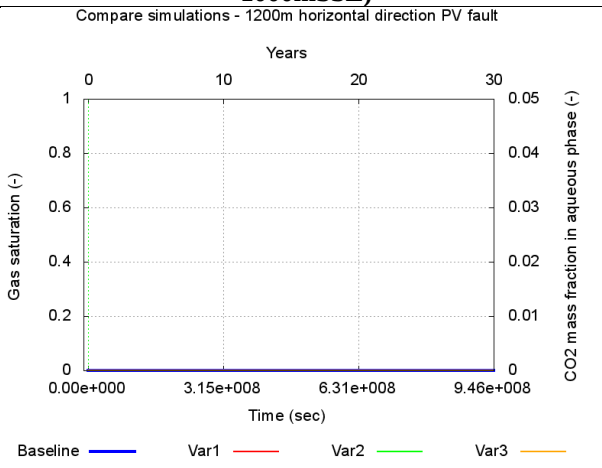

Figure 94: 1200 m horizontal from injection

In the horizontal direction the migration of CO_2 appears similar; within the first year supercritical CO_2 reaches 100 m (330 ft) NE from injection point (Figure 93), stabilizing at a saturation of 65% and no CO_2 appears at a distance of 1200 m (3935 ft) in the direction of the PV fault – SW (Figure 94) during the entire 30 year period of injection.

The simulation results for the geologic baseline model indicate that after 30 years of injection, the CO_2 plume migrated and extended 1000 m (3280 ft) in the horizontal direction and 450 m (1475 ft) in the vertical direction (Figure 95). The CO_2 is not fully contained within the desired vertical interval.

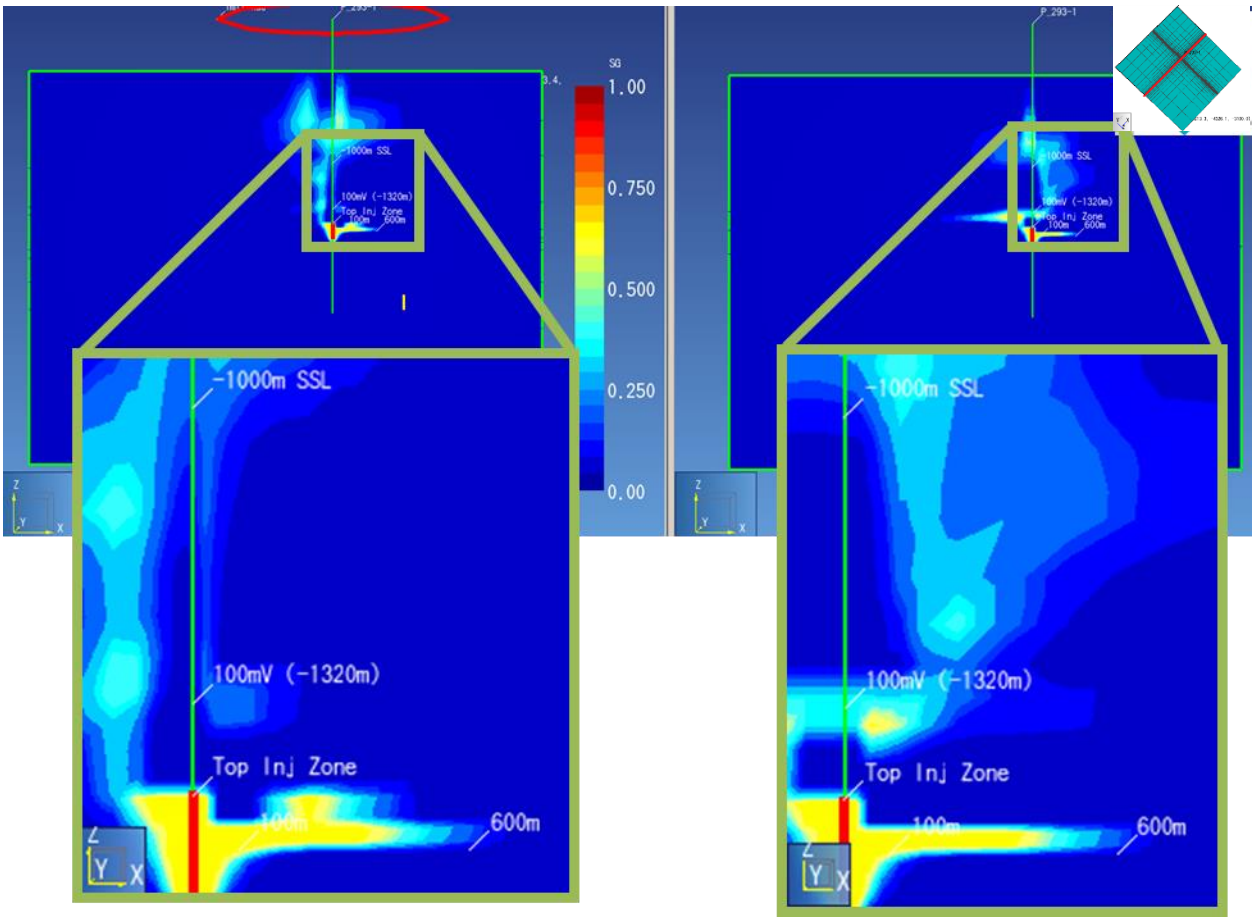

Figure 95: Baseline model (left, Mod25_sim008); shaley model –Var 1(right, Mod26sim05); both after 30 years of injection; SW-NE cross sections

CO_2 plume cross sections of simulations for alternative scenarios are presented in Figure 96 -Figure 99. The simulation results indicate that even with higher shale content, lower vertical shale permeability, or better shale continuity due to mesh refinement, CO_2 is not fully contained within the desired vertical interval when injection is conducted at depths of around 1525 m (5000 ft). Table 22 lists a summary of these results. Since all variations leaked during injection, we did not investigate further the migration of the leaking plume during an observation phase.

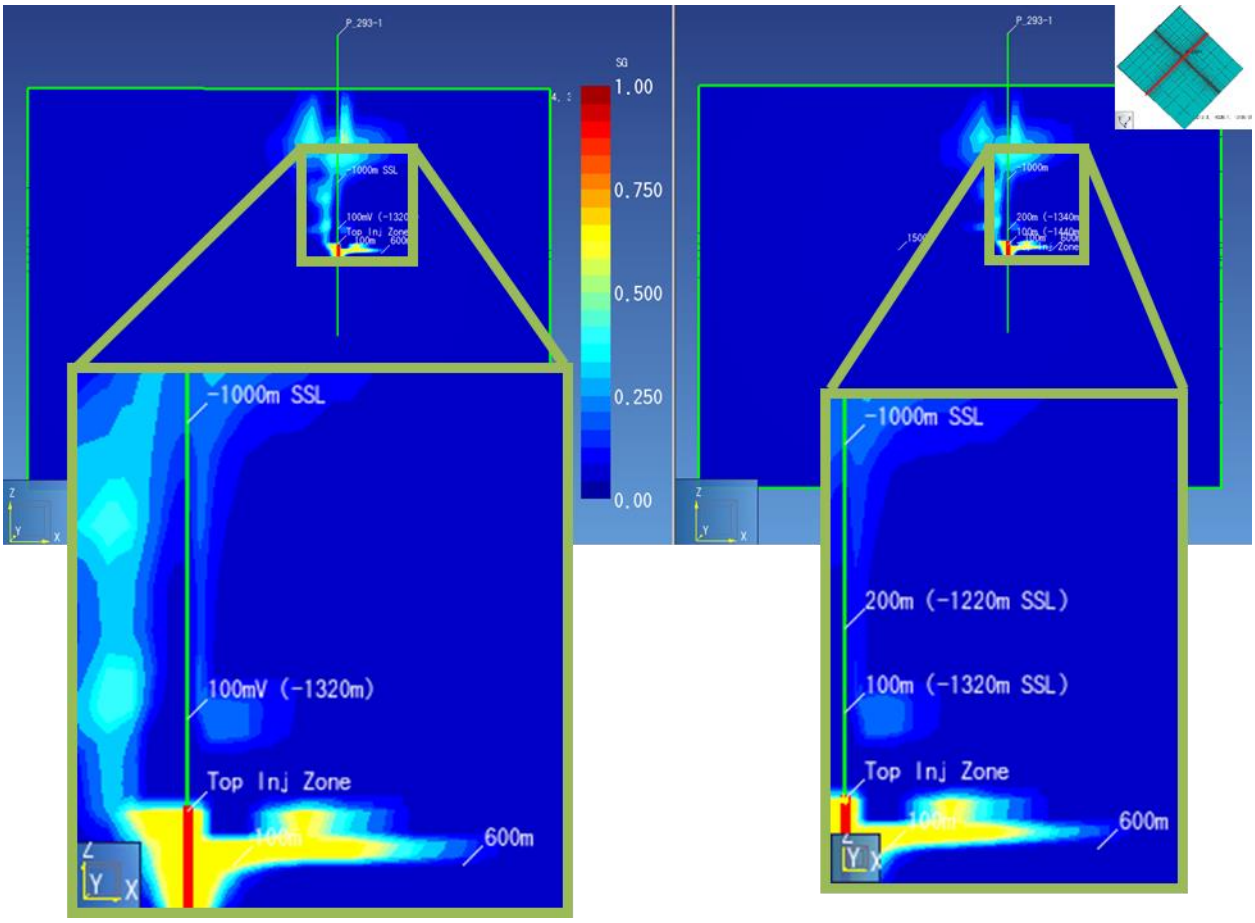

Figure 96: Baseline model (left, Mod25_sim008); lower shale permeability –Var 2(right, Mod25sim009); both after 30 years of injection; SW-NE cross sections

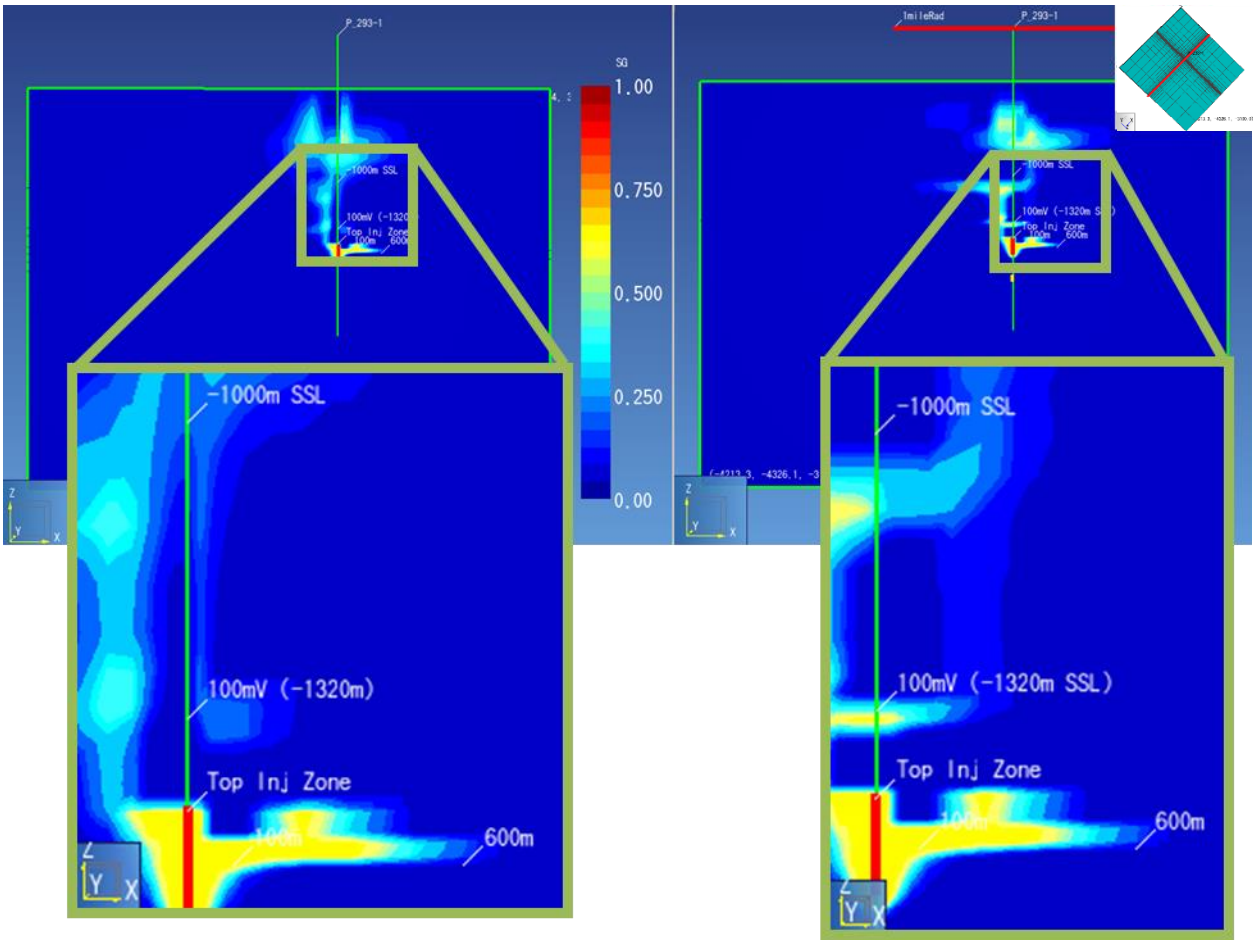

Figure 97: Baseline model (left, Mod25_sim008); Upper Repetto Refinement –Var 3(right, Mod27sim002); both after 30 years of injection; SW-NE cross sections

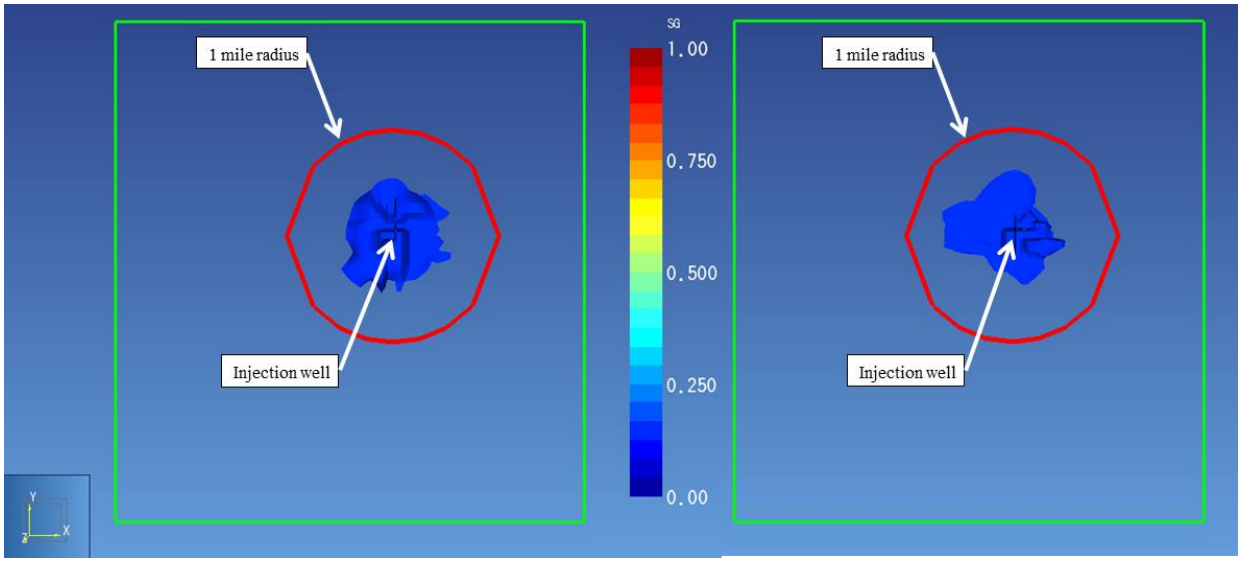

Figure 98: Baseline (left, Mod25_sim008) and shaly model – Var 1(right, Mod26_sim005) gas plume after 30years top view

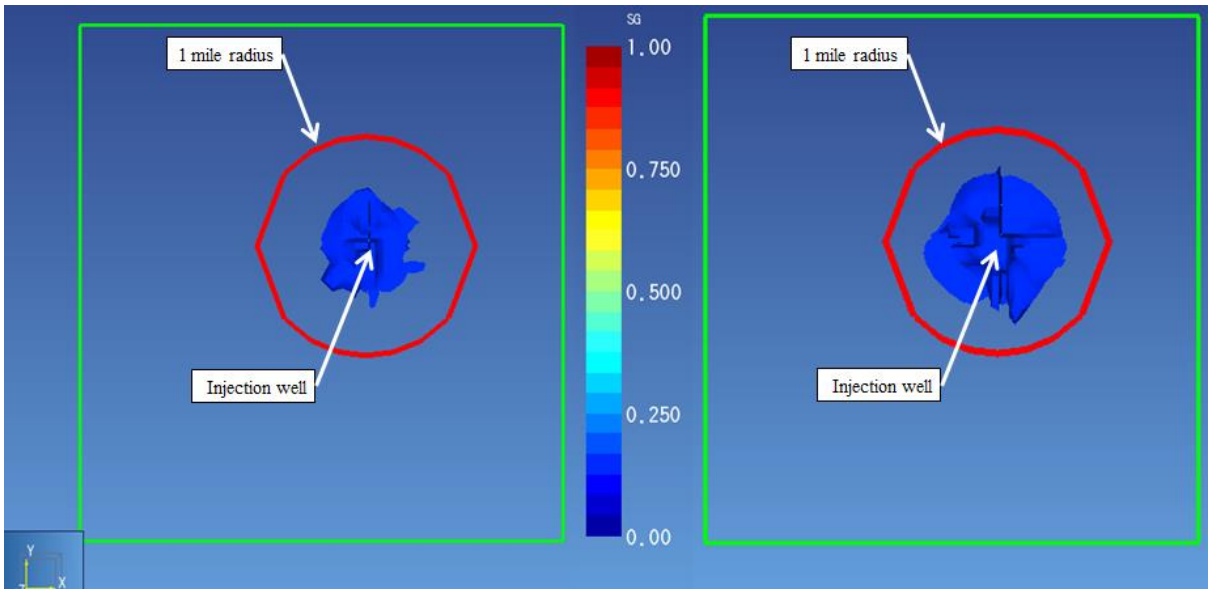

Figure 99: Lower shale permeability – Var 2 (left, Mod25_sim009) and Upper Repetto Refinement – Var 3 (right, Mod27_sim002) gas plume after 30years top view

Table 22: Results after 30 years of injection in central Graben area

CASE	Shallowest CO_2 (m SSL)	Leaking ?
Baseline	-360	Y
High Shale model (**Var1**)	-360	Y
Low Vertical shale perm model (**Var2**)	-630	Y
Refined Upper Repetto model (**Var3**)	-360	Y

We conclude from this modeling effort that large scale CO_2 injection in the Wilmington Graben cannot be safely performed within the relatively shallow middle Pliocene formation.

This conclusion motivated efforts to further characterize the deeper Miocene formation for injection targets. Fortunately the deeper well DOE#2 drilled in 2014 for this project did encounter deeper target sand intervals at depths on the order of 2135 m to 2285 m (7000 ft to 7500 ft). More importantly, the deeper sand intervals were overlain by relatively thick shale intervals (more than 30 m (100ft) thick).

7.3 Conclusions

Several CO_2 injection scenarios have been modeled in two different areas of the Wilmington Graben, only two out of eight scenarios do not leak CO_2 into shallower layers above potential cap rock (Upper Repetto Unconformity) after 30 years of injection at economically reasonable rates. Observing the migration of the plumes of these two injections for an additional 30 years, only two results show full containment of CO_2 below caprock. Thus we see a high risk of leakage and do not recommend shallow intervals for CO_2 injection and storage. To lower risks for loss of containment, injection operations would require: A) a minimum injection depth of 7000 ft; B) minimum offset well spacing of 1 mile; and C) maximum injection rates per well of approximately 250,000 tons per year, or about 1,000,000 tons per year total in four wells. Based on the area reviewed, four wells is a practical limit in order to maintain a minimum 1 mile offset distance to nearby poorly cemented wells.

8 Geomechanical modeling

Geomechanical models were assembled for both the northern and central graben areas. The purpose of these models was to assess stress changes induced by injection operations, fracturing risks, fault activation risks, and surface deformations. Pressure and temperature changes resulting from the Tough2 flow simulation were used as input data for the geomechanics models.

8.1 Estimation of in situ stress

Estimating *in situ* stresses involve the virgin stresses in the earth before any alteration or induced stress caused by any activities related to geomechanics or geotechnical activities related to the oil or mining industry, respectively. *In situ* stress comprises the 3 principal stresses, and in many cases, it's aligned with the vertical and horizontal directions. Also, it can be characterized by its orientation and magnitude. The orientation of the maximum horizontal stress is estimated in many part of the world, and it is compiled and shown in the World Stress Map (WSM; Heidbach et al, 2001), see Figure 100. For the area around southern California, the map suggests that the maximum horizontal stress is oriented N20°E (± 10°). This is consistent and similar to the study performed by Wilde and Stock (1997) which looked at the Los Angeles Basin to determine the maximum stress orientation using breakout data (Figure 101).

Title: Characterization of Pliocene and Miocene Formations in the Wilmington Graben, Offshore Los Angeles, for Large-Scale Geologic Storage of CO_2

PI: Dr. Michael Bruno Final Report

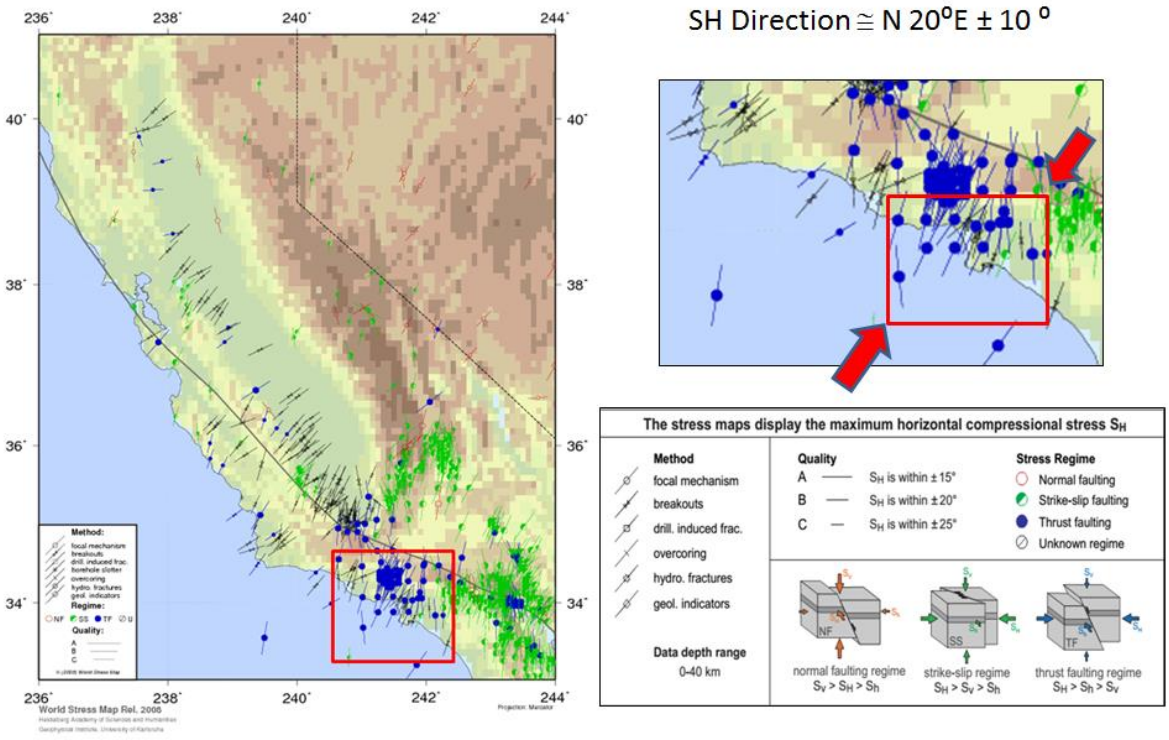

Figure 100: Maximum horizontal stress orientation from World Stress Map
(Heidbach et al., 2001)

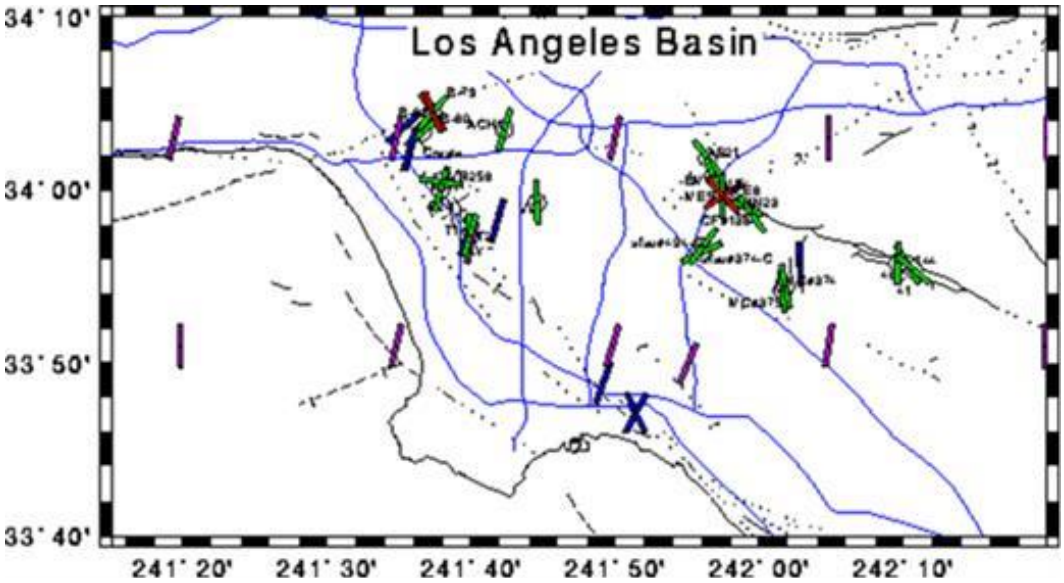

Figure 101: Los Angeles Basin maximum horizontal principal stress orientation
From: Wilde, M. and Stock, J., 1997

To estimate *in situ* stress magnitudes, a geopressure analysis was initially developed to determine pore pressure and fracture pressure based on overburden pressure, which represents the vertical stress.

8.1.1 Geopressure

After well data were reviewed and analyzed, a geopressure model was developed by taking into account the overburden, pore pressure and fracture pressure for the wells. The first step in the analysis process was to determine overburden pressure, which was calculated with density log data. The next step was to estimate pore pressure using an empirical relationship and comparing it with field data. Finally, fracture pressure was calculated also using an empirical relationship.

8.1.2 Overburden (OB)

The overburden for any given depth is the sum of the weight of air from Kelly Bushing (KB) to mean sea level, plus the weight of seawater from mean sea level to mud line, plus the weight of sediments from mud line to the depth of interest. It depends on the formation density, which changes from bottom to top. Generally, it increases progressively from top to bottom but can be affected by any particular material with non-regular density such as salt domes or water

columns. As defined by Holasek (2001), the general equation is described as the integration of density considering water column and sediment:

$$OB = \int_{TVD_{MSL}}^{TVD_{mudline}} \rho_w \cdot g \cdot dTVD + \int_{TVD_{mudline}}^{TVD_{interest}} \rho_{sed} \cdot g \cdot dTVD$$

Where ρ_w and ρ_{sed} are the water density and the sediment bulk density in gr/cc, respectively,

g is the gravity,

TVD_{MSL}, $TVD_{mud\ line}$, $TVD_{interest}$ are the vertical depth at mean sea level, mud line and point of interest in feet.

In this case, we simplified the general equation by neglecting the water column term since the wells are onshore:

$$OB = \int_{TVD_{kb}}^{TVD_{interest}} \rho_{sed} \cdot g \cdot dTVD$$

Another approach was to utilize the density log (RHOB) available for the surface section, run below 457.2 m (1500 ft) depth. But the ommited section impacts the result, resulting in underestimation of the overburden. Thus, a complementary empirical relationship defined by Holasek (2001) was applied to approximate the density on the surface section ($RHOB_{surface}$), assuming an initial density as similar to that defined by Holasek at the mud line:

$$RHOB_{surface} = C1 + \frac{(C2 - C1)}{\exp\left(C3/\left(TVD - Air\ gap - Water\ depth\right)^{0.8 \cdot n}\right)}$$

Where C1 is the density at the mud line (typically 2 gr/cc),
C2 is the density at infinity (typically 2.8 gr/cc),
C3 is the comparison factor (range between 1000 and 6000),
n is the exponential modifier (typically 1).

Figure 102 shows the density using both the density log and the Holasek (2001) empirical relationship at the surface section. Finally, an overburden gradient was estimated for the wells as shown in Figure 103. Note that overburden gradient increases with depth, with a maximun value of 2.12 s.g. (17.7 ppg).

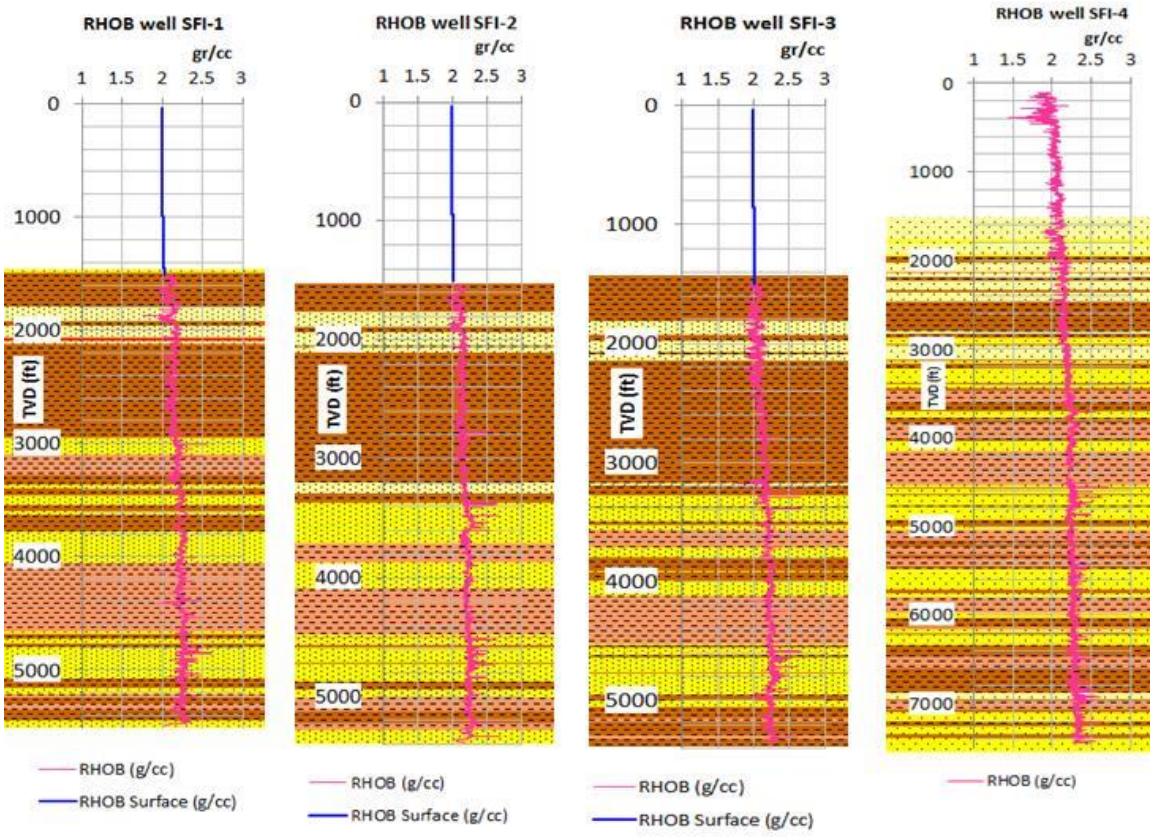

Figure 102: Density log and surface estimation for SFI wells

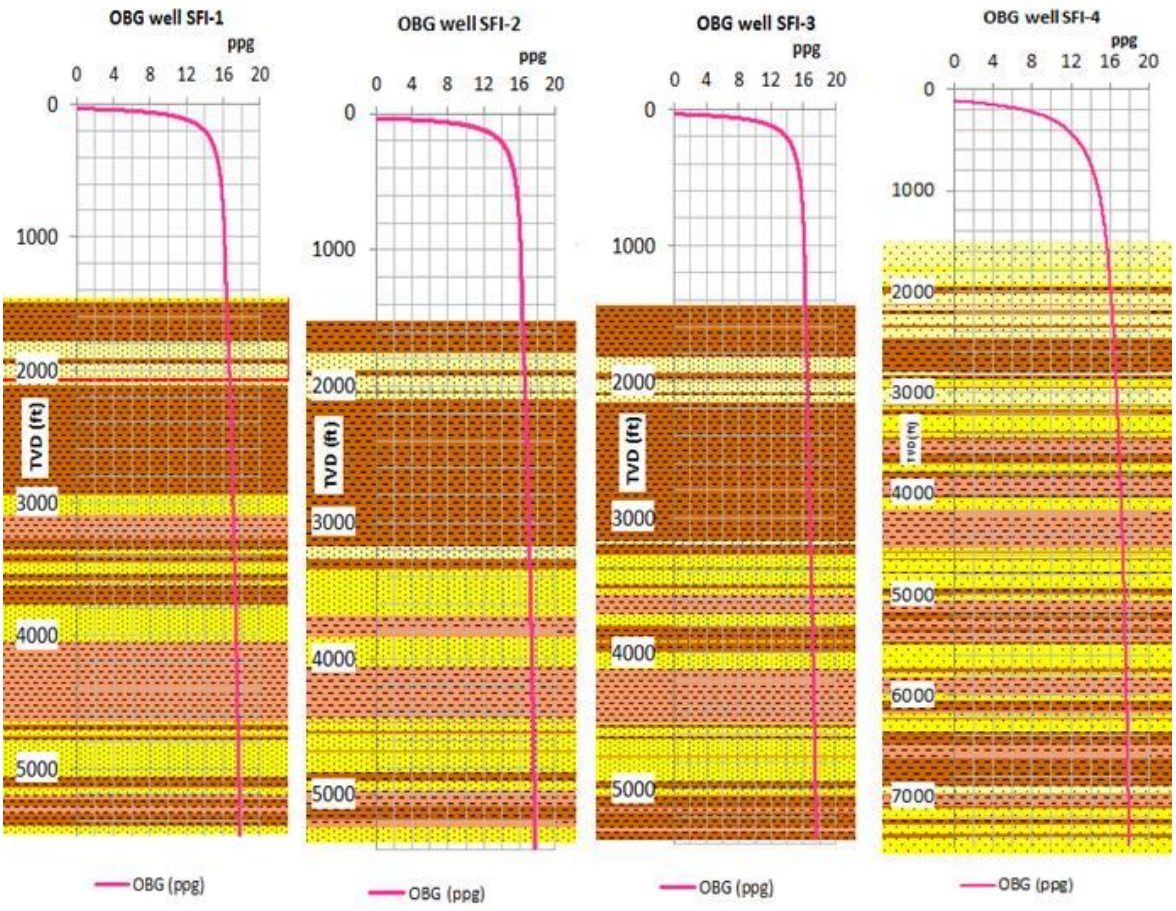

Figure 103: Overburden gradient for SFI wells

8.1.3 Pore pressure

Briefly reviewing the basics, pore pressure can be defined as the pressure exerted by the fluid inside porous rocks. It can be normal, sub-normal or abnormal. It is *normal* when its magnitude is similar to the hydrostatic gradient of a typical water column, about 1.03 s.g (8.33 ppg), *sub-normal (underpressure)* when its magnitude is lower than the normal gradient and *abnormal (overpressure)* when its magnitude is higher than the normal gradient. For our model, an empirical method for pore pressure estimation was applied using the Eaton correlation (Eaton, 1975), based on the compressional interval transit time, normal pore pressure and the overburden pressure. It is one of the most practical methods widely used to estimate pore pressure. The correlation can be defined as:

$$P_P = OB - (OB - P_{PN}) \cdot (\Delta tcn / \Delta tco)^X$$

Where P_{PN} is the normal pore pressure,
Δtcn is the normal compressional interval transit time in us/ft,
Δtco is the observed compressional interval transit time in us/ft,
X is the Eaton's exponent (typically 3).

The Eaton method, as well as other empirical correlations for pore pressure estimation (e.g., Bowers, Equivalent Depth, and so on), can only be applied for shale formations in which compaction changes are expected. Because of this, a discrimination procedure was performed for the shale interval to define the Normal Compaction Trend (NCT) thusly (Figure 104):

1. Define the minimum and maximum GR indicator.
2. Estimate the shale index from GR Log and define the GR cutoff.
3. Transfer the shale point from GR Log to Sonic Log.
4. Define the NCT on shale point.

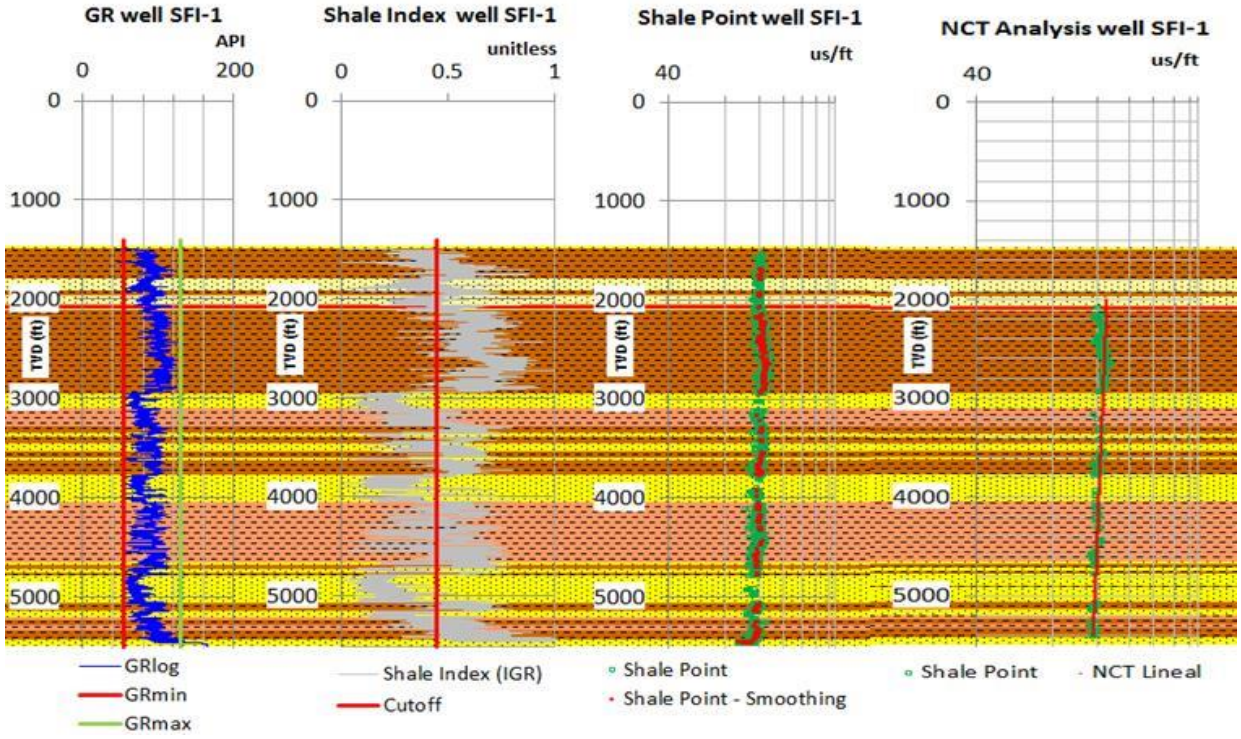

Figure 104: Shale discrimination and Normal Compaction Trend analysis

Once the NCT was defined, we estimated the pore pressure for SFI wells (Figure 105). Two main over-pressured zones with 1.08 s.g (9 ppg) in Repetto shale were identified, ranging from 762 m to 914.4 m (2500 ft to 3000 ft) and 1219.2 m to 1371.6 m (4000 ft to 4500 ft). For the sandstone/shale interbed, an interruption on the normal compaction process lead to these two zones. No risk of influx and migration were expected through these formations because of the low permeability of the shale. However, borehole collapse can be a critical issue for drilling operations, but can be mitigated with wellbore stability analysis and an optimized mud window, as mentioned in *Geologic model development* above. For calibration purposes, a formation pressure point measured from a step rate test at 1584.96 m (5200 ft) was chosen to calibrate the pore pressure curve as shown in Figure 105 below.

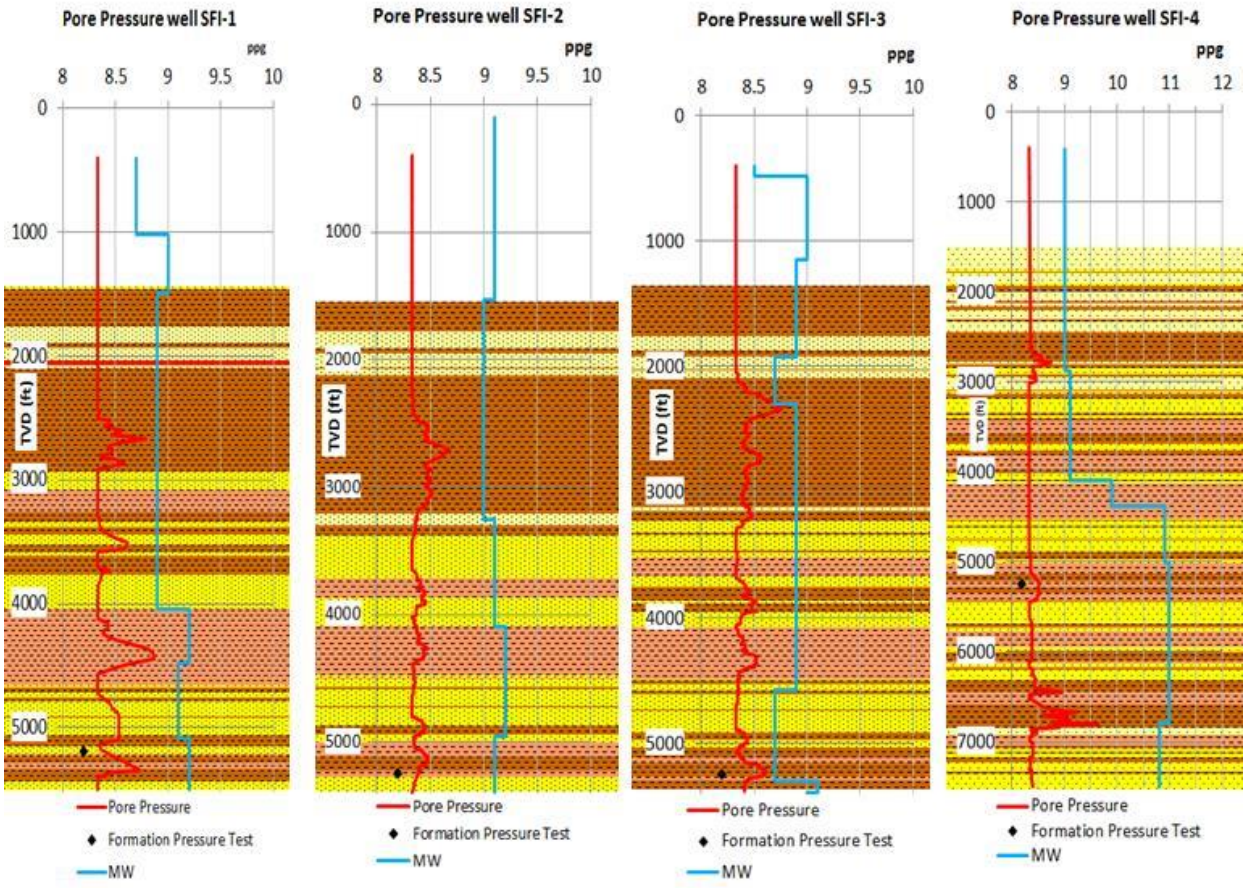

Figure 105: Pore pressure for SFI wells

8.1.4 Fracture pressure

The fracture pressure was estimated by the Matthews and Kelly method (1967). The correlation can be expressed as:

$$F_P = P_P + (OB - P_P) * k$$

Where k is the matrix stress coefficient.

This coefficient was calibrated to 0.66 using a step rate test conducted on SFI-1 well (Figure 106) at the injection depth 1600.2 m (5250 ft), with an equivalent fracture pressure of 270.61 bar (3925 psi). In addition, based on the last step rate test performed in August 2014, the current fracture opening pressure of 274.41 bar (≅3980 psi) was consistent with the fracture pressure identified at the beginning of the project in September 2008 (Figure 107). Figure 108 presents the fracture pressure for SFI wells. In general, note that there is a trend for fracture pressure to increase with depth, with some changes on the over-pressured zones in Repetto shale. This was expected because of the fact that not only was it affected by overburden, but also changes in pore pressure. Finally, the Geopressure for SFI wells is shown in Figure 109 and Figure 110.

Title: Characterization of Pliocene and Miocene Formations in the Wilmington Graben, Offshore Los Angeles, for Large-Scale Geologic Storage of CO_2

PI: Dr. Michael Bruno Final Report

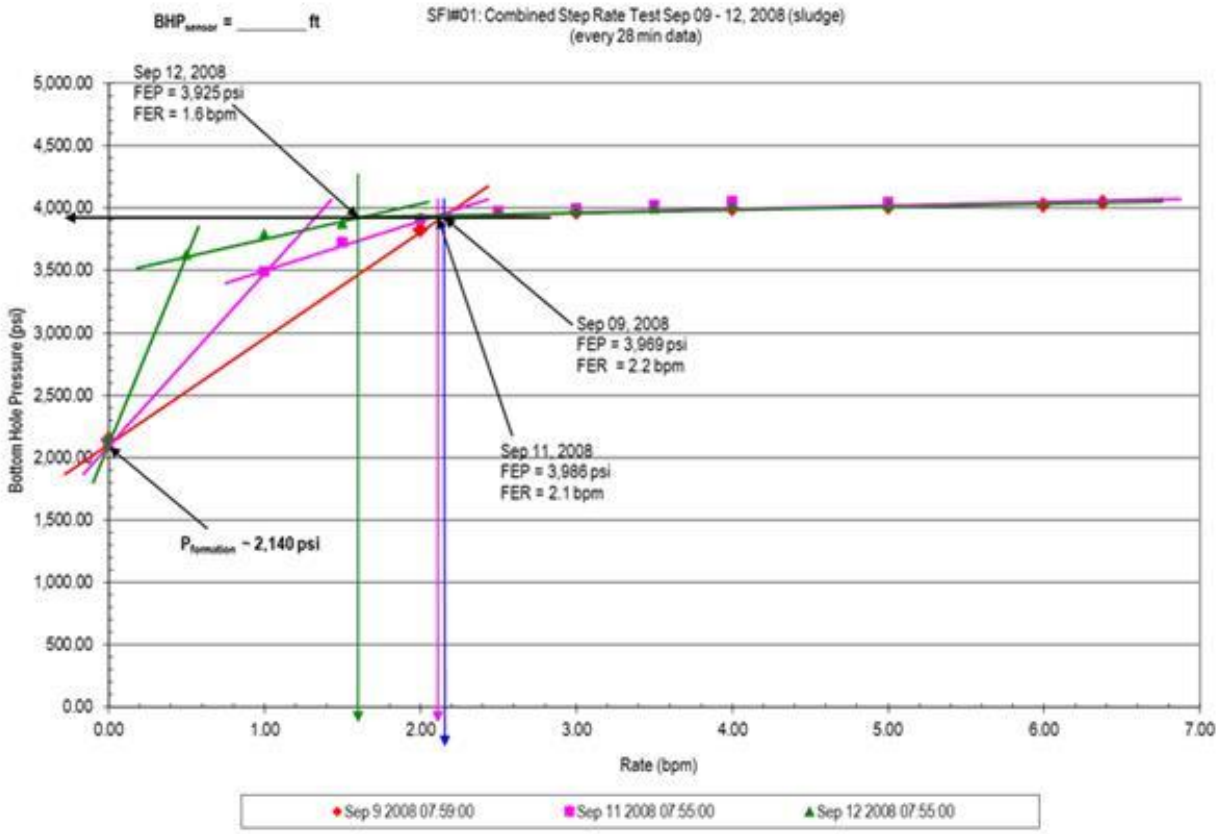

Figure 106: Step rate test for well SFI-1 performed in 2008

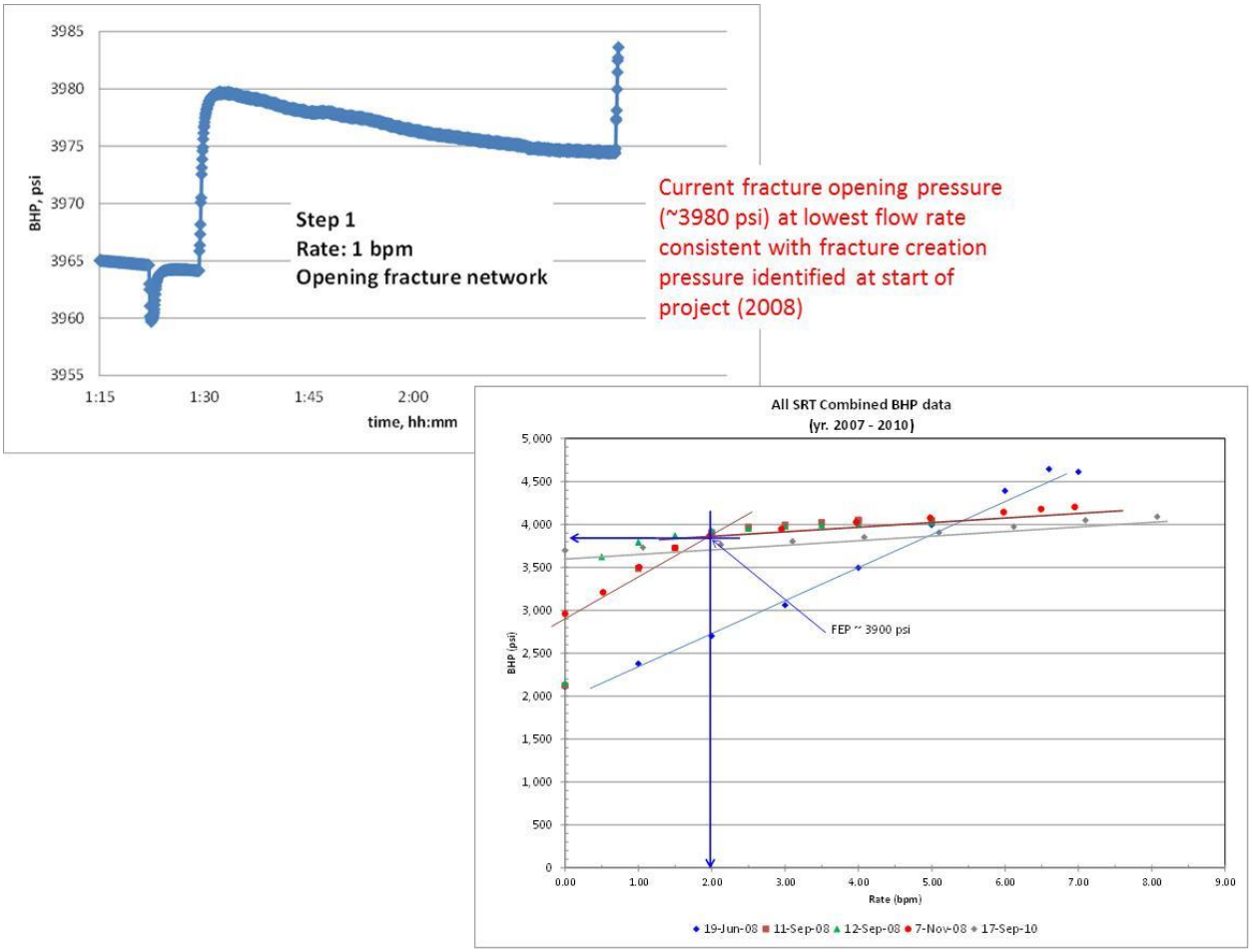

Figure 107: Step rate test for well SFI-1

Title: Characterization of Pliocene and Miocene Formations in the Wilmington Graben, Offshore Los Angeles, for Large-Scale Geologic Storage of CO_2

PI: Dr. Michael Bruno Final Report

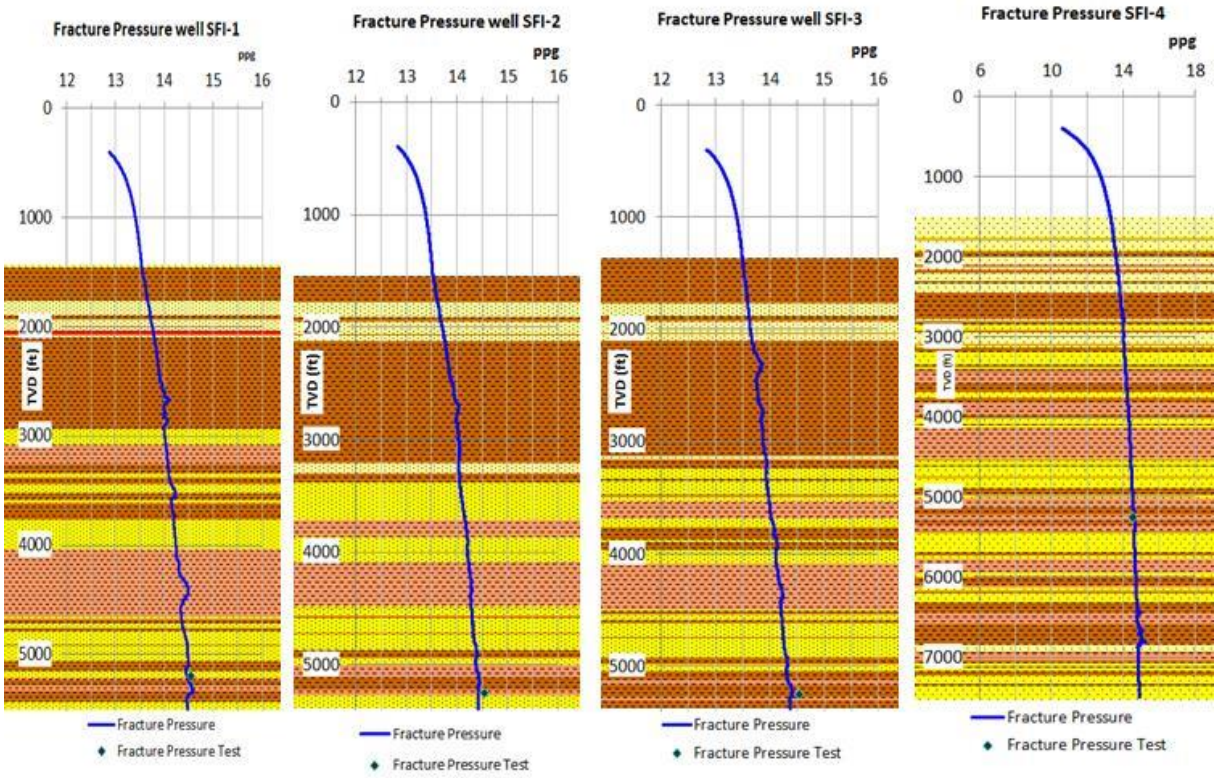

Figure 108: Fracture pressure for SFI wells

Title: Characterization of Pliocene and Miocene Formations in the Wilmington Graben, Offshore Los Angeles, for Large-Scale Geologic Storage of CO_2

PI: Dr. Michael Bruno Final Report

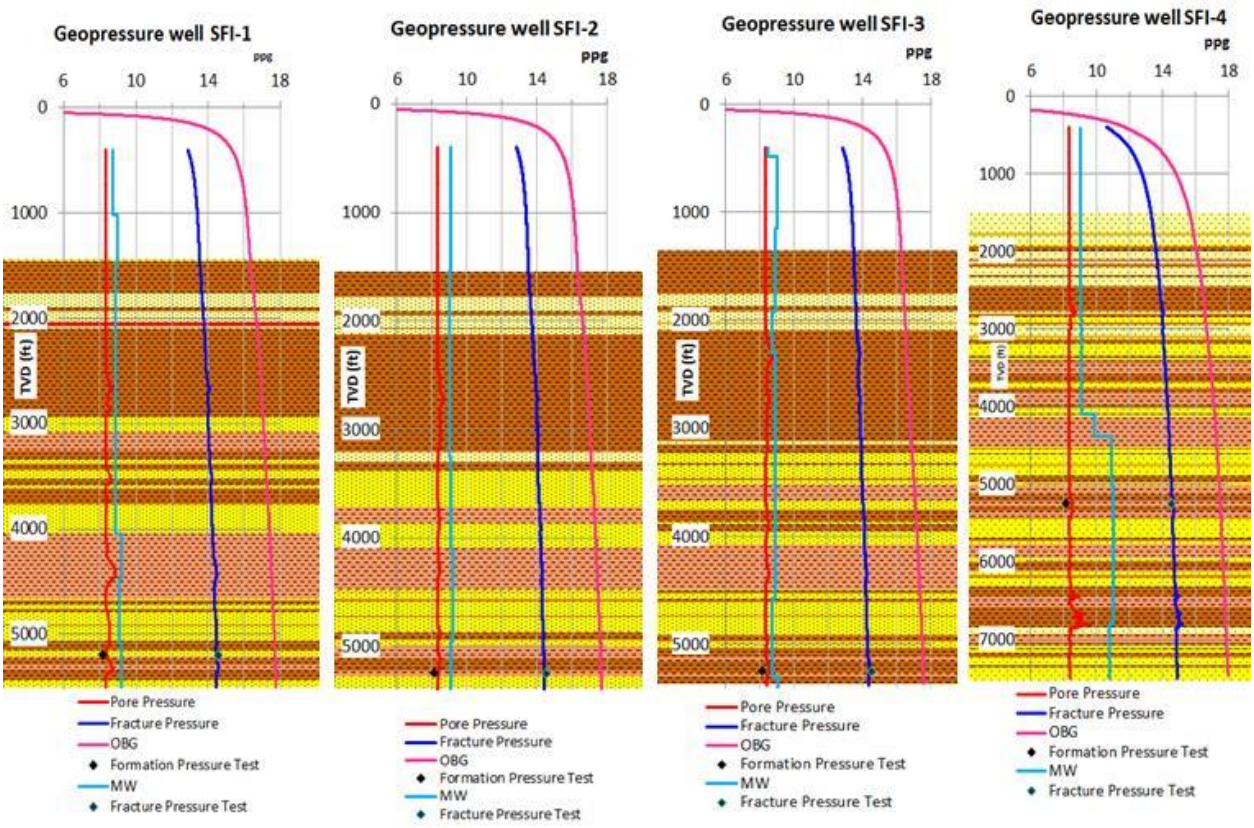

Figure 109: Geopressure for SFI wells in ppg

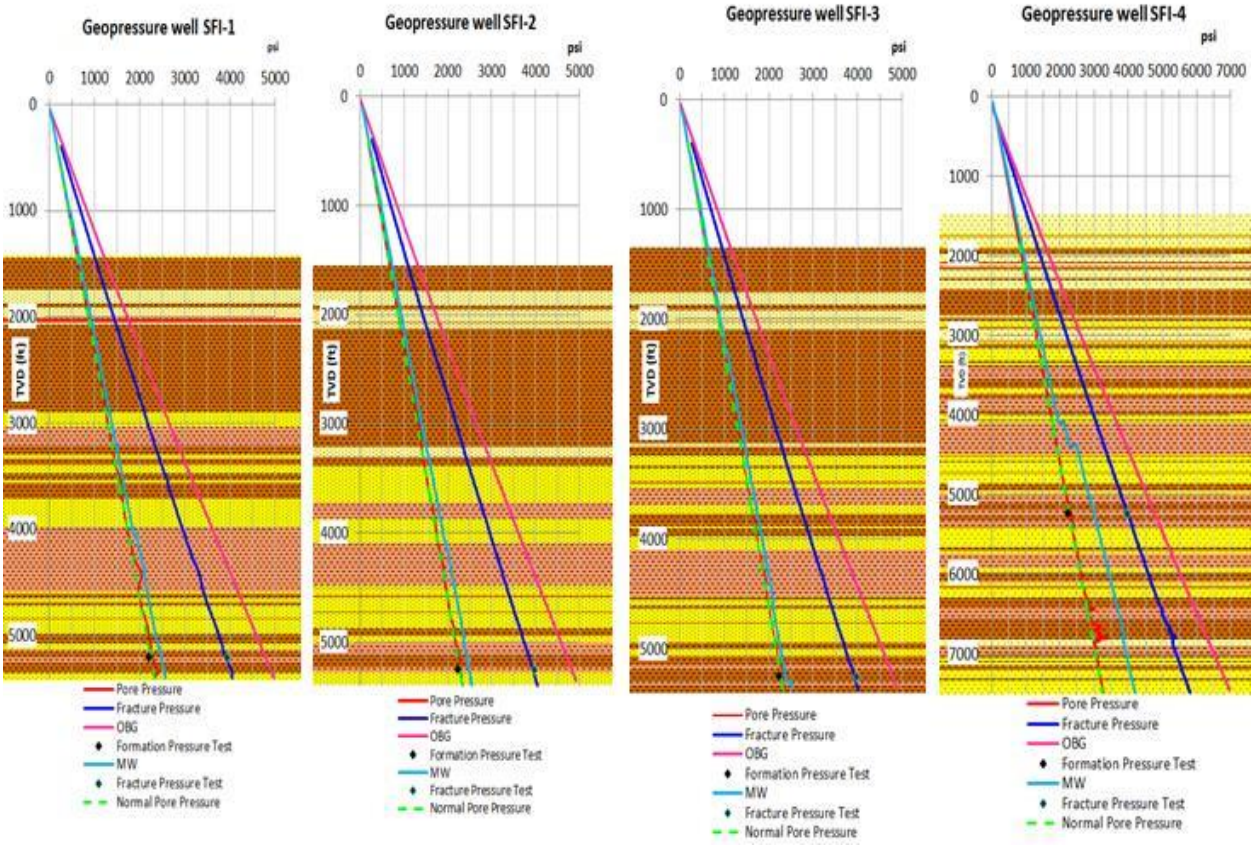

Figure 110: Geopressure for SFI wells in psi

8.1.5 Minimum and maximum horizontal stresses

The minimum and maximum horizontal stresses were estimated from the industry-standard method defined by Anderson (1951) and by considering the tectonic stain effect as detailed by Blanton & Olson (1999):

$$Sh = \alpha \cdot Pp + \frac{\upsilon}{1-\upsilon}(Sv - \alpha \cdot Pp) + \frac{E}{1-\upsilon^2}\varepsilon_h + \frac{\upsilon \cdot E}{1-\upsilon^2}\varepsilon_H$$

$$SH = \alpha \cdot Pp + \frac{\upsilon}{1-\upsilon}(Sv - \alpha \cdot Pp) + \frac{E}{1-\upsilon^2}\varepsilon_H + \frac{\upsilon \cdot E}{1-\upsilon^2}\varepsilon_h$$

Where α is the Biot coefficient,
υ is the Poisson's ratio,
ε_h is the tectonic strain coefficient in the minimum horizontal stress orientation,
ε_H is the tectonic strain coefficient in the maximum horizontal stress orientation.

These equations were solved to estimate the tectonic strain coefficients by applying an iterative process. Thus, maximum horizontal stress was defined as 1.15 times the minimum horizontal stress and calibrated by the step rate test. Figure 111 presents the *in situ* stress profiles for SFI wells. As can be seen, the results reveal a normal stress regime (SV>SH>Sh) with a trend toward a strike-slip regime (SH>SV>Sh) in the Puente formation below 2133.6 m (7000 ft) for well SFI-4 (Miocene epoch).

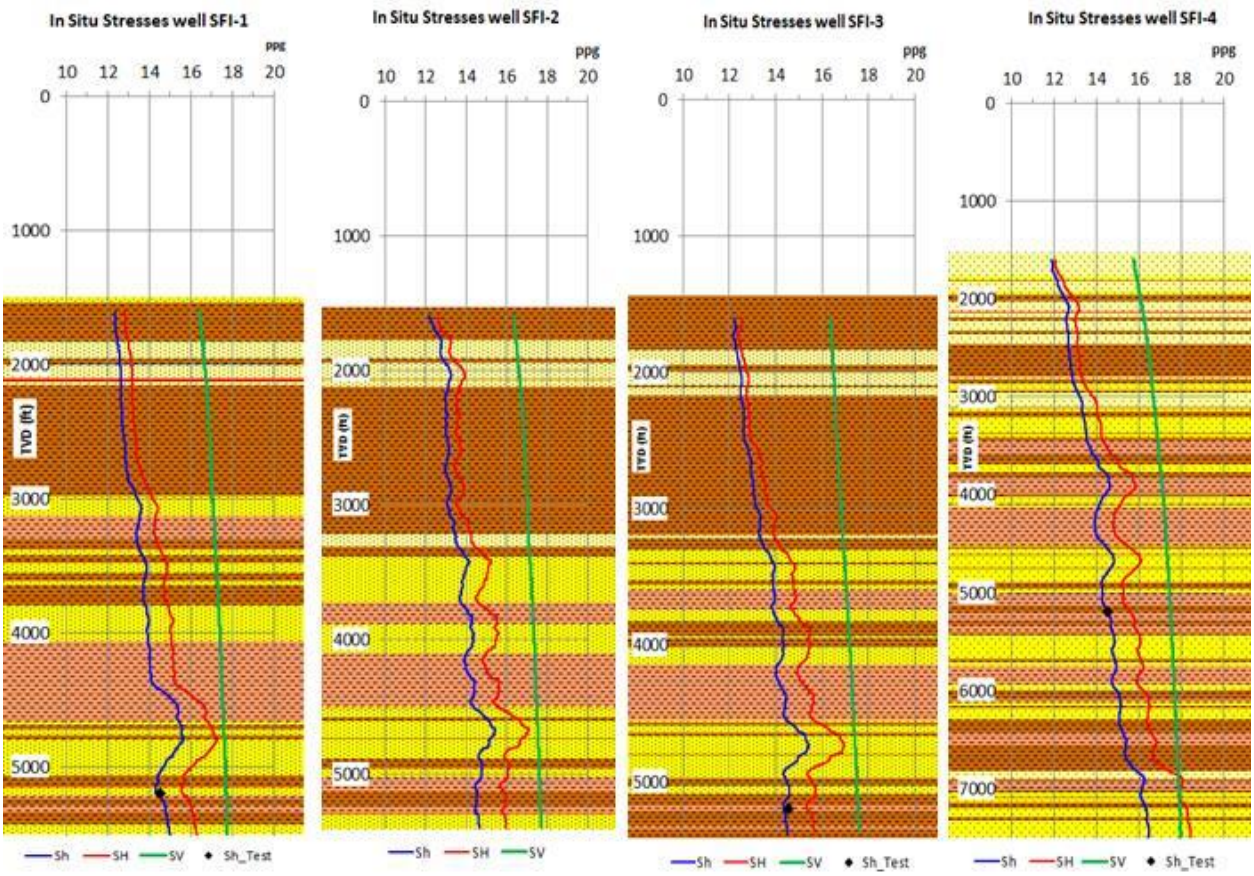

Figure 111: In *situ stress* profiles for SFI wells

8.2 Estimation of mechanical stiffness and strength properties

Rock mechanical properties were estimated using empirical relationships and were calibrated with lab test measurements. Lab tests were limited to well SFI-2 and only focused on elastic properties such as Young's modulus and Poisson's ratio. Furthermore, these tests were only conducted in a sandstone formation, excluding the shale formation. Lab tests with shale are more complex than sandstone because of its petrophysics and anisotropy conditions (low permeability and laminar structure). Table 23 summarizes a triaxial compression test performed by TerraTek.

Table 23: Triaxial compression test from well SFI-2

Sample ID	Depth (ft)	Orientation	Bulk Density (g/cm^3)	Confining Pressure (psi)	Pore Pressure (psi)	Volumetric Yield Compressive Strength (psi)	Residual Effective Compressive Strength (psi)	Quasi-Static Young's Modulus (psi)	Quasi-Static Poisson's Ratio
TL-1	5002.15	Vertical	2.206	4000	2500	4625	NA	446,000	0.11
TL-5	5002.40		2.211			4590		412,100	0.15
TL-3	5002.80		2.220			4795		423,000	0.22
TL-7	5005.95		2.129			4820		351,000	0.14
TL-9	5008.95		2.193			4710		399,000	0.13
TL-11	5010.95		2.177			4260		312,000	0.10

For overburden and other formations, empirical relationships were applied to estimate rock mechanical properties based on the compressional and shear waves recorded on sonic logs, commonly known as dynamic properties. These are described as follows (Chang, 2004):

8.2.1 Unconfined compression strength (UCS)

For sandstone formations, McNally (1987) the empirical correlation applied was:

$$UCS = 1200 \cdot \exp(-0.036 \cdot \Delta tc) \cdot 145.04$$

For shale formations, we applied Horsrud's (2001) and Lal's (1999) empirical relationships. These are, respectively, expressed as:

$$UCS = 0.77 \cdot (304.8/\Delta tc)^{2.93} \cdot 145.04$$

$$UCS = 10 \cdot (304.8/\Delta tc - 1) \cdot 145.04$$

8.2.2 Friction angle (FA)

The friction angle was also estimated by using Horsrud's (2001) and Lal's (1999) empirical correlations. These are, respectively, expressed as:

$$FA = 11 \cdot (304.8/\Delta tc - 10.2)$$

$$FA = ASIN \cdot (((304.8/\Delta tc) - 1)/(304.8/\Delta tc + 1)) \cdot 57.29582$$

8.2.3 Cohesion (CS)

For the cohesion estimation we also applied Horsrud's (2001) and Lal's (1999) relationships. These are shown as, respectively:

$$CS = UCS \cdot ((1 - SIN(FA \cdot 0.01745))/(2 \cdot COS(FA \cdot 0.01745)))$$

$$CS = 5 \cdot ((304.8/\Delta tc - 1)/\sqrt{304.8/\Delta tc}) \cdot 145.04$$

8.2.4 Young's modulus (E)

This property was defined using both waves (compressional and shear) recorded on sonic logs. The empirical relationship can be approximated by:

$$E = (RHOB/\Delta ts^2) \cdot ((3 \cdot \Delta ts^2 - 4 \cdot \Delta tc^2)/(\Delta ts^2 - \Delta tc^2)) \cdot 13400$$

8.2.5 Poisson's ratio (v)

Poisson's ratio (v) was also estimated by applying the compressional and shear waves from sonic logs. The empirical relationship is described by:

$$Poisson = (1/2 \cdot (\Delta ts/\Delta tc)^2 - 1)/((\Delta ts/\Delta tc)^2 - 1)$$

Where:

Δtc, Δtc are the compressional and shear interval transit time, respectively, in us/ft, and

RHOB is the formation density in gr/cc.

8.2.6 Estimations

Figure 112 through Figure 115 show these rock mechanical properties. Overall from the plots, a general trend for mechanical properties can be gleaned: the mechanical properties increase with increasing depth due to higher rock compaction from overburden. Nevertheless, shale formations present lower unconfined compression strength between 103.42 bar and 172.36 bar (1500 psi and 2500 psi) and experiences higher deformation when subjected to loading (a Poisson's ratio higher than 0.2), which is typical for these plastic formations of weak rock. Conversely, sandstone formations exhibit higher unconfined compression strength (>172.36 bar (2500 psi)) and lower deformation (Poisson's ratio (ν) lower than 0.2). For calibration purposes, a relationship between static and dynamic properties was defined based on the lab test measurements. Thus, the static Young's modulus was defined as 3.42 times the dynamic value and the static Poisson's ratio was defined as 1.54 times the dynamic value.

Title: Characterization of Pliocene and Miocene Formations in the Wilmington Graben, Offshore Los Angeles, for Large-Scale Geologic Storage of CO_2

PI: Dr. Michael Bruno Final Report

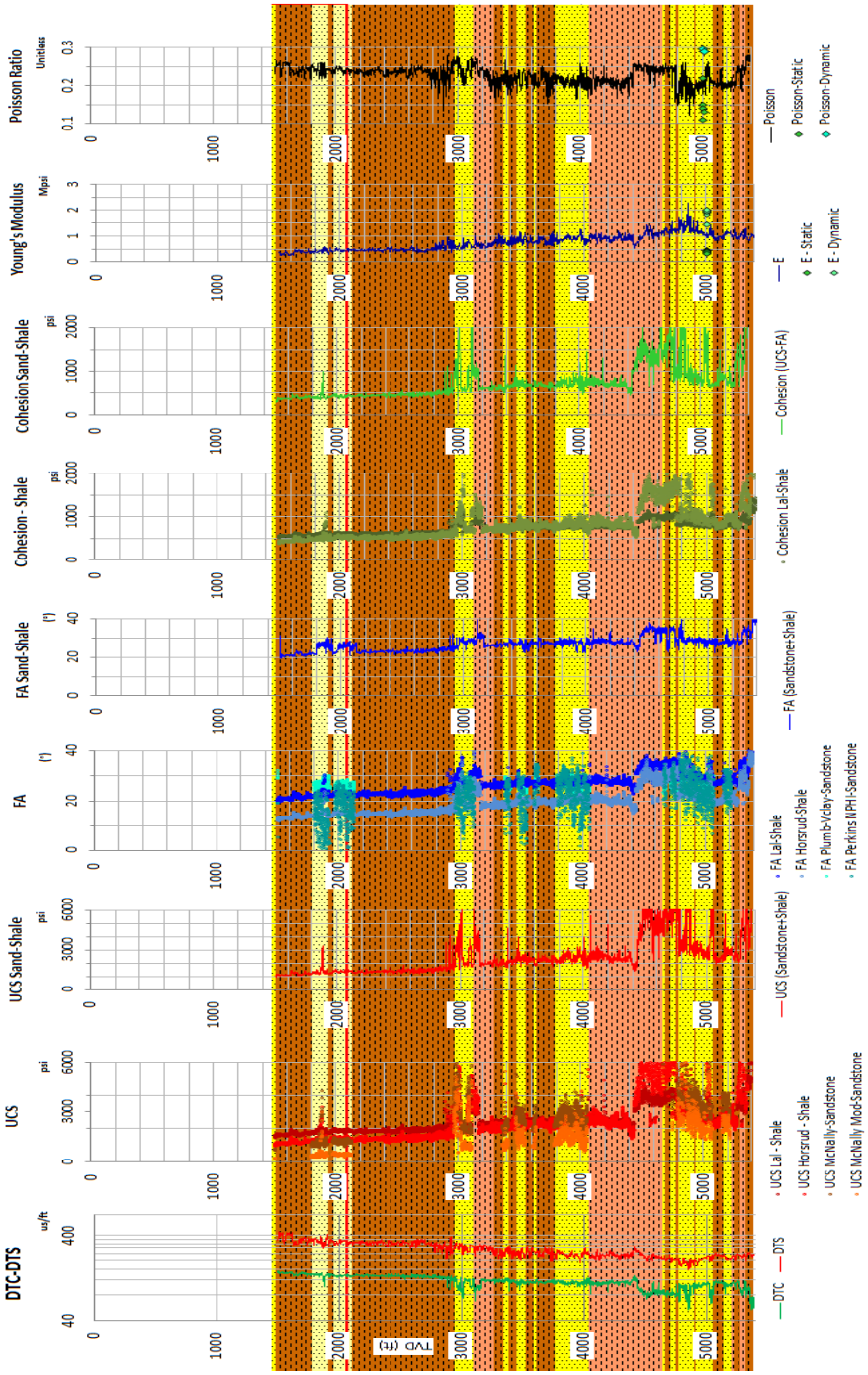

Figure 112: Rock mechanics properties for well SFI-1

Title: Characterization of Pliocene and Miocene Formations in the Wilmington Graben, Offshore Los Angeles, for Large-Scale Geologic Storage of CO_2

PI: Dr. Michael Bruno Final Report

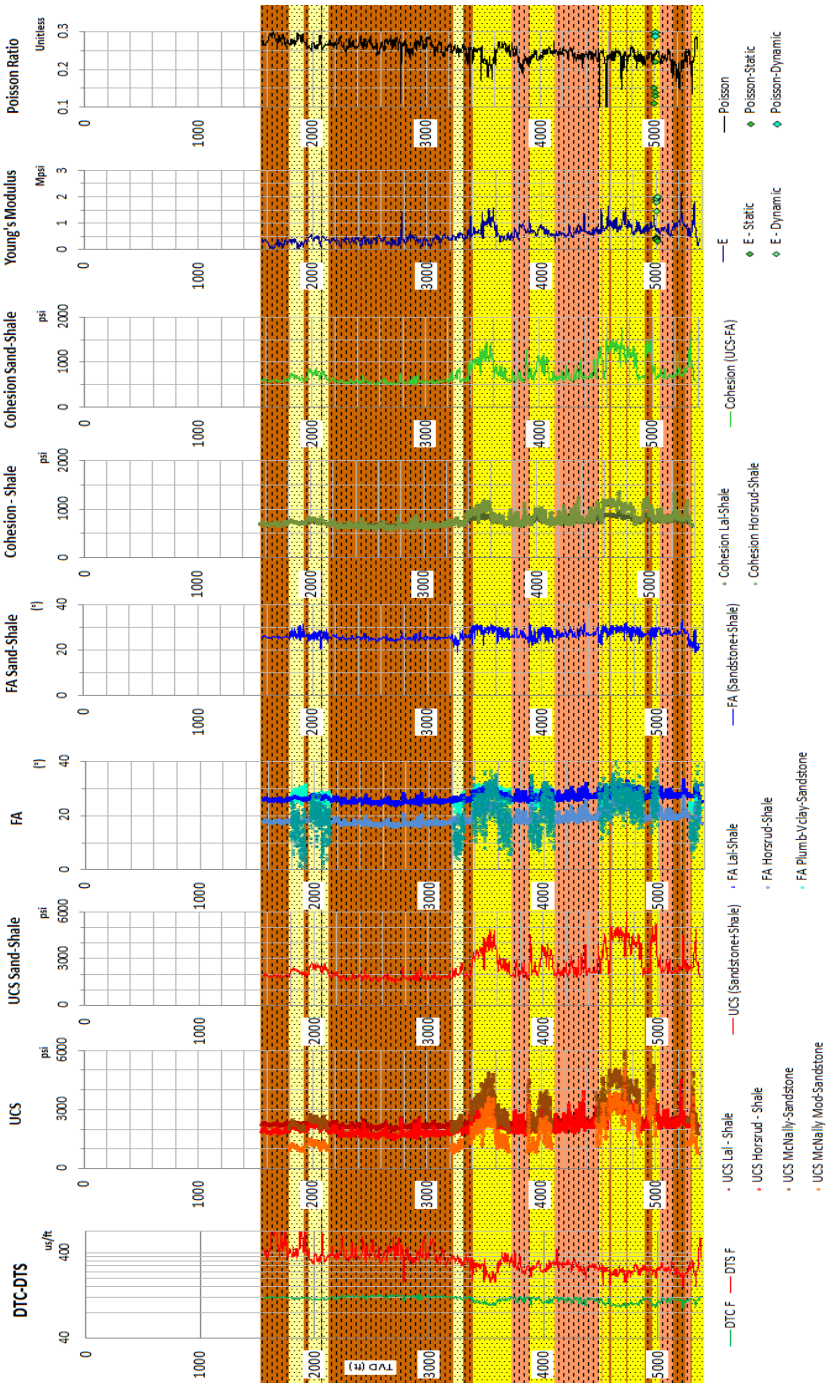

Figure 113: Rock mechanics properties for well SFI-2

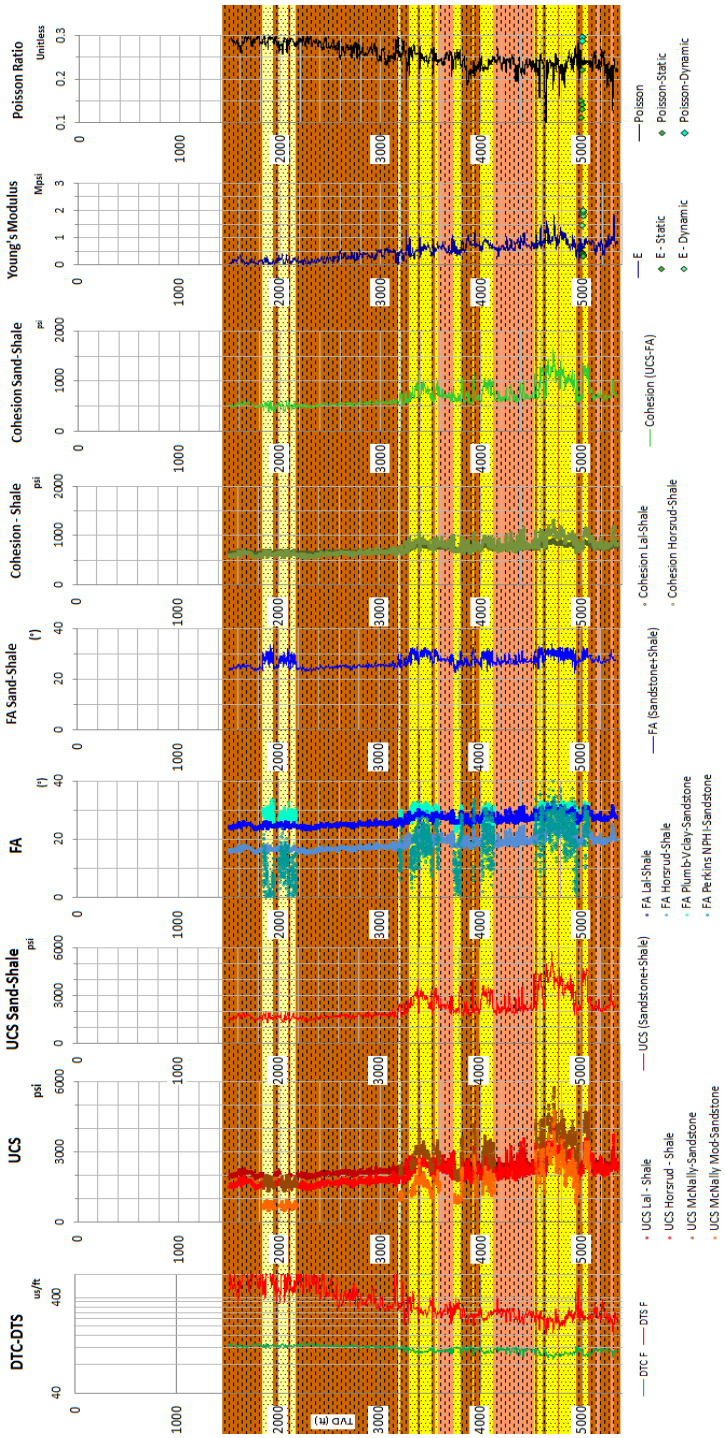

Figure 114: Rock mechanics properties for well SFI-3

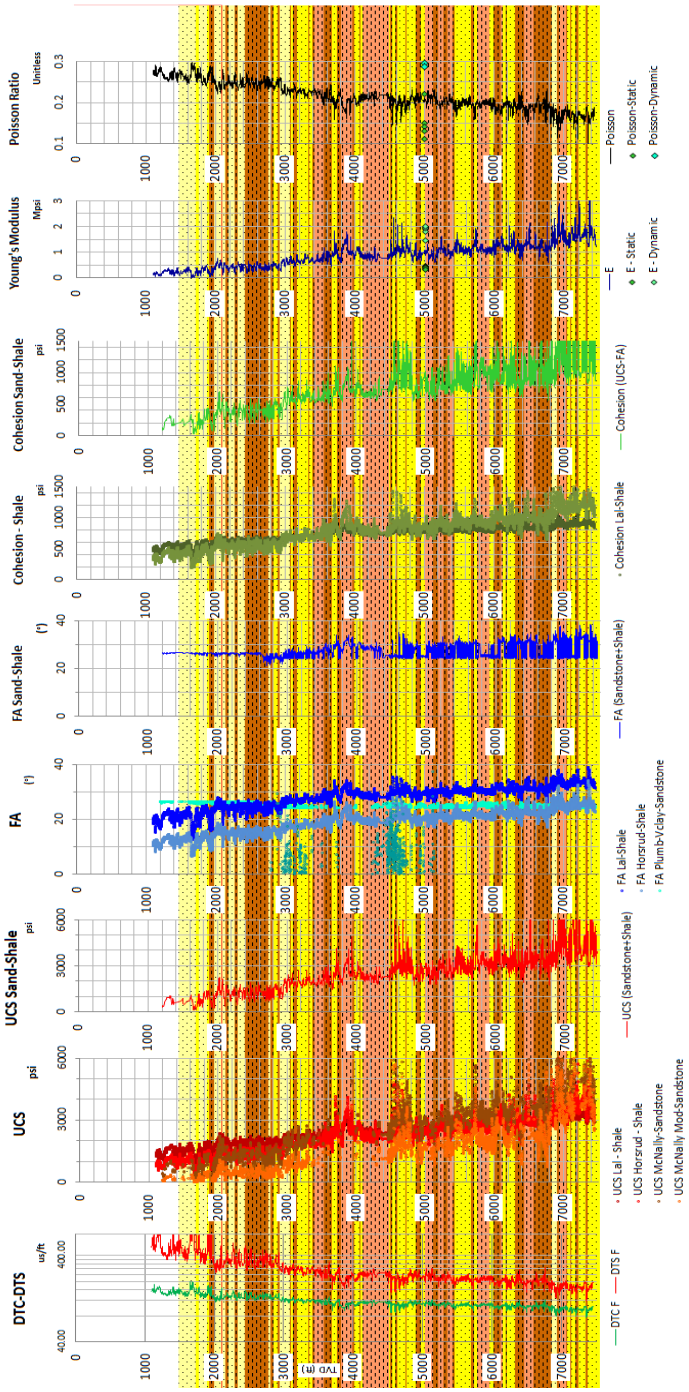

Figure 115: Rock mechanics properties for well SFI-4

Based on the 1D rock mechanics model previously discussed, static Young's modulus was defined as 3.42 times the dynamic value and the static Poisson's ratio was defined as 1.54 times the dynamic value. For 3D model, an average was defined for each formation.

Table 24 summarizes the elastic properties for young's modulus, Poisson's ratio, bulk modulus and shear modulus respectively.

Table 24: **Rock mechanics estimation for 3D geomechanics model on Northern Graben area**

Formation	E-psi	Poisson ratio (ν)	K psi	G psi
San Pedro	1.92E+05	0.28	1.46E+05	7.49E+04
Pico	2.26E+05	0.27	1.64E+05	8.92E+04
Repetto	3.96E+05	0.23	2.49E+05	1.60E+05
Repetto1	3.05E+05	0.25	2.04E+05	1.22E+05
Repetto2	4.86E+05	0.22	2.90E+05	1.99E+05
Repetto3	5.02E+05	0.22	2.99E+05	2.06E+05
Puente	7.32E+05	0.19	3.93E+05	3.07E+05
Schist	6.50E+05	0.20	3.61E+05	2.71E+05

8.3 Geomechanical models

8.3.1 Material parameters

The main mechanical parameters for geomechanical models are the average bulk (K) and shear moduli (G) and the average uniaxial compressibility (Cm) for each stratigraphic unit. We have used an elastic material model for all formations.

8.3.1.1 Bulk Modulus:

For the bulk modulus input, initially Young's modulus (E) was determined for various lithologic ranges from the DOE#1 well (pre-existing Shell OCS P-293-1 for cross section B-B') sonic logs, a mile to the northwest, and then correlated with Chevron SP LA 2 and SP LA 2 R1 well logs to the southwest. We have assumed a Poisson's ratio (ν) of 0.2 for sand, 0.25 for sand/shale interbeds, and 0.3 for shale. Employing these two properties, the bulk modulus (K) can be calculated from the following equation:

$$K = \frac{E}{3(1-2v)}$$

Equation 1: Bulk Modulus from Young's Modulus and Poisson's Ratio

8.3.1.2 Shear Modulus:

For the shear modulus, the same two quantities are needed: Young's modulus (E) and the Poisson's ratios (v). Employing these two properties again, the shear modulus (G) can be calculated from the following equation:

$$G = \frac{E}{2(1+v)}$$

Equation 2: Sheer Modulus from Young's Modulus and Poisson's Ratio

8.3.1.3 Uniaxial Compressibility:

Bulk compressibility (Cbc) is simply the inverse of the bulk modulus (1/K). Given this relationship and Poisson's ratio (v) above, uniaxial compressibility can be calculated with the following equation:

$$C_m = \frac{(1+v)}{3(1-v)} C_{bc}$$

Equation 3: Uniaxial Compressibility from Bulk Compressibility and Poisson's Ratio

The values for uniaxial compressibility, arrived at for relatively small, homogeneous lithologic ranges, are then averaged over the five stratigraphic units' ranges, and assigned to those units in our geomechanical model. For the geomechanical cross section A-A' these quantities are in Table 25 (see Table 26 for cross section B-B').

Table 25: Material Parameters for Geomechanical Cross Section AA'

Stratigraphy: // Material Properties:	Bulk Modulus (K) (psi)	Sheer Modulus (G) (psi)	Uniaxial Compressibility (C_m) (1/psi)
San Pedro	6.23E+04	5.27E+04	7.55E-06
Pico	7.56E+04	6.47E+04	6.21E-06
Repetto	1.24E+05	1.12E+05	3.97E-06
Puente	1.75E+06	8.07E+05	3.54E-07
Schist	2.13E+05	1.73E+05	2.26E-06

Table 26: Material Parameters for Geomechanical Cross Section BB'

Stratigraphy: // Material Properties:	Bulk Modulus (K) (psi)	Sheer Modulus (G) (psi)	Uniaxial Compression (C_m) (1/psi)
San Pedro	6.24E+04	5.27E+04	8.01E-06
Pico	3.86E+05	2.29E+05	1.61E-06
Repetto	1.06E+06	6.34E+05	5.58E-07
Puente	1.75E+06	8.07E+05	3.54E-07
Schist	1.28E+06	1.03E+06	3.76E-07

8.3.2 2D geomechanics model

From the second quarter of 2011 to the third quarter of 2012, we developed a geomechanical cross section through the northwest of the basin, A-A', and through the center of the basin, B-B' (Figure 116) for preliminary geomechanical model analyses.

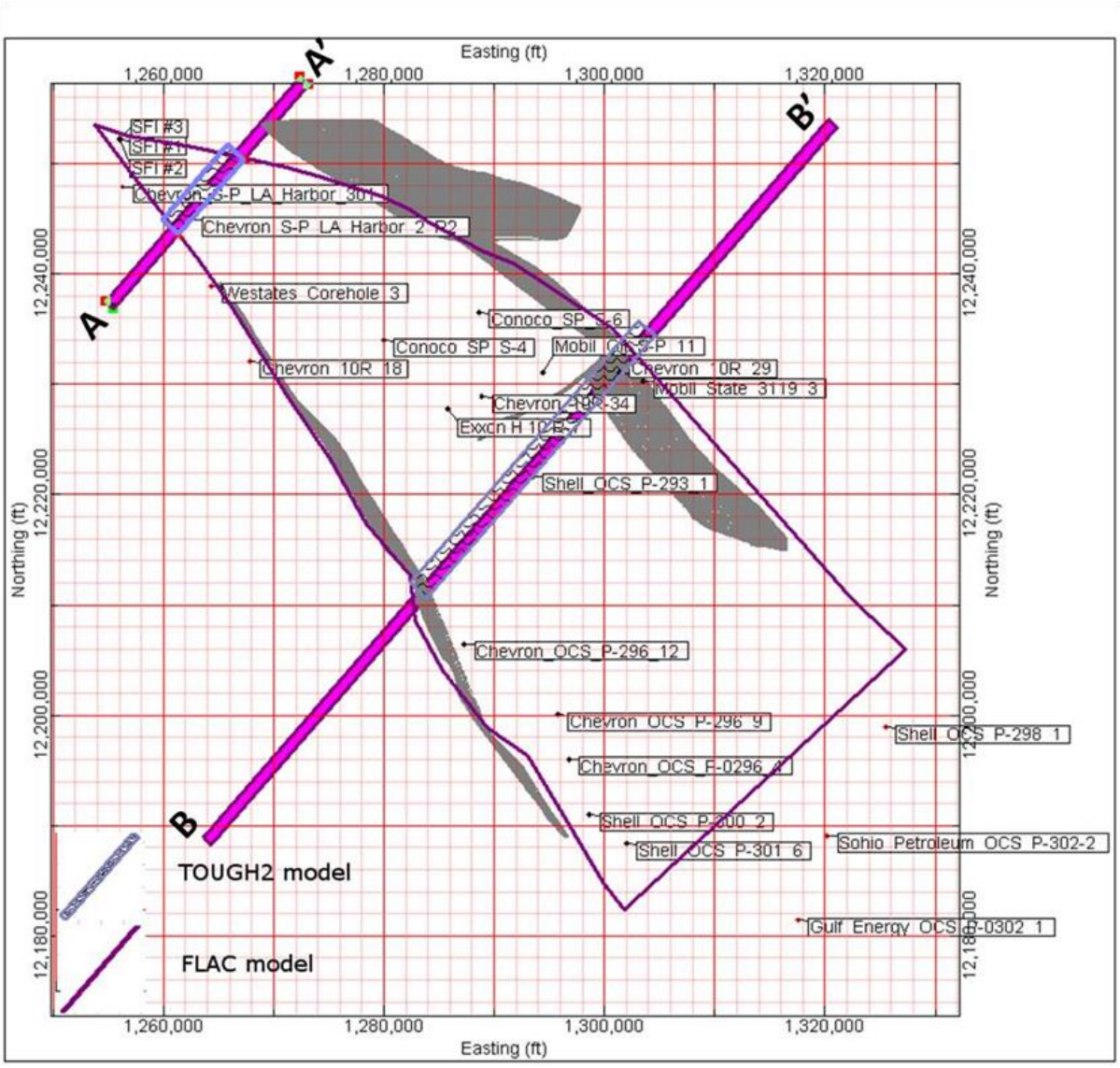

Figure 116: Location of Tough2 – CO_2 gas migration model and geomechanical FLAC mode

The A-A' geomechanical model has been developed to be consistent with and based on the defined stratigraphic horizons of the area. The lithology and proposed injection zone are based on the Chevron SP LA 2 and SP LA 2 R1 (Shell OCS P-293-1 for B-B') well logs. These wells indicate several hundred feet of clean sand packages near the top of the Puente Formation in stratigraphic cross section A-A' (Figure 117), 2133 to 2438 m (7000 to 8000 ft), and for stratigraphic cross section B-B' (Figure 118) at 304 to 457 m (1000 to1500 ft) above basement,

which placing this attractive injection zone in the middle of the Repetto Formation. The modeled injection coincides with the axes of the graben syncline, as extrapolated from the Chevron SP LA 2 and SP LA 2 R1 wellbores (Shell OCS P-293-1 wellbore for B-B'), where we have well logs establishing this section as an important control point for our entire model.

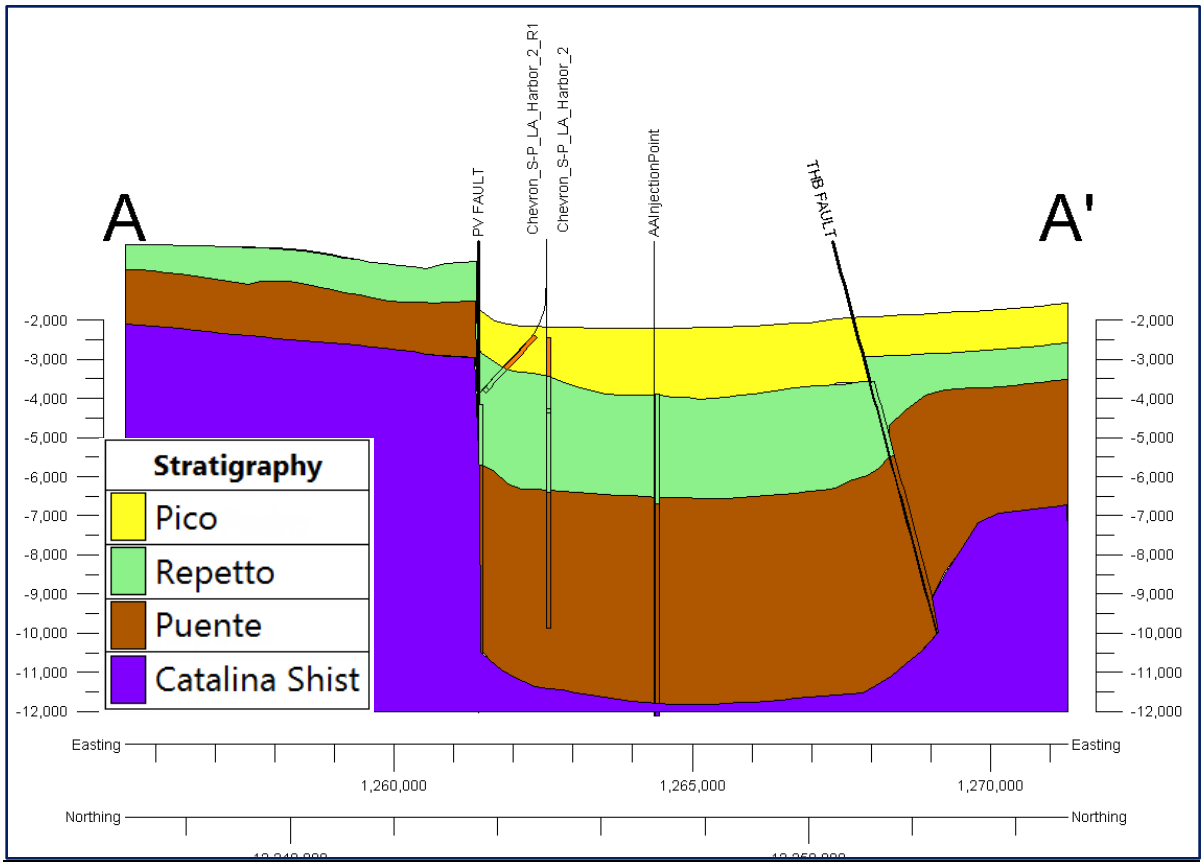

Figure 117: Cross section A-A' based on geologic interpretation

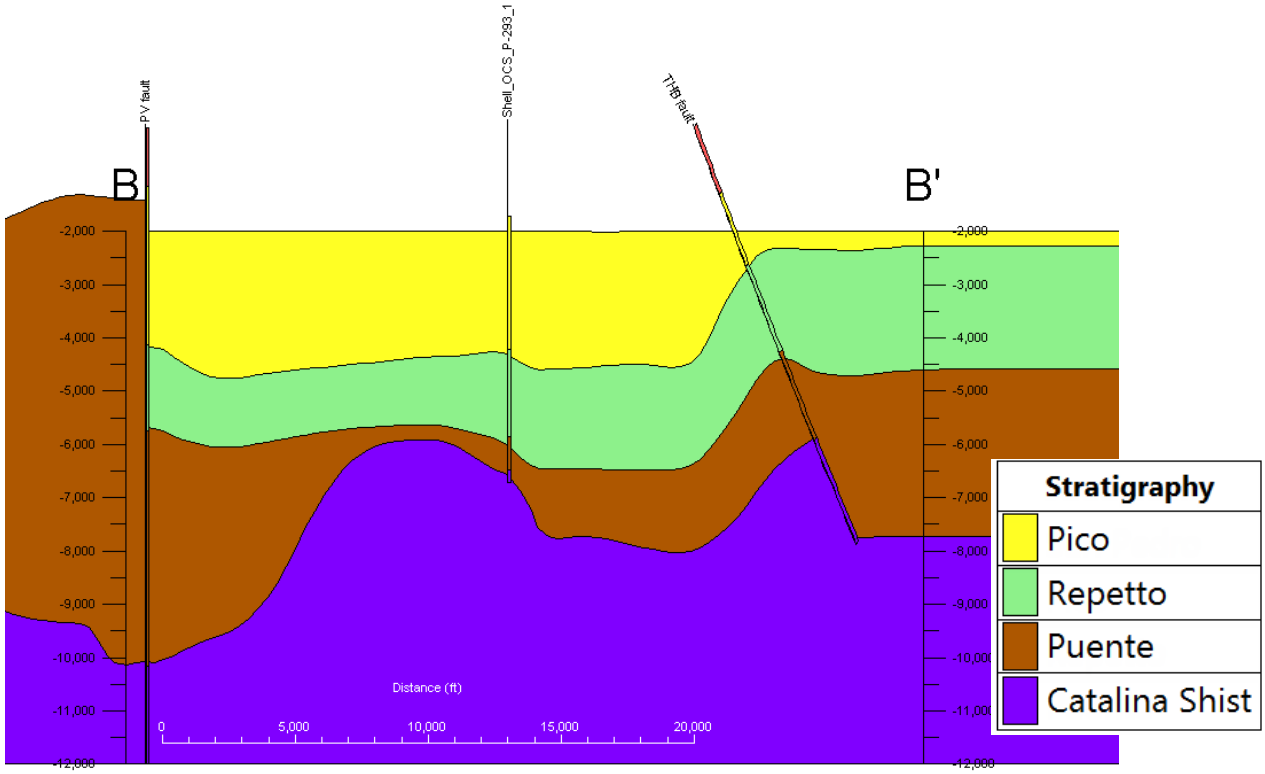

Figure 118: Stratigraphic Rockworks model of section B-B' (2XVE)

The dimensions for the A-A' geomechanical model (Figure 119) are: about 8230 m (27,000 ft) wide (x), 30 m (100 ft) thick (y) and 3660 m(12,000 ft) vertically (z). There are about 16,200 elements. The Palos Verdes and THUMS Huntington Beach faults are defined as impermeable boundaries.

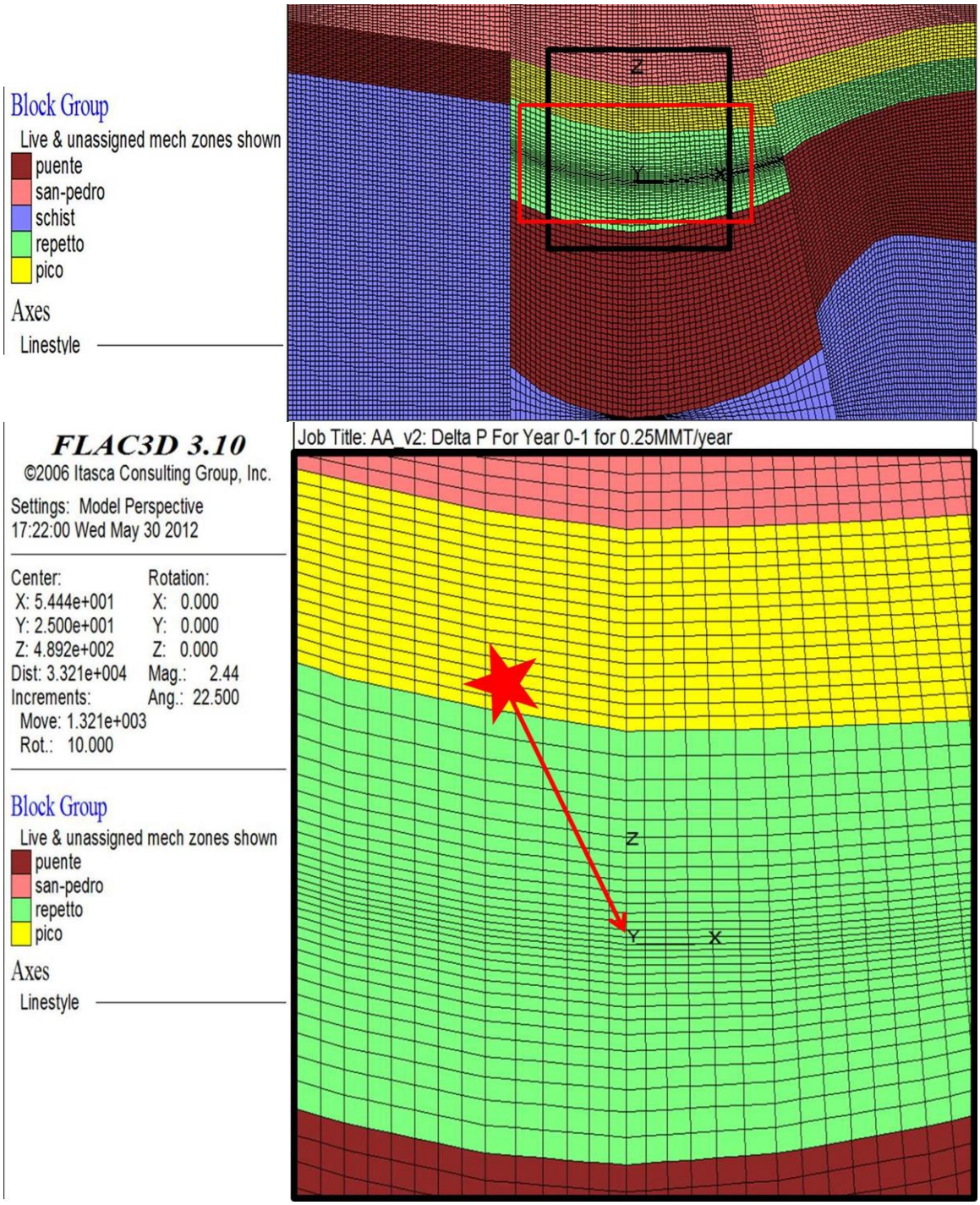

Figure 119: AA' cross section detail, geomechanically modeled with FLAC3D software (injection zone indicated by red arrow)

The dimensions for the B-B' geomechanical model (Figure 120) are: about 26,215 m (86,000ft) wide (x), 30 m (100 ft) thick (y) and 3200 m (10,500 ft) vertically (z). There are about 30,000 elements. The Palos Verdes and THUMS Huntington Beach faults are defined as impermeable boundaries.

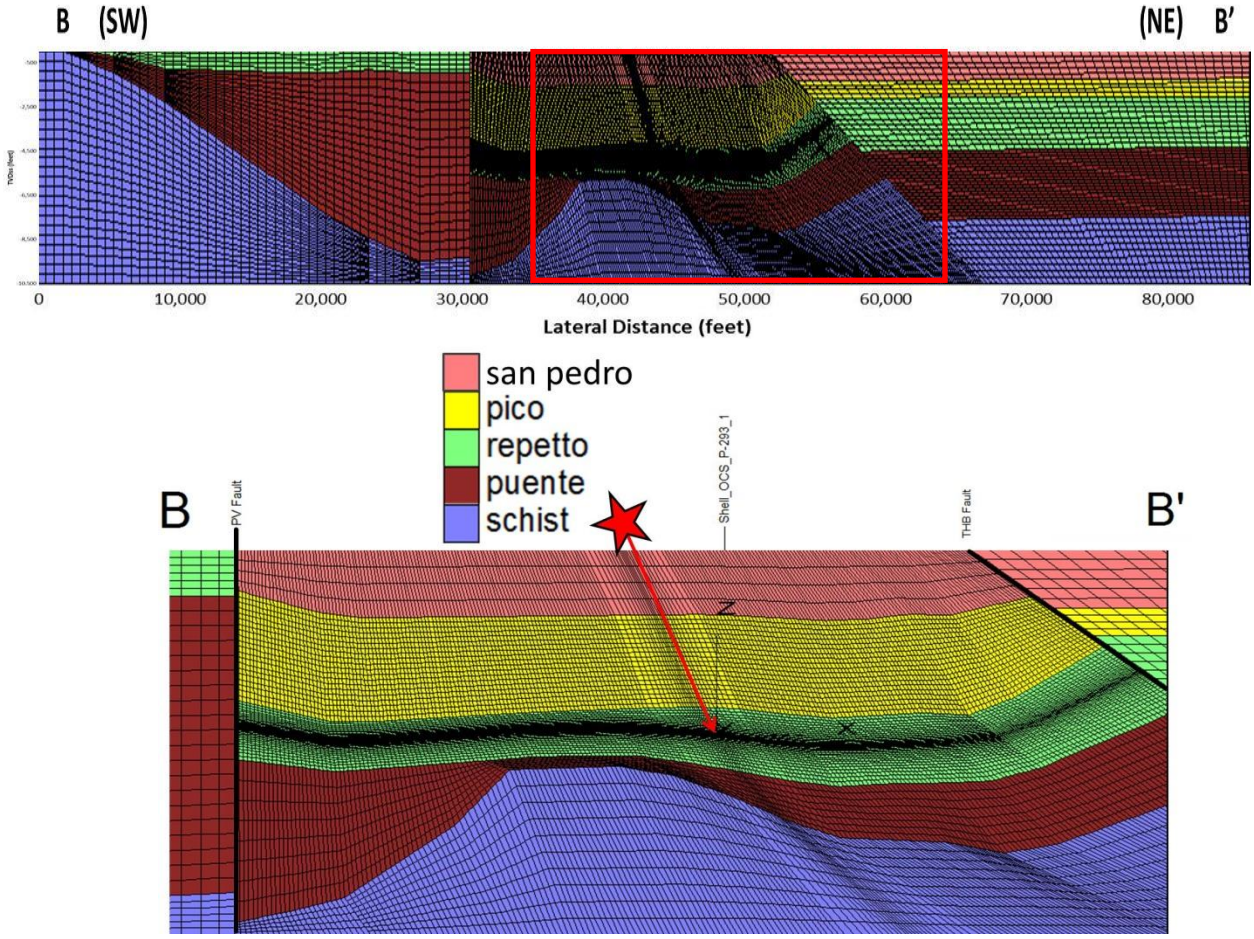

Figure 120: B-B' cross section detail, geomechanically modeled with FLAC3D software (injection zone indicated by red arrow)

Initial boundary conditions were established for the 2D geomechanical models. Zero normal displacement ('roller' boundary condition) was applied to all sides of the model except the top of the model, which was allowed to move freely in the z-direction, up and down. An isotropic elastic material model has been chosen for all simulations.

We have run the geomechanical models using the delta pressure as inputs from Tough2 fluid flow model results. Preliminary simulations include the first year at 0.25 million Mt of CO_2 injection for one well. With the different mesh and eventual zone sizes, the geomechanical model (FLAC) and fluid flow model (Tough2) grid points do not spatially correlate in a straightforward manner, making assignment of delta pressure values from the Tough2 grid to the FLAC3D grid difficult. However for initial approximations, looking at a contour plot of the Tough2 results for changes in pressure for the first year of injection, it is clear that the change in pressure is virtually zero throughout most of the area represented (Figure 121), with the only significant increases present in the few thousand feet around the injection zone.

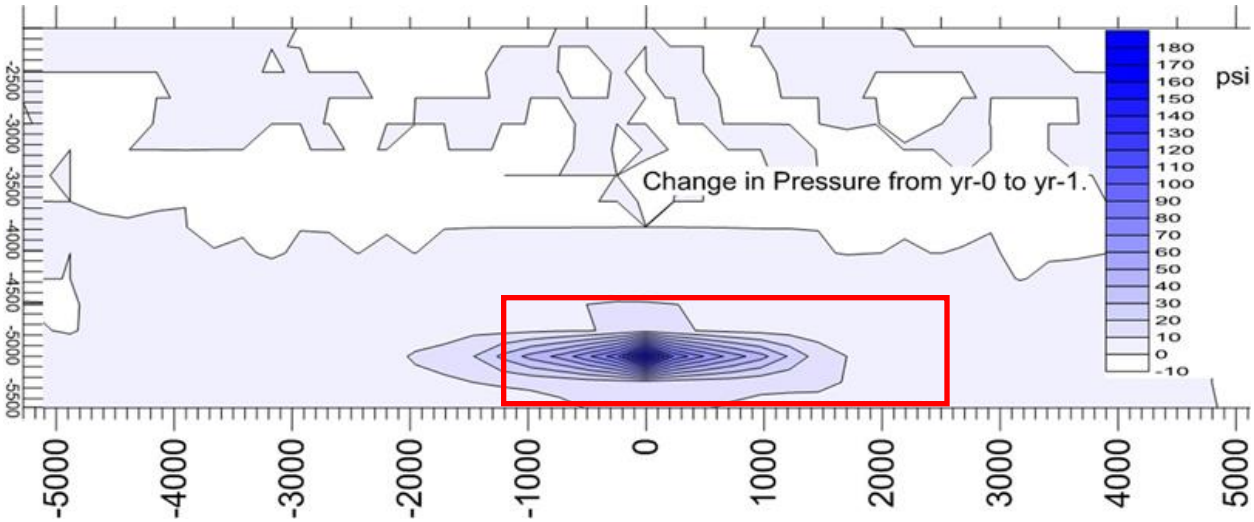

Figure 121: Change in pressure from year 0 to year 1, as a result of 0.25MMt of CO_2 injection, according to Tough2 simulation. (cross section B-B'; red box here indicates area of significant delta pressure results)

Drawing vertical and horizontal lines tangent to every 2nd or 3rd contour line, generally elliptical, in the injection zone, we were able to create five circumscribed and nested rectangles which were used as geometric go-betweens, assigning average Tough2 pressure changes to grid points in FLAC3D falling within the coordinates specified by the rectangles (Figure 122). A sixth rectangle was constructed around most of the area represented to assign the minimum of 10 psi change for the rest of the area in Figure 121 falling between the 0 and 10 delta psi contours.

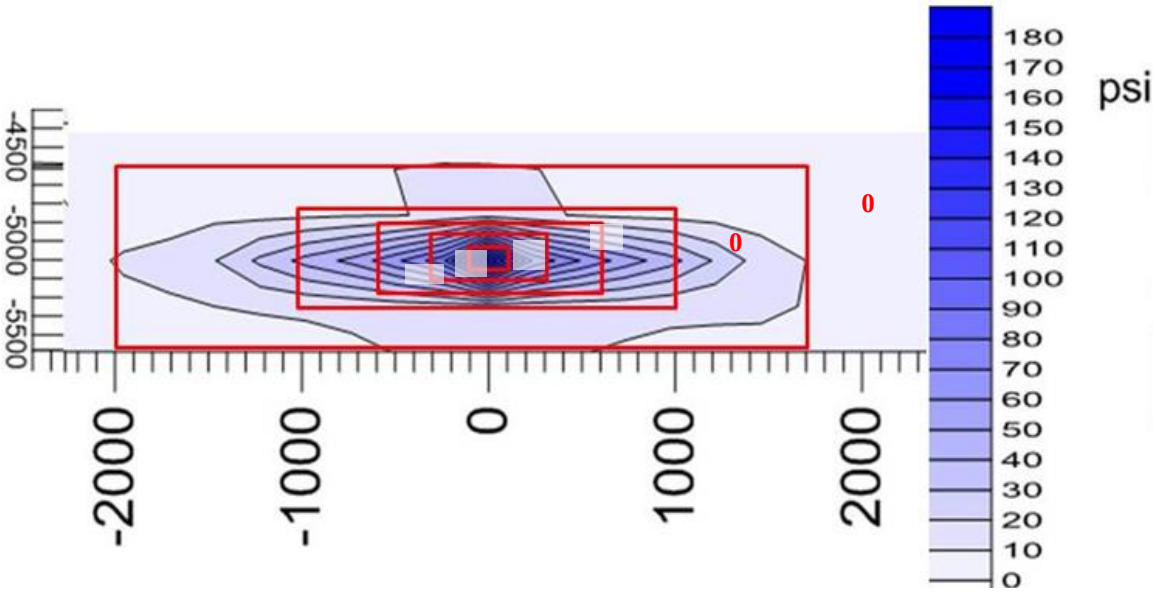

Figure 122: Detail of Figure 121, with constructed delta P contours for assignment to FLAC3D model

After applying the pressure data from the Tough2 model, the vertical displacement is virtually zero (0) throughout most of the model area (Figure 123, dark green is just above 0, lighter blue just below, negative numbers indicating downward displacement). Just below the injection zone the displacement is a negligible ~-0.18 cm (~-0.07 in). The greatest displacement is ~305 m (~1000 ft) above the injection zone, ~+1.12 cm (~+0.44 in). But the results indicate there could be as much as 0.84 cm (0.33 in) vertical displacement near the surface.

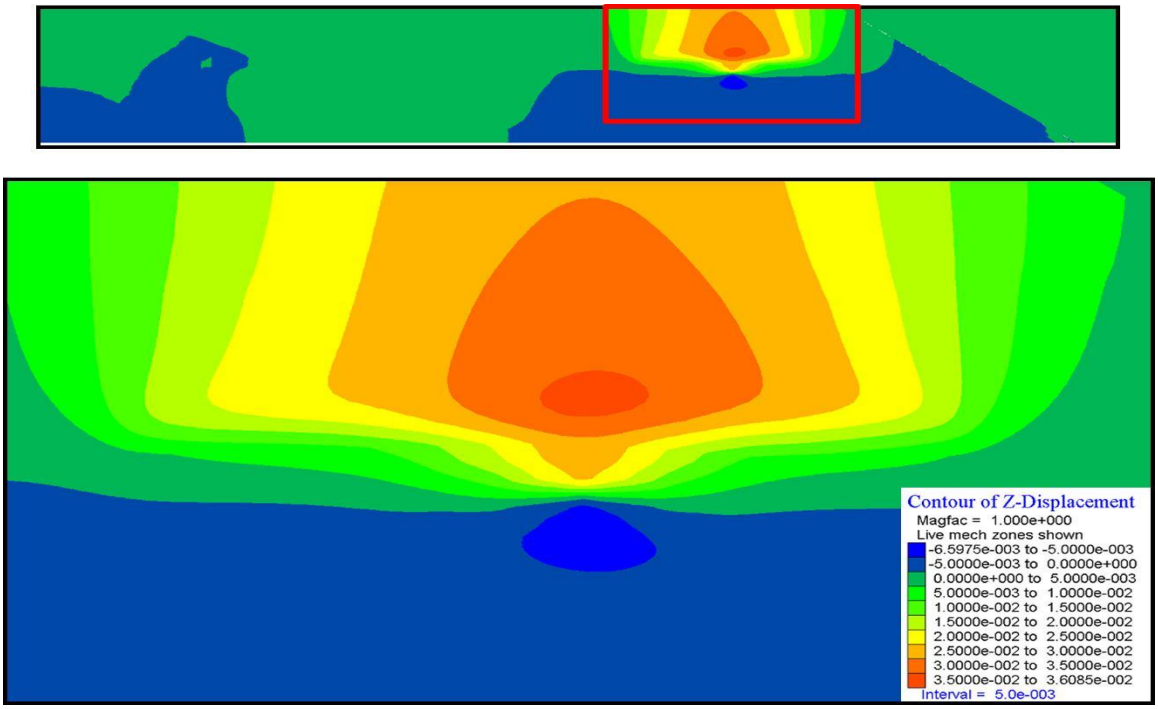

Figure 123: Contour plot of total vertical displacement after running of model (most of cross section (top) and detail (bottom)), 1 year of 0.25 million MT of CO_2 injection

There is virtually no induced normal stress, i.e., compression, throughout most of the Graben, except in the few thousands of feet around the injection zone (Figure 124, dark orange indicates values just above 0, light orange just below, negative numbers represent compression). Obviously the contours here mimic the spatial pattern of the delta pressures as they were earlier assigned (Figure 122). The greatest compression is ~0.87 MPa (~126 psi) right at the point of injection, lessening to less than 0.7 MPa (100 psi) just a few hundred feet from the point of injection.

Title: Characterization of Pliocene and Miocene Formations in the Wilmington Graben, Offshore Los Angeles, for Large-Scale Geologic Storage of CO_2

PI: Dr. Michael Bruno Final Report

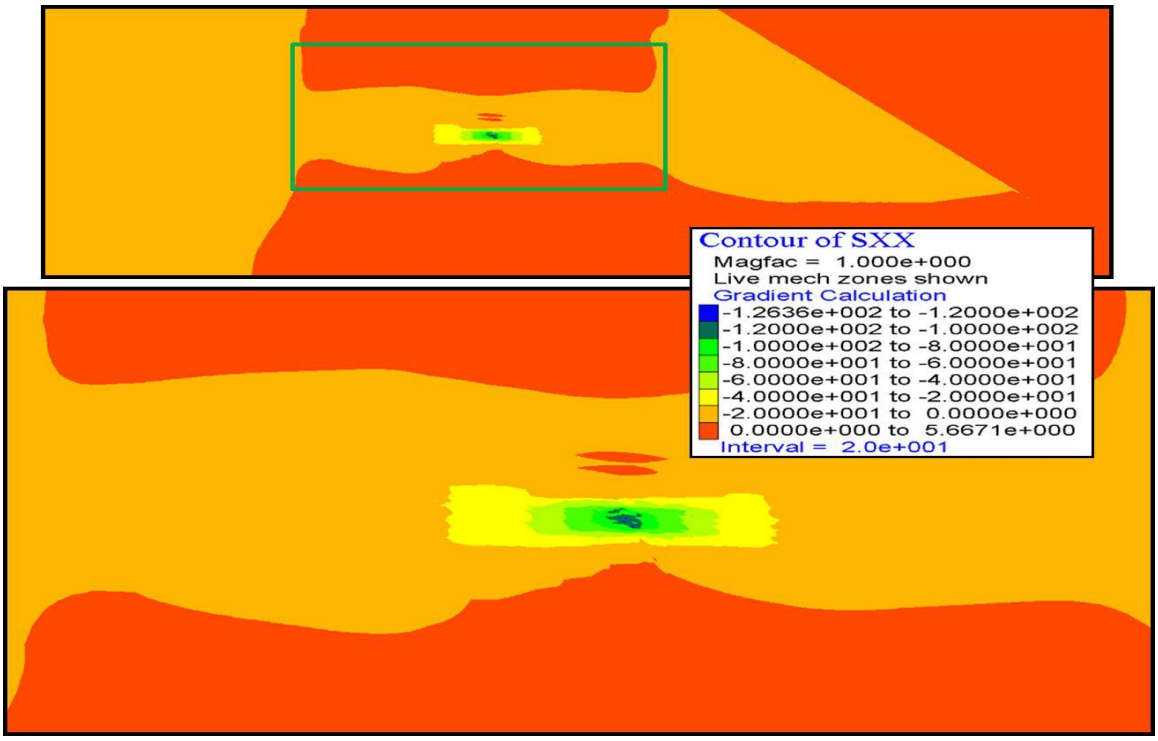

Figure 124: Contour plot of induced normal stress after running of model (most of cross section (top) and detail (bottom), 1 year at 0.25 million MT of CO_2 injection

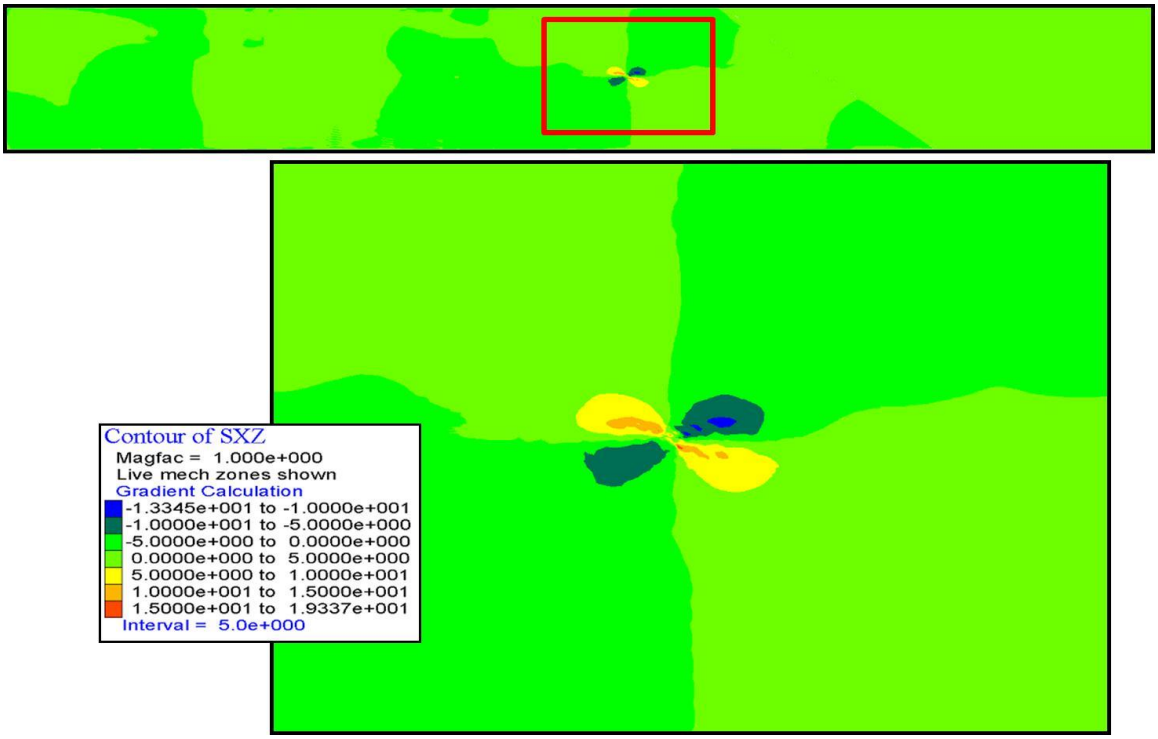

Figure 125: Contour plot of induced shear stress after running of model (full cross section (top) and detail (bottom), 1 year at 0.25 million MT of CO_2 injection

There is virtually no induced shear stress throughout most of the central Graben, except in the few thousands of feet around the injection zone (Figure 125, light green indicates values just above 0, dark green just below). Obviously the zone of significant induced shear stress here also mimics the spatial pattern of the delta pressures as they were earlier assigned (Figure 122). The greatest shear stress is just under 0.14 MPa (20 psi) near the point of injection, lessening to less than 0.07 MPa (10 psi) just a few hundred feet from the point of injection.

Similarly, we applied these same preliminary procedures to study the cross section A-A', by simulating the geomechanics model using FLAC with Tough2 the first month pressure input data at 0.25 million MT/year of CO_2 injection for a single well. These preliminary results are not presented here since no significant induced stress or deformations are present. We instead decided to focus our geomechanical effects on full 3D models for both the northern and central graben, coupled with 3D fluid flow models as presented in the following sections.

8.3.3 3D geomechanical model for Central Graben

In 2014 we developed a full 3D geomechanical model through the center of the Wilmington Graben (Figure 126), consistent with the latest geologic model and Tough2 fluid flow model. The dimensions of this geomechanical model are about 8400-8600 m (27,560-28,215 ft) in the lateral directions, and 2950 m (9680 ft) in the vertical direction starting from 133 m (435 ft) above the seafloor. The injection well is located at the center of the model. The geomechanical model has a total of 35100 elements, with a finer mesh across the injection well and the Repetto (Pliocene) injection formation. We apply roller boundary conditions on all surfaces except the top surface, which is free to move in both vertical and lateral directions.

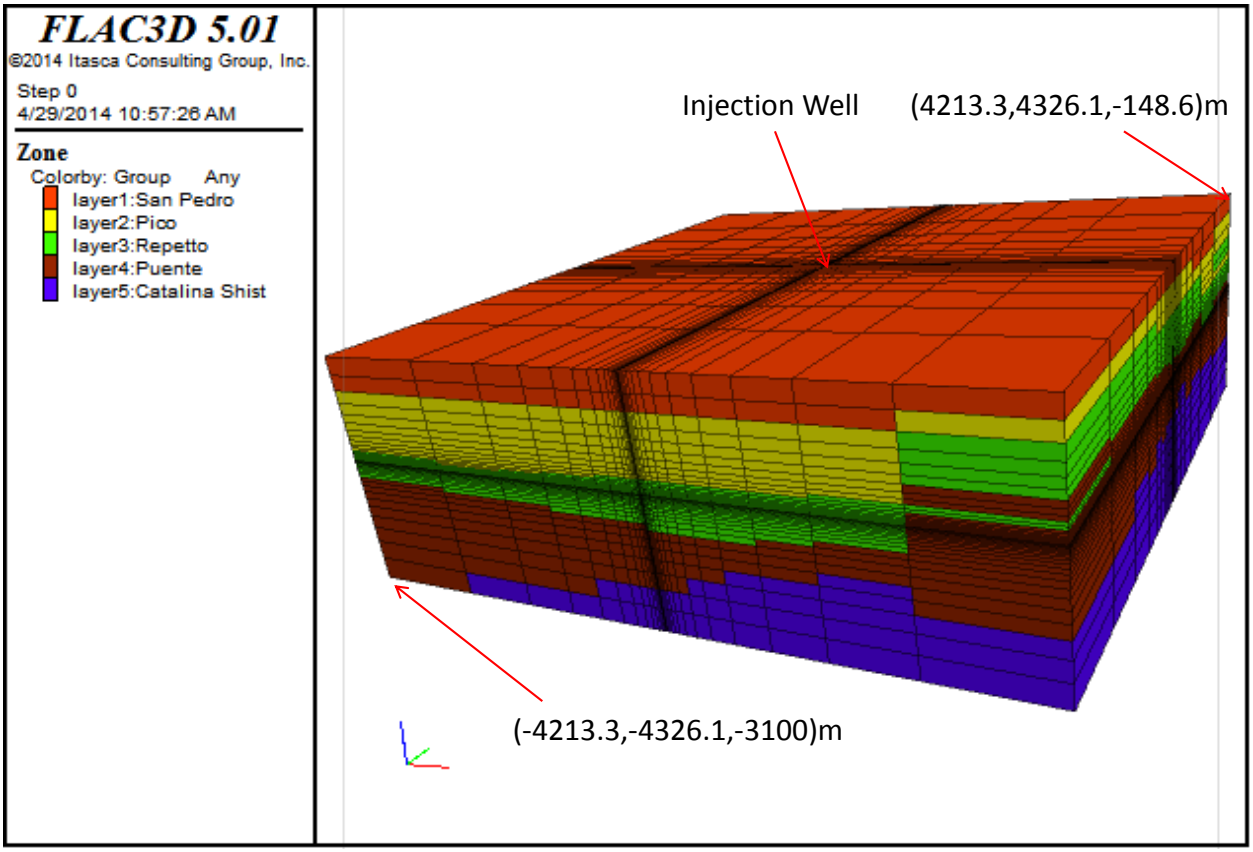

Figure 126: 3D Wilmington Graben geomechanics model with FLAC3D software.

8.3.3.1 Baseline

The results of baseline simulations are described below. Figure 127 shows the pressure distribution across the injection well in NE-SW and NW-SE directions, after 30 years of injection from the Tough2 fluid flow model. These pressure data are directly transferred from the fluid flow model to the geomechanical model. The highest pressure concentration area is above the injection interval, with a maximum magnitude of 9.7E5 Pa (2.03E4 psi).

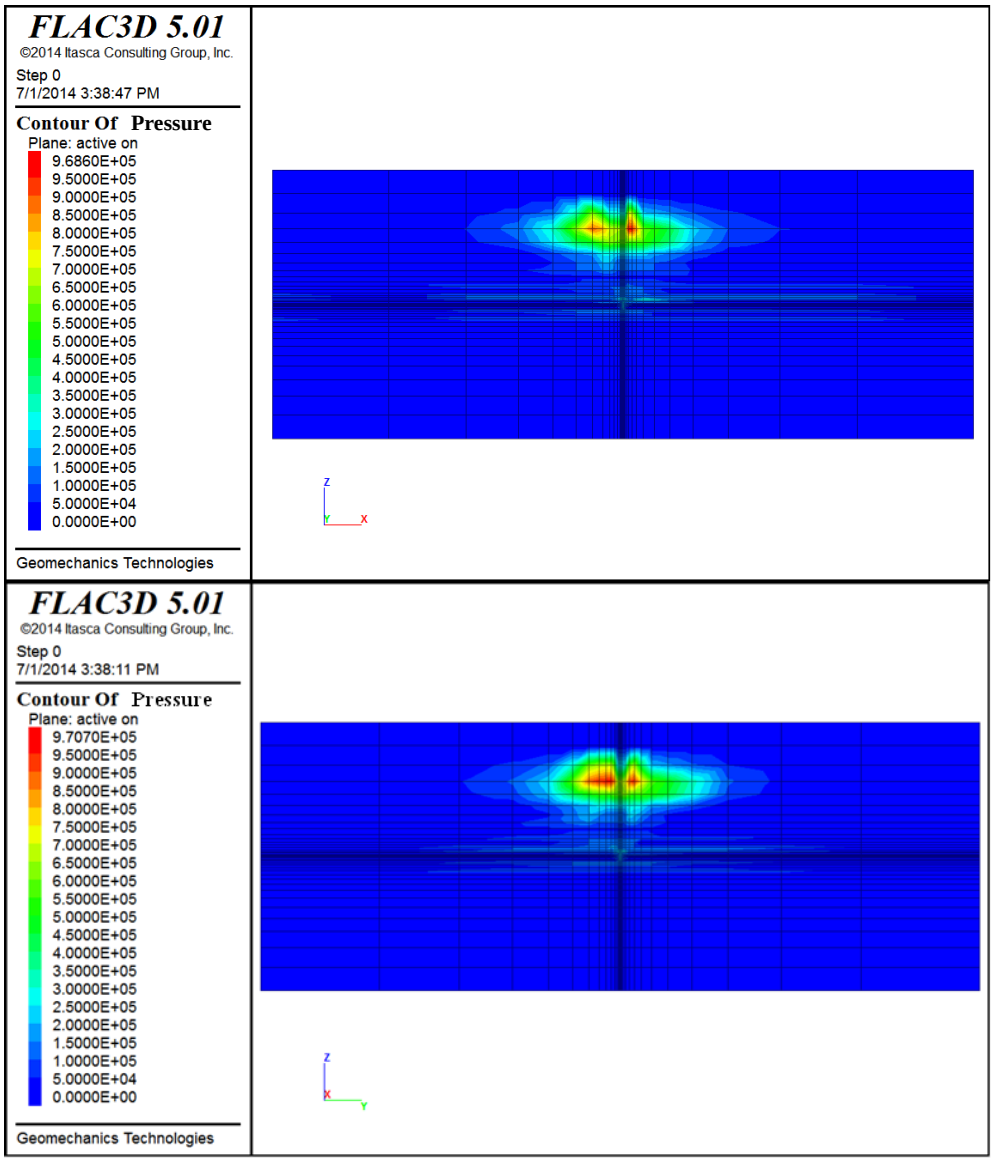

Figure 127: Baseline scenario - Pressure distribution after 30 years of injection in NE-SW (above) and NW-SE (bottom) directions through the injection well (Pa).

Figure 128 shows the induced horizontal XX stress across the injection well in the NE-SW direction, with the maximum compressive stress of 7.7E5 Pa (1.61E4 psi) localized within the maximum pressure concentration area; and the maximum tensile stress of 1.7E5 Pa (3.55E3 psi) localized above and below the pressure concentration area. Figure 129 presents the induced XZ shear stress across the injection well in NE-SW direction, and the maximum shear stresses are about 1.0E5 Pa (2.01E3 psi). Figure 130 shows the induced ZZ vertical stress across the injection well in NE-SW direction, with the maximum compressive and tensile stresses located above and below the injection point, about 3.8E5 Pa (7.94E3 psi) and 9.8E4 Pa (2.05E3 psi), respectively.

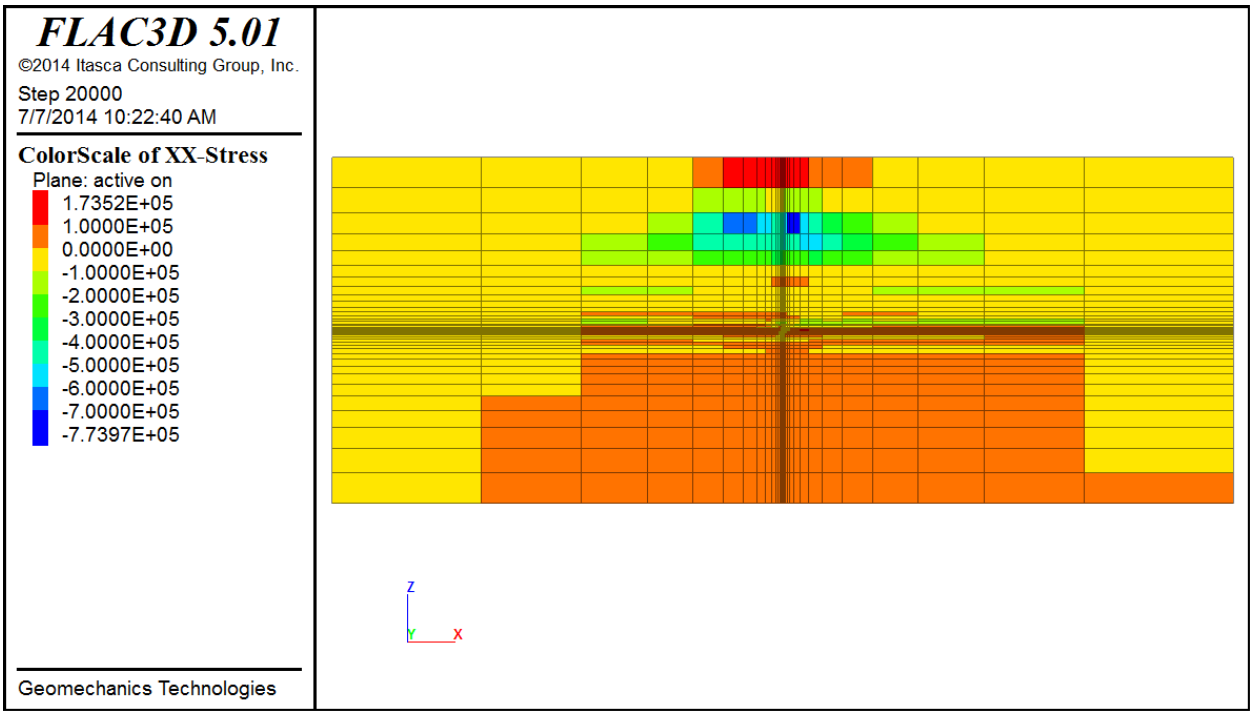

Figure 128: Baseline scenario - Induced XX stress, NE-SW direction through the injection well (Pa).

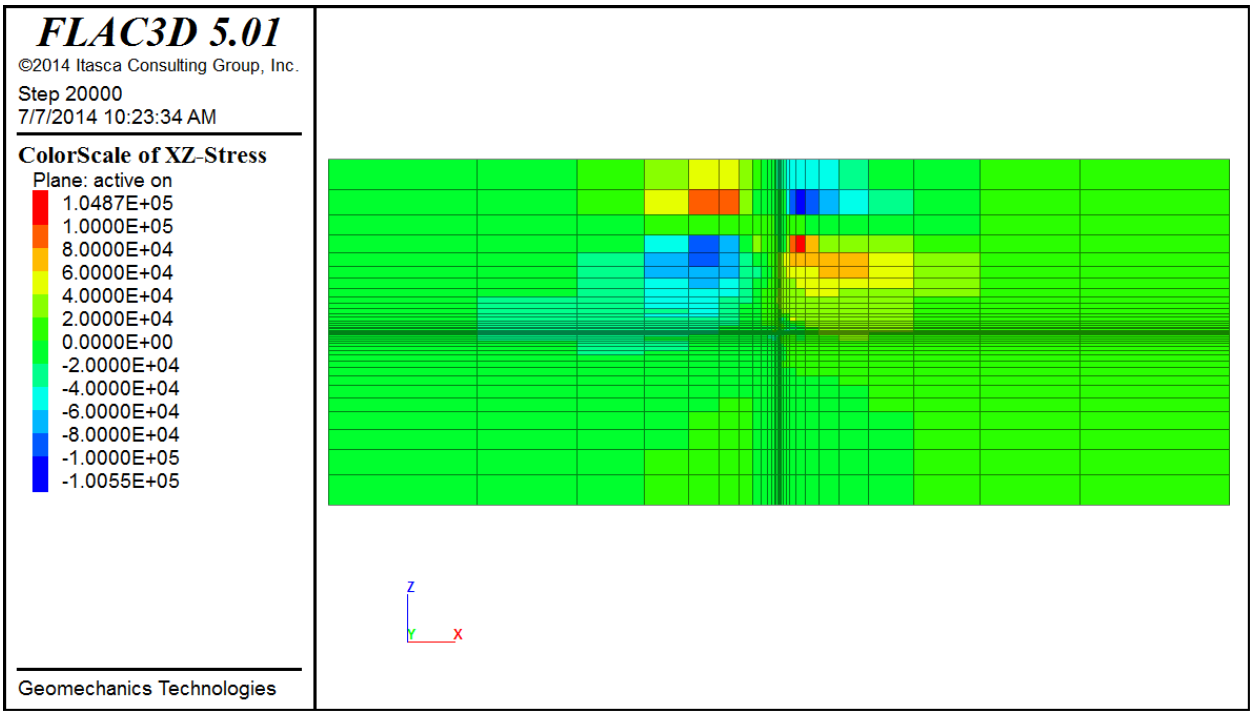

Figure 129: Baseline scenario - Induced XZ stress, NE-SW direction across injection well (Pa).

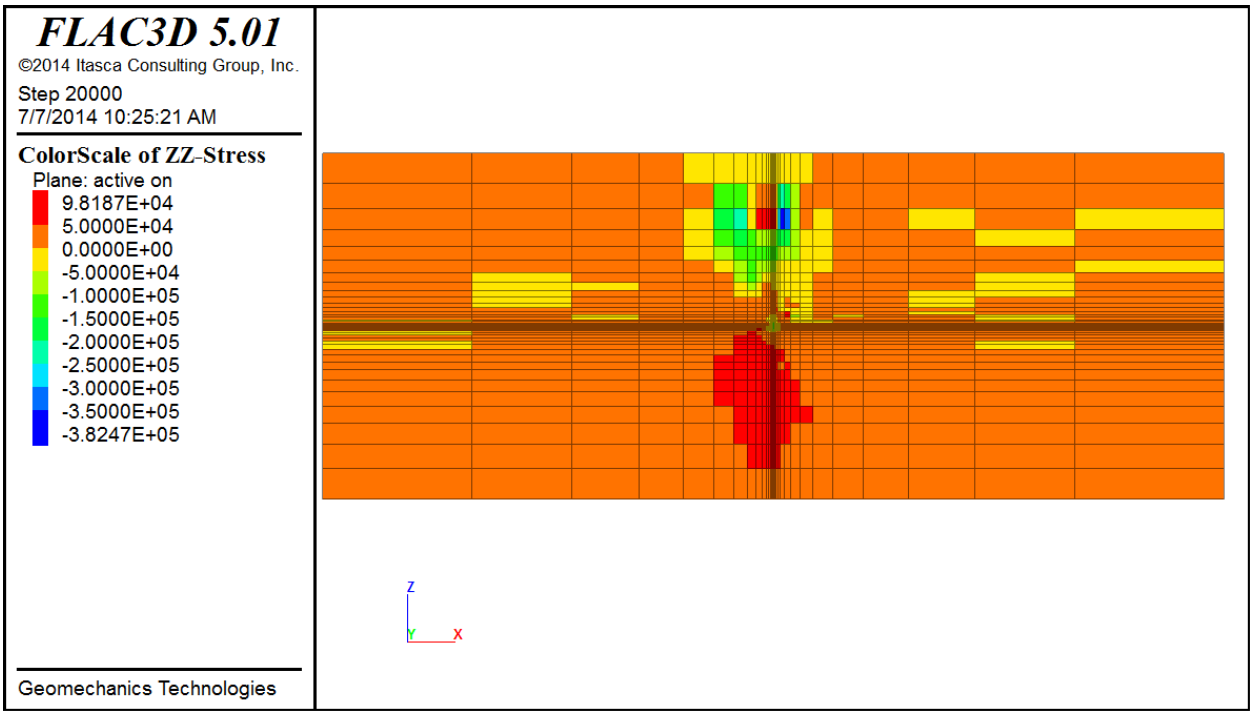

Figure 130: Baseline scenario - Induced ZZ/vertical stress, NE-SW direction across injection well (Pa).

Figure 131 shows the induced vertical Z-displacement in isometric and cross-section views across the injection well in the NE-SW direction. The surface uplift above the injection well is a maximum of about 29 cm (11.5 in).

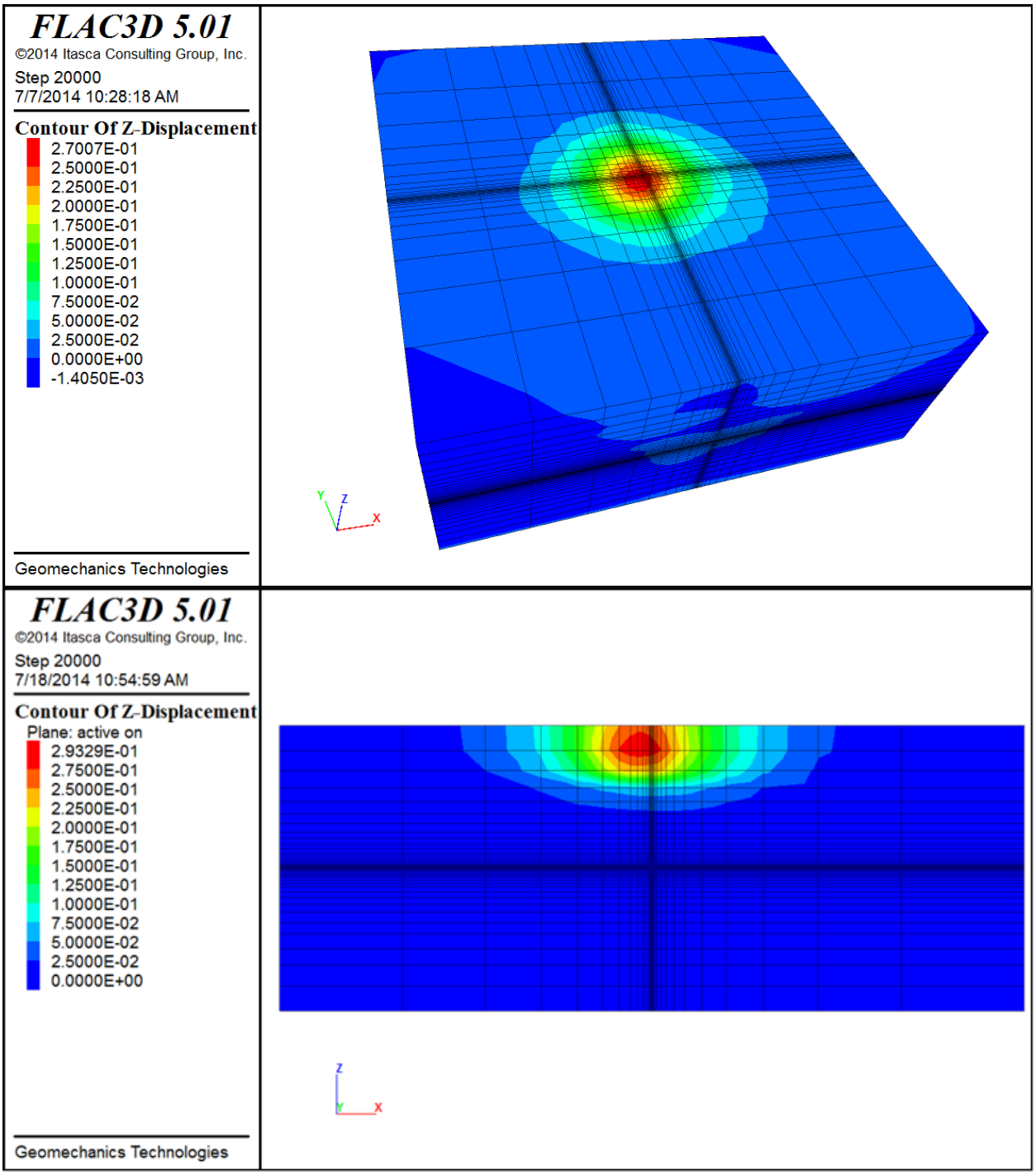

Figure 131: Baseline scenario - Induced Z displacement, 3D view (above) and in NE-SW direction across injection well (bottom) (m).

8.3.3.2 More shale

Next, models assuming more shale were run. Figure 132 shows the pressure distribution across the injection well in NE-SW and NW-SE directions, after 30 years of injection from Tough2 simulations. These pressure data are directly transferred from the fluid flow model to the geomechanical model. The highest pressure concentration area is above the injection interval, with maximum magnitude of about 6.8E5 Pa (1.42E4 psi).

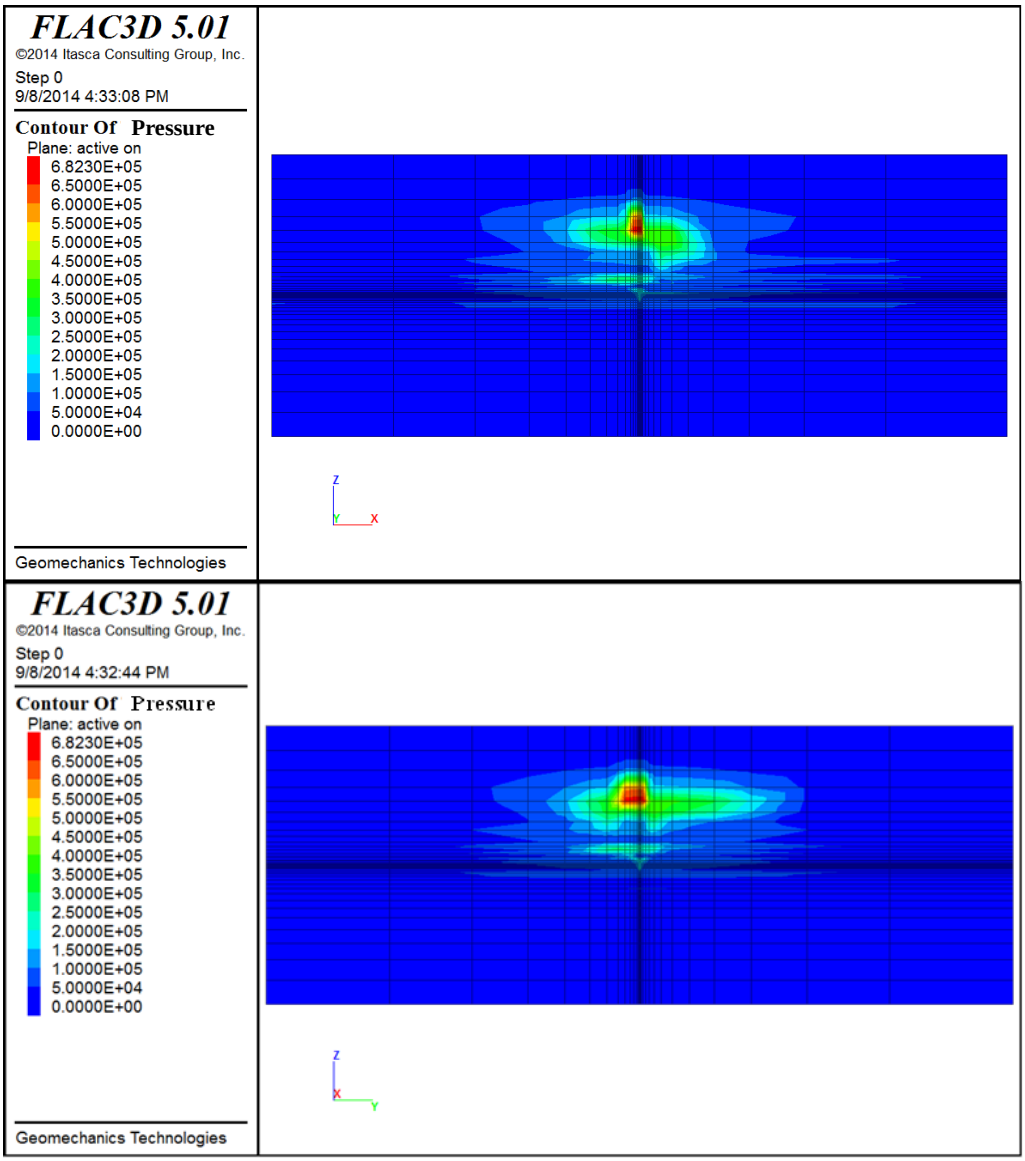

Figure 132: More shale - Pressure distribution after 30 years of injection in NE-SW (top) and NW-SE (bottom) directions through the injection well (Pa).

Figure 133 shows the induced horizontal XX stress across the injection well in the NE-SW direction, with a maximum compressive stress of about 3.4E5 Pa (7.1E3 psi) localized within the maximum pressure concentration area; and a maximum tensile stress of about 4.4E4 Pa (9.19E2 psi) localized above and below the pressure concentration area. Figure 134 presents the induced XZ shear stress across the injection well in NE-SW direction, with a maximum shear stresses of about 5.8E4 Pa (1.21E3 psi). Figure 135 shows the induced ZZ vertical stress across the injection well in NE-SW direction, with maximum compressive and tensile stresses located above and below the injection point, of about 3.1E5 Pa (6.47E3 psi) and about 3.5E4 Pa (7.31E2 psi), respectively.

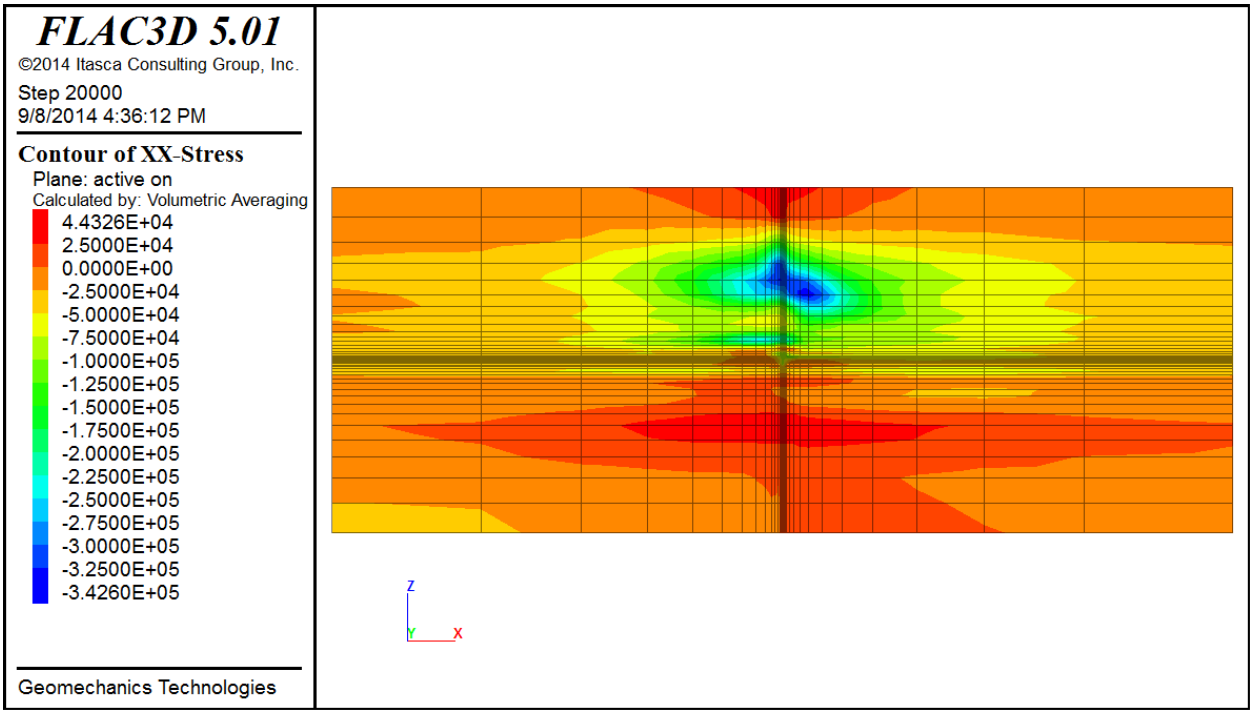

Figure 133: More shale - Induced XX stress, NE-SW direction through the injection well (Pa).

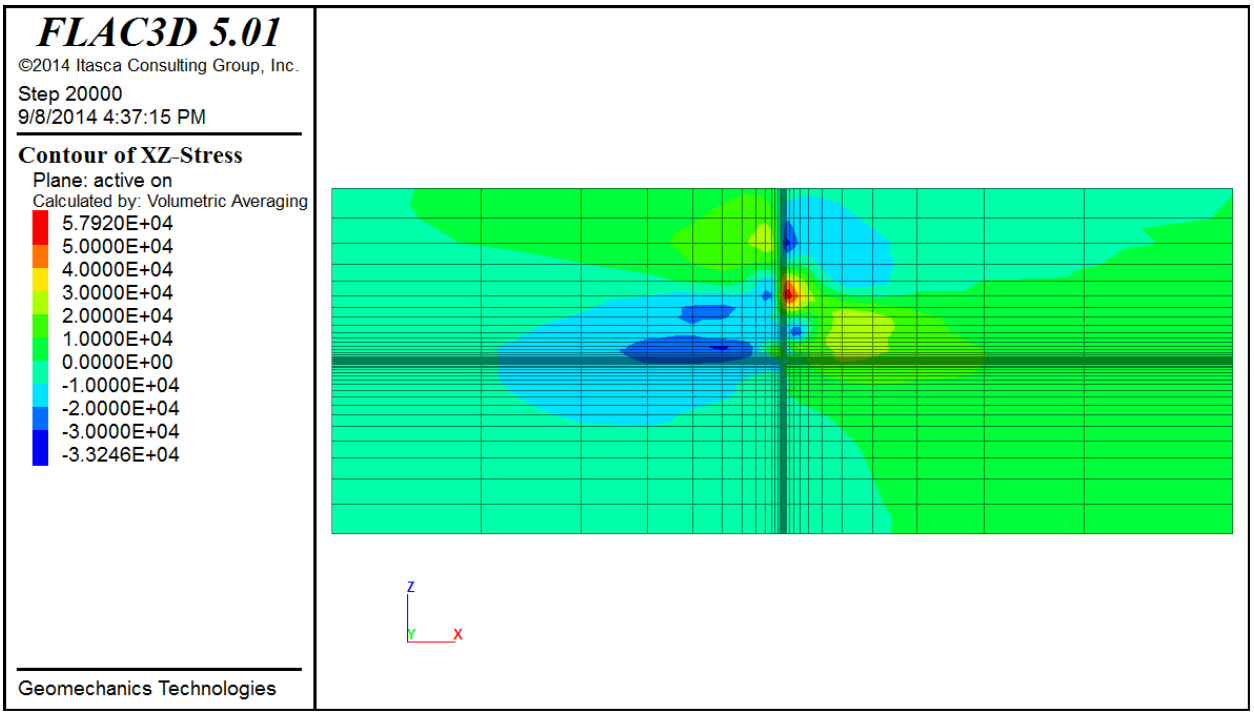

Figure 134: More shale - Induced XZ stress, NE-SW direction across injection well (Pa).

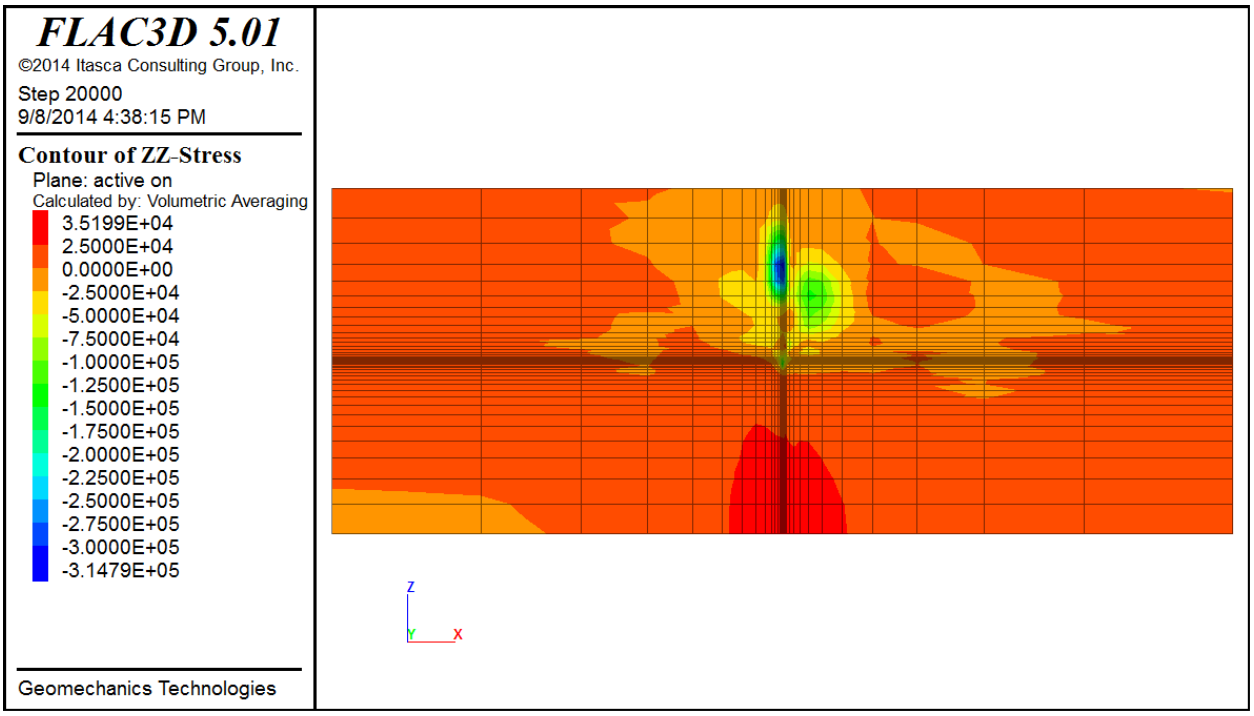

Figure 135: More shale - Induced ZZ/vertical stress, NE-SW direction across injection well (Pa).

Figure 136 shows the induced vertical Z-displacement in isometric and cross-section views. The surface uplift above the injection well is a maximum of about 8 cm (3.2 in).

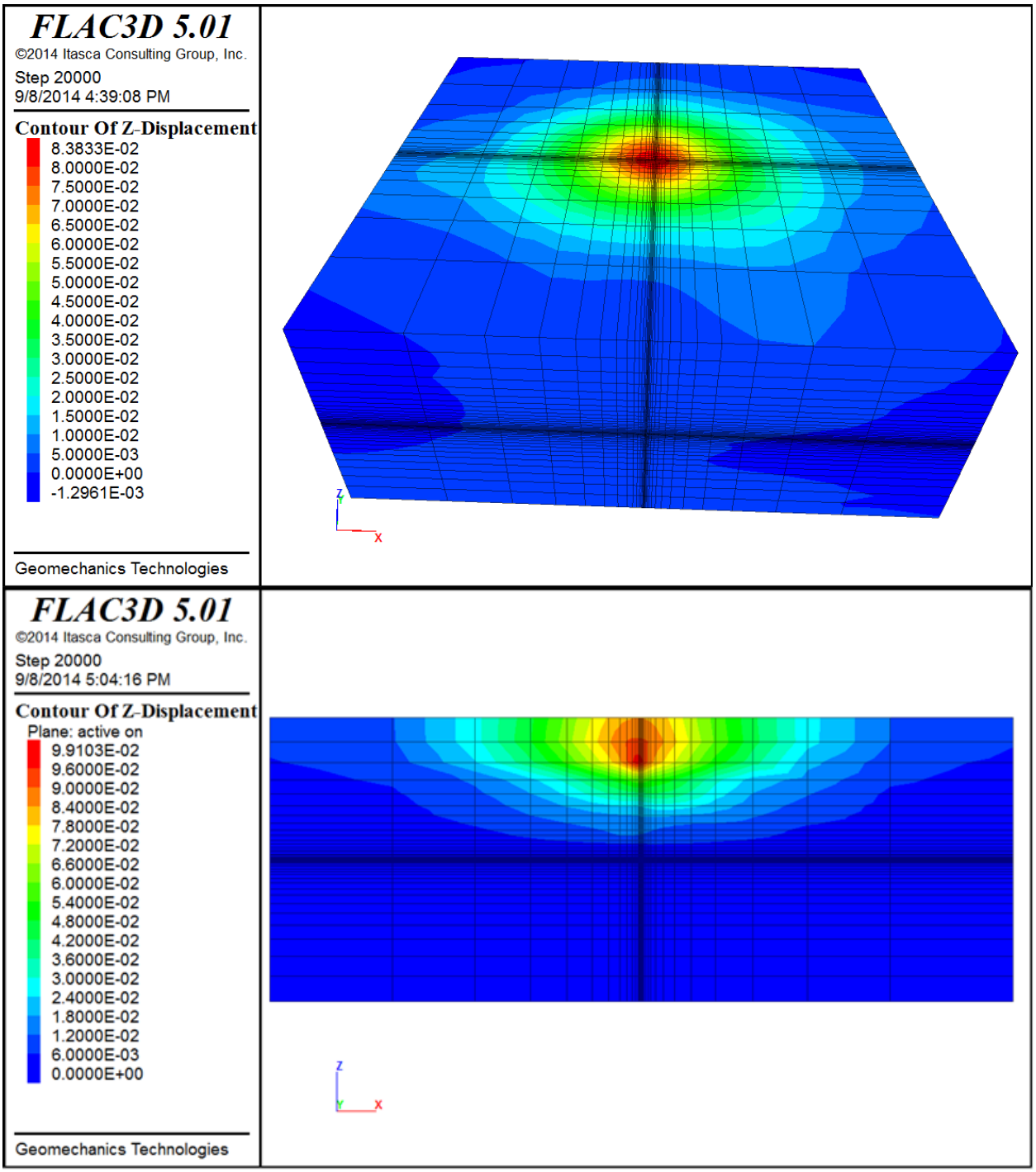

Figure 136: More shale - Induced Z displacement 3D view (top) and in NE-SW direction across injection well (bottom) (m).

In conclusion, for the central graben simulations, after 30 years of CO_2 injection, the geomechanical models (baseline and more shale) showed that there are little or no risks of induced formation fracturing, with maximum induced normal and shear stresses of less than 6.9E5 Pa (100 psi). There is also little or no risk of induced fault activation.

8.3.4 3D geomechanical model for Northern Graben

A 3D geomechanical model was developed for the northern graben area consistent with horizontal data from the geological model. A total number of 123,750 elements were used with higher resolution near the injection zone as shown in Figure 137 and Figure 138. Stratigraphic units were assigned based on the geological model. Because there are significant rock mechanics properties within the Repetto formation, based on the 1D rock properties estimation, a subdivision was carried out on Repetto formation inside of the Graben, resulting in 3 sub-units.

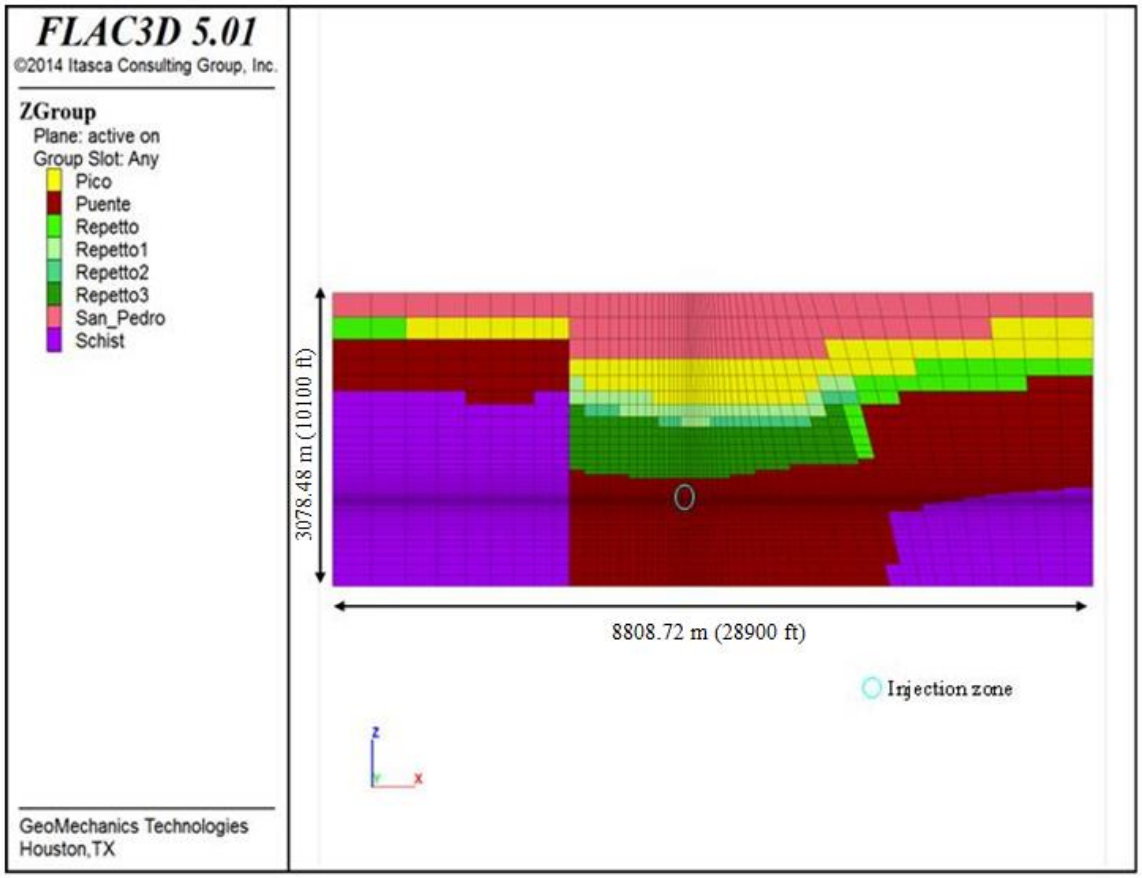

Figure 137: West-east view for the geomechanics mesh at the injection zone, Northern Graben

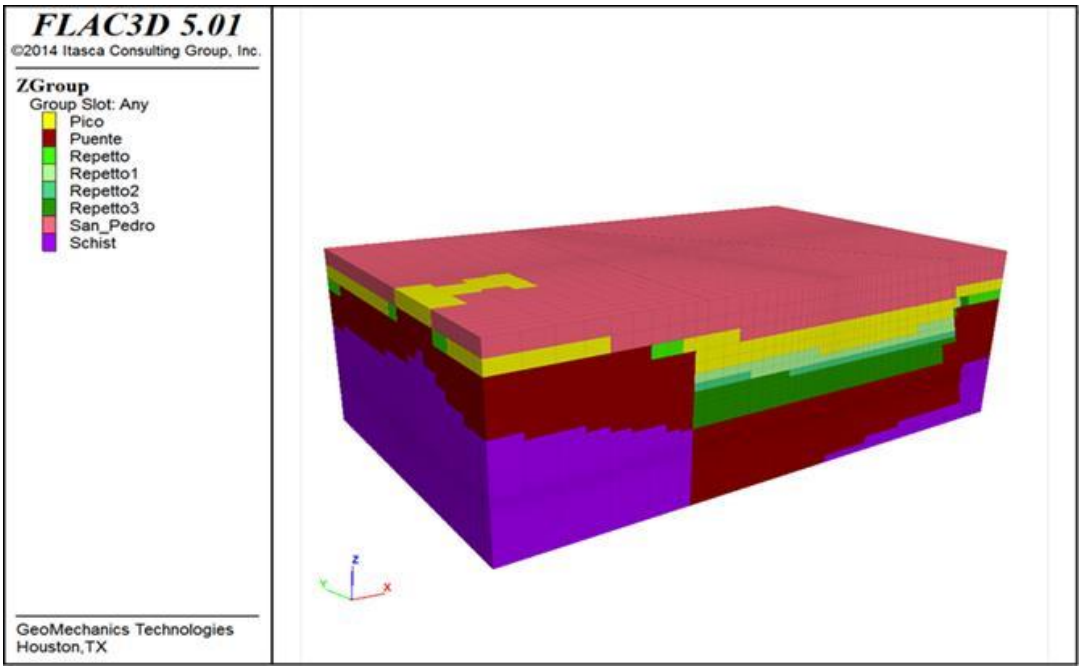

Figure 138: 3D view for the geomechanics mesh, Northern Graben

Once the geometry and mesh were established, initial and boundary conditions were assigned for the model. We applied roller boundary conditions with no lateral movements on *x*- and *y*-directions, as well as no vertical movement at the bottom. Vertical and horizontal movements were allowed for the top of the model (Figure 139).

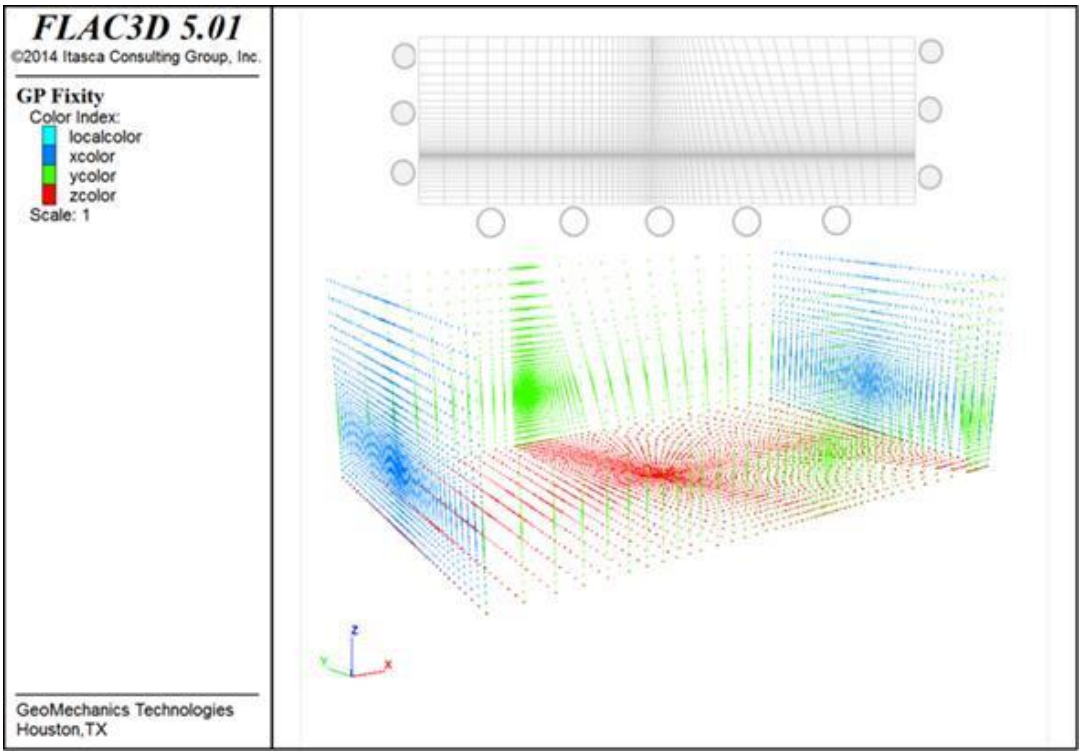

Figure 139: Boundary conditions, Northern Graben

Two interfaces were created in the 3D geomechanical model to represent the PV and THB faults (Figure 140). The fault on the left/west (PV) was modeled as a vertical plane and the one on the right/east (THB fault) as a complex plane with a strike azimuth of 105° and a dip of 75° from the horizontal plane, with an azimuth of 15°.

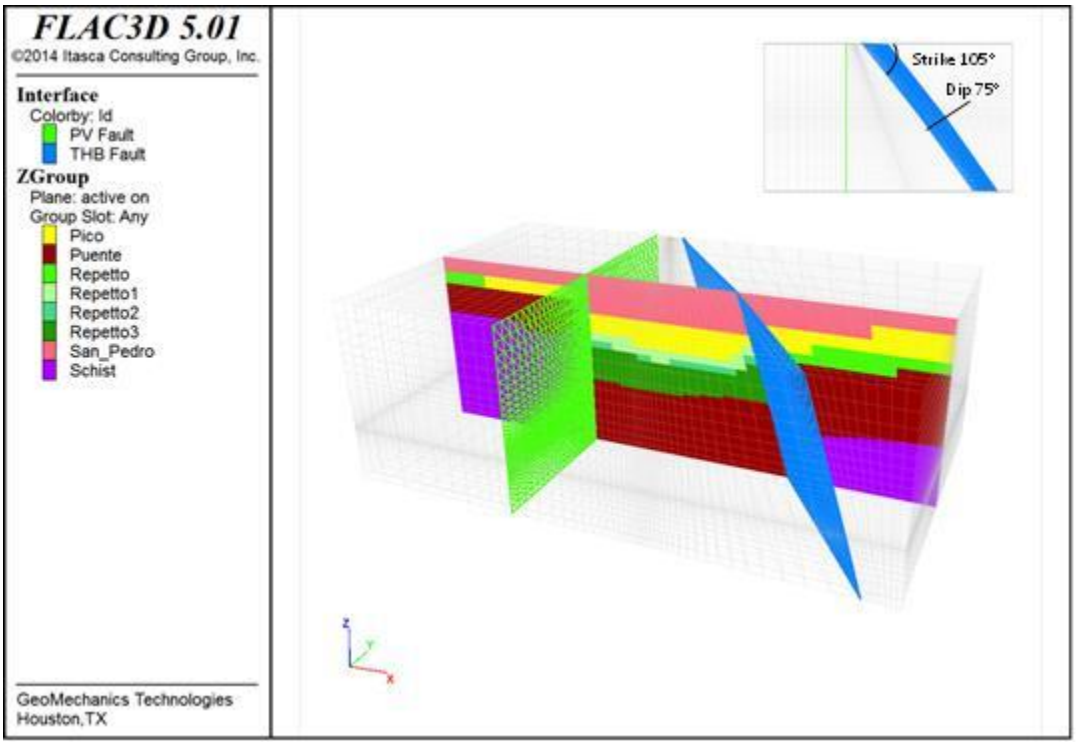

Figure 140: Interface planes for fault modeling (PV and THB faults), Northern Graben

8.3.4.1 Model Results: Induced stress, displacements and fault activation analysis after 30years of CO_2 injection

After 30 years of CO_2 injection, pressure changes were propagated from the injection zone. Figure 141 and Figure 142 show 3D and plan views of pressure changes for cases Var-1 and Var-3, respectively. A more compact gas plume is seen in case Var-1, in which shale is more abundant. Similar results can be observed in the west-east view illustrated in Figure 143. In general, note that case Var-3 shows pressure effects around the injection point propagating to the faults.

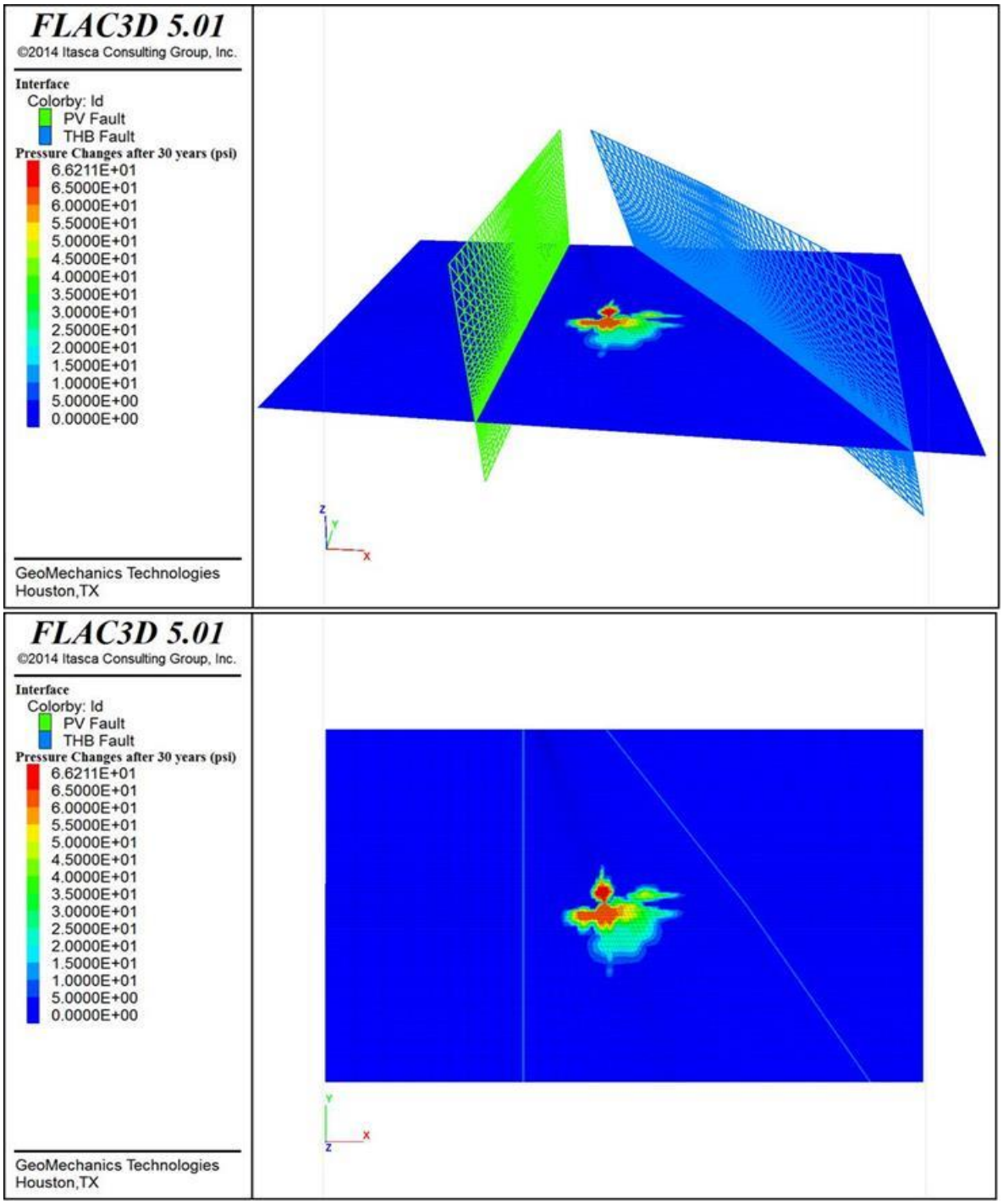

Figure 141: Var-1 - 3D (top) and plan (bottom) views of pressure distribution after 30 years of CO_2 injection

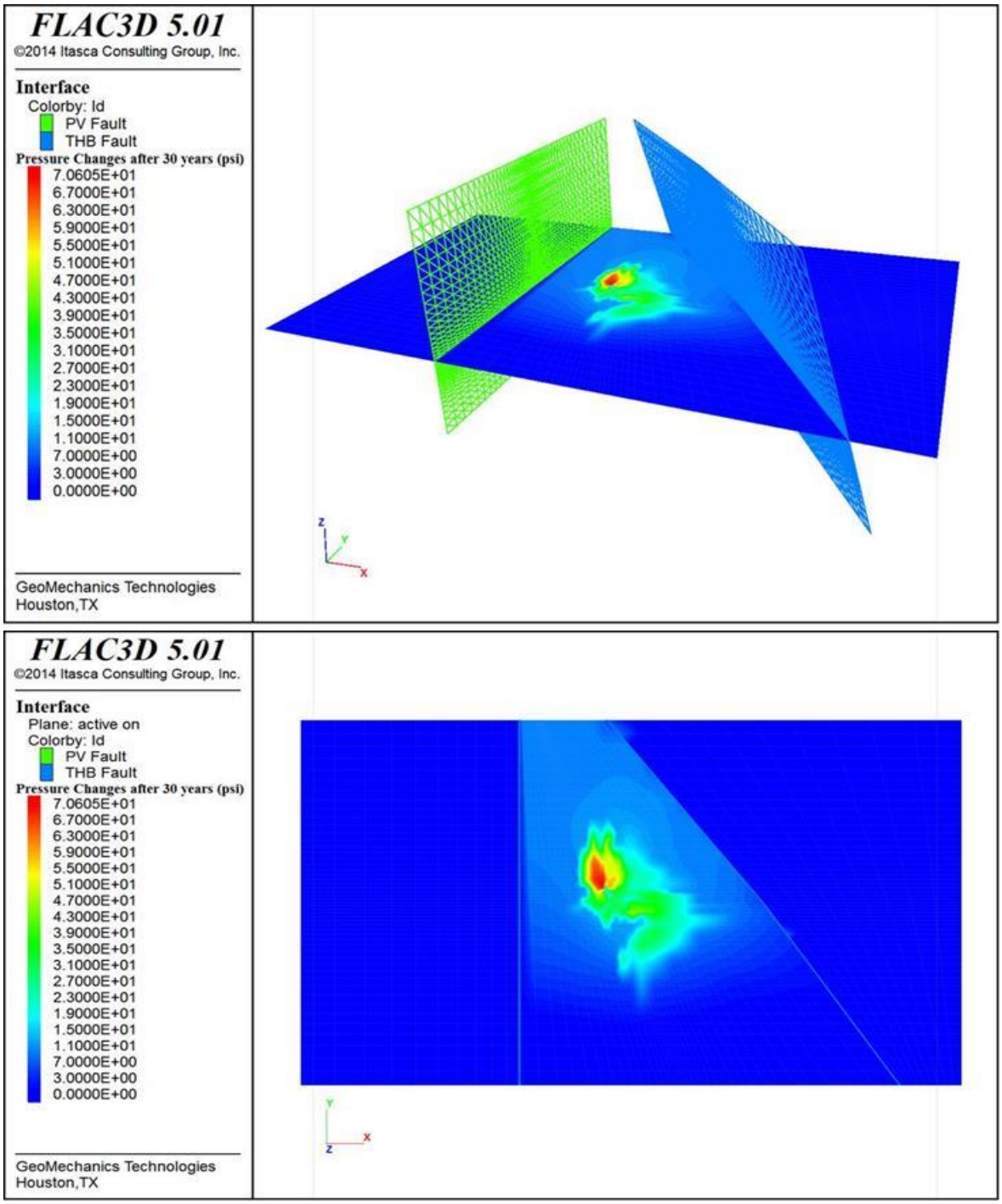

Figure 142: Var-3 - 3D (top) and plan (bottom) views of pressure distribution after 30 years of CO_2 injection

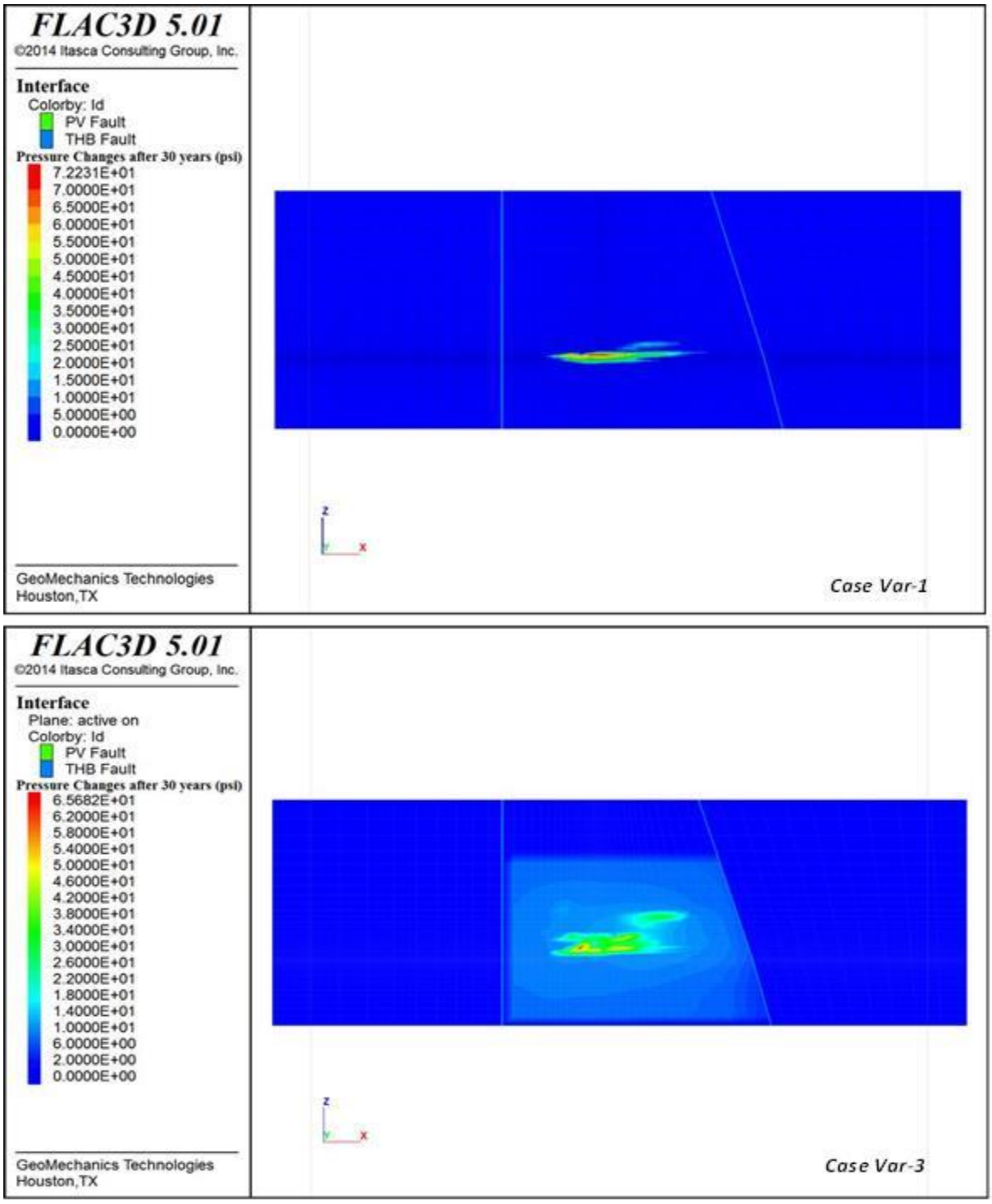

Figure 143: West-east view of pressure distribution after 30 years of CO_2 injection

Induced stresses are shown in Figure 144 to Figure 146. Note that compressive horizontal stresses can be seen across the injection zone with a maximum induced horizontal stress of 4.34 bar (63 psi) and 2.82 bar (41 psi) along the *x*-direction for cases Var-1 and Var-3, respectively. Figure 144 and Figure 145 show induced vertical stresses of 1.03 bar (15 psi) and 1.10 bar (16 psi) along the z-direction for cases Var-1 and Var-3, respectively. Lastly, induced shear stresses are shown in Figure 146.

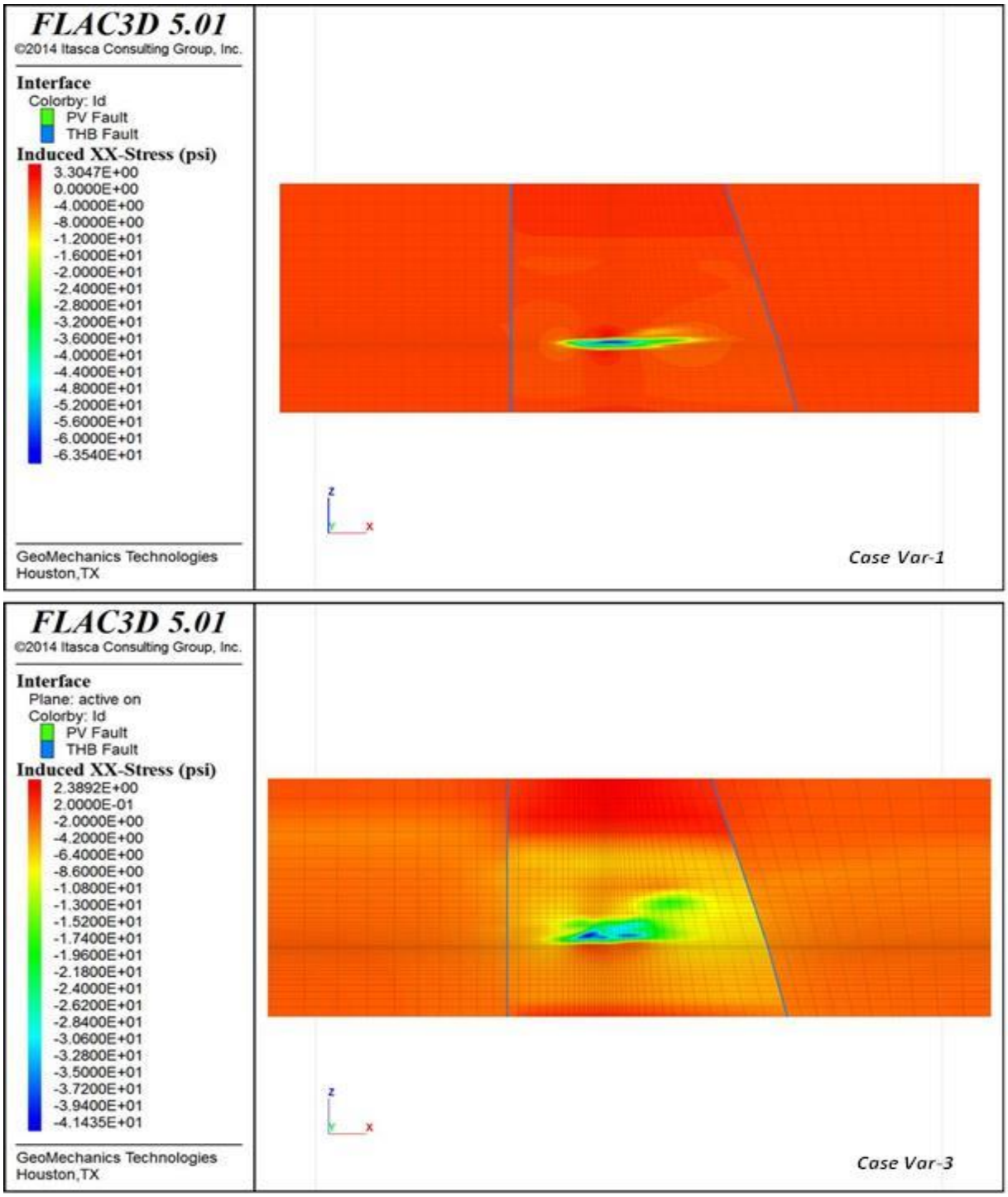

Figure 144: West-east view of induced XX-stress across injection zone

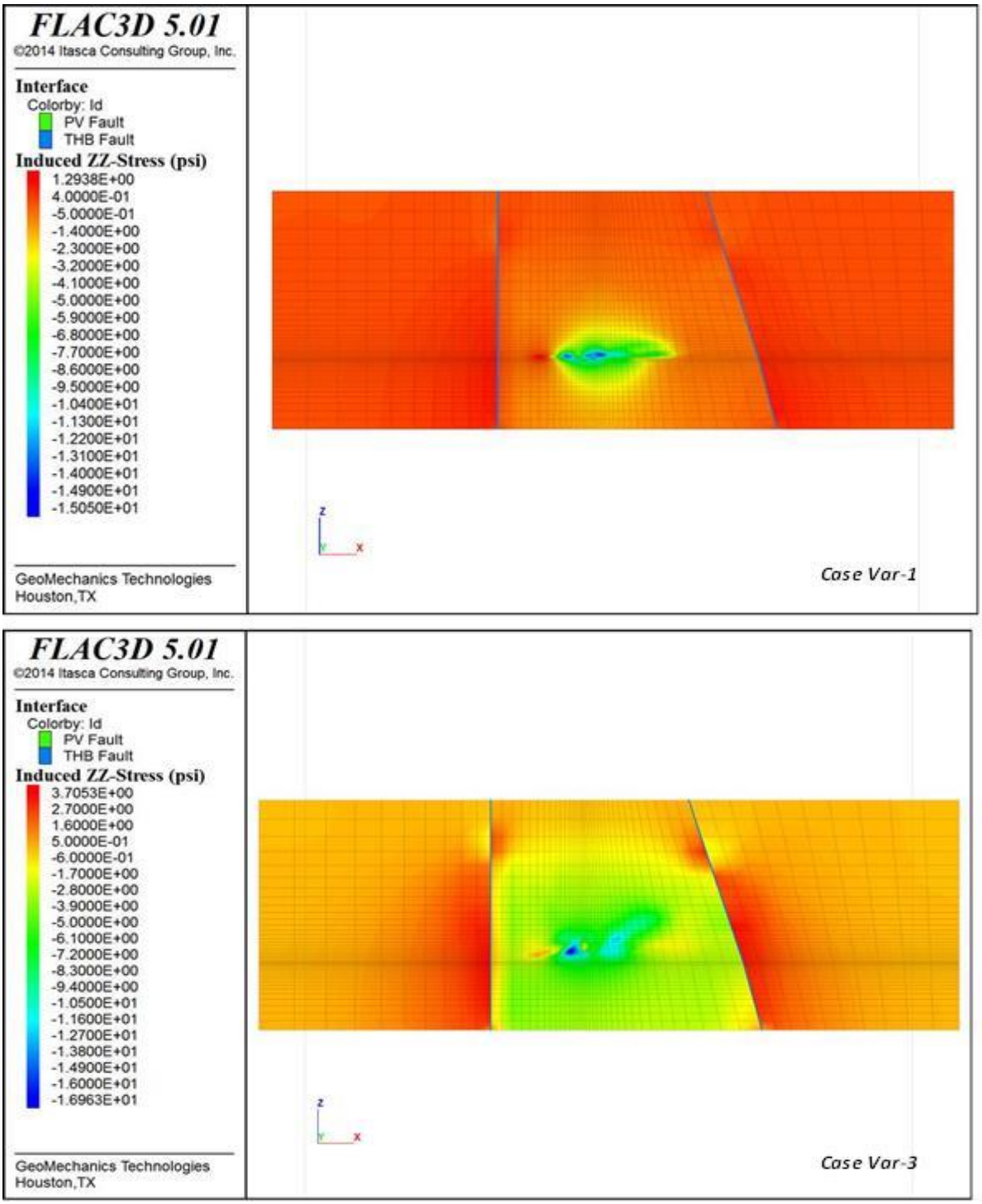

Figure 145: West-east view of induced ZZ-stress across injection zone

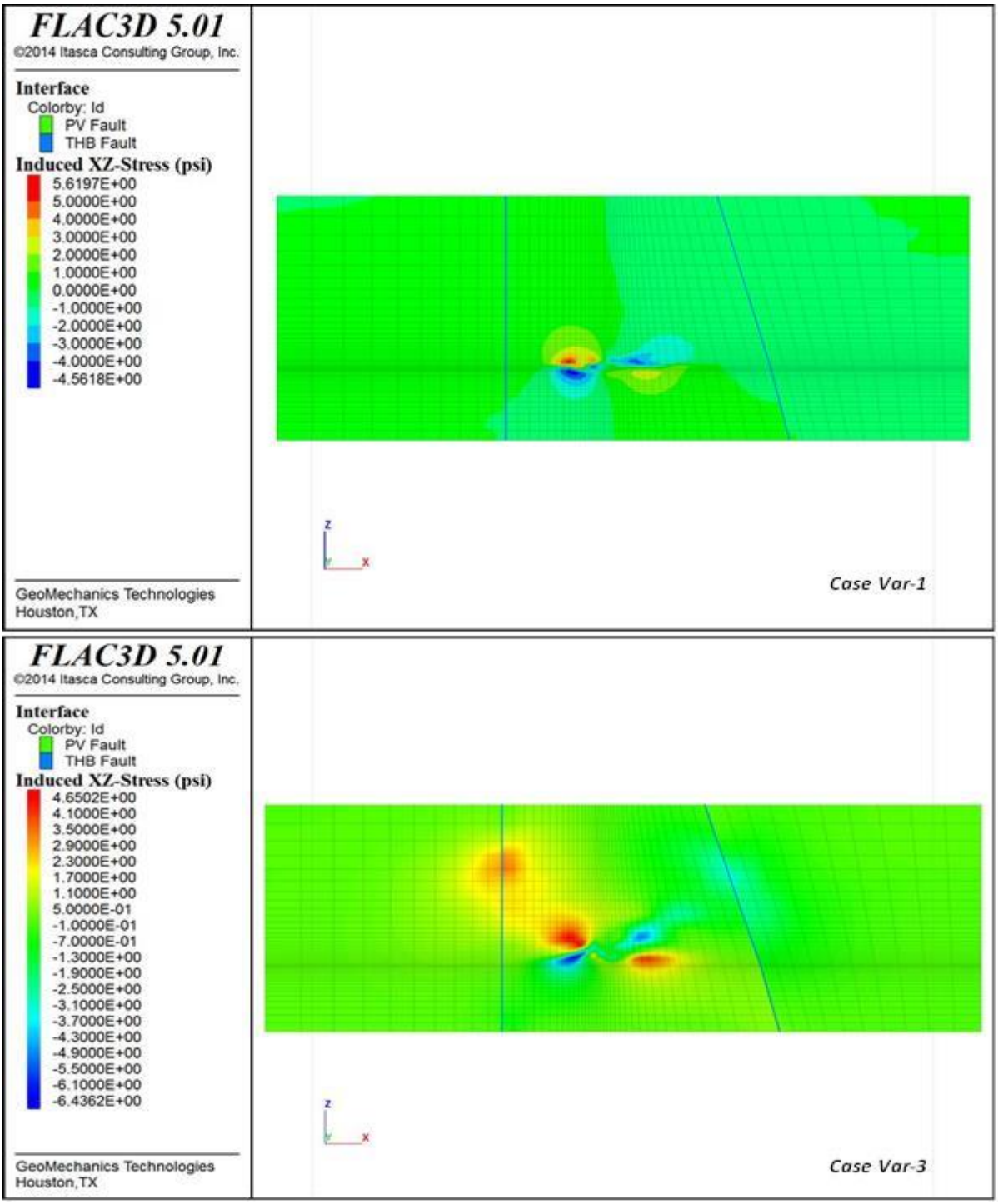

Figure 146: West-east view of induced XZ-stress across injection zone

Figure 147 illustrates the induced vertical Z-displacement for a west-east view across the injection zone. As shown, maximum vertical displacement of less than 0.0085 m (0.028 ft) and 0.039 m (0.13 ft) can be observed for both cases, Var-1 & Var-3, respectively. At the surface, a small uplift can be seen with a maximum vertical displacement of 0.0073 m (0.024 ft) and 0.03353 m (0.11 ft) for cases Var-1 and Var-3, respectively, (see Figure 148 and Figure 149). Generally, a bit higher value for displacement was induced in case Var-3 due to a higher pressure distribution across the injection point.

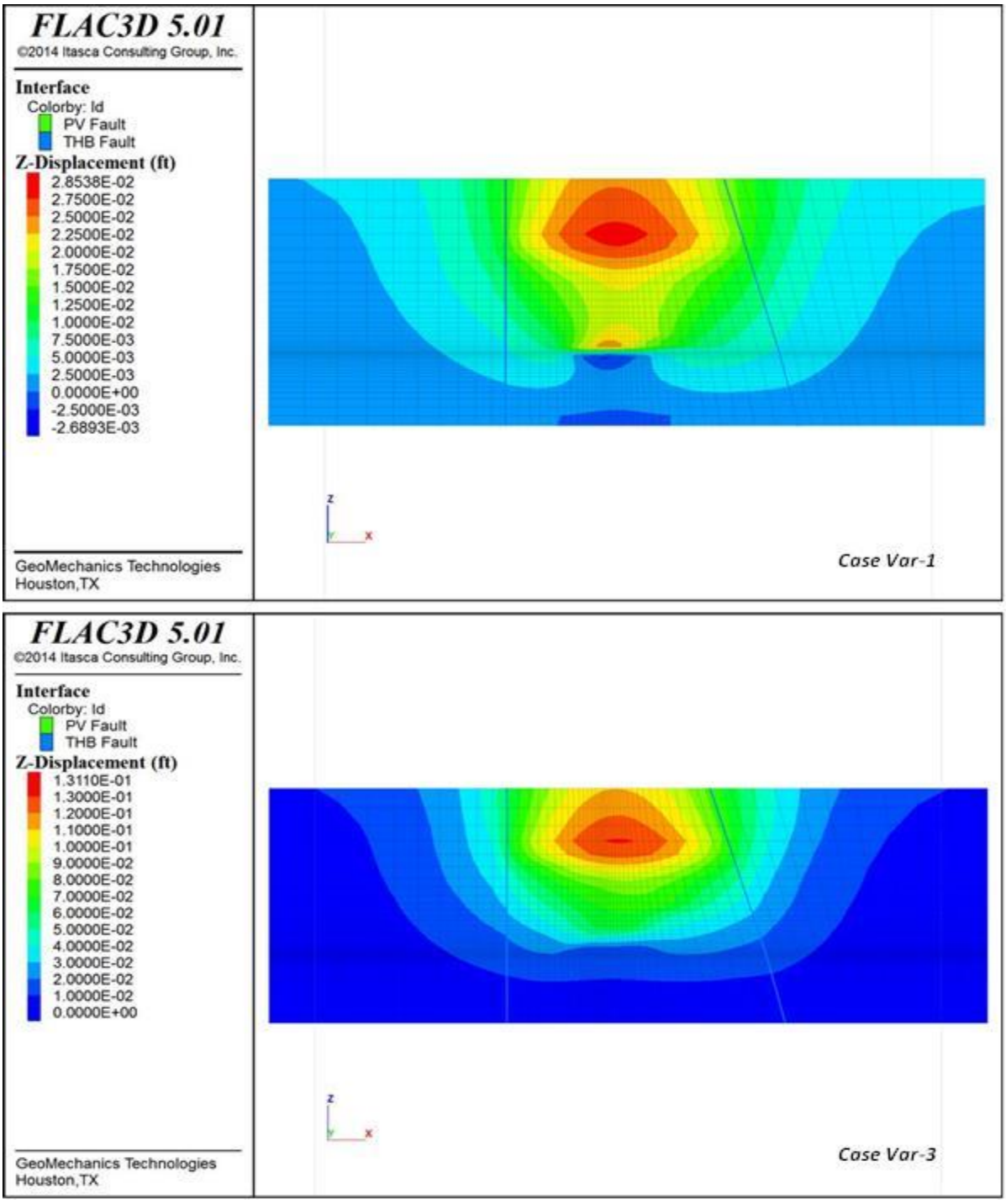

Figure 147: West-east view of induced Z-displacement across injection zone

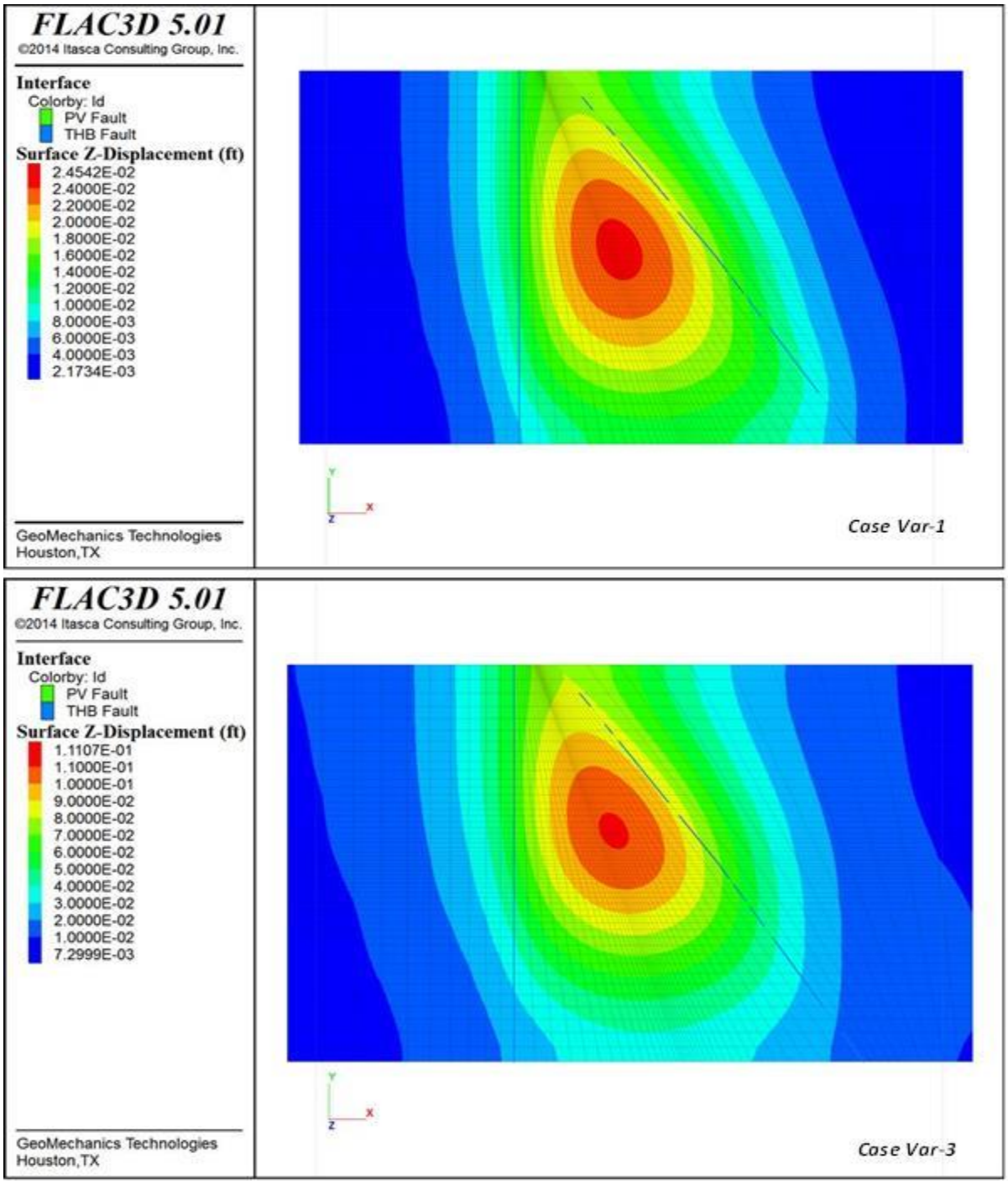

Figure 148: Plan view of induced Z-displacement at the surface

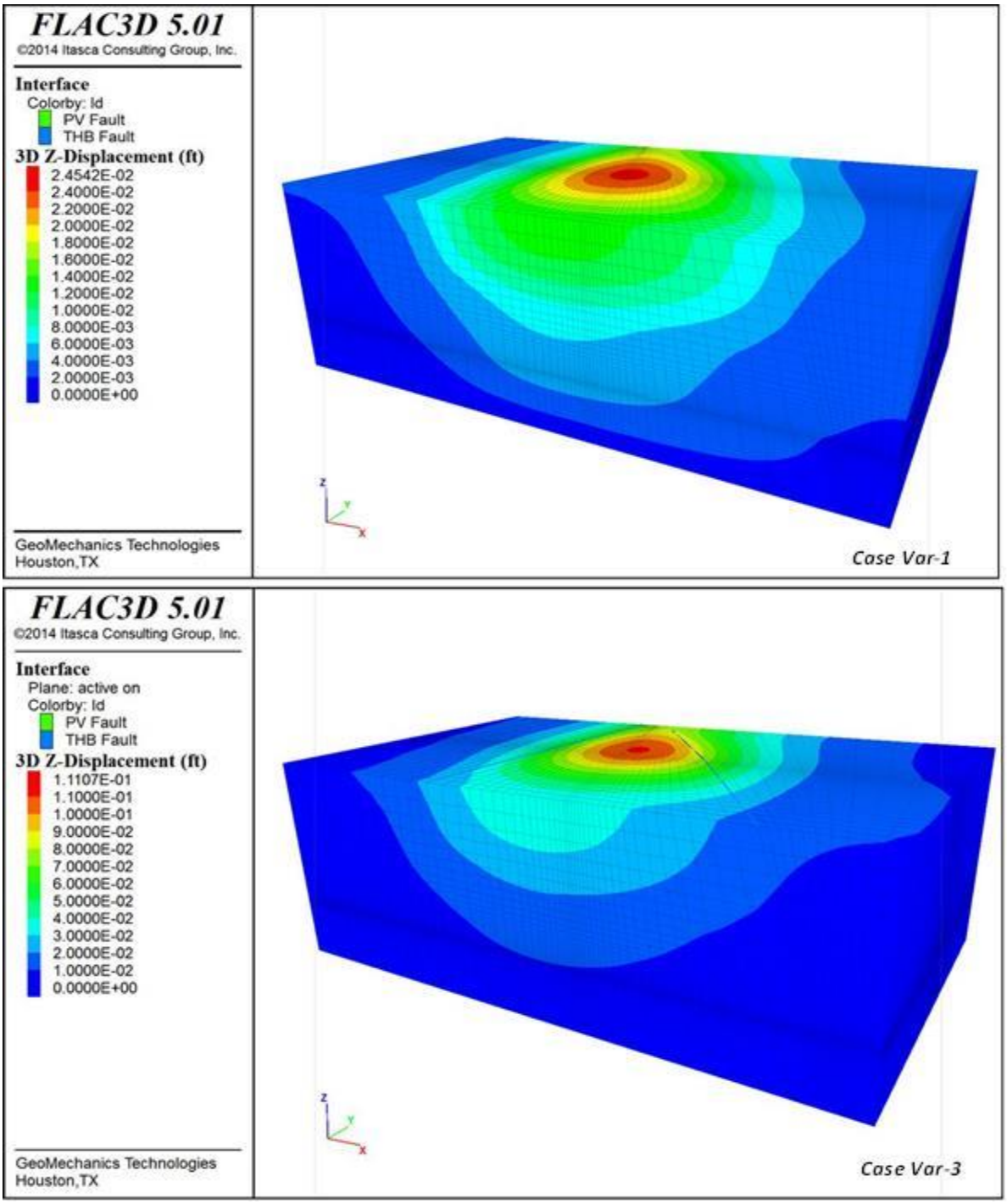

Figure 149: 3D view of induced Z-displacement

For fault reactivation analysis, interfaces were modeled in Flac3D based on Coulomb sliding criteria. Each interface is represented as a collection of triangular elements (interface elements), each of which is defined by three nodes, so called 'interface nodes.' During each time step, the absolute normal penetration and the relative shear velocity are calculated for each interface node and its contacting target face. Both of these values are then used by the interface constitutive model to calculate a normal force and a shear-force vector. The behavior of the interface is defined by the friction, cohesion, and stiffness. The Coulomb shear-strength criterion limits the shear force by the following relationship (Itasca, 2013):

$$F_{s\max} = cA + \tan\phi\,(F_n - pA)$$

Where:
Fsmax is the maximum shear force
Fn is the normal force
c is the cohesion along the interface;
ϕ is the friction angle of the interface surface
p is the pore pressure
A is the representative area associated with the interface node

Base on this equation, slipping takes place on the interface when the shear force exceeds the maximum limit defined by the Coulomb shear-strength criterion. Figure 150 shows the interface shear slip for both cases Var-1 and Var-3. No fault slip is observed, even with the most conservative fault property inputs (cohesions and friction angles), for either interface in either case, after 30 years of CO_2 injection.

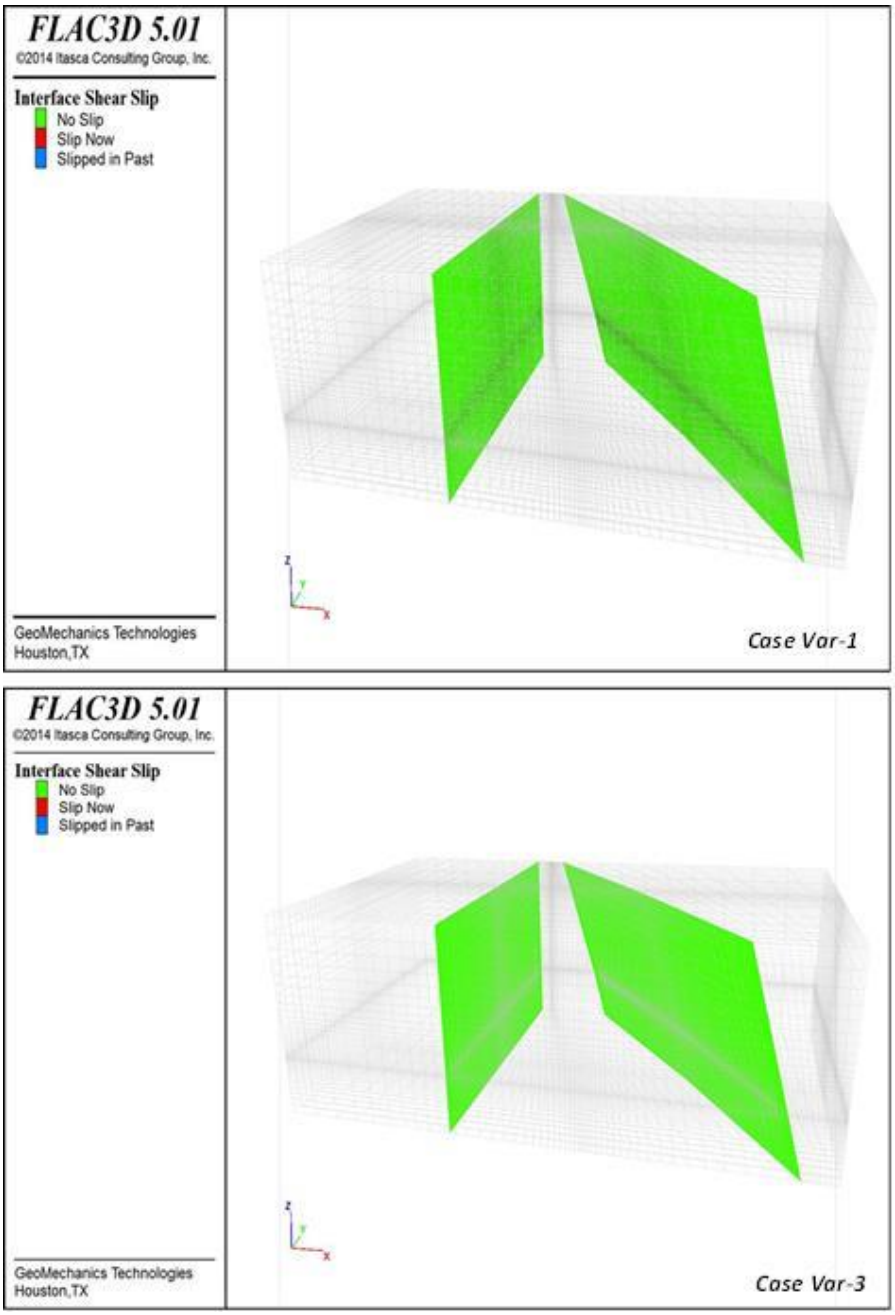

Figure 150: Interface shear slip after 30 years of CO_2 injection

Additionally, a sensitivity analysis was carried out to assess the mesh resolution, grid orientation, and boundary condition effects (*Appendix 4: Sensitivity Analysis for Northern Graben geomechanical model*).

9 Risk assessment and characterization

GeoMechanics has completed a comprehensive analysis of risks associated with CO_2 injection in the Wilmington Graben, including but not limited to the previously described issues of gas migration and geomechanical stress effects. The various risk factors evaluated and discussed here include:

1. Lateral Migration to Poorly Cemented Offset Wells
2. Caprock Integrity Analysis
3. Natural Seismicity Risks
4. Induced Seismicity Risks
5. CO_2 Migration to Sea Floor and resulting consequences

Risk is defined as the product of the probability of an event or outcome and the likely cost or consequences of that event or outcome. With regard to geologic sequestration, the baseline 'most likely' scenario is for a storage system to evolve as designed, with no leaks occurring. However, a project needs to also consider plausible CO_2 fluxes and areas that might be associated with CO_2 leakage and possible impact scenarios. The risks associated with CO_2 storage, although considered very low, increase once the CO_2 enters the geologic reservoir, its fate being transferred from mostly human control to a natural system (Kaldi et al, 2009). Numerical models are used to predict the movement and effects of injected CO_2, thus serving as tools for identifying and estimating the risk for different injection scenarios.

9.1 Lateral Migration from offset wells

One potentially serious problem associated with injection into mature sedimentary basins is the possible leakage of injected CO_2 through or along existing wells. Over long time scales, these wells may serve as short-circuit pathways for leakage, with possible contamination of shallow subsurface zones, and ultimate leakage back into the atmosphere. Leakage to the surface is a major concern in the onshore CO_2 storage context, most likely through high permeability conduits and in particular these abandoned or orphaned wells.

A number of possible leakage scenarios can materialize in abandoned wells (Figure 151). Besides those failures illustrated, leakage is also possible through completion equipment (packers, plugs and safety valves) and tubing hangers.

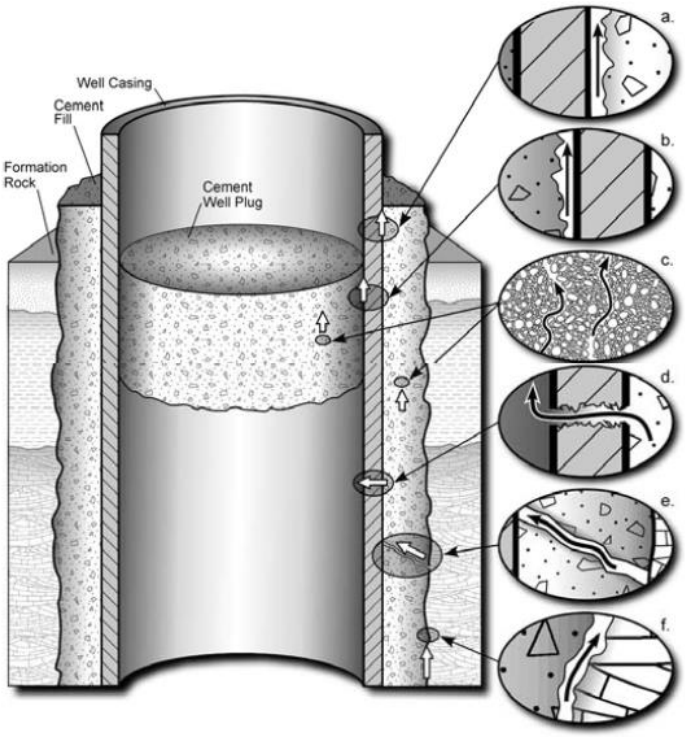

Figure 151: Generic Failure Modes for Well Integrity Under Exposure to CO_2 (Celia et al, 2005)

a: leakage between the cement and the outside of the casing
b: leakage between the cement and the inside of the metal casing
c: leakage within the cement plug
d: leakage through deterioration (corrosion) of the metal
e: leakage through deterioration of the cement in the
f: leakage in the annular region between the formation and the cement

9.1.1 Offset wells

When wells are adequately plugged and completed, it has been thought they trap CO_2 at depth effectively; however, large numbers of orphaned or abandoned wells may not be adequately plugged, completed, or cemented, and such wells represent potential leak points for CO_2 (Ide et al, 2006). Cementation data from each wellbore (12 total wells) within the graben were reviewed for any possible migration risks (Figure 152). The well data history indicated that at least six wells within the graben are not properly cemented, which may constitute risks for vertical gas migration. These 1960's exploratory wells (Chevron SP LA Harbor #2, Conoco SP S-4 and S-6, Mobil SP #11, Chevron 10R-34, and Exxon H10 R7) were not cased below the

surface casing. Well history was not available for two OCS wells (Shell OCS P-293-1 and Chevron OCS P293-9); therefore open-hole conditions were assumed. Only the 4 new wells (SFI #1, #2, DOE # 1 and #2) drilled in the northern graben during the 2000's are cased and cemented to surface. Figure 153 - Figure 162 are the well schematics for 10 of these wells.

Table 27: Federal offshore OCS wells

Well	Drill Date	TD (ft)
P293-1	1977	6825
P296-9	1977	8400

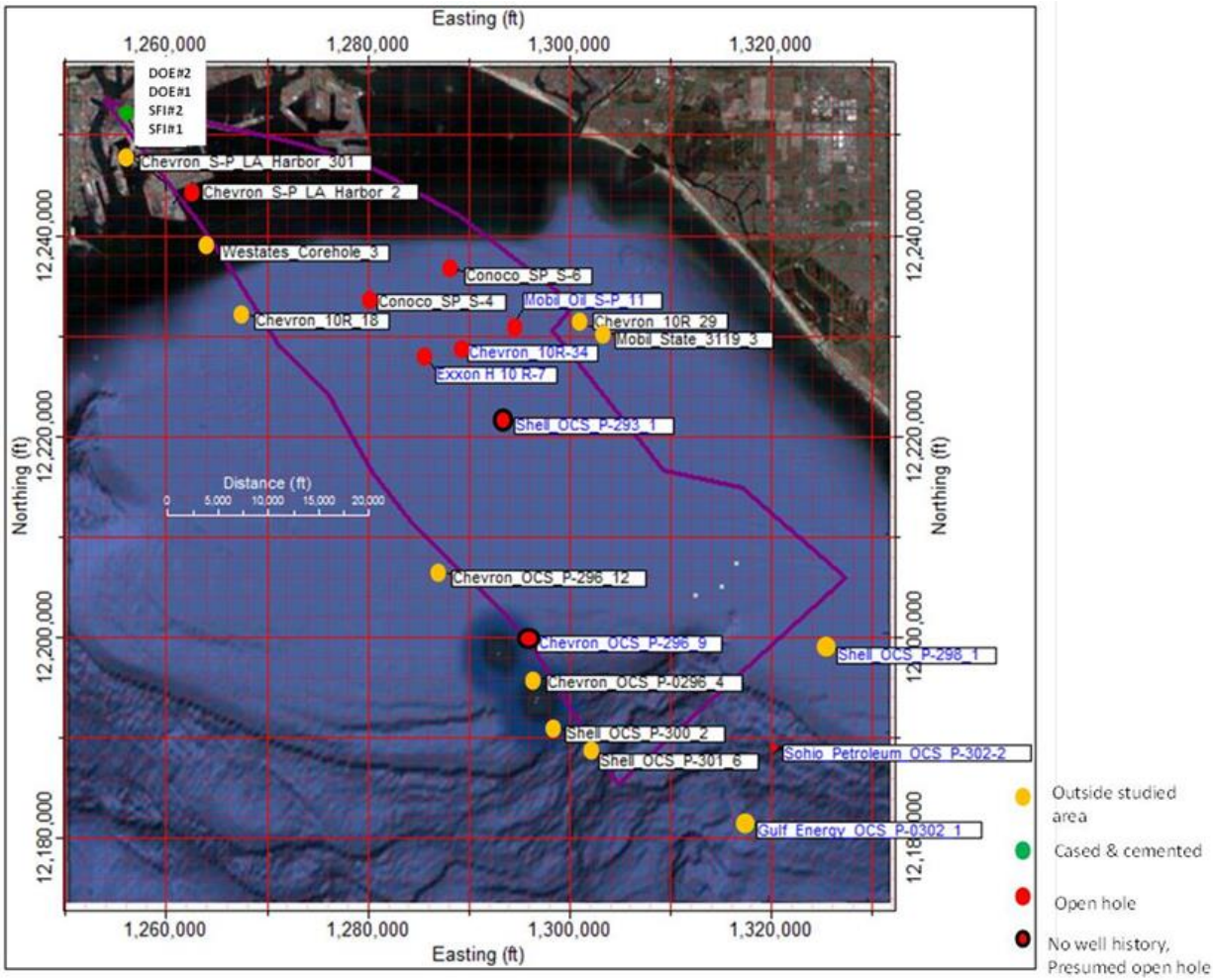

Figure 152: Casing and cement evaluation for previously drilled wellbores in the Wilmington Graben

Title: Characterization of Pliocene and Miocene Formations in the Wilmington Graben, Offshore Los Angeles, for Large-Scale Geologic Storage of CO_2

PI: Dr. Michael Bruno Final Report

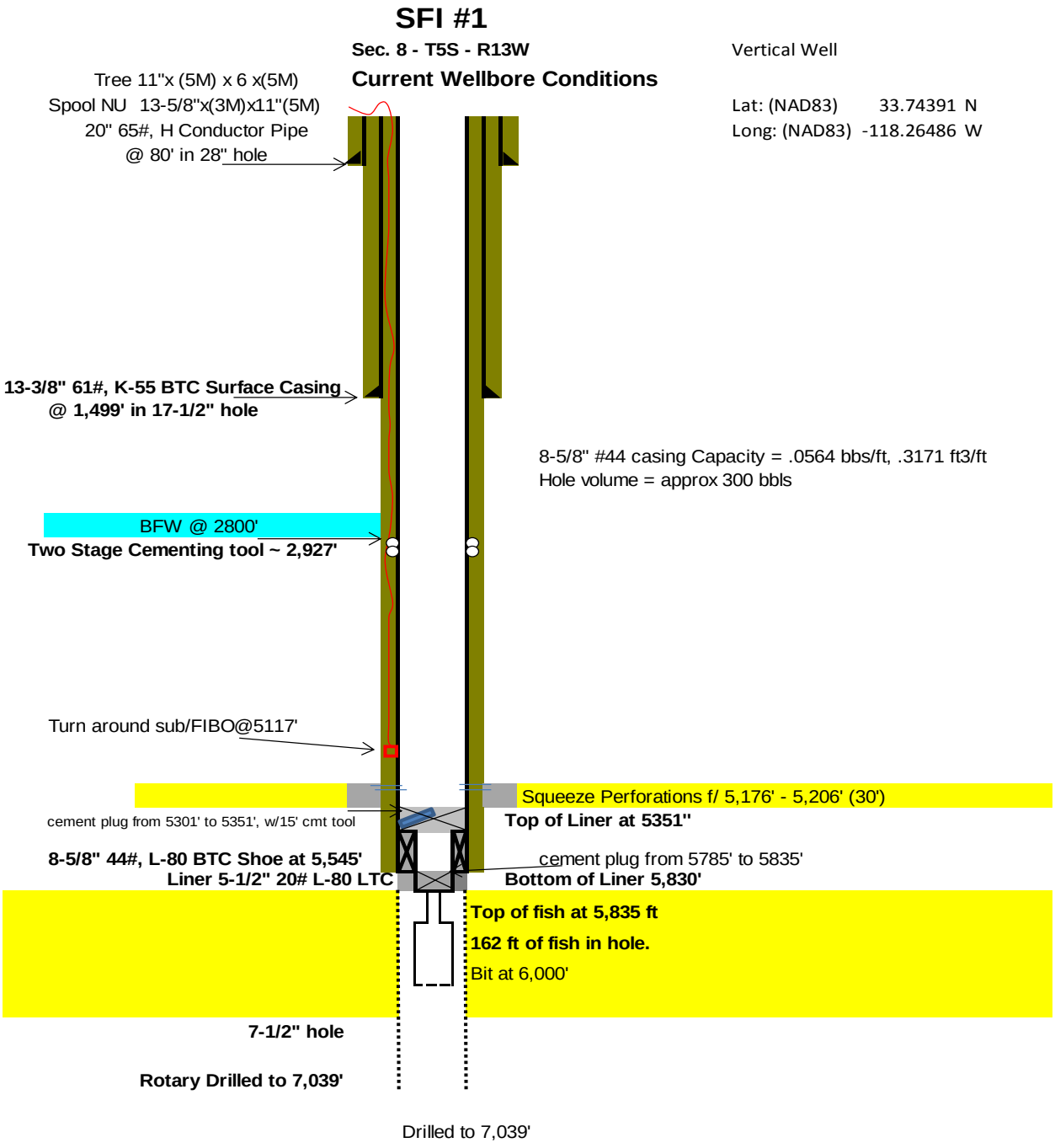

Figure 153: SFI#1 well schematic

Title: Characterization of Pliocene and Miocene Formations in the Wilmington Graben, Offshore Los Angeles, for Large-Scale Geologic Storage of CO_2

PI: Dr. Michael Bruno Final Report

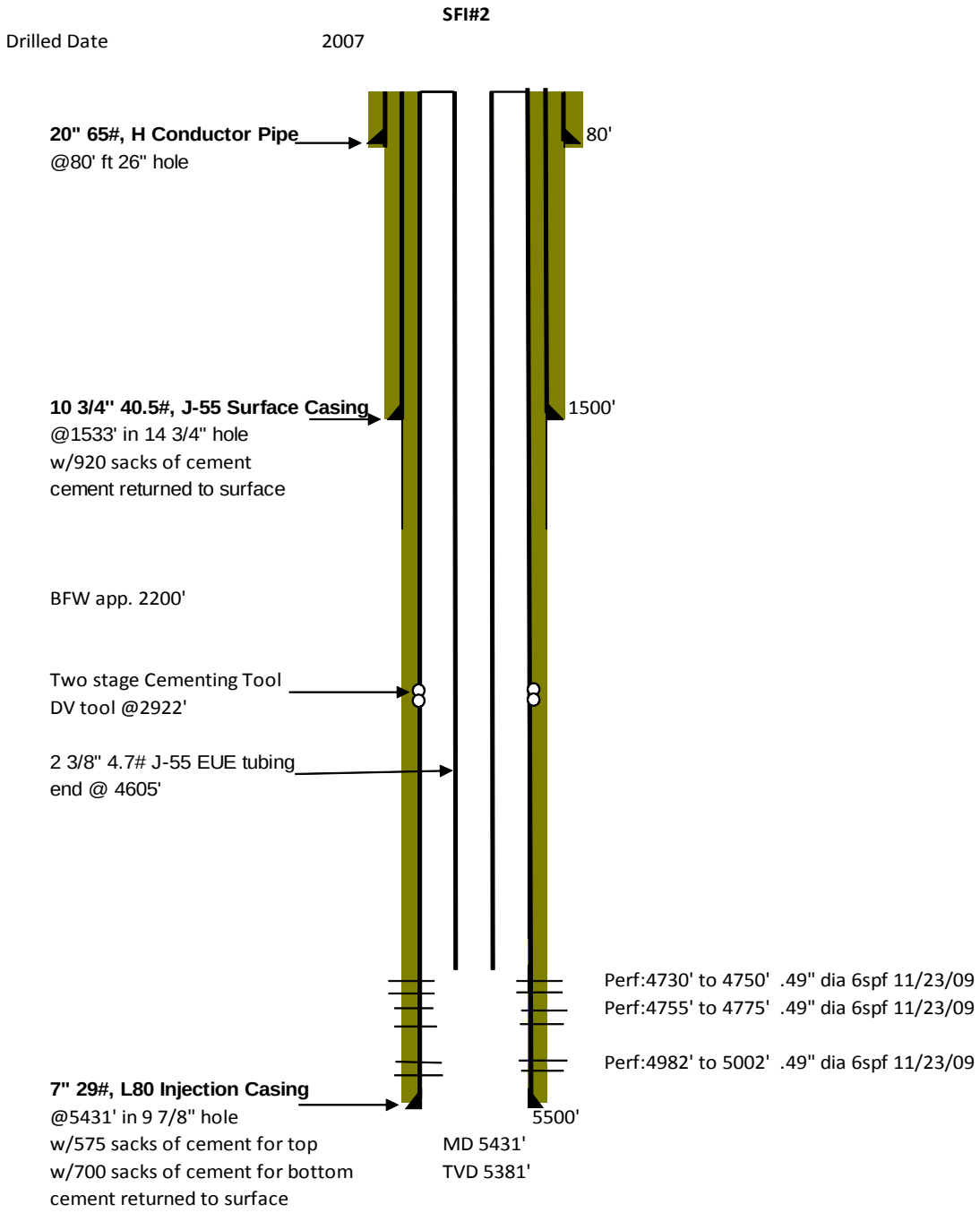

Figure 154: SFI#2 well schematic

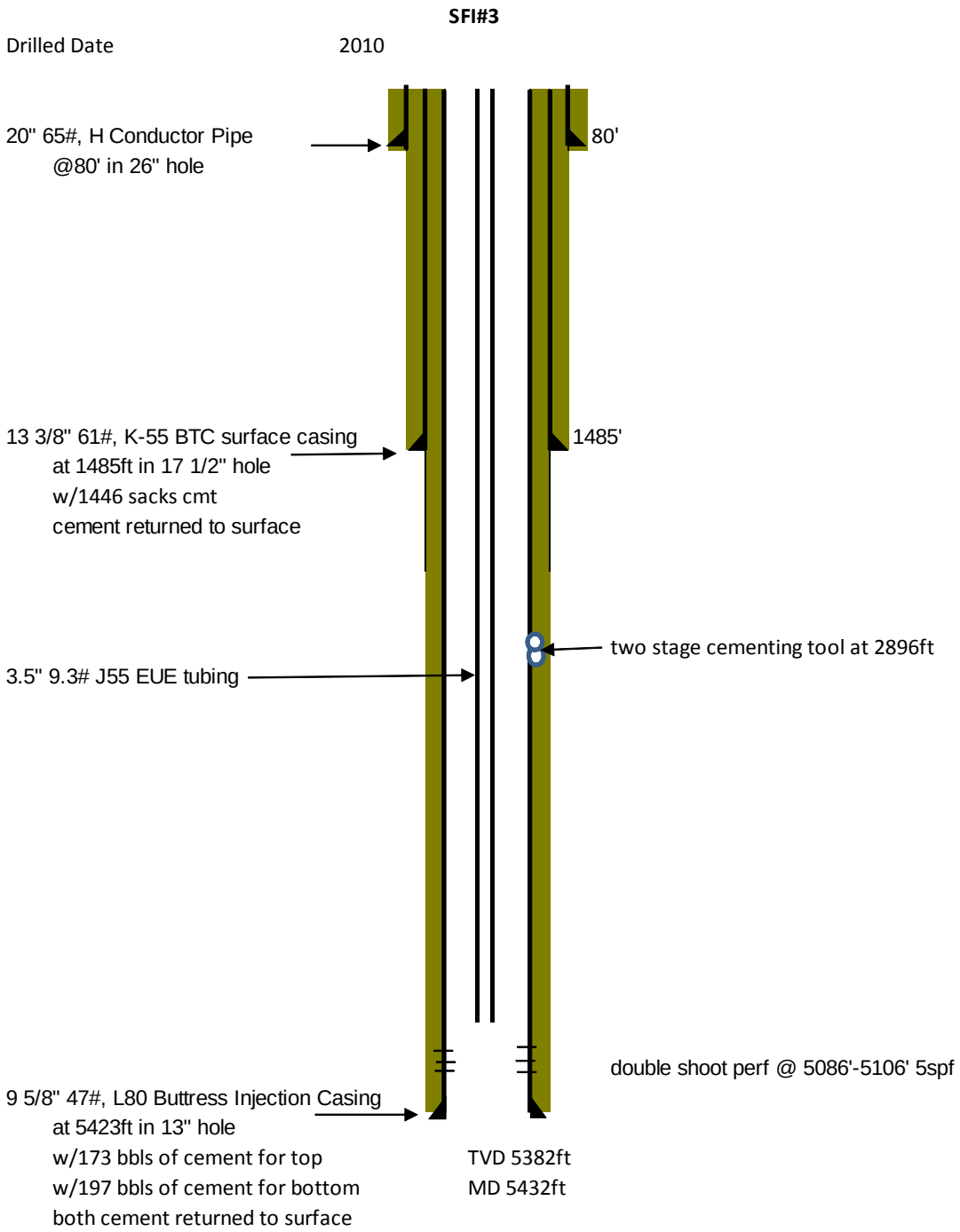

Figure 155: DOE#1 (aka SFI#3) well schematic

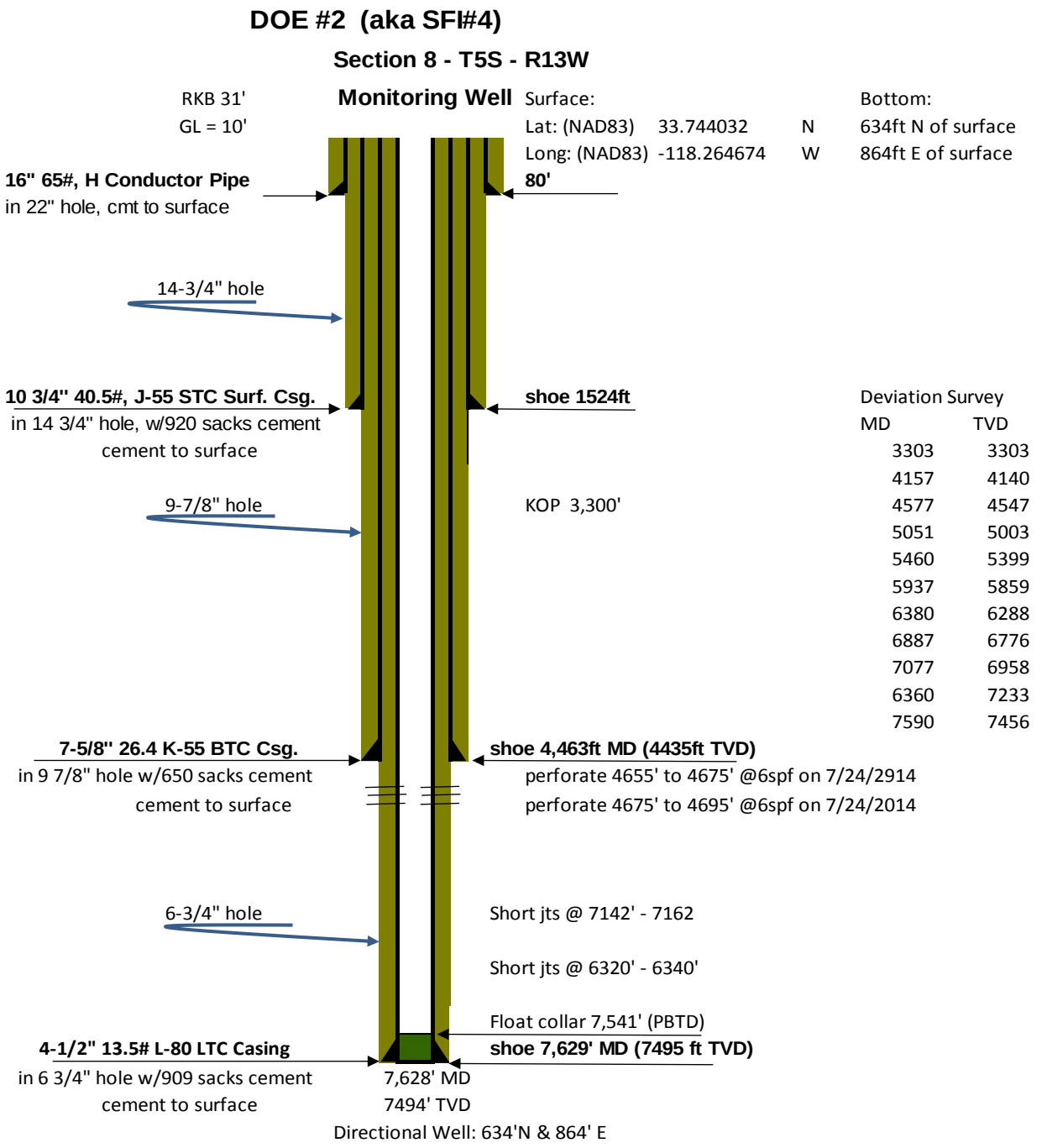

Figure 156: DOE#2 (aka SFI#4) well schematic

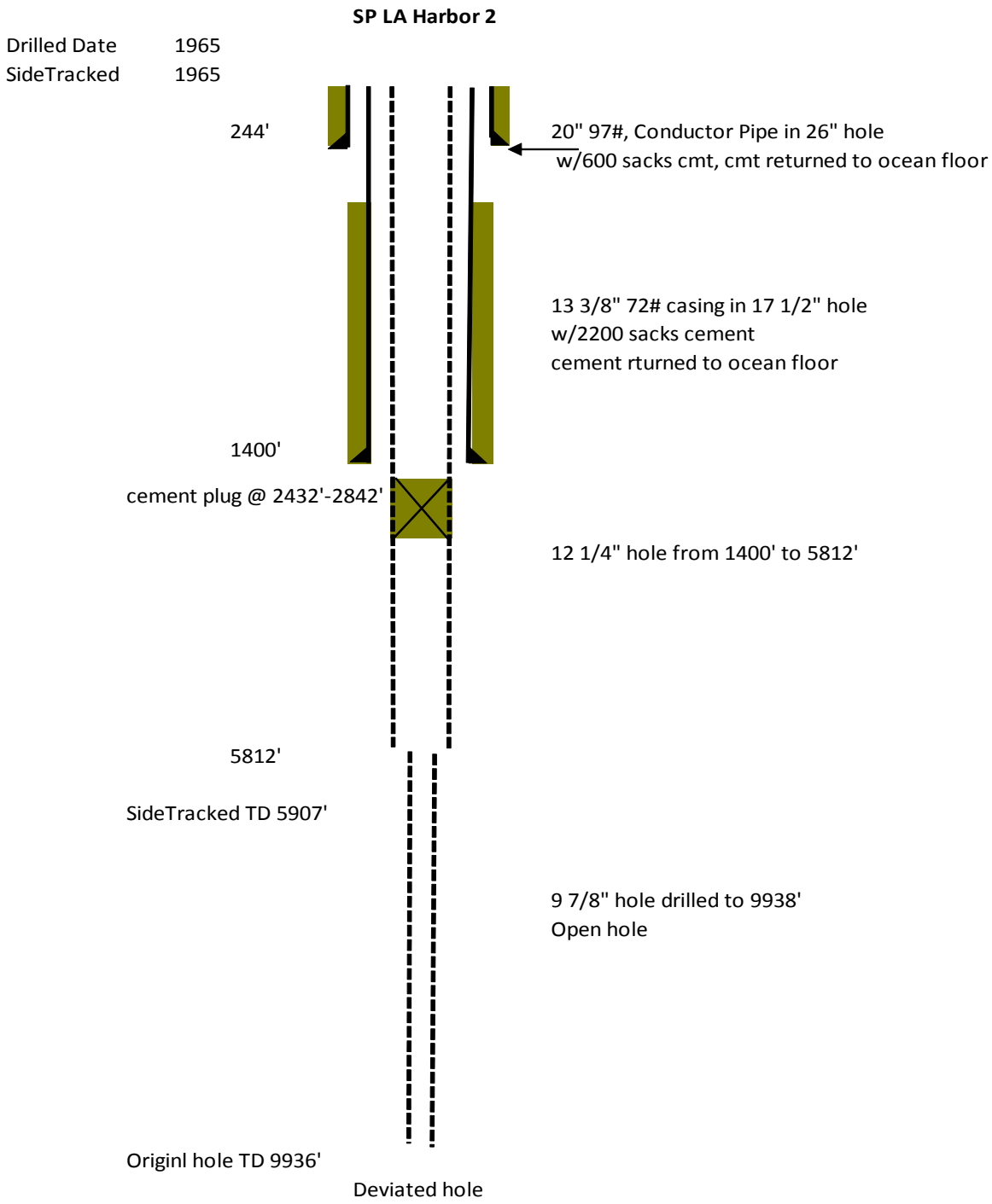

Figure 157: SP LA Harbor #2 well schematic

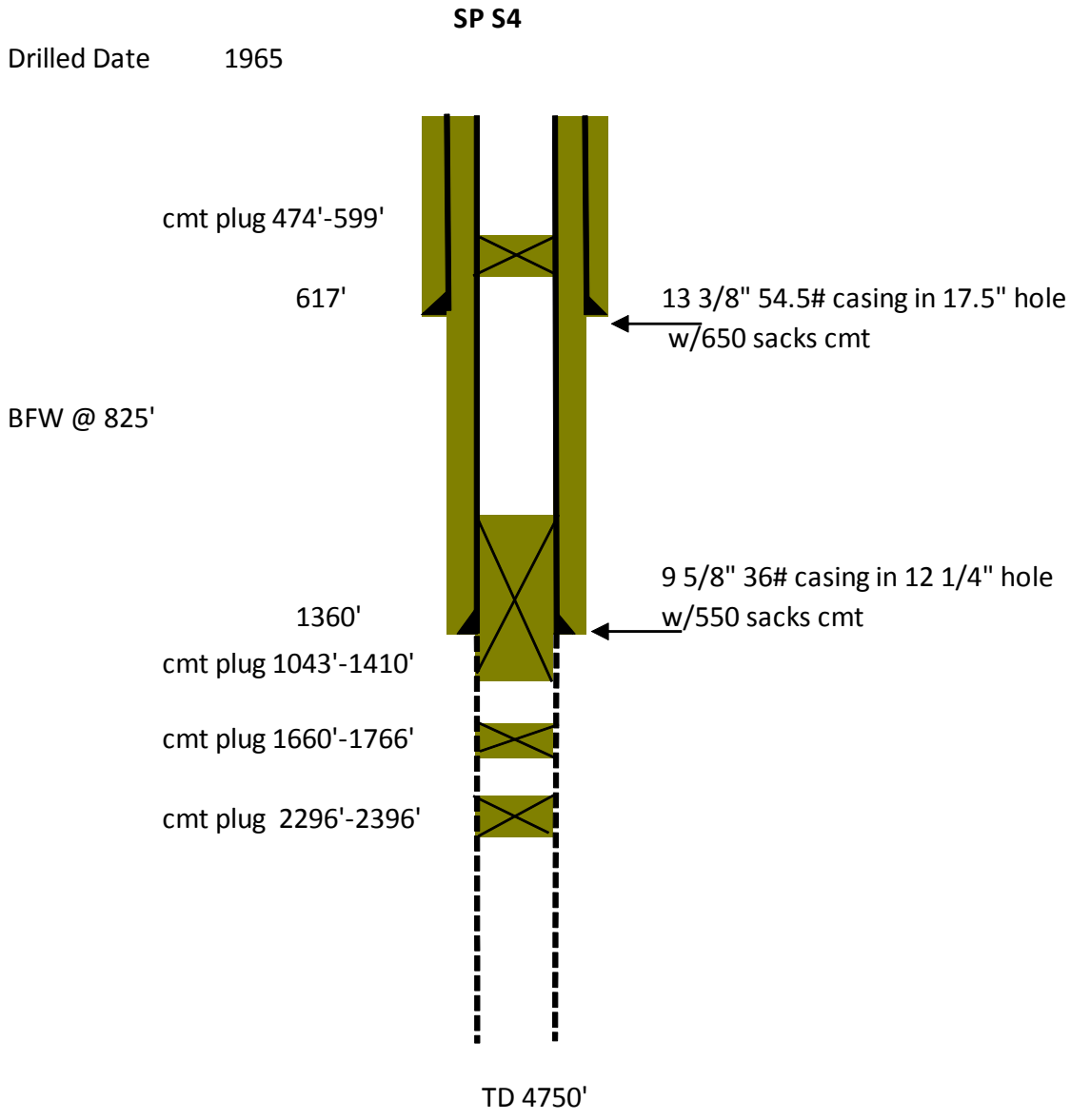

Figure 158: Conoco SP S-4 well schematic

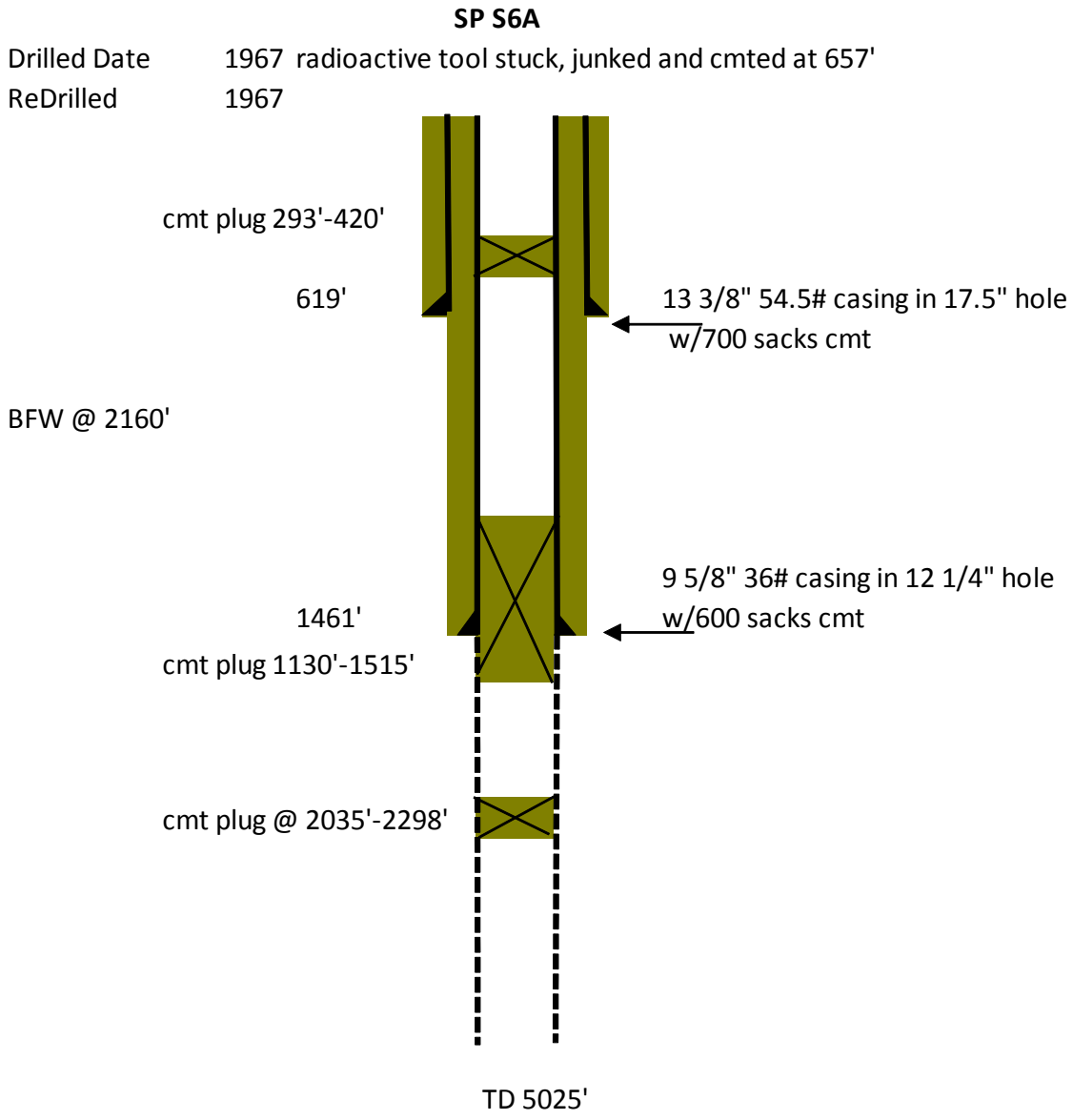

Figure 159: Conoco SP S-6 well schematic

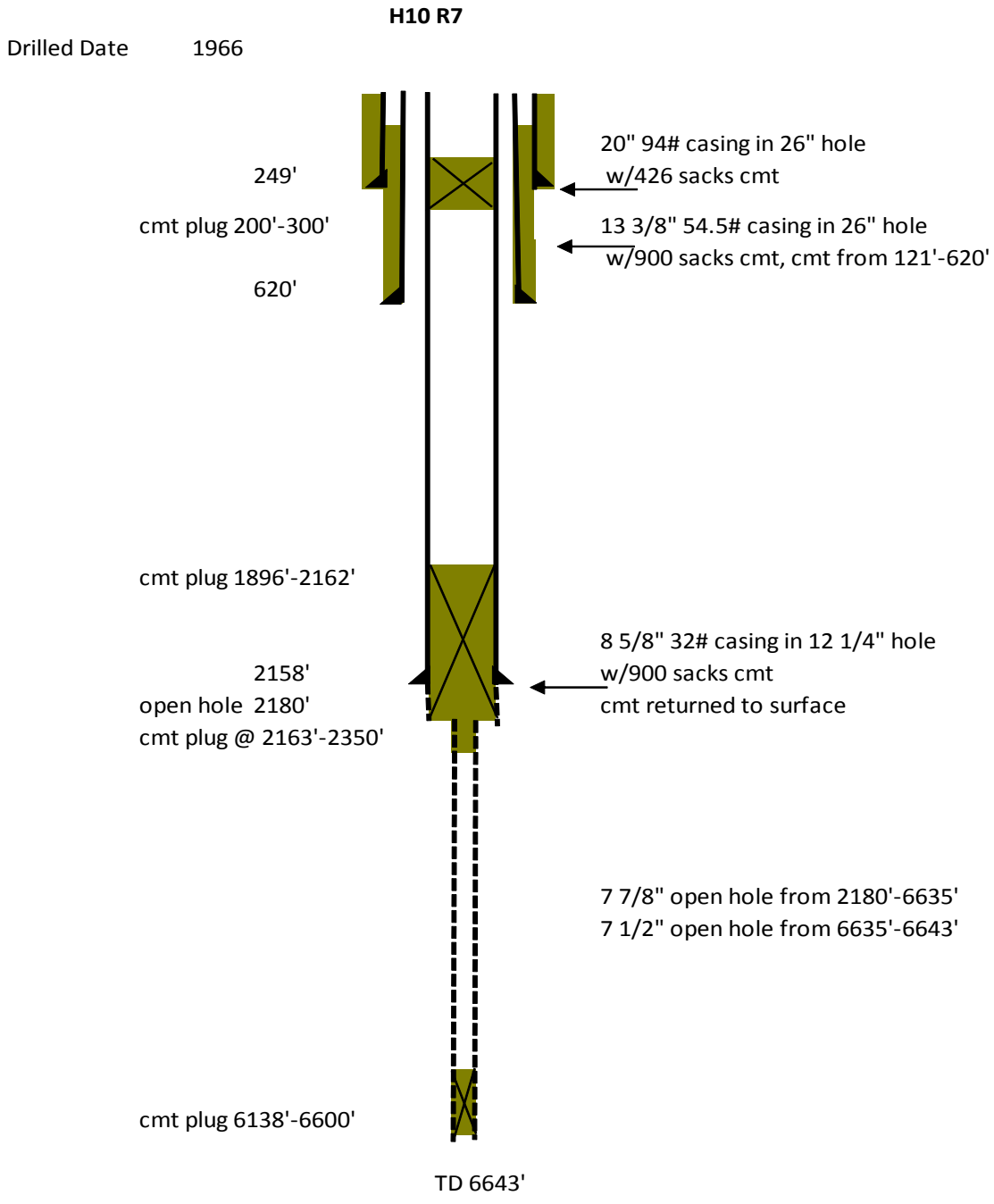

Figure 160: Chevron H10 R7 well schematic

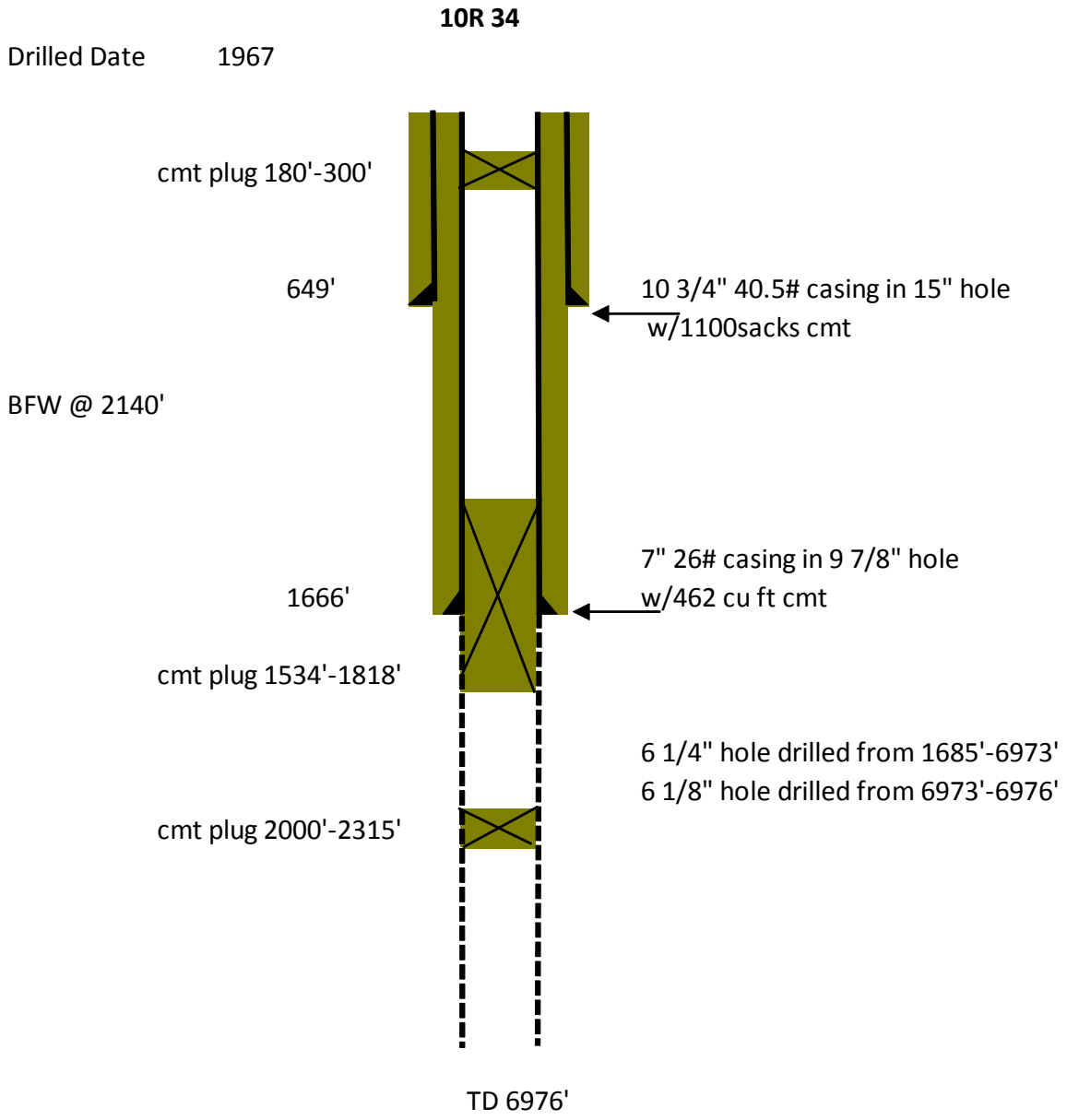

Figure 161: Exxon 10R 34 well schematic

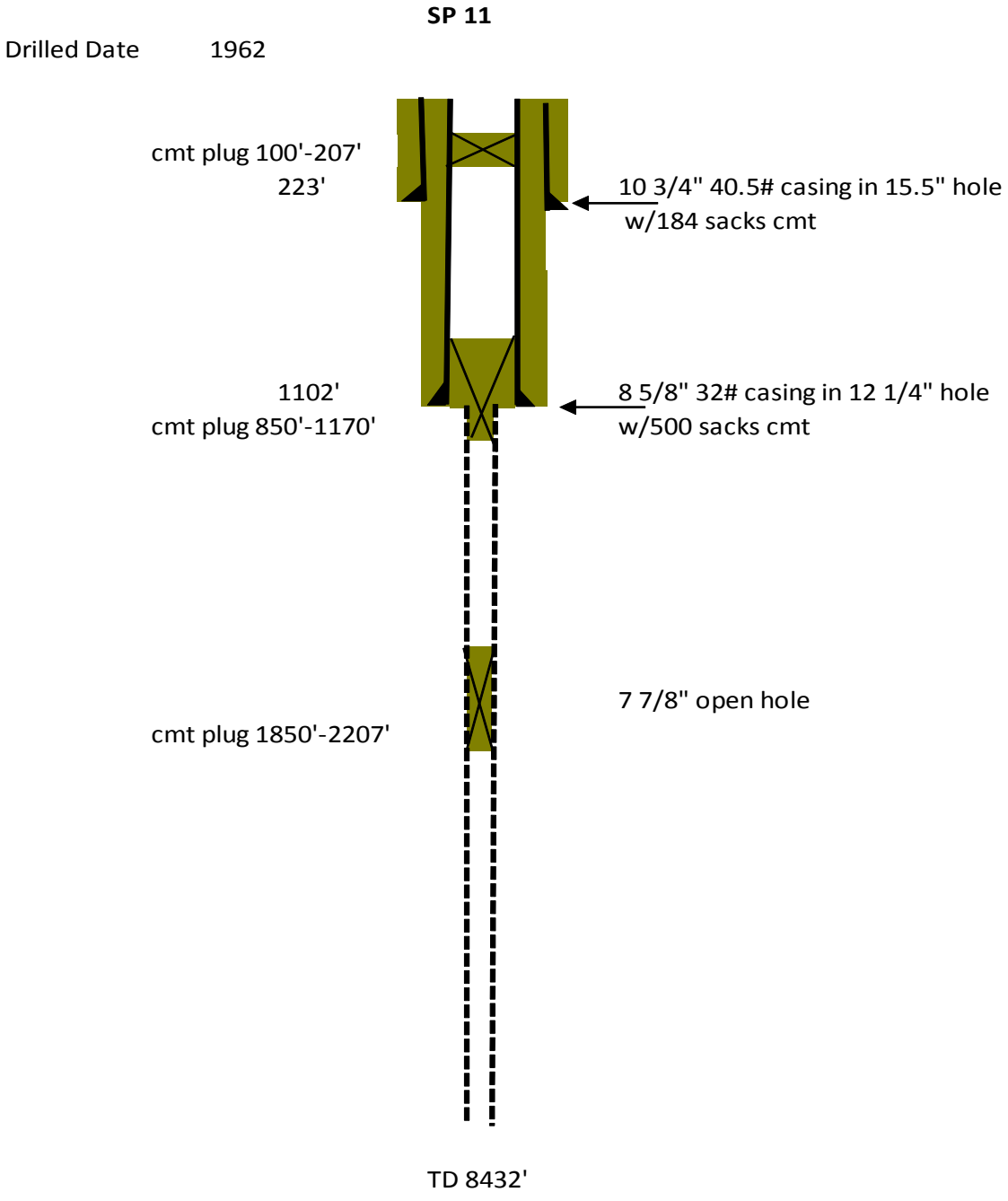

Figure 162: Mobil SP 11 well schematic

9.1.2 Lateral migration of CO_2 plume

The results of our fluid flow model indicate that the prospective CO_2 injection well should be placed a minimum distance of 1,609 m (1 mi) away from any known poorly cemented wellbores to prevent migration into unauthorized zones.

To assess the risk, our first step was to estimate the extent of the CO_2 plume. Using data gathered from logs of previously drilled wells in the graben, as well as interpreted seismic data, we developed a geologic characterization of the entire graben. To formulate a detailed model for numerical simulation, we chose a location with CCS-requisite lithology (caprock overlying reservoir), at requisite depths over 914 m (3000 ft) and sufficiently detailed data (presence of a well with log data). These criteria are met along the cross section including well Shell OCS P-293-1 (Figure 163).

Figure 163: Extent of Plume after 20 years of Injection and 20 Years of Observation.
Relative to Abandoned Exploration Wells (Shell OCS P-293-1 is Hypothetical Injection, White Circle is Plume Extent)

Using Tough2 simulation software, this model was run with 0.25 MMT/year injection of CO_2, followed by 20 years of post-injection observation. The CO_2 plume was projected to extend no further than 1000 m (3280 ft) in the lateral direction (SW of injection zone at 1555 m (5100 ft) SSL for well Shell OCS P-293-1), see Figure 164 and Figure 165.

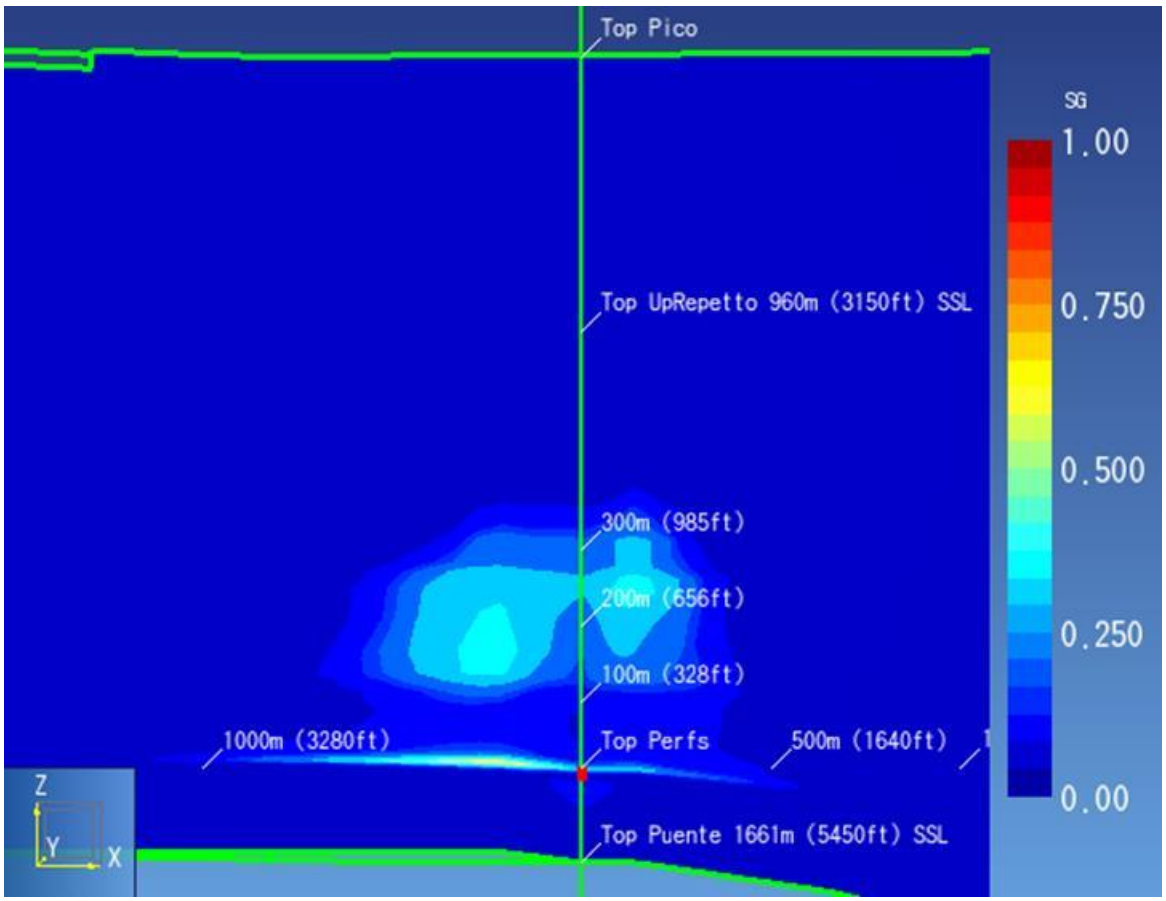

Figure 164: Gas Saturation after 40 Years (20 Years Injection, 20 Years Observation) – Plane in NE-SW Direction of Wilmington Graben (Parallel to *x*-axis of Model) – 2xVE

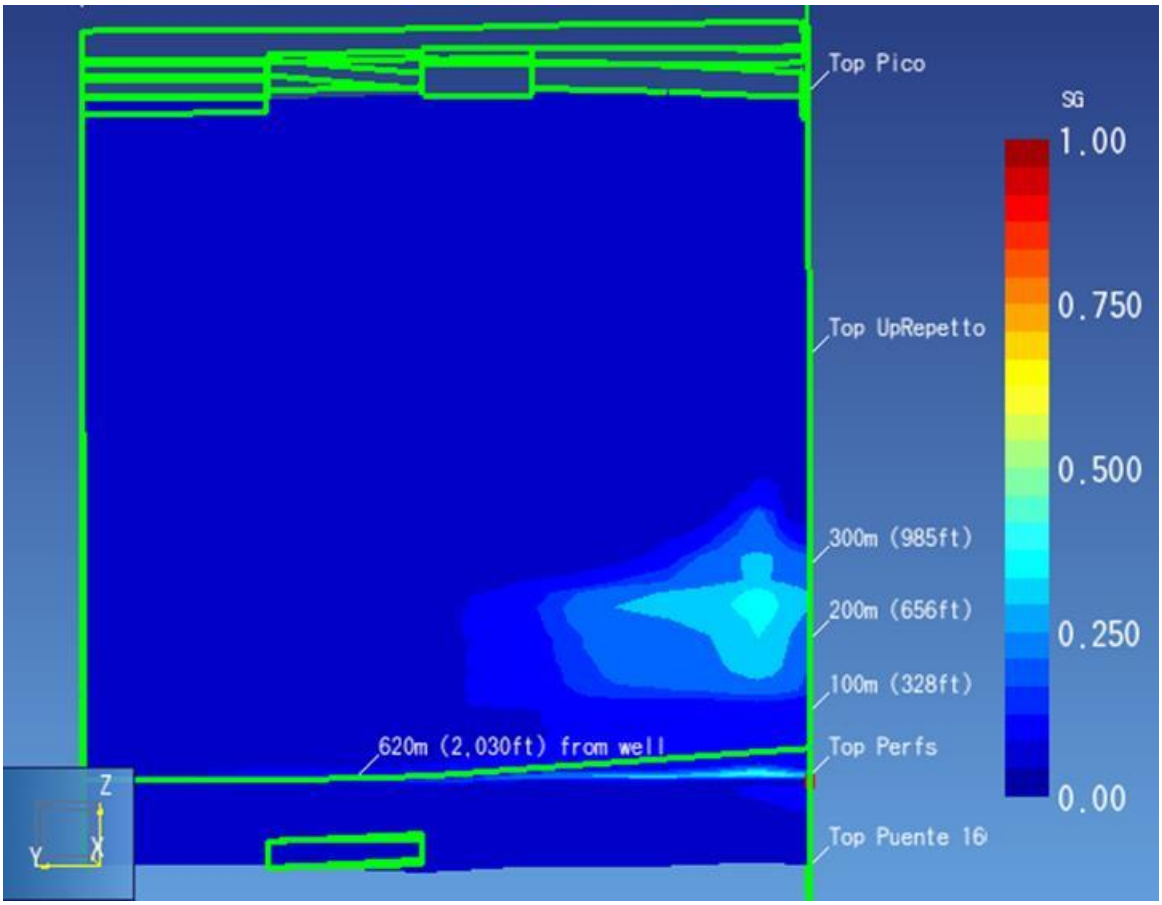

Figure 165: Gas Saturation after 40 Years (20 Years Injection, 20 Years Observation) – Plane in NW-SE Direction of Wilmington Graben (Parallel to y-direction of Model)) – green lines mark outer boundaries of model projected onto the cross section.

Conservatively, the CO_2 gas plume remains within a 1-mile radius of injection, which, at our chosen hypothetical location of injection, precludes it from intersecting any other wellbores in the graben (Figure 163).

9.2 Caprock Integrity Analysis

We have developed a Quantitative Risk & Decision Analysis Tool (QRDAT) for caprock integrity evaluation, with the aim of assessing the potential for leakage during CO_2 injection. For this purpose we have established a set of parameters (risk factors) that influence the likelihood of caprock failure. We established order of magnitude value ranges for each parameter, which,

when applied to particular geologic and operational settings, enable quantification of risk and offer a means by which to compare potential and active storage sites.

We consider three primary leakage mechanisms. These are tensile fracturing of the caprock, fault activation, and well damage. The set of risk factors can be divided into three main groups:

1. Mechanical state of the storage system, which includes stresses, pressures and faults;
2. Caprock and storage zone system, including reservoir and caprock geometry and properties; and
3. Operations, which include the status of the wells and injection practices.

The process of applying QRDAT for caprock integrity evaluation has been discussed in detail in Geomechanics Technologies' *Development of Improved Caprock Integrity and Risk Assessment Techniques* (2014), a report submitted to the DOE for a different grant and project, and will not be repeated here.

Table 28 shows the ranges for separate risk factors considered, and Figure 166 to Figure 168 summarize the Mechanical State Factors, Caprock-Storage Zone System Factors and Operation Risk Factors used to perform the caprock integrity evaluation.

Table 28: Risk factor value ranges in current QRDAT version

Risk factor	Risk factor value ranges		
	High risk	**Moderate risk**	**Low risk**
Lateral extension of the storage zone/formation depth	<25	25-100	>100
Storage zone thickness/storage zone depth	> 0.5	0.1-0.5	< 0.1
Stress regime	Compressional	Transform	Extensional
Caprock strength	Weak	Moderate	Strong
Caprock thickness	≤ 3 m	3-30 m	≥ 30 m
Fault boundaries	Multiple	One	None
Natural seismicity	High	Moderate	Low
Number of caprocks	No	One	Multiple
Maximum formation pressure/formation depth	≥ 0.75	0.625-0.75	≤ 0.625
Desired maximum formation pressure/discovery pressure	≥ 1.5	1.25-1.5	≤ 1.25
Well density	> 15	5-15	< 5
Number of uncased wells/total number of wells	> 0.6	0.2-0.6	< 0.2
Temperature difference between the injected CO_2 and the ambient storage zone temperature	≥ 60 ◦C	30-60 ◦C	≤ 30 ◦C
Caprock heterogeneity	Significant	Moderate	Strong
Caprock permeability	> 10^{-15} m^2	10^{-18}-10^{-15} m^2	< 10^{-18} m^2
Caprock lateral extend/storage zone thickness	<25	25-100	>100
Caprock dip	≥ 8°	2°-8°	≤ 2°
Minimum horizontal stress/vertical stress (stress ratio)	<0.55	0.55-0.65	>0.65

MECHANICAL STATE						
	tens frac		fault reac		well fail	
1. STRESS						
Max P/min princ stress						
a. ≥ 0,75	0	100	0	100	0	100
b. 0,5-0,75	1	10	1	10	1	10
c. ≤ 0,5	0	1	0	1	0	1
Stress regime						
a. Compressional	1	100	1	100	1	100
b. Transform	0	10	0	10	0	10
c. Extensional	0	1	0	1	0	1
Shmin/Sv						
a. < 0.55	0	1	0	100	0	100
b. 0.55-0.65	0	1	0	10	0	10
c. > 0.65	1	1	1	1	1	1
2. PRESSURE						
Desired Max P/Discovery P						
a. ≥ 1.5	0	100	0	100	0	100
b. 1.25-1.5	0	10	0	10	0	10
c. ≤ 1.25	1	1	1	1	1	1
Max P/formation depth						
a. ≥ 0.75	0	100	0	100	0	100
b. 0.625-0.75	0	10	0	10	0	10
c. ≤ 0.625	1	1	1	1	1	1
3. FAULTS						
Fault boundaries						
a. Multiple bounding faults	1	1	1	100	1	100
b. One bounding fault	0	1	0	10	0	10
c. None	0	1	0	1	0	1
Natural seismicity						
a. High	1	100	1	100	1	100
b. Moderate	0	10	0	10	0	10
c. Low	0	1	0	1	0	1

Figure 166: Mechanical state risk factors and ranges included in risk assessment tool

CAPROCK-STORAGE ZONE SYSTEM	tens frac		fault reac		well fail	
4. STORAGE ZONE SPECIFIC						
Lateral extent/storage zone depth						
a. <25	1	100	1	100	1	100
b. 25-100	0	10	0	10	0	10
c. >100	0	1	0	1	0	1
Storage zone thickness/storage zone depth						
a. > 0.5	0	100	0	100	0	1
b. 0.1-0.5	0	10	0	10	0	1
c. < 0.1	1	1	1	1	1	1
5. CAPROCK SPECIFIC						
Caprock heterogeneity						
a. Significant	1	100	1	100	1	1
b. Moderate	0	10	0	10	0	1
c. Low	0	1	0	1	0	1
Caprock strength						
a. Weak	0	100	0	100	0	100
b. Moderate	1	10	1	10	1	10
c. Strong	0	1	0	1	0	1
Caprock thickness						
a. ≤ 3m	0	100	0	100	0	1
b. 3-30 m	1	10	1	10	1	1
c. ≥ 30 m	0	1	0	1	0	1
Caprock lateral extent/caprock thickness						
a. <25	1	100	1	100	1	100
b. 25-100	0	10	0	10	0	10
c. >100	0	1	0	1	0	1
Caprock permeability						
a. k > 1E-15 m2	0	100	0	1	0	1
b. 1E-18 m2 ≤ k ≤ 1E-15 m2	1	10	1	1	1	1
c. k < 1E-18 m2	0	1	0	1	0	1
Number of caprocks						
a. Single	0	100	0	100	0	100
b. Double	0	10	0	10	0	10
c. Multiple	1	1	1	1	1	1
Caprock dip						
a. γ ≥ 8°	1	1	1	100	1	1
b. 2°≤γ≤8°	0	1	0	10	0	1
c. γ ≤ 2°	0	1	0	1	0	1

Figure 167: Caprock and storage zone risk factors and ranges included in risk assessment tool

OPERATIONS						
	tens frac		fault reac		well fail	
6. OPERATIONS						
Well density						
a. > 15 km-2	0	1	0	1	0	100
b. 5-15 km-2	0	1	0	1	0	10
c. < 5 km-2	1	1	1	1	1	1
No. of uncased wells/total no. of wells						
a. > 0.6	0	1	0	1	0	100
b. 0.2-0.6	0	1	0	1	0	10
c. < 0.2	1	1	1	1	1	1
ΔT between CO2 and storage zone						
a. ≥ 60 °C	0	100	0	100	0	1
b. 30 °C - 60 °C	1	10	1	10	1	1
c. ≤ 30 °C	0	1	0	1	0	1

Figure 168: Operating parameters risk factors and ranges included in risk assessment tool

Table 29 and Table 30 compare the Wilmington Graben's relative risk score to that of operational injection projects present and past, Sleipner and In Salah, respectively, using QRDAT. The Wilmington Graben scored 1839, relatively high compared to In Salah's 444 and Sleipner's 453.

Table 29: The relative risk ranking based on three types of risk factors

Category	Range of risk scores	Wilmington Graben	Sleipner	In Salah
Mechanical state	21-1902	840	102	390
Caprock-Storage Zone system	27-2007	972	342	27
Operations	9-405	27	9	27
TOTAL	57-4314	1839	453	444

Table 30: The relative risk ranking based on failure type

Category	Range of risk scores	Wilmington Graben	Sleipner	In Salah
Tensile fracturing	19-1405	559	154	145
Fault (re)activation	19-1603	748	154	154
Wellbore failure	19-1306	532	145	145
TOTAL	57-4314	1839	453	444

9.3 Natural Seismicity Risks

The Southern California area is seismically active, with historically strong ground motion throughout the basin. The Southern California area is also a very prolific oil and gas producing region, with more than 100 years of production (and associated injection operations) from more than 50 medium to very large scale oil and gas fields. There are more than 24,000 deep production and injection wells in Los Angeles and Orange Counties, including more than 1000 wells within and a few miles of the Wilmington Graben. These existing wells have experienced decades of seismic activity with no dangerous release of gas to the surface during or following earthquakes. This is primarily due to the fact that metal casings on wells merely deform slightly under seismic strains, rather than break.

Wells that would be drilled for a CO_2 injection project would be new wells, designed and constructed according to higher standards than existing wells in the area, with more extensive and more sophisticated monitoring than any of these existing wells. Thus, although the area is seismically active, there is no reason to suggest that seismicity will damage the injection wells and cause a dangerous release of fluids or gas to the surface. Again, this conclusion is based on:

1) almost 100 years of historical data demonstrating the safe coexistence of oil and gas wells in this seismically active zone;
2) higher standards of design and construction for more modern CO_2 injection wells; and,
3) more stringent monitoring and operational safeguards for this project than historically applied to other wells in the area.

9.3.1 Geological Conditions and Seismic History

Southern California is a seismically active area. Figure 169 shows seismic events greater than magnitude 4.0 that have occurred in southern California since 1910 and the surface traces of the major faults in the area (SCEC).

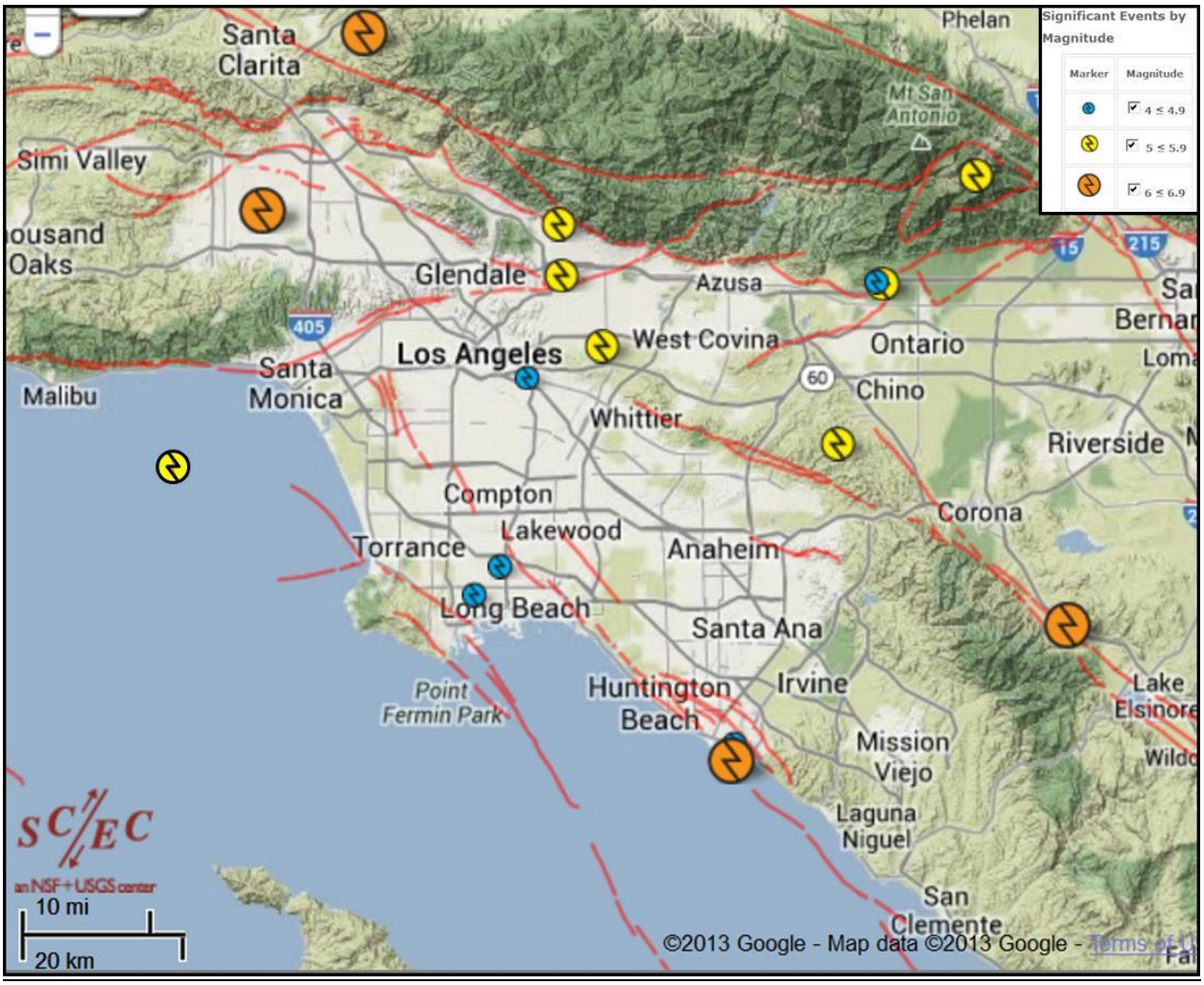

Figure 169: Earthquakes since 1910 (>4.0 Magnitude) & Significant Faults in Los Angeles Basin and Environs (SCEC)

Table 31 details those seismic events considered 'major,' i.e., greater than magnitude 5.0. Notice that major earthquakes in southern California occur in deep (>7620 km (>25,000 ft)),

brittle basement rock, and the shallower (3048 m (<10,000 ft)), soft sediments penetrated by wells are less affected by deformation.

Table 31: Major earthquakes (>5.0 magnitude, >6.0 in bold) in the Los Angeles Basin

Name	Date	Magnitude	Depth (ft)	fault/Location
Elsinor	**May-10**	**6**		**Elsinor/35 mi east of graben**
Long Beach	**Mar-33**	**6.4**	**33-39,000**	**Elsinore/35 miles east of graben**
Lytle Creek	Sep-70	5.2	29,525	San Jacinto?/40 miles northeast of graben
San Fernando/Sylmar	**Feb-71**	**6.6**	**27,550**	**San Fernando/ 45 miles north of graben**
Malibu	Jan-79	5.2	37,000	Anacapa-Dume/25 northwest of graben
Whittier Narrows	Oct-87	5.9	31,175	Puente Hills/ approximately 20 miles north of graben
Pasadena	Dec-88	5	51,175	Raymond/25 miles north of graben
Upland	Feb-90	5.5	25,925	San Jose/30 miles northeast of graben
Sierra Madre	Jun-91	5.8	39,375	Sierra Madre/30 miles north of graben
Northridge	**Jan-94**	**6.7**	**60,375**	**Northridge (Pico)/35 miles northwest of graben**
Chino Hills	Jul-08	5.5	47,500	Yorba Linda Trend/25 miles northeast of graben

(SCEC)

The CO_2 injection wells would not penetrate deep basement schist rocks, where major earthquakes are generated, as previously mentioned. In fact, all injection scenarios envisioned thus far would penetrate no deeper than 2743 m (9,000 ft), and the shallowest of the major earthquakes of the past century was sourced below 7620 m (25,000 ft).

The closest fault to the Wilmington Graben (apart from its defining faults) is the Newport-Inglewood fault (of which the THUMS-Huntington Beach fault is a splay), which lies just to the northeast (extending to the southeast). This is a right-lateral strike-slip fault "zone", consisting of a system of northwest-trending active strike-slip and oblique-slip faults, roughly parallel to the San Andreas Fault. The southern portion of the fault last moved in the 1933 Long Beach earthquake, magnitude 6.3, but there was no surface rupture. The estimated depth of this earthquake was approximately10 to 12 km (33,000 to 39,000 ft, Hauksson and Gross, 1991). The fault zone may include the THUMS-Huntington Beach fault, defining the northeast edge of the graben. This splay is deeply buried and does not appear to displace Holocene or Pleistocene strata. No activity on this fault has been recorded in the past 200 years, nor is there any evidence of activity in the past 100,000 years, but it is not well understood and future activity is not precluded (Port of Los Angeles).

Though the Newport-Inglewood fault zone is clearly active, evidence suggests that its splay that defines the northeast boundary of the Wilmington Graben, the THUMS-Huntington Beach fault, is most likely not. However, the graben's southwestern defining fault, the Palos

Verdes fault, is thought to have ruptured at some point in the past 15,000 years and is thought to have a current slip rate of 3mm/yr. Furthermore, currently the Palos Verdes fault is a vertical right slip fault, with a visible expression on the seabed and reaching to a depth of about 13,304 m (42,650 ft, CGS, 2002).

Concerning the seismic stability of surface facilities, data for the Wilmington Graben suggests that peak ground acceleration during an earthquake would be 60-80%g, with a 2% chance of exceedance in 50 years (potentially damaging, but with a recurrence rate of only every 2500 years, Figure 170), and less than 40%g, with a 10% chance of exceedance in 50 years (safe for a modern facility, and with a recurrence rate of every 500 years, Figure 171), based on USGS seismic hazard data. Using the USGS's Ground Motion Interpolater (http://www.quake.ca.gov/gmaps/PSHA/psha_interpolator.html), and inputting the coordinates for our current plant operations, values of 70.1%g and 37.2%g, respectively, are returned.

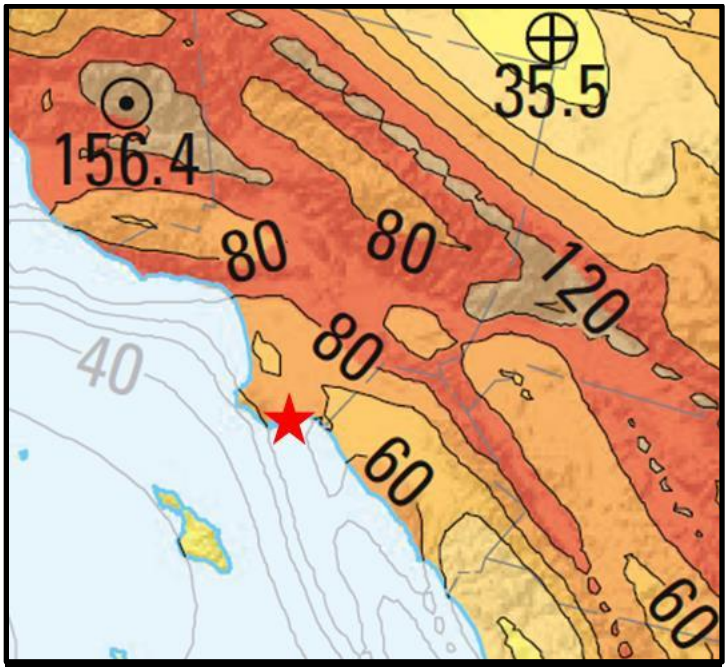

Figure 170: Map showing peak horizontal acceleration with 2% probability of exceedance in 50 years for the Los Angeles Basin and environs (%g).
Star indicates northwest extent of Wilmington Graben. (Petersen et al, 2011)

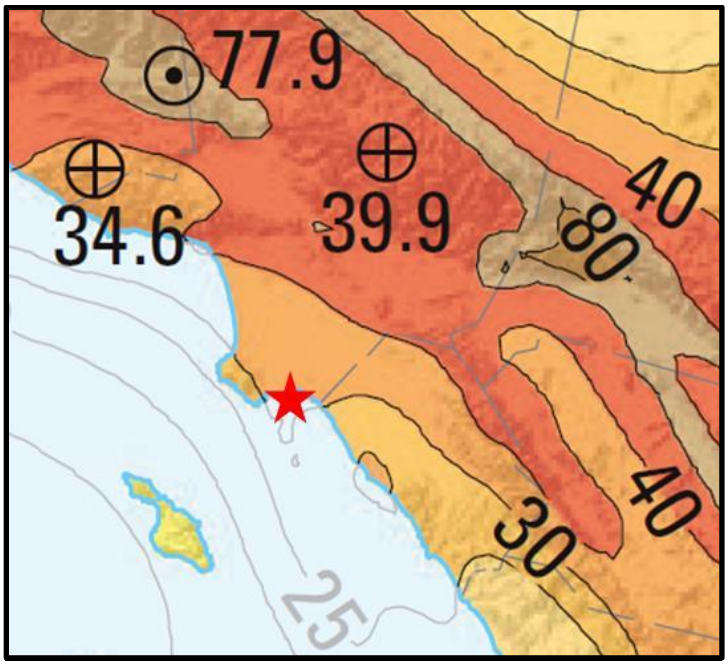

**Figure 171: Map showing peak horizontal acceleration with 10% probability of exceedance in 50 years for the Los Angeles Basin and environs (%g).
Star indicates northwest extent of Wilmington Graben. (Petersen et al, 2011)**

9.3.2 Injection and Production Wells in Los Angeles Basin and Historical Impact of Seismicity

There are 89 active oil and gas fields in California Department of Oil, Gas and Geothermal Resources (DOGGR) District 1, which comprises fields mainly in Los Angeles and Orange counties (Figure 172). There are currently about 6500 producing oil and gas wells in District 1and about 1500 injection wells, mainly for water flood (DOGGR, 2007). In 2006, almost 770 MMbbl of water/steam were injected into District 1 fields (DOGGR, 2007).

Title: Characterization of Pliocene and Miocene Formations in the Wilmington Graben, Offshore Los Angeles, for Large-Scale Geologic Storage of CO_2

PI: Dr. Michael Bruno Final Report

Figure 172: Major Oil Fields in the Los Angeles Basin (DOGGR District 1) and Location of the Wilmington Graben

Wells are designed to sustain typical seismic deformations. Oil and gas fields throughout Southern California have experienced major seismic events with no significant problems. Wells designed for CCS projects will exceed typical design standards for oil and gas wells in the State of California. These can withstand several percent deformation strain (see for example, Bruno, 2001). Strain waves generated by earthquakes have amplitudes several orders of magnitude smaller (except right at the location of fault rupture). Major earthquakes in southern California occur in stiff, brittle, basement rock at depths on the order of 7620 m (25,000 feet) or more. **CO_2** injection wells into the Wilmington Graben would only penetrate soft shallow sediments to a maximum depth of about 2743 m (9000 ft).

Historically, the Southern California area has experienced three large magnitude earthquakes (Long Beach, Whittier Narrows and Chino Hills) in the immediate vicinity of oil and gas fields without causing problems. Additionally, most oil fields have some natural gas associated with the oil, but there has been no evidence of damaging gas leakage due to

earthquake activity. The Inglewood and Seal Beach oil fields straddle the large Newport Inglewood Fault, while the Wilmington oil field was formed by wrenching between, and adjacent to, the Palos Verdes, THUMS and Newport Inglewood Faults. Large earthquakes have occurred near the Wilmington field (Long Beach), near the Whittier field (Whittier Narrows and Chino Hills), and immediately adjacent to the Aliso Canyon oilfield and gas storage field (Northridge), with no damaging gas leaks.

9.3.3 Gas Storage Fields in the Los Angeles Basin and Historical Impact of Seismicity

Another important analog to consider is that large volumes of natural gas are injected and stored in subsurface formations throughout the Los Angeles basin. In these operations gas is injected once or twice per year and extracted once or twice per year, primarily to take advantage of price swings and supply and demand timing. Five gas storage fields that have operated in the Los Angeles area include Honor Ranch, Aliso Canyon, Playa Del Rey, Whittier, and Montebello (the latter two have been abandoned, Figure 173).

Figure 173: Gas Storage Fields (brown squares) in Southern California (Southern California Gas Company)

Title: Characterization of Pliocene and Miocene Formations in the Wilmington Graben, Offshore Los Angeles, for Large-Scale Geologic Storage of CO_2

PI: Dr. Michael Bruno Final Report

The magnitude 6.7 Northridge Earthquake of 1994 occurred almost directly beneath (within 5 miles of) the Aliso Canyon Gas Storage Field, which stores more than 100 billion cubic feet of gas for the metropolitan Los Angeles Area (Figure 174). The main quake occurred at a depth of almost 19 km (12 mi), aftershocks up to magnitude 3 were scattered within the field itself at typical well depths, as shown in Figure 175 and Figure 176. There was neither gas leakage detected nor significant well problems from this event. Only one out of 400 wells was deformed slightly, without gas release. Damage to the well casing occurred at a depth of about 2133 m (7000 ft) at the interface between a thick overlying sand and a thick underlying shale. The damage was caused primarily by formation shear localization or faulting induced or triggered by the Northridge earthquake, in an area highly stressed by gas storage operations (GeoMechanics Technologies internal report).

Title: Characterization of Pliocene and Miocene Formations in the Wilmington Graben, Offshore Los Angeles, for Large-Scale Geologic Storage of CO_2

PI: Dr. Michael Bruno Final Report

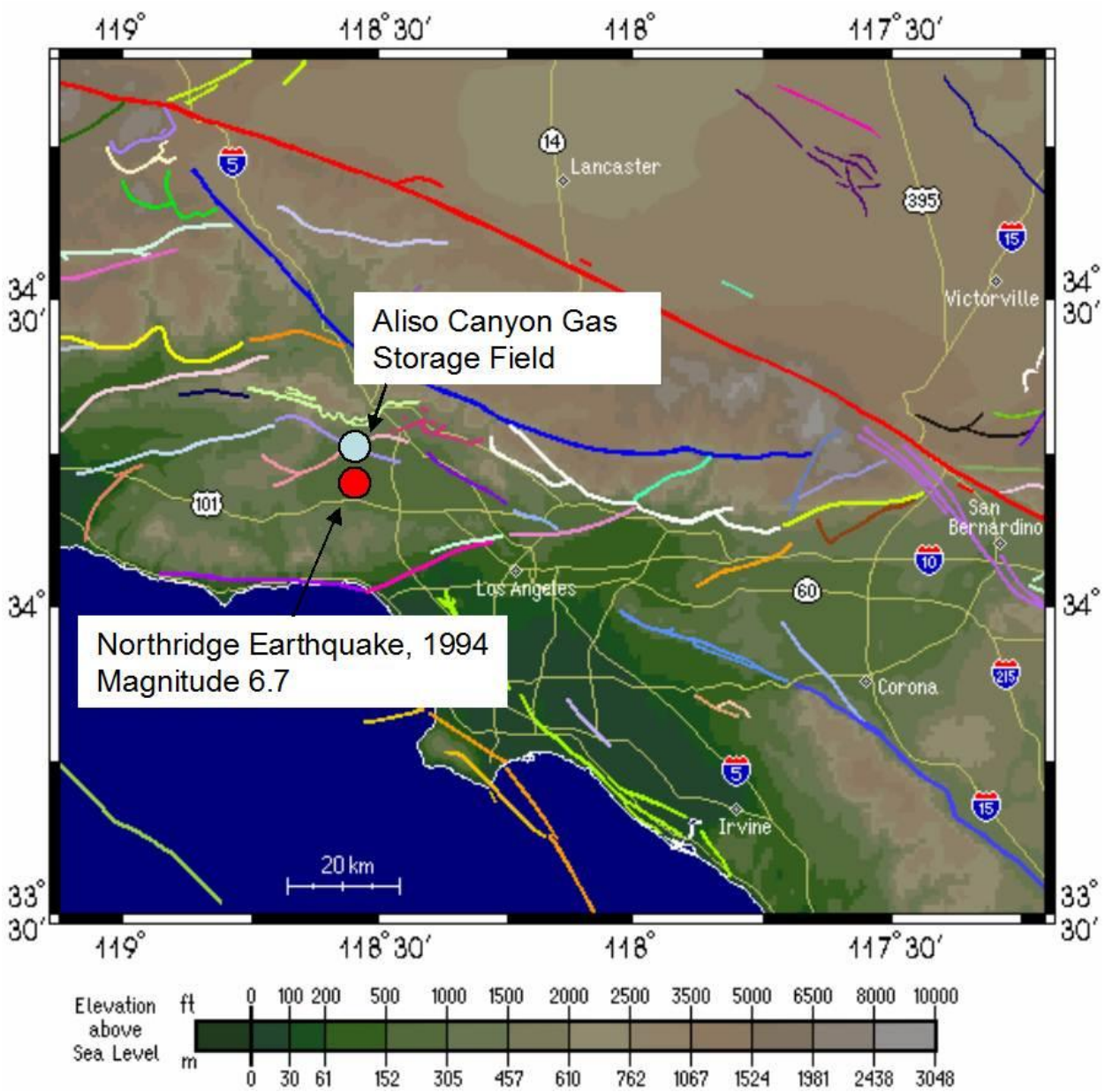

Figure 174: Approximate Location of the Aliso Canyon Gas Storage Field and the Epicenter of Northridge Earthquake (Southern California Earthquake Center)

Title: Characterization of Pliocene and Miocene Formations in the Wilmington Graben, Offshore Los Angeles, for Large-Scale Geologic Storage of CO_2

PI: Dr. Michael Bruno Final Report

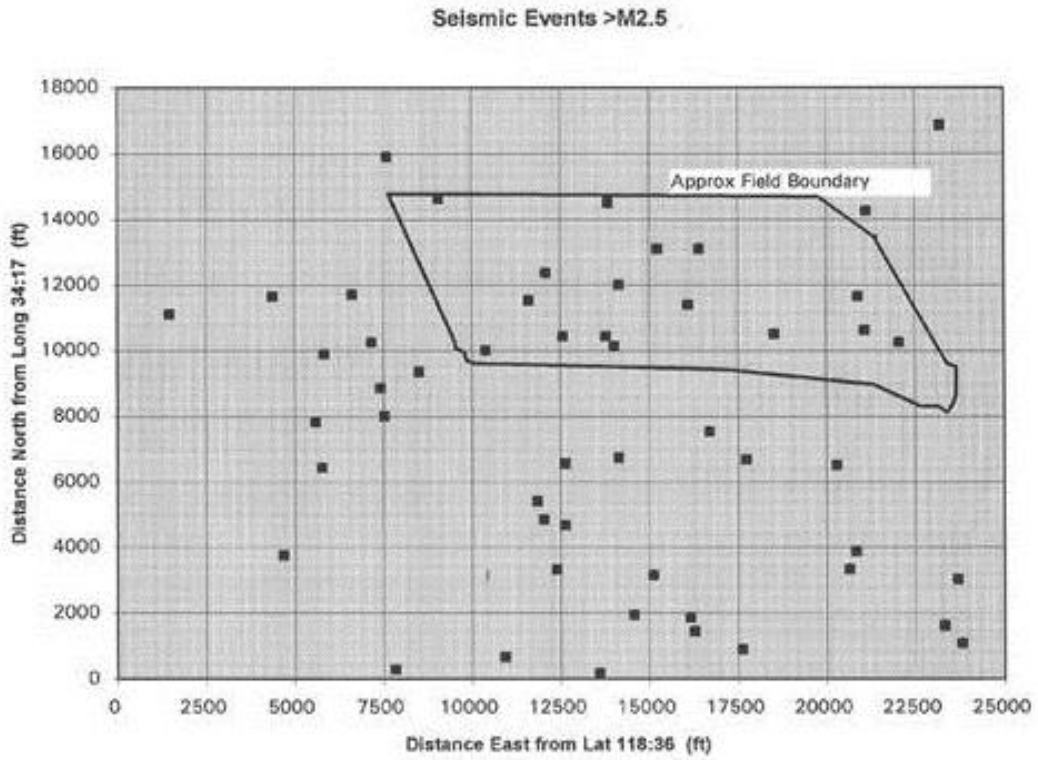

Figure 175: Distance from the Aliso Canyon gas storage field of aftershocks from the 1994 Northridge earthquake (GeoMechanics Technologies Internal Report)

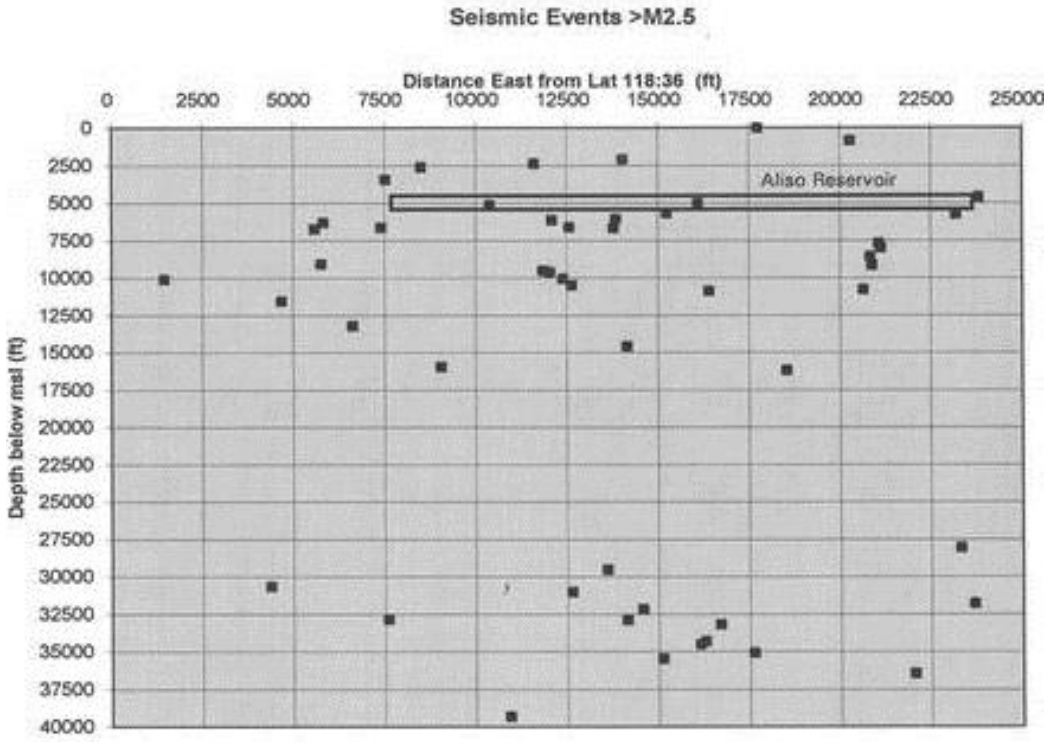

Figure 176: Depth of aftershocks from the 1994 Northridge earthquake in relation to the Aliso Canyon gas storage field (GeoMechanics Technologies Internal Report)

9.4 Induced Seismicity Risks

An additional hazard is *induced seismicity*: injection caused earthquakes. Wesson and Nicholson (1987) noted that injection usually triggers activity in an already seismically unstable area, rather than causing stable areas to become unstable. Forces of the pressurized fluids themselves are not large on a geologic scale, and cannot provide enough energy to cause a significant earthquake on their own. They can, however, trigger the release of energy already stored in a fault (Price et al, 2008).

9.4.1 Historical Cases

Seismicity induced by human activity has been observed and documented since at least the 1920s (Pratt and Johnson, 1926). The number of seismic events of M > 0 caused by or likely related to human activities are aggregated below (Table 32; in several cases the causal relationship between the technology and the event was suspected but never confirmed). These event locations are shown by technology and magnitude on the U.S. map (Figure 177).

Table 32: Observations of Induced Seismicity (CISPET et al, 2012)

Technology	Global (United States only)
Waste water injection	11 (9)
Oil and gas extraction (withdrawal)	38 (20)
Secondary recovery (water flooding)	27 (18)
Geothermal energy	25 (3)
Hydraulic fracturing (shale gas)	2 (1)
Surface water reservoirs	44 (6)
Other (e.g. coal and solution mining)	8 (3)

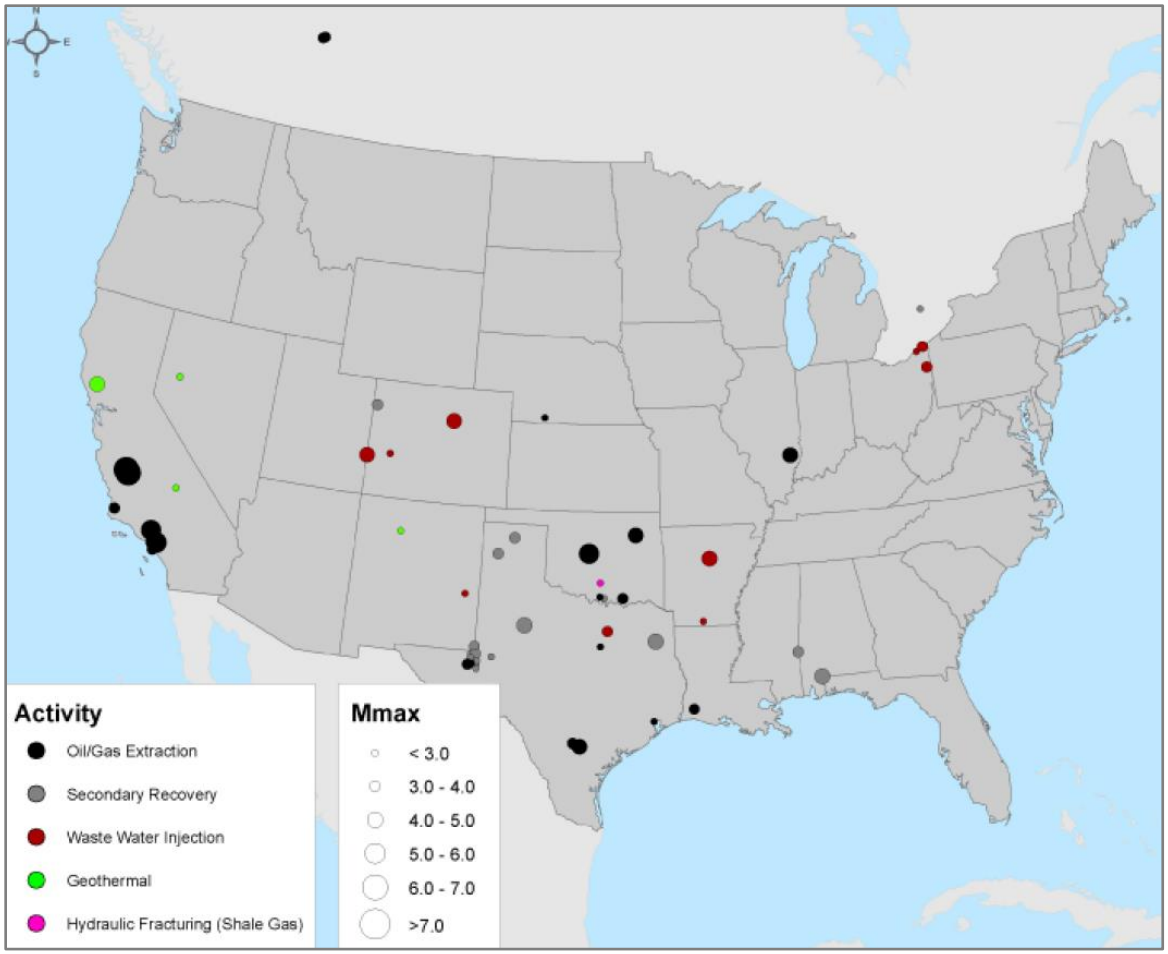

Figure 177: Locations of seismic events caused by or *likely related to human* activities within the coterminous United States and portions of Canada as documented in the technical literature (CISPET et al, 2012).

Title: Characterization of Pliocene and Miocene Formations in the Wilmington Graben, Offshore Los Angeles, for Large-Scale Geologic Storage of CO_2

PI: Dr. Michael Bruno Final Report

It has been known for almost 40 years that, under some circumstances, injection of large fluid volumes can generate earthquakes. Though usually small, these earthquakes can be quite large. Injection-induced seismicity was first observed in Denver, Colorado in the 1960s. Waste fluids from chemical manufacturing operations were being injected into a deep disposal well at the Rocky Mountain Arsenal, located northeast of Denver. Fluids were injected on a routine basis between March 1962 and September 1963 at a rate of 181,000 gal/day. Injection stopped between October 1963 and August 1964. Then fluid was placed into the well using gravity flow at a rate of 65,800 gal/day until April 1965, when injection resumed at a rate of 148,000gal/day (CISPET et al, 2012).

At the same time of the Denver waste injection activities, two seismograph stations in the Denver area began to record earthquakes. However, a search of historical records found no evidence of seismic activity before 1962 that were similar in nature to the earthquakes that had been occurring after 1962. In 1965, geologist David Evans showed that there was a correlation between the injection activities at the Rocky Mountain Arsenal and seismic activity in Denver (Evans, 1966).

In this case, injection of large volumes of water produced earthquakes as large as magnitude 5.3 (Healy et al, 1968). It is important to note that the target rocks were very impermeable basement rocks and, as a consequence, sustained very large pressure build ups. CCS sites require good permeability, i.e. aseismic sites (Burton et al, 2007).

Another significant case of induced earthquakes involves the Rangely oil field in northwestern Colorado. This site was the target of a series of experiments led by Stanford University to intentionally generate small earthquakes in the hope of preventing larger events. Between 1969 and 1972, the researchers injected very large volumes of water into a fault to induce seismic activity. The fault was selected because it was thought to be already close to failure. After several series of injections, the team was able to generate seismic events. The largest of these events was magnitude 3.1, which could barely be felt at the surface. The overwhelming majority of the earthquakes were too small to feel at the surface (Raleigh et al, 1976). After these experiments, the Rangely field became a site of active CO_2 injection. Since 1986 and with nearly 25MMt of injection, only microseepage has been detected at the surface (Klusman, 2003).

Besides these two well-studied historical cases, there have been well-documented recent seismic events also apparently related to various types of fluid injection, for example (CISPET et al 2012):

- Basel, Switzerland, 2006, an enhanced geothermal system (M 3.4);
- Dallas-Ft. Worth airport area, 2008-09, waste water disposal from shale gas development (M 3.3);
- Blackpool, England, 2011, hydraulic fracturing (shale gas) (M 2.3)

9.4.2 Microseismic Monitoring Experiment at Wilmington Graben (Terminal Island Biosolids) Injection Site

A new microseismic array was hung in SFI#2 well during September and October 2014 to measure any induced seismic activity during the injection of biosolids. The array contains 12 levels 3- component array placed over a depth range of 1258 to 1423 m (4128.6 to 4670 ft, MD), above the injection zone, which is defined by perforations between 1550 to 1556 m (5086 to 5106 ft, MD). The array was oriented with two string shots in nearby DOE#2 (aka SFI#4) well (string shot #1 at 1356 m or 4450 ft, and string shot #2 at 1219 m or 4000 ft, both MD) on Sept. 19, 2014 at 2:13pm. Receiver depths were at:

Level 1	4128.6ft
Level 2	4177.9ft
Level 3	4227.1ft
Level 4	4276.3ft
Level 5	4325.5ft
Level 6	4374.7ft
Level 7	4423.9ft
Level 8	4473.1ft
Level 9	4571.6ft
Level 10	4522.4ft
Level 11	4620.8ft
Level 12	4670ft

Existing injection operations ended in SFI#1 well on Sept. 19 at 9:30 am, and started in the new well SFI#3 (aka DOE#1) well on Sept. 22 at 3 am. More than 169,000 continuous data files were recorded and analyzed. The processing workflow chart is shown in Figure 178. The calibration was conducted using the string shot at 1356 m (4450 ft, MD) and the calibration errors are less than 15 ft in *x*-, *y*-, and *z*- directions.

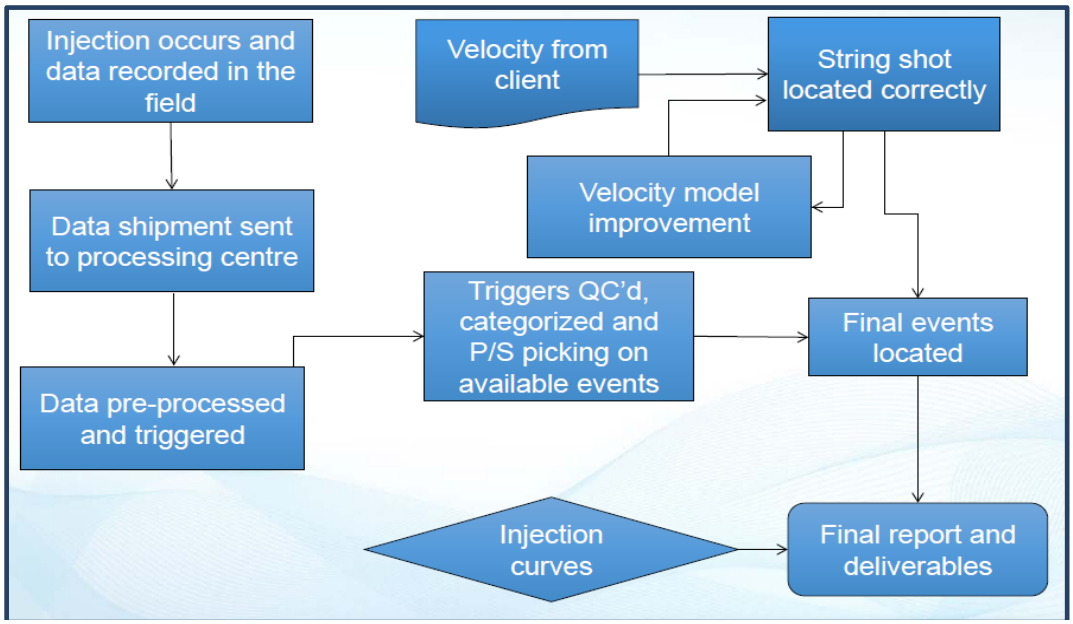

Figure 178: Microseismic Process Workflow Chart

Summary of results:

- There were 40 events exhibiting microseismic characters that were processed and located during the monitoring period Sept. 19 to Oct. 10, 2014.
- There is no injection related seismicity observed.
- One deep event located at 1463 m (4800 ft), magnitude -2.54 was recorded on Sept 19 at 6:56 pm after injection operation and string shot were concluded. This is attributed to natural seismicity.
- All other events (39 events, magnitude range from -1.19 to -2.97) were related to mechanical activity in or around the SFI#2 monitoring well and generally occurred on the same day as the string shot, thus can be attributed to vibration and activity in SFI#2 well.
- String shot magnitude was -1.92

All microseismicity activities were plotted in the following Figure 179. As expected, the string shot has the largest magnitude, followed by the mechanical events. The deep event occurred during the shut-in period with no injection activity, and has a magnitude that is expected of natural microseismicity.

Microseismic events associated with injection were noted during the first three months of the project (the same period when fracturing was occurring) and then died off and no longer occurred. As expected, when there is no fracturing there is no associated microseismic event. The microseismic analyses are consistent with our step-rate data and pressure fall-off analyses

from the nearby injection operations, in which no new fracturing has occurred for the past 5 years.

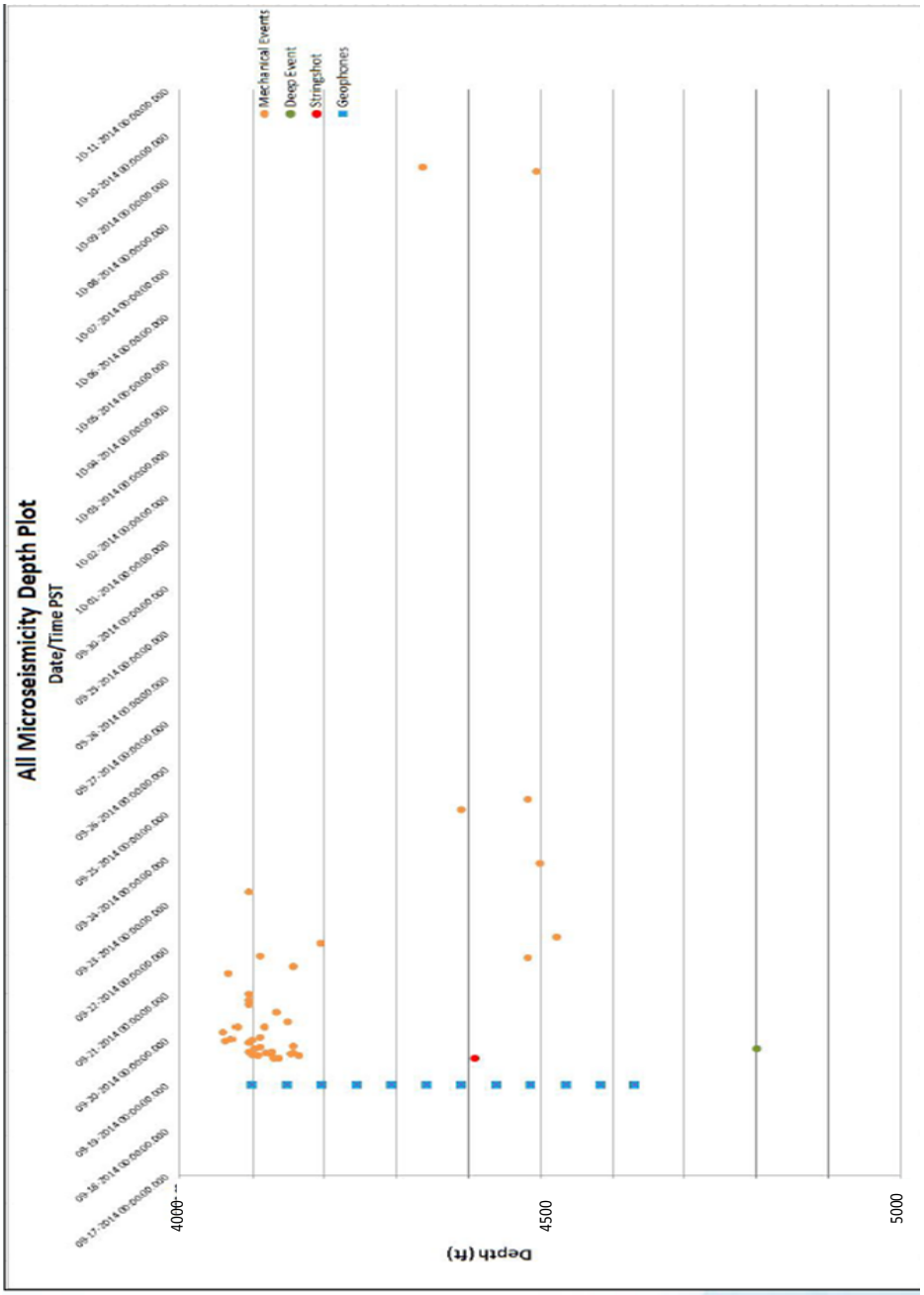

Figure 179: All microseismic activities plotted: depth versus time during Sept. 19 to Oct. 10, 2014 recording

9.5 CO_2 Migration to Sea Floor and resulting consequences

For storage sites that are offshore, CO_2 that has leaked may reach the ocean bottom sediments and then, if lighter than the surrounding water, migrate up through the water column until it reaches the atmosphere. Depending upon the leakage rate, it may either remain as a separate phase or completely dissolve into the water column. When CO_2 dissolves, biological impacts to ocean bottom and marine organisms will be of concern. For those sites where separate-phase CO_2 reaches the ocean surface, hazards to offshore platform workers may be of concern for very large and sudden release rates (IPCC, 2005).

Seepage from offshore geological storage sites may pose a hazard to benthic environments and organisms as the CO_2 moves from deep geological structures through benthic sediments to the ocean. But while leaking CO_2 might be hazardous to the benthic environment, the seabed and overlying seawater can also provide a barrier, reducing the escape of seeping CO_2 to the atmosphere. These hazards are distinctly different from the environmental effects of the dissolved CO_2 on aquatic life in the water column (IPCC, 2005).

Little is known about the short-term and long-term impacts of CO_2 storage on marine ecosystems even though CO_2 has been stored sub-seabed in the North Sea (Sleipner) for over 15 years and for over 5 years in the Barents Sea (Snøhvit). To date most research concerned with the effects of CO_2 released into the ocean have focused on release at depths greater than 300 m (1000 feet) for the purpose of oceanic sequestration (Brewer, 2001; Caldeira et al, 2001; Drange et al, 2001; Herzog et al, 2001 De Figueiredo, 2003), whereas unintended releases in the Wilmington Graben would most likely be at a depth of about 30 m (100 ft). At depths of less than 60 m (2000 ft) CO_2 would typically be released as a gas (Pruess, 2010), and would rise toward the surface and maybe dissolved into the seawater.

Some recent research has looked at shallower depth offshore seepage. Volcanic CO_2 seeps have been studied in detail by ECO_2 partners in recent years. The Mediterranean Panarea gas seeps located in shallow waters, 10-40 m (30-130 ft) water depth, off Panarea Island. The Panarea Island is located north of Sicily in the Southern Tyrrhenian Sea. It is part of the Aeolian Archipelago, which is influenced by the active volcano Stromboli. Fumarolic activities and submarine gas seeps are common features around Panarea (Aliani *et al.*, 2010; Caramanna *et al.*, 2011). The released gas is mainly composed of CO_2 (94%), but may also contain traces of hydrogen sulphide and methane. The total emitted CO_2 for this area is estimated to be about 1,670 Mt/m^2 (1,670MMt/km^2) each year. The acidification of the water caused by the presence of CO_2 has affected the local biota with a strong reduction of the life-forms based on calcareous skeletons or shells. General damage to the sea grass Posidonia oceanica has also been observed (Caramanna *et al.*, 2011).

Quantifying and Monitoring Potential Ecosystem **I**mpacts of Geological **C**arbon **S**torage (QICS, a consortium of British academic research institutions) is a scientific research project established to understand the sensitivities of the UK marine environment to a potential leak from a CCS system. The project's primary experiment is a world-first, releasing moderate levels of

CO_2 into shallow sediments in a Scottish Bay, enabling scientists to study the progress and effects of a controlled CO_2 leak and extrapolate these to real-life situations, which might occur in the future. While the observations of natural CO_2 seepage sites and laboratory experiments are both informative, using natural seep sites effects cannot easily be quantified because no pre-seepage (baseline) measurements exist and laboratory mock-ups can never fully replicate the complexity of the real world (QICS, 2012). Preliminary findings indicate that the impact of the CO_2 on the structure and diversity of the seafloor community is largely restricted to the zone immediately above the release point and that the sediments further away remain unaffected. Further findings include:

- results indicate that the movement of CO_2 through shallow sediments is complex, but nevertheless detectable above certain thresholds by geo-acoustic imaging;
- significant buffering in the sediments effects both impacts and monitoring
- biological impacts exist, but are not significantly damaging, at least for the duration and flux of CO_2 used in the experiment;
- while geophysical methods, such as seismic reflection, are effective in detecting free gas in the sediment and for imaging the migration of CO_2 through sediments to the sea floor, since they survey a large area, only relatively large features can be detected, and the type of gas and leakage rates cannot be measured;
- once a suspected leak has been discovered, the origin and presence of CO_2 must be confirmed and the leakage rate quantified by collecting fluid samples or deploying CO_2 sensors at or near the sediment-water interface;
- using a combination of these techniques, it is estimated that approximately 15% of the CO_2 injected into the sediments during the QICS experiment escaped as free gas, while the rest may have dissolved into the sediment pore waters or migrated away from the injection site;
- CO_2 gas bubbles did reached the sea surface, and the resulting increase in atmospheric CO_2 was mapped using sensors deployed just above the sea surface, the depth of water at sites ear-marked for CO_2 storage, deeper than the 12 m (40 ft) here, is almost certainly to prevent free gas reaching the sea surface, so rendering this technique unhelpful as a monitoring tool.

9.6 Conclusion

GeoMechanics has completed a comprehensive analysis of risks associated with CO_2 injection in the Wilmington Graben. Using our Quantitative Risk & Decision Analysis Tool (QRDAT) for caprock integrity evaluation, we compared Wilmington Graben's risk to that of In Salah and Sleipner. We found Wilmington Graben is riskier then both.

We also investigated natural and induced seismicity risks in relation to CO_2 injection and storage, and the effects of potential leakage to the sea floor.

10 Infrastructure Assessment

Carbon capture and storage (CCS) is of great interest because of the large amount of CO_2 emitted from the burning of fossil fuels. Carbon capture technologies can potentially remove 80-95% of CO_2 from electric power plant or other industrial source emissions (Parfomak & Folger, 2007). Power plants are the most likely initial candidates for CCS since they are large single point sources that contribute approximately 30% of US CO_2 emitted from the burning of fossil fuels. One common condition for all large-scale CCS is a system for transporting CO_2 from capture sites to storage sites, which requires a dedicated interstate/intrastate pipeline network.

GeoMechanics has completed a study of the infrastructure assessment associated with CO_2 injection and storage in the Los Angeles Basin. The various factors evaluated include:

1. Top 20 industrial sources of CO_2 emissions, see Figure 180, and
2. Engineering review and analysis of existing and new pipeline and gas storage systems in the Los Angeles Basin

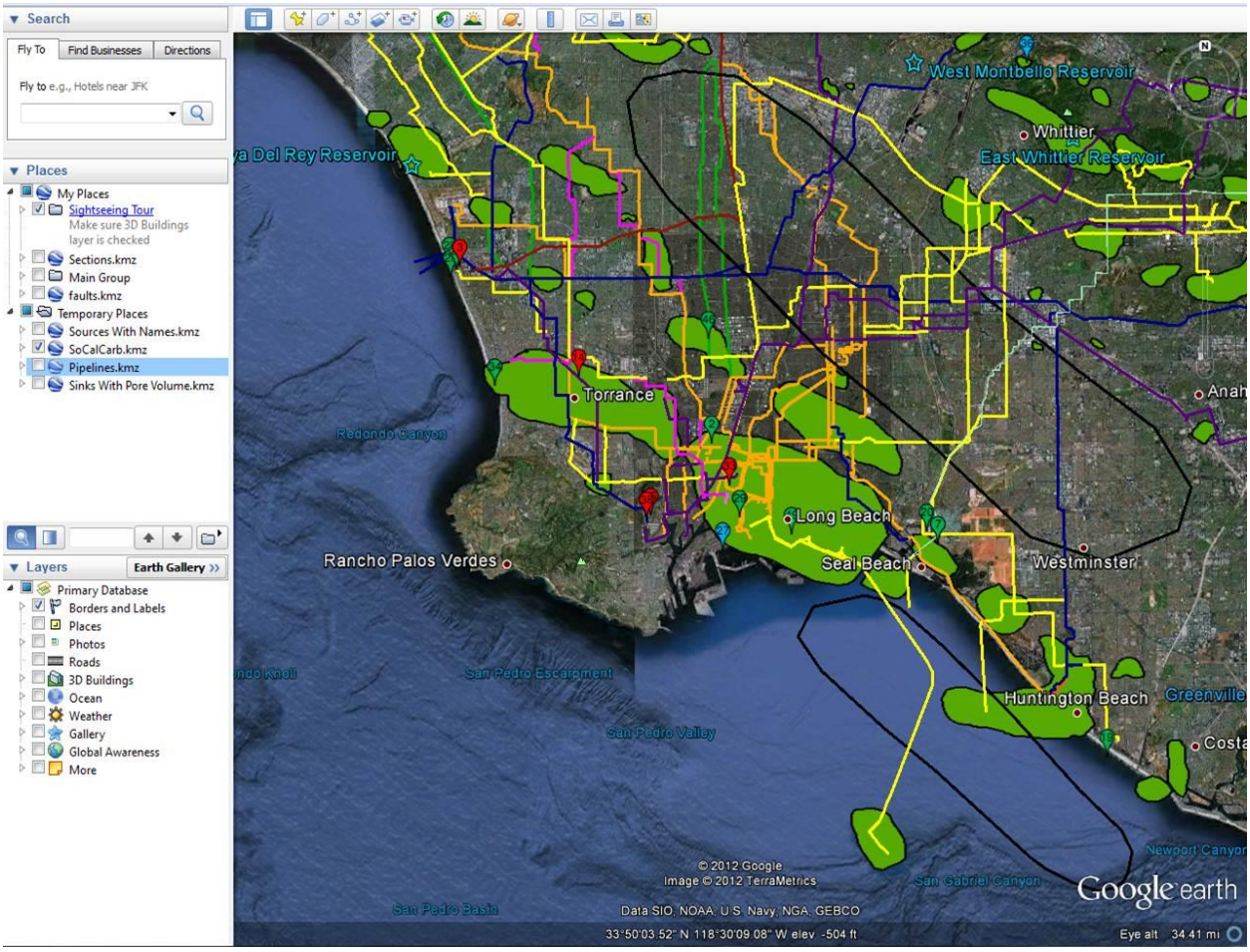

Figure 180: Source, sink and pipeline interactive map

10.1 Top 20 industrial sources of CO_2 emission

Geomechanics Technologies has identified and reviewed the top industrial sources of CO_2 emissions within the Los Angeles Basin. We used WESTCARB, CARMA, and the CEC Energy Almanac data to put together a list of the top 50 carbon dioxide producers in Southern California. The information from WESTCARB reflects the 2012 September data and is the most current data available. We decided to use WESTCARB data as precedence when there is a conflict. Figure 181 shows graphically the top 20 industrial sources within the LA Basin and their source type while Table 33 lists the sources and the amount of CO_2 produced per year per location. We have used the same color scheme to represent the different source types.

Title: Characterization of Pliocene and Miocene Formations in the Wilmington Graben, Offshore Los Angeles, for Large-Scale Geologic Storage of CO_2

PI: Dr. Michael Bruno Final Report

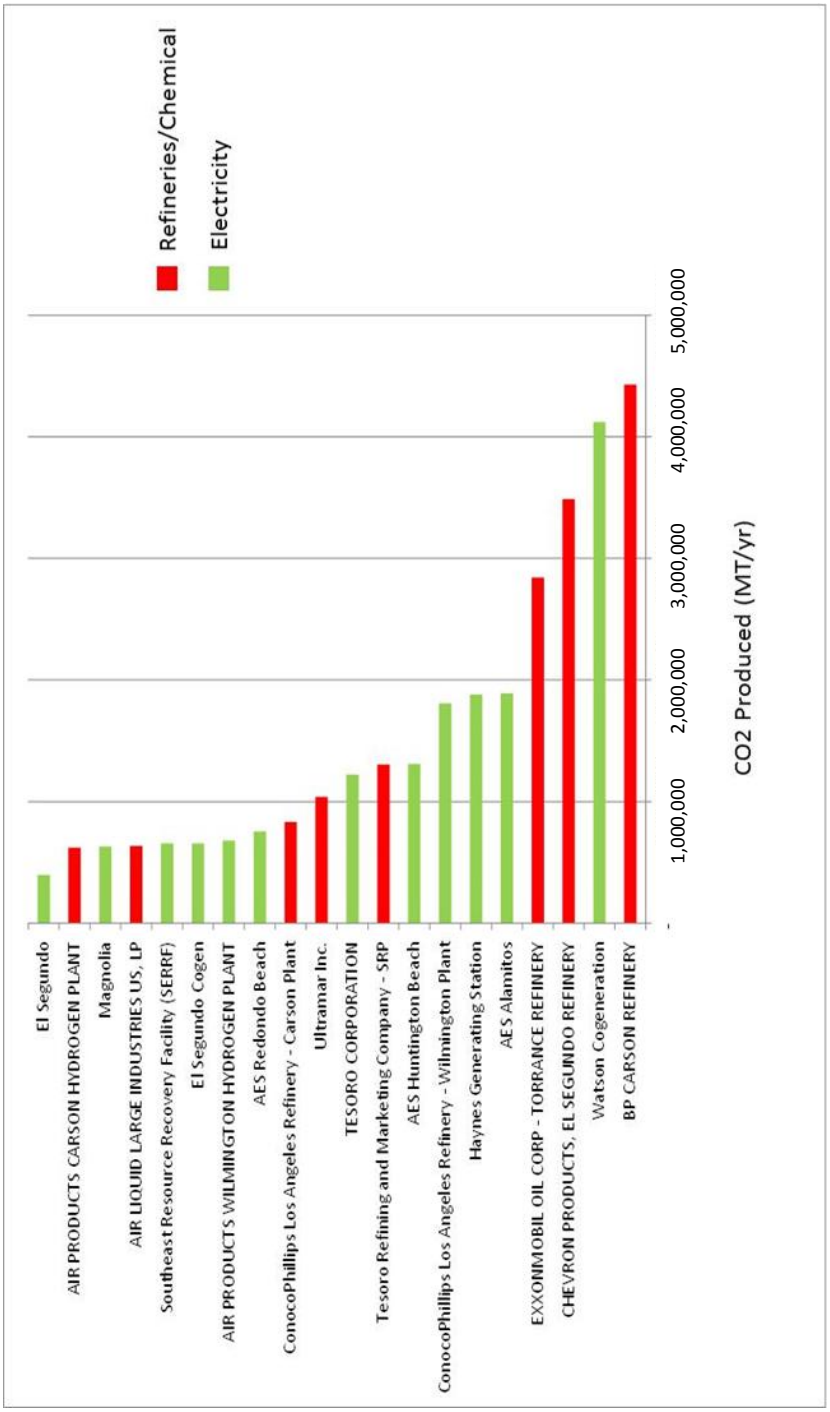

Figure 181: Top 20 CO_2 Producers
WESTCARB database: http://gif.berkeley.edu/westcarb/

Table 33: Top 20 CO_2 Industrial Sources

SOURCE NAME	CO2 PRODUCED MT/yr WESTCARD 2012 DATA	SOURCE TYPE	OPERATOR	ADDRESS	CITY
BP CARSON REFINERY	4,429,898	REFINERIES/CHEMICAL	BP Carson	2350 E. 223rd Street	CARSON
Watson Cogeneration	4,122,415	ELECTRICITY	BP Amoco	22880 S. Wilmington Ave	Carson
CHEVRON PRODUCTS, EL SEGUNDO REFINERY	3,487,157	REFINERIES/CHEMICAL	Chevron Corp	324 W El Segundo Blvd	El Segundo
EXXONMOBIL OIL CORP - TORRANCE REFINERY	2,842,376	REFINERIES/CHEMICAL	Exxon Mobil	3700 WEST 190TH STREET	TORRANCE
AES Alamitos	1,889,507	ELECTRICITY	AES NUGs	690 N STUDEBAKER ROAD	LONG BEACH
Haynes Generating Station	1,879,527	ELECTRICITY	Los Angeles City of	6801 E 2ND ST	LONG BEACH
ConocoPhillips Los Angeles Refinery - Wilmington Plant	1,806,373	ELECTRICITY	ConocoPhillips	1660 WEST ANAHEIM STREET	WILMINGTON
AES Huntington Beach	1,308,481	ELECTRICITY	AES NUGs	21730 NEWLAND ST	HUNTINGTON BEACH
Tesoro Refining and Marketing Company - SRP	1,304,531	REFINERIES/CHEMICAL	Tesoro Corp (formerly Equilon En	23208 South Alameda Street	Carson
TESORO CORPORATION	1,221,493	ELECTRICITY	Tesoro Corp (formerly Equilon En	2101 EAST PACIFIC COAST HIGHWA	WILMINGTON
Ultramar Inc.	1,037,999	REFINERIES/CHEMICAL	Ultramar Inc	2402 East Anaheim Street	Wilmington
ConocoPhillips Los Angeles Refinery - Carson Plant	832,463	REFINERIES/CHEMICAL	ConocoPhillips	1520 EAST SEPULVEDA BOULEVARD	CARSON
AES Redondo Beach	752,967	ELECTRICITY	AES NUGs	1100 N HARBOR DRIVE	REDONDO BEACH
AIR PRODUCTS WILMINGTON HYDROGEN PLANT	677,727	ELECTRICITY	AIR PRODUCTS & CHEMICALS, IN	700 HENRY FORD AVENUE	WILMINGTON
El Segundo Cogen	655,468	ELECTRICITY	Chevron Corp	637 S Sepulveda Blvd	El Segundo
Southeast Resource Recovery Facility (SERRF)	655,034	ELECTRICITY	Covanta Energy (formerly Montel	120 PIER S. AVE	LONG BEACH
AIR LIQUID LARGE INDUSTRIES US, LP	633,987	REFINERIES/CHEMICAL	AIR LIQUIDE LARGE INDUSTRIES	324 W EL SEGUNDO BLVD	EL SEGUNDO
Magnolia	629,132	ELECTRICITY	Burbank (City of) Water and Powe	164 WEST MAGNOLIA BOULEVARD	BURBANK
AIR PRODUCTS CARSON HYDROGEN PLANT	620,798	REFINERIES/CHEMICAL	AIR PRODUCTS & CHEMICALS, IN	23300 SOUTH ALAMEDA STREET	CARSON
El Segundo	397,206	ELECTRICITY	NRG Energy	301 Vista Del Mar	El Segundo

10.1.1 SoCal Carbon Atlas

A southern California Carbon Atlas was produced by integrating known sinks, sources, and pipelines. This interactive atlas can be viewed on our website: www.socalCARB.org. SoCalCarb has identified the major stationary sources of CO_2, such as power plants and oil refineries; determined the potential for storing captured CO_2 in geologic formations; and assessed the feasibility of transporting CO_2 via pipelines from major CO_2 sources to storage sites. Storage sites include numerous mature oil fields, gas storage facilities and deep saline formations. SoCalCarb's objective is to determine the technical and economic feasibility of using these geologic formations for long-term storage, as well as link options for capture, transportation, and geological storage within the environmental and regulatory framework, thus defining sequestration scenarios and potential outcomes for the region.

The top 50 CO_2 industrial producers were plotted using the location identified in the Energy Almanac (http://energyalmanac.ca.gov/powerplants/index.html). Some locations were hard to find, or were given multiple locations. Research was conducted to come up with the correct location and it was plotted on the socalCARB.org website. Figure 182 shows the source map which includes locations and the amount of CO_2 produced per year.

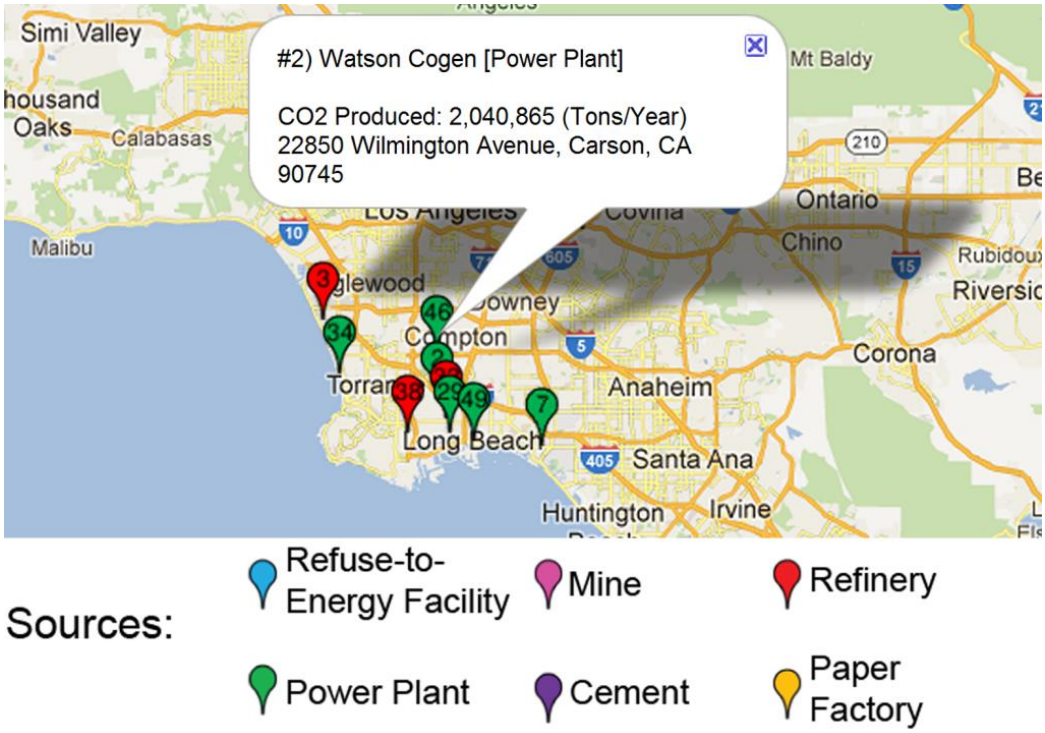

Figure 182: LA Basin source map

The known CO_2 sinks (oil and gas fields) in southern California have been digitized using DOGGR (1992) maps. Next we combined the known gas storage reservoirs with our own studies of the saline aquifers in the Los Angeles Basin. We calculated the estimated pore volumes and maximum storage resources for each sink, identified the potential CO_2 reservoirs, and noted the potential reservoir formation estimated depths. Using Google Earth, this data was plotted and is displayed as shown in Figure 183.

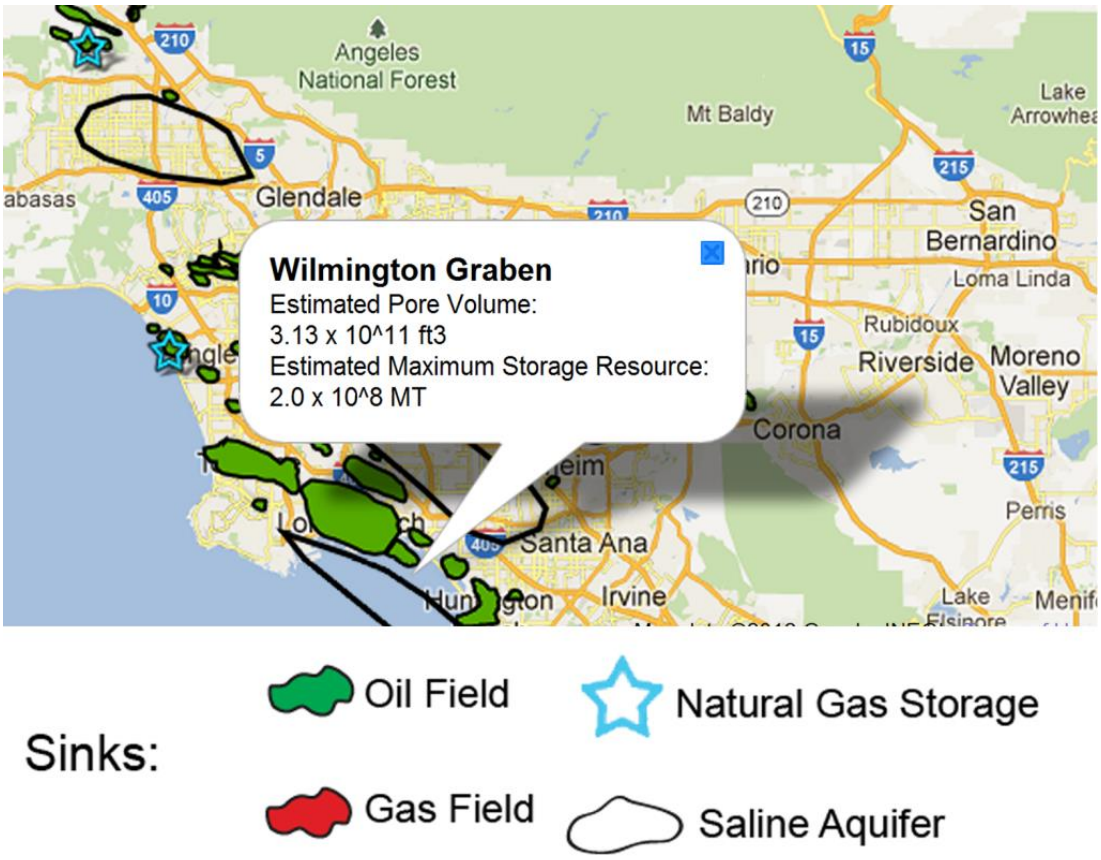

Figure 183: LA Basin sink map

We followed the DOE methodology described in the NETL 2010 Carbon Sequestration Atlas for estimating pore volumes and maximum storage resources.

The pipelines within Southern California have also been digitized. The featured pipeline locations in socalCARB.org are strictly estimates. This information was obtained from the California Energy Commission's Systems Assessment & Facilities Division, Cartography Unit.

Even though the pipeline operators are required to keep a current map displaying all the location of the pipes, this information is not in the public domain. We made our best estimates on the pipeline locations based on common pipeline practices. The pipelines are categorized as oil or gas (see Figure 184 and Figure 185).

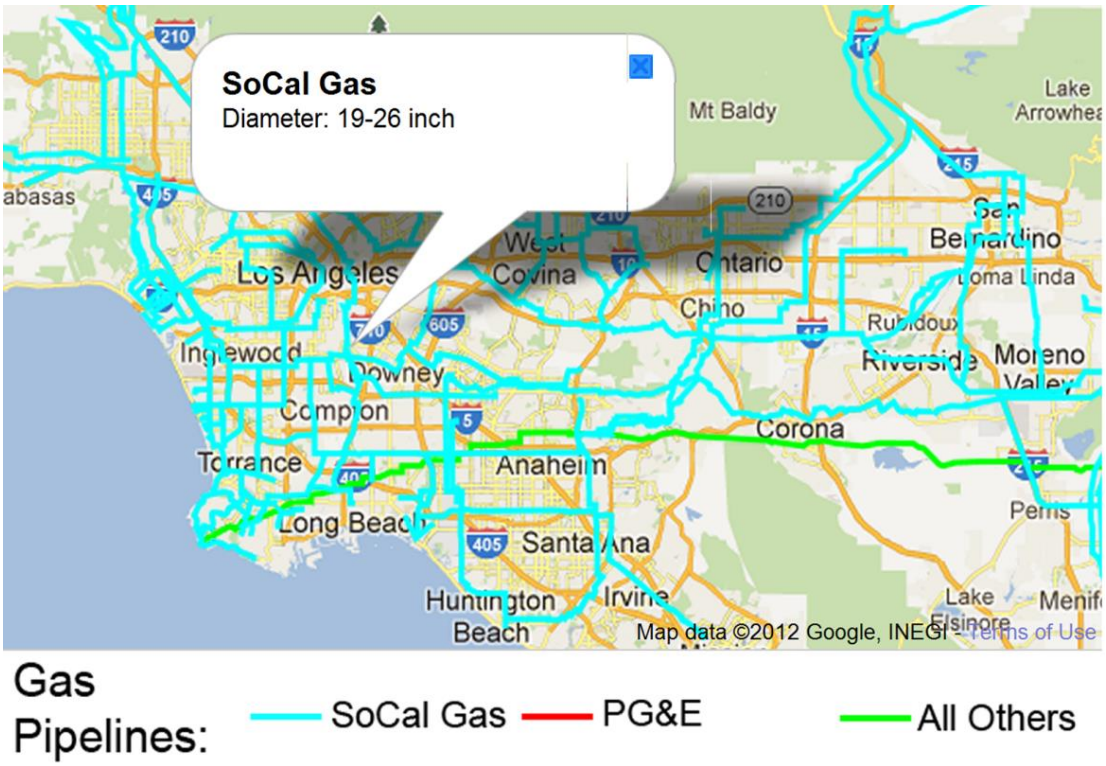

Figure 184: LA Basin gas pipelines

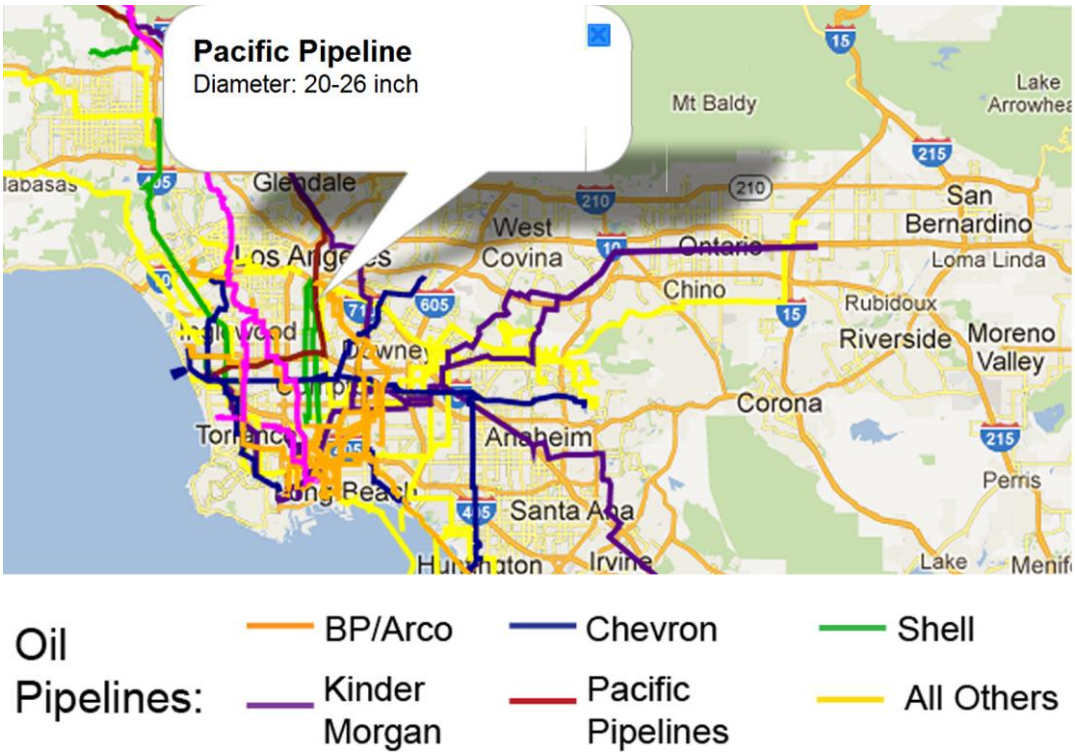

Figure 185: LA Basin oil pipelines

10.2 Engineering Review and Analysis of Existing and New Pipeline and Gas Storage System in the LA Basin

Capture and storage have been identified as significant components for reducing CO_2 emissions to the atmosphere. Pipelines are likely to be the primary means of transporting CO_2 from source (capture) to sink (storage). There is limited experience in CO_2 transportation through pipelines in dense phase (liquid and/or supercritical phase). There are a number of CO_2 pipeline issues that should be addressed and the associated risks managed.

We have identified existing oil and gas pipelines within the southern California area (see previous section above). Geomechanics Technologies also performed a feasibility study on the potential for converting existing oil or gas pipelines for CO_2 transport by reviewing existing pipeline regulations, researching CO_2 pipeline guidelines and interviewing pipeline operators. Oil pipelines are operated by common carriage while the gas pipelines are operated by public utilities.

10.2.1 Existing CO_2 Pipeline

There are regional CO_2 pipeline networks already operating in the US for enhanced oil recovery (EOR), but developing a more extensive national CO_2 pipeline network for carbon capture and storage (CCS) could pose numerous regulatory and economic challenges. The oldest long distance CO_2 pipeline in the US is the 225 km (140 mi) Canyon Reef Carriers Pipeline in Texas. This pipeline began operation in 1972 for EOR purposes. Approximately 5800 km (3600 mi) of CO_2 pipeline are in operation today in the US compared to about 800,000 km (497,097 mi) of natural gas pipelines (Parfomak & Folger, 2007). In Figure 186 refer to yellow lines for existing CO_2 pipelines and the blue/silver lines for natural gas pipelines. The red and green lines are proposed CO_2 pipelines.

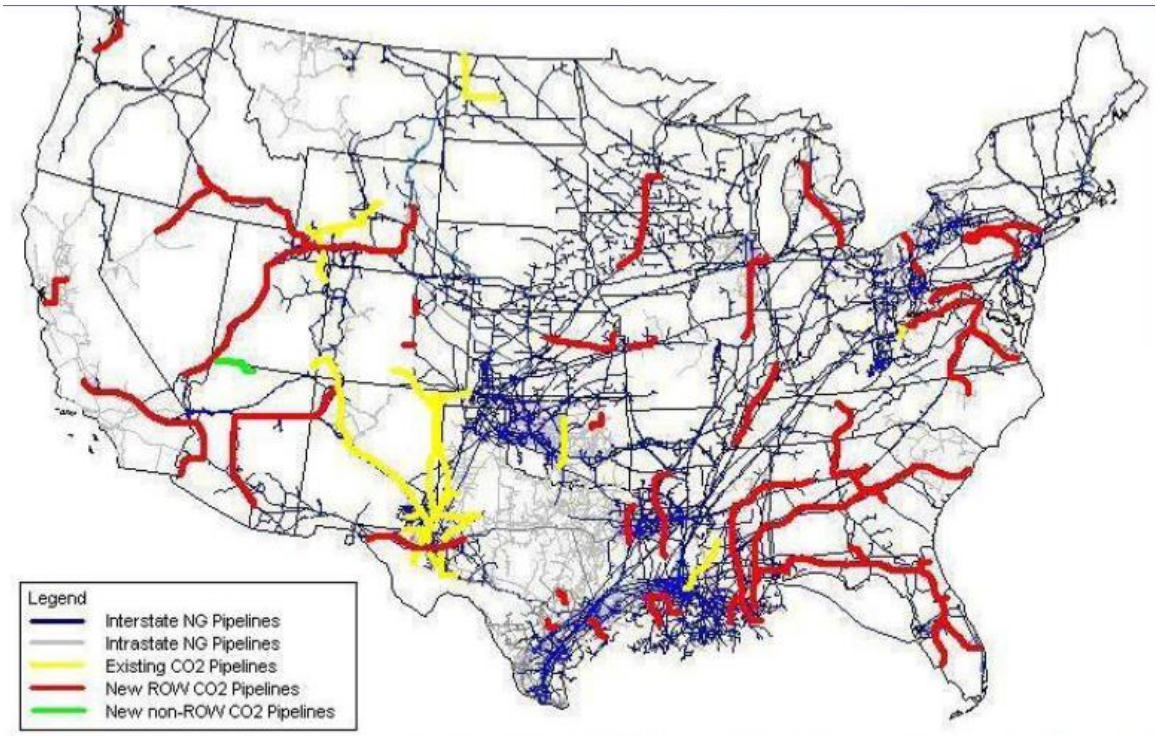

Figure 186: CO_2 pipelines

ROW- Rights Of Way NG – Natural Gas

At this time there are no CO_2 pipelines in California (CA Carbon Capture and Storage Review Panel, 2010).

10.2.2 Pipeline Regulatory Authority

The construction of pipelines falls under the jurisdiction of US Surface Transportation Board (STB), an independent federal agency within the Department of Transportation. The Surface Transportation Board has regulatory authority over CO_2 pipelines, but its oversight is limited when compared to the Federal Energy Regulatory Commission (FERC) who has oversight over the natural gas and oil pipelines (Parfomak & Folger, 2007).

A company seeking to construct a CO_2 pipeline must secure siting approval from relevant regulatory authorities and must secure Rights of Way (ROW) from landowners along the pipeline route by purchasing easements or by eminent domain. However, STB has no authority in pipeline construction, nor can it provide eminent domain authority to secure ROW for construction of the new pipelines. FERC under the Natural Gas Act (15 U.S.C. §717) provides certificates of public convenience and necessity ensuring safety and security and conferred eminent domain authority (Parfomak & Folger, 2007) for gas and oil pipelines. For example, the 500 mile long Cortez EOR Pipeline extends from Colorado through New Mexico into Texas. This pipeline crosses 130 miles of federal land, 18 miles of Navajos land, 30 miles of Native American reservations, 70 miles of state land, and 300 miles of 700 different landowners private land. Long CO_2 pipelines are impractical if not impossible to site without the power of imminent domain (CA Carbon Capture and Storage Review Panel, 2010).

Securing ROW along existing easements may be one way to facilitate the siting of new CO_2 pipelines. The absence of federal siting authority and the varying degree of regulations imposed by the states may present complications.

California does not have a statute authorizing the use of eminent domain for CO_2 pipelines (CA Carbon Capture and Storage Review Panel, 2010). However, public utilities can use the power of eminent domain when needed for their facilities. Utilizing this authority means that the operator of the CCS pipeline must be a public utility which limits the emitters (such as refineries) from implementing carbon sequestration.

10.2.2.1 Pipeline Rate Regulation

The STB is charged to ensure pipelines fulfill common carrier obligations by charging reasonable rates, establishing reasonable classifications, rules and practices. Pipeline operators are free to set their own rates and service practices with no requirements to file their rates with STB. STB may not begin a rate proceeding for an existing pipeline on its own initiative, and may only do so upon a complaint filed against a pipeline operator by a third party. Thus, it might be difficult for regulators to ensure reasonable pricing for CO_2 until after the pipelines were already in service. In contrast, the natural gas and oil pipeline operators must obtain rate approval from FERC prior to placing a new pipeline in service, and the Commission may review rates on its own initiative. In addition, STB currently has limited resources for pipeline regulatory activities.

10.2.3 Commodity versus Pollutant Classification

Captured CO_2 could be classified as either a commodity or as a pollutant. CO_2 used in EOR (Enhanced Oil Recovery) is considered to be a commodity, because captured CO_2 may be sold for EOR operations and may have further economic potential for enhanced recovery of coal bed methane (ECBM). However, it is unlikely that all the captured CO_2 could all be absorbed in EOR or ECBM applications. In the long run, significant quantities of captured CO_2 will have to be disposed of as industrial pollution, with negative economic value. Furthermore, on April 2, 2007, the U.S. Supreme Court stated that the Clean Air Act gives the U.S. Environmental Protection Agency (EPA) the authority to regulate greenhouse gas emissions, thus Class VI regulation was promulgated Dec. 10, 2010 (75 FR 77230). EPA has developed specific risk based factors for determining whether the injection well is considered an EOR or Class VI geologic sequestration well.

In the US, CO_2 is not considered to be a hazardous waste (EPA CO_2 website). EPA is conditionally excluding the CO_2 stream from hazardous waste regulations, provided that the operator: (i) complies with applicable transportation and related pipeline requirements; (ii) injects the CO_2 into Class VI Underground Injection Control (UIC) wells for the purposes of geologic sequestration; and (iii) prohibits the mixing of the hazardous waste with the CO_2.

10.2.4 Accidents

CO_2 pipelines have experienced few serious accidents. According to the Office of Pipeline Safety (OPS), there were 12 leaks from CO_2 pipelines reported from 1986 through 2006, and none resulted in injuries to people. By contrast, there were 5610 accidents causing 107 fatalities and 520 injuries related to natural gas and hazardous liquids pipelines during the same period (Parfomak & Folger, 2007). Since CO_2 account for <1% of the total natural gas and hazardous liquid pipelines, it is difficult to draw firm conclusions. It appears that mile for mile, CO_2 pipelines are safer than other types of pipelines regulated by OPS. However, when the CO_2 pipeline network expands significantly to support CCS, more CO_2 pipeline accidents are likely to occur.

10.2.5 Existing Pipeline Regulations

The Hazardous Liquid Pipeline Act of 1979 was amended to regulate interstate transport of CO_2 (49 U.S.C. §601). Department of Transportation (DOT) regulates the design, construction, operation and maintenance, and spill response planning for CO_2 pipelines No person may transport any hazardous liquid or CO_2 unless the hazardous liquid or CO_2 is chemically compatible with the pipelines, including all components, and any other commodity that it may come into contact with while in the pipeline (49CFR§195.4). Pipeline safety is regulated under Title 49 of the Code of Federal Regulations, Parts 190-199.

All pipelines that fall under the regulations will have to be regularly tested, maintained, and records kept for the life of the pipeline by each operator. In addition a CO_2 pipeline system must also be designed to mitigate the effects of fracture propagation (49CFR§195.111). The operator must maintain current maps showing location, and identification of the pipeline facilities, all crossing of public roads, railroads, rivers, buried utilities and foreign pipelines. Operators must also maintain records showing maximum operating pressure for each pipeline, diameter, grade, type and nominal wall thickness for all pipes. This information, even though exists, is not under the public domain because the government deems this as sensitive information vital to the security of the country. The featured pipeline locations in socalCARB.org are strictly estimates. This information was obtained from the California Energy Commission's Systems Assessment & Facilities Division, Cartography Unit.

Under the pipeline regulations, provisions are provided for the installation of new pipes and for conversion of existing pipes to transport CO_2. All requirements must be met before any transportation of CO_2 can commence. For detail requirements, please review Title 49 of the Code of Federal Regulations, Parts 190-199. Additional information on pipeline safety can be viewed on the PHMSA website.

10.2.6 CO_2 Properties

CO_2 occurs naturally in the atmosphere at a concentration of 0.038% by volume. At normal atmospheric pressure and temperature, the stable CO_2 phase is in vapor phase. Dense phase (liquid and supercritical fluid) varies with temperature and pressure, occurs in the blue areas shown in the CO_2 phase diagram (Figure 187). Pipeline transportation of CO_2 over long distance is most efficient and economical when CO_2 is in a dense phase. This is due to the lower friction drop along the pipeline per unit mass of CO_2 compared to transporting the CO_2 as a gas or as a two-phase combination of both liquid and gas. Thus it is important to keep the CO_2 in a single phase. CO_2 is transported through pipelines in the dense phase (liquid and/or supercritical phase) between 86-200 bar (1250-2900 psi; Element Energy, 2010). This section is recapped mostly from DNV (2010).

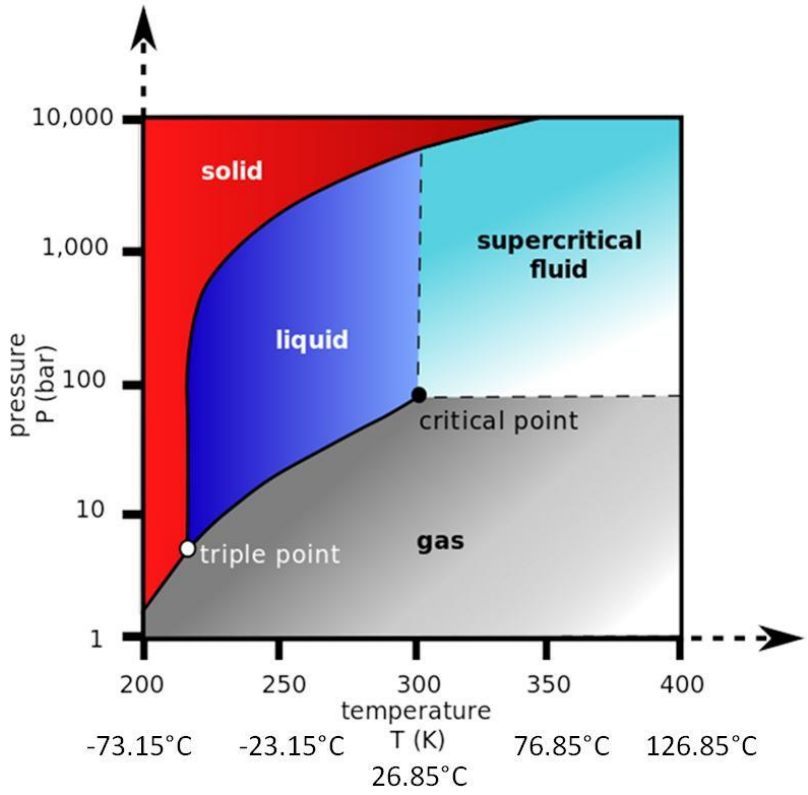

Figure 187: CO_2 Phase Diagram
Wikipedia

Supercritical CO_2 is a highly volatile fluid that will rapidly evaporate when depressurized to ambient conditions. High pressure CO_2 will undergo significant cooling when released into the atmosphere. When the temperature of CO_2 is dropped to below the dew point (-79°C), the cooling effect will condense the water vapor in the atmosphere to form a cloud which is visible to humans, making it difficult to distinguish CO_2 solids from the condensed water within the cloud.

Table 34 states the physical properties of pure CO_2. When designing the pipeline system, the CO_2 stream composition should be considered to assess the hazards that may arise from the other chemical components.

It is important to note that CO_2 is odorless; adding some odor additives may be a beneficial strategy for an early detection of a leak (Barrie et al, undated).

Table 34: Physical Properties of pure CO_2
DNV 2010

Property	Value
Molecular Weight	44.01 g/mole
Critical Pressure	73.8 bar
Critical Temperature	31.1°C
Triple Point Pressure	5.18 bar
Triple Point Temperature	-56.6°C
Aqueous Solubility at 25°C, 1 bar	1.45 g/L
Gas Density at 0°C, 1 bar	1.98 kg/m3
Density at Critical Point	467 kg/m3
Liquid Density at 0°C, 70 bar	995 kg/m3
Sublimation temp, 1 bar	-79°C
Latent heat of vaporization (1 bar at sublimation temp)	571 kJ/kg
Solid density at freezing point	1562 kg/m3
Color	none
odor	none

10.2.6.1 CO_2 composition

The physical properties of a CO_2 stream are defined by its individual chemical components and may vary depending on:

- its captured source, such as from combustion and processing of fossil fuels (e.g. pre-combustion, post-combustion or oxy-fuel processes, Table 35),
- its generation from industrial processes (e.g. steel or cement manufacturing, refineries or chemical industries),
- whether it was extracted from high concentrated CO_2 hydrocarbon streams, or expelled from natural sources.

Depending on the process, different types and amounts of chemical components may also be included with the CO_2 stream and can create issues with the transport of CO_2. The characteristic of these chemical components must be considered when designing the pipeline.

Table 35: Predicted composition of CO_2 from power plant capture
Element Energy 2010

Coal Fired Power Plants	Component	Coal Fired % vol	Gas Fired % vol
Post combustion capture	SO2	<0.01	<0.01
	NO	<0.01	<0.01
	N2/Ar/O2	0.01	0.01
Pre combustion capture	H2S	0.01-0.6	<0.01
	H2	0.08-2.0	1
	CO	0.03-0.4	0.04
	CH4	0.01	2
	N2/Ar/O2	0.03-0.6	1.3
Oxyfuel	SO2	0.5	<0.01
	NO	0.01	<0.01
	N2/Ar/O2	3.7	4.1

10.2.6.2 Solvent Properties

The solvent properties of CO_2 increase with additional pressure and temperature. Supercritical CO_2 is a highly efficient solvent. However, when CO_2 changes from dense phase to the gaseous state there is virtually no solvent capability. There is a potential for any substance that is in solution within a high pressure CO_2 pipeline to be precipitated out when the pressure drops. The precipitation of any hazardous substance may result in harmful human exposure or environmental damage at or near the point of release, and should be considered as part of a safety risk assessment.

10.2.6.3 Water Solubility

In the gaseous phase, the ability of CO_2 to dissolve in water increases with a decrease in pressure and increase in temperature. However, in the liquid phase, the solubility of water increases with increasing pressure. Currently there is limited knowledge on water solubility models for CO_2 streams including other chemical compounds. The ability of the CO_2 stream to dissolve in water may be significantly affected by the different chemical components and should be considered when designing the pipelines.

10.2.6.4 Chemical Reactions

Chemical reactions due to temperature and pressure variations and the mixture of the CO_2 stream must be addressed to avoid potential issues listed in Table 36 below. For example, even though water is non-toxic, water in CO_2 can form hydrates when combined with other chemical components within the CO_2 stream thereby causing corrosion problems, weakening of the piping

material, and create material fatigue and fracture. These problems can impinge on the safe operation of the pipeline system. Element Energy (2010) reported that carbon steel can corrode at a rate of more than 10mm/year in wet, pure CO_2.

Table 36: Main issues related to various components in CO_2 stream
DNV 2010

Component	*Properties*									*Comment*
	Health & Safety	Pipeline capacity	Water solubility	Hydrate formation	Materials	Fatigue	Fracture	Corrosion	Operations	
CO_2	●	●	●	●	●	●	●	●	●	Non-flammable, colourless, no odour at low concentrations, low toxicity, vapour heavier than air
H_2O				●	●	●	●	●	●	Non-toxic
N_2		●	●							Non-toxic
O_2			●					●		Non-toxic
H_2S	●	(●)			●	●	(●)	●		Flammable, strong odour, extremely toxic at low concentrations
H_2		●	●				●			Flammable, non-condensable at pipeline operating condition
SO_2	●		●					●		Non-flammable, strong odour
CO	●		●							Non-flammable, toxic
CH_4+		●	●						●	Odourless, flammable
Amines	●									Potential occupational hazard
Glycol	(●)							(●)		Potential occupational hazard
Ref. Sec.	3.3.3	4.5.3	2.3.5	4.5.11	5	5.6	5.5	5.1	7	

10.2.6.5 Safety Evaluations

Pipelines should be designed with acceptable risk. The risk needs to consider the likelihood of failure and the consequence of failure, which is linked to the content of the pipeline and the level of human activity around the pipeline. A systematic risk assessment and risk management plan identifying major hazards and incidents should be performed.
Although CO_2 is not considered a hazardous liquid, it is effectively treated as such. CO_2 is listed as a non-flammable hazardous material under DOT regulations (CFR § 172.101), the agency applies the same safety requirements to CO_2 pipelines as it does to pipelines carrying hazardous liquids such as crude oil, gasoline and anhydrous ammonia (49CFR § 195). According to ASME B31.4, dense (liquid and supercritical phase) is classified as a Hazardous Liquid. CO_2 is dangerous when inhaled at concentrations above 7%. Table 37 and Table 38 show the acute health effects and occupational exposure limits for CO_2. In addition to the health hazards related to pure CO_2, the toxicity of individual chemical components (e.g. H_2S, CO, etc.) should be considered as part of a safety risk assessment.

CO_2 may affect the flora and fauna. Animals exposed to high CO_2 concentrations are assumed to experience the same effects as humans. The consequences associated with accidental or planned release of CO_2 and its impact on flora, fauna, livestock and environment should be included as part of the risk assessment.

Table 37: Acute health effects of high concentrations of inhaled CO_2
DNV 2010

CO_2 Concentration in Air (% v/v)	*Exposure*	*Effects on Humans*
17 – 30	Within 1 minute	Loss of controlled and purposeful activity, unconsciousness, convulsions, coma, death
>10 – 15	1 minute to several minutes	Dizziness, drowsiness, severe muscle twitching, unconsciousness
7 – 10	Few minutes	Unconsciousness, near unconsciousness
	1.5 minutes to 1 hour	Headache, increased heart rate, shortness of breath, dizziness, sweating, rapid breathing
6	1 – 2 minutes ≤ 16 minutes Several hours	Hearing and visual disturbances Headache, difficult breathing (dyspnoea) Tremors
4 – 5	Within a few minutes	Headache, dizziness, increased blood pressure, uncomfortable breathing (Equivalent to concentrations expired by humans)
3	1 hour	Mild headache, sweating, and difficult breathing at rest
2	Several hours	Headache, difficult breathing upon mild exertion
0.5-1	8hrs	Acceptable occupational hazard level

Table 38: Occupational exposure limits
DNV 2010

Exposure Time	*% CO_2*	*Comment*	*Reference*
10 hours	0.50%	Time weighted average	NIOSH (US)
8 hours	0.50%	Time weighted average	OSHA (US)
	0.50%	Occupational Long Term Exposure Limit (LTEL)	COSHH HSE (UK)
60 min	4%	Emergency Exposure Level for submarine operations	USA Navy
	2.5%	Emergency Exposure Level for submarine operations	National (US) Research Council
	5%	Suggested Long Term Survivability Exposure Limit	HSE (UK)
	2%	Maximum exposure limit	Compressed Gas Association 1990
20 min	3%	Maximum exposure limit	Compressed Gas Association 1990
15 min	1.5%	Occupational Short Term Exposure Limit (STEL)	COSHH HSE (UK)
	3%	Short Term Exposure Limit (STEL)	Federal occupational safety and health regulations (US)
10 min	4%	Maximum exposure limit	Compressed Gas Association 1990
7 min	5%	Maximum exposure limit	Compressed Gas Association 1990
5 min	5%	Suggested Short Term Exposure Limit (STEL)	HSE (UK)
	6%	Maximum exposure limit	Compressed Gas Association 1990
3 min	7%	Maximum exposure limit	Compressed Gas Association 1990
1 min	15%	Exposure limit	NORSOK (Norway)
<1 min	4%	Maximum Occupational Exposure Limit	Federal occupational safety and health regulations (US)

Other health effects that should be evaluated include injuries caused by direct exposure of the released solid state particles or cryogenic burns, inhalation of solid CO_2 particles within a release. Inhalation of air containing solid CO_2 particles within a release cloud is particularly hazardous since this could result in cryogenic burns to the respiratory tract as well as toxicological impact upon sublimation.

10.2.6.6 Accidental release of CO_2

The decompression of CO_2 differs from that of hydrocarbons in that the release may appear as a combination of gaseous and solid state CO_2. The solid CO_2 particles released should be considered in case there is potential for direct impingement on nearby critical equipment. The release of cool CO_2 will most likely cause condensation of water and form a cloud visible to the human eye until the release cloud warms to above the air's dew point temperature. However, a release of warm or hot CO_2 above the air's dew point temperature will be invisible since there is no condensing of water or solid CO_2. Dispersion of gaseous CO_2 can best be compared and modeled with an equivalent release of propane (C_3H_8) due to their comparable physical properties.

10.2.7 Pipeline Concept and Design

CO_2 pipelines should be designed in accordance with the industry recognized standards and applicable regulatory requirements. Pipeline transportation for CO_2 over longer distances is most efficient and economical when the CO_2 is in the dense (liquid or supercritical) state. Pipeline design should also consider the following, details can be found in Det Norske Veritas, Design and Operation of CO_2 Pipelines (DNV, 2010):

- Access to transport network and pipeline layout -- pipeline layout is a critical part of the pressure safety functions and also determines the accessibility for maintenance and repair.
- Pressure control and protection system -- comprises the pressure control system for maintaining the operating pressure within acceptable limits during normal operation, and the pressure safety system and associated instrumentation/ alarm systems for protecting the downstream system during incidental operation.
- Pipeline Protection -- the minimum cover depth over roads, crossing, lakes, etc. for onshore and offshore pipelines should be followed as suggested by the regulatory and pipeline guidelines.
- Dewatering -- performance and reliability of CO_2 stream dewatering is essential for hydrate formation control.
- Flow Assurance -- the pipeline should be able to operate at a reduced rate without significant operational constraints or upsets.
- Seasonal temperature variations -- there is a significant reduction in specific gravity of supercritical CO_2 with increasing temperature which may cause the rapid sublimation of CO_2 with a corresponding increase in fluid volume by 750 times.
- Flow/internal coating -- generally is not recommended because of concerns of detachment of the internal coating in a pressure reduction situation causing process upsets or plugging of injection wells. Sempra Energy, a gas utility company in California believes the flow coating detachment issue can be managed, and should be applied if needed (Personal communication, 2012).
- Thermal Insulation – to prevent a rapid depressurization situation which may cause sub-zero temperatures, potentially causing external icing on the pipeline.
- Hydrate formation, prevention and remediation -- the primary strategy for hydrate prevention should be sufficient dewatering of the CO_2 stream. Water content should be controlled and monitored at the inlet of the pipeline.
- Pigging stations -- the pig launcher/trap is to enable dewatering during commissioning and pigging either as part of commissioning or during operations.
- Vent stations -- needed for depressurizing sections of the pipeline during inspection, maintenance and repair. The design and operation of the vent station shall be based to

handle a robust release of the worst case scenario with reasonable foreseeable CO_2 flow and weather conditions as well as account for all hazardous components within the CO_2 stream.

- Pipeline routing -- onshore pipelines should consider the density population of the area using dispersion modeling. For offshore pipelines, surface vessel activities shall be considered in the same manner as natural gas pipelines.
- CO_2 stream composition evaluations -- if mixing of different CO_2 streams occur in a pipeline network, it must be assured that the mixing of the individual compounds do not cause risk of water dropout due to reduced solubility in the comingled stream and any cross chemical reactions or effects.
- Water content -- maximum water content in the CO_2 stream at the upstream battery limit shall be controlled to ensure that no free water may occur at any location in the pipeline.
- Toxic or environmentally hazardous substance content -- limitations on toxic or environmentally hazardous substances should be determined based on the appropriate toxic harm criteria.
- Pipeline internal corrosion protection -- dry pure CO_2 and pure CO_2 that contains dissolved water well below the saturation limit are non-corrosive to carbon steel at operation conditions. However, carbon steel can corrode at a rate of more than 10mm/year in wet pure CO_2 (Element Energy, 2010). Internal polyethylene liners may be a cost effective alternative to stainless pipelines used for corrosion protection.
- Linepipe Materials -- Carbon Manganese (C-Mn) steel linepipe is considered feasible where water content of the CO_2 stream is controlled to avoid formation of free water in the pipeline.
- Table 39 shows the compatibility of different materials with dense and vapor CO_2.

Table 39: Material types compatible with dense and vapor CO_2
304 -- stainless steel grade
316 – stainless steel grade
DNV 2010

	No free water		*With free water*	
Material types	Pure CO_2	$CO_2 + H_2S$	Pure CO_2	$CO_2 + H_2S$
C-and low alloy steel	•	•		
304	•	•	•	•
316	•	•	•	•
13Cr	•	(•)	•	(•)
22Cr (duplex)	•	(•)	•	(•)
25Cr (duplex)	•	(•)	•	(•)
Nickel based alloys	•	•	•	•

- Internal Lining/cladding -- use of an internal liner or cladding for corrosion protection is normally not cost efficient for longer pipelines.
- External corrosion -- is not considered significantly different to the hydrocarbon pipelines.
- External coating/nonmetallic seals/lubricants -- should be compatible with the operating envelope in terms of pressure and temperature of the pipeline.
- Wall thickness design -- is normally governed by pressure (internal and external) containment criteria.
- Running ductile fracture control -- The pipeline shall have adequate resistance to propagating fracture.

10.2.7.1 Re-qualification of existing pipeline

Existing pipelines should comply with the same requirements as pipelines designed specifically for the transport of CO_2. Historical information regarding how the system has been operated should be assessed. A flow assessment to identify the feasibility of re-qualification of the existing pipeline should include the following steps as shown in Figure 188.

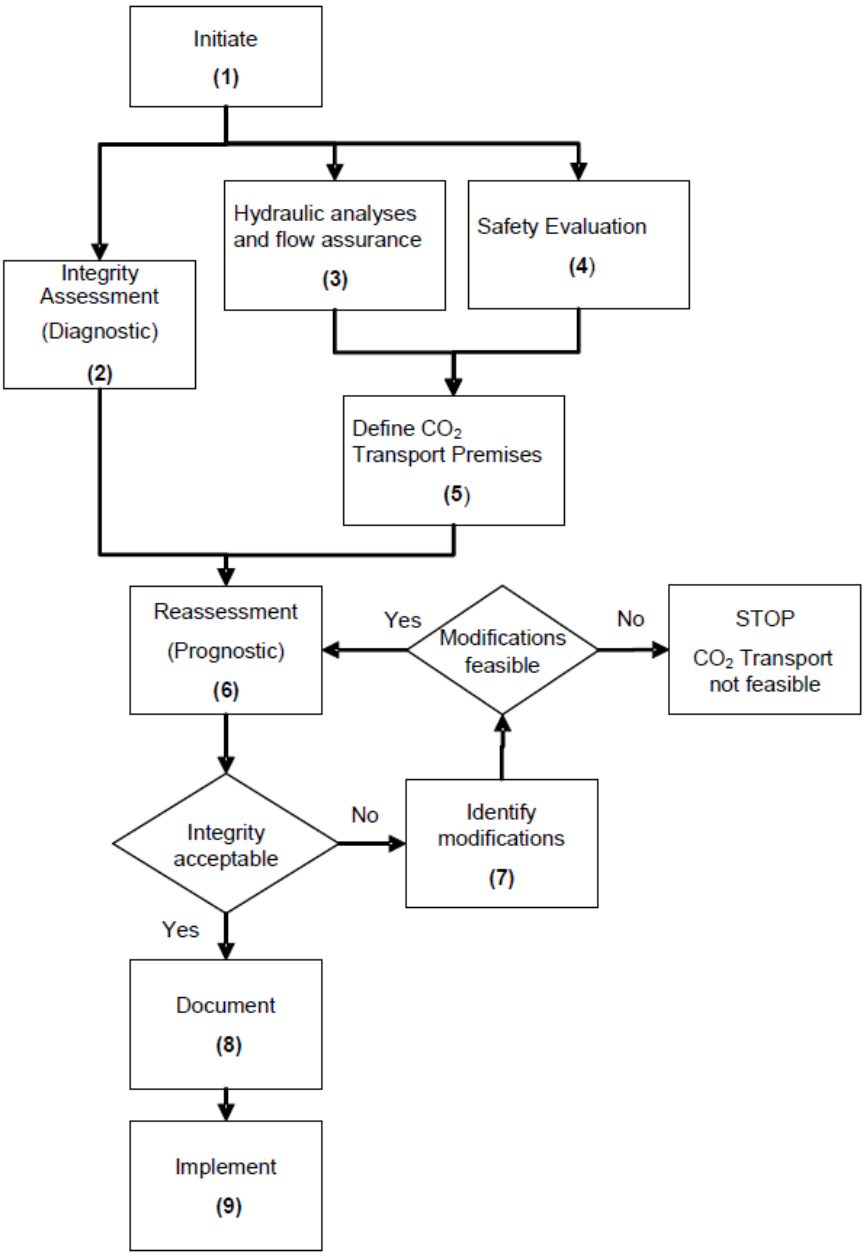

Figure 188: Re-qualification Process for pipeline system change into CO_2 transport
DNV, 2010

10.2.7.2 Feasibility of re-qualification of existing pipeline

A meeting was held with Sempra Energy, a gas utility company to discuss their experience with pipeline risk. In addition, permitting and cost of new pipelines, re-certification of existing gas pipelines to CO_2, and other maintenance and logistic issues were discussed. The conclusions were:

- There are virtually no un-used gas transmission pipelines that can be converted for CO_2 usage.
- Transmission gas pipelines operate at about 700psi while the gas pipeline buried under streets operates at about 70psi. Normal operating pressure for CO_2 is between 86-200 bar (1250-2900 psi; Element Energy, 2010). Basically, the existing gas pipeline is not capable of handling the pressure requirements needed for the transportation of CO_2 without a major improvement.
- Cost for converting a gas pipeline to CO_2 pipeline is as high as for constructing a new pipeline.
- The cost for constructing a new pipeline is approximately about $1million per mile (labor material, labor and ROW).
- Chrome pipe and stainless steel will be too expensive to use, nano-steel coated, or plastic coated steel pipes are a good substitute for the CO_2 pipeline. Sempra does not think flow coating will be an issue as indicated by the Det Norske Veritas (2010) guidelines. Detachment of the internal coating can be monitored and managed.
- An Amine Absorption or Pressure Swing Adsorption (PSA) unit (about $4 million) can be used to separate CO_2 at existing energy infrastructure, a dryer unit is needed to eliminate the water in the CO_2 stream, a methane reformer (approximately $1 million) is required to remove methane, and the captured hydrogen can be re-used at the refinery.
- A CO_2 sensor and blower can be incorporated in low lying areas where CO_2 pipelines are laid to disperse a CO_2 leak, if any.
- Oil pipeline can also be converted to CO_2 pipeline, but the cost will be high as well.

The Alaska pipeline maximum operating pressure is at 1180psi (BP Alaska Pipeline Fact Sheet, 2006). A personal conversation with Kinder Morgan verifies that oil pipelines operate at about 1000psi, which is too low for CO_2 transport. An oil pipeline can be converted to transport CO_2, but at a substantial cost also.

10.2.8 Estimating Pipeline Diameter

There are several equations to estimate the diameter of CO_2 pipelines. However, none of them account for changes in altitude. The MIT formula (Canadian Clean Power Coalition, 2011; MIT, 2006 updated 2009) is copied below:

$$D = (32Lfm^2 / [(P_1-P_2)\pi^2\rho])^{0.2}$$

Where: D is the diameter in meters
L is the length of pipe in meters
f is the Fanning friction factor
m is the mass flow rate in kg/m3
P_1 and P_2 are the pressures in Pascals at the beginning and end of the pipe
ρ is the density in kg/m3

Table 40 shows the diameter of the pipeline and the potential CO_2 flow rate. Geomehanics Technologies has studied the feasibility of transporting 1 MMt of CO_2 per year from the one of top industrial sources (Chevron El Segundo Refinery, Table 33: Top 20 CO2 Industrial Sources) to the injection site, Wilmington Graben, 20 miles to the south (Figure 183: LA Basin sink map). Our numerical modeling analysis recommends a minimum of 4 injection wells each injecting 250,000 Mt of CO_2 and placed with a minimum distance of 1000 m (32850 ft) apart to each other to avoid extensive CO_2 plume interference (Geomechanics Technologies Progress Report, March, 2012). A 12" pipe will be sufficient to transport 1 MMt of CO_2 to these 4 injection wells.

Table 40: Pipeline Diameter and CO_2 Flow rate Range
MIT, 2006, updated 2009
Mt = Metric ton

Pipeline Diameter (inch)	CO_2 Flow Rate (Mt/yr)	
	lower bound	upper bound
4		0.19
6	0.19	0.54
8	0.54	1.13
12	1.13	3.25
16	3.25	6.86
20	6.86	12.26
24	12.26	19.69
30	19.69	35.16
36	35.16	56.46

10.2.9 Pipeline Estimate Cost

Analysts commonly develop cost estimates for CO_2 pipelines based on comparable construction costs for the natural gas pipelines. According to the University of California study analyzing the cost of US transmission pipelines constructed between 1991 and 2003, on average, the labor, materials, rights of way and miscellaneous costs accounted for 45%, 26%, 22% and 7% respectively. In 2002, it cost on average $800,000 per mile (Parfomak & Folger, 2007). The price of large diameter pipe was around $600 per ton in late 2001, but by mid-2006, the price has jumped to $1200 per ton. Three estimates on cost for pipeline are described briefly in this report; the first is from National Energy Technology Laboratory (NETL), the second from Oil and Gas Journal, and the third price estimate was obtained from Sabine Pipeline Company.

10.2.9.1 NETL Capital Cost Estimates:

NETL (Canadian Clean Power Coalition, 2011; NETL/DOE, 2010) has established an approach to estimate several components of the capital cost of the CO_2 pipeline. These equations were originally developed by the University of California and modified to include escalation to bring the costs to June 2007 year dollars. The pipeline cost is broken down into 4 categories: (i) Materials, (ii) Labor, (iii) Miscellaneous, and (iv) Right of Way. The Miscellaneous costs include survey, engineering, supervision, contingencies, allowances, overhead and filing fees.

Pipeline Cost

Materials = $\$64,632 + \$1.85L(330.5D^2 + 686.7D + 26,960)$

Labor = $\$341,627 + \$1.85L(343.2D^2 + 2074D + 170,013)$

Misc = $\$150,166 + \$1.58L(8,417D + 7,234)$

Right of Way (ROW) = $\$48,037 + \$1.2L(577D + 29,788)$

Where D = diameter in inches

L = length in miles

Other Capital Cost

CO_2 surge tank = $1,150,636

Pipeline control system = $110,632

Transport Operating and Maintenance Cost

Fixed O&M = $8,632/mile/year

The NETL study also provided rough estimates costs of pipelines for various terrains. See Table 41 below.

Table 41: Pipeline Cost Multiplier for Terrain
DOE/NETL, 2010 and Element Energy, 2010

	Kinder-Morgan ($/inch/mile)	Cost Multiplier
Flat, dry	$50,000	1.0
Mountains	$85,000	2.5
March, wetland	$100,000	
River	$300,000	
High population	$100,000	
Offshore (150' – 200' depth)	$700,000	
Desert		1.3
Forest		3.0
Offshore (<500m depth)		1.6
Offshore (>500m depth)		2.7

10.2.9.2 Oil and Gas Journal Estimate:

The November 1, 2010 the Oil and Gas Journal published costs for natural gas pipelines over the past decade. The equations (Canadian Clean Power Coalition, 2011) below calculate the same 4 components as the NETL above. The data suggested that the cost of pipelines have double compared to the costs in 2008 and 2009, and have increased by a factor of 4 since 2006 (Canadian Clean Power Coalition, 2011).

Materials = L(22,800D + $14,480)
Labor = L(26,390D + $203,000)
Misc = L(13,500D + $286,000)
Right of Way (ROW) = L(893D + $10,800)

Where D = diameter in inches
L = length in miles

10.2.9.3 Actual pipeline cost:

For comparison purposes, we also priced-out 3 different material of 12" pipe for CO_2 transportation (Table 42). The cost below is straightly material cost only. The use of stainless steel is too prohibitive. The most likely scenario will be carbon steel with some compatible coating.

Table 42: 12" Pipe, Costs per foot of different materials
(Sabine Pipe, Aug 2010)

Type	Cost per foot
12" 100# stainless steel	$1700/ft
12" 49.61# chrome	$137.29/ft
12" 49/61# carbon steel with 2 coats 90HS Epoxy 4-6mils	$45.95/ft

10.2.9.4 Comparison between the 3 different estimates:

We perform a quick calculation based on the 3 different methods discussed above for a 1 mile length of 12" pipeline. NETL's cost is the lowest for the material only estimate. Oil and Gas has the highest cost estimate while the actual price quote falls in between the range (Table 43). After adding in the Labor, miscellaneous and ROW cost, NETL cost per mile is about $1.45 million per mile, while the Oil and Gas Journal cost is about $1.16. This is roughly in line with the estimate given by Sempra Energy. In a recent interview with Sempra Energy (Personal communication, 2012), the average cost to construct an all-inclusive new pipeline is estimated to be $1 million per mile.

Thus a 20 mile pipeline from Chevron El Segundo Refinery to the Wilmington Graben injection site will be $28 million using the NETL estimate, $23 million using the O&G estimate, and $26 million using Sempra's estimate; -- $20 million for pipeline, $4 million for Pressure Swing Adsorption unit, $1 million for dryer unit and $1 million for methane reformer unit. (see Feasibility of re-qualification of existing pipeline section above).

Table 43: Estimated 12" Pipeline Cost per Mile

Diameter = 12"	NETL Estimate	O&G Estimate	Sabine quote
Materials - carbon steel w/2 coats of Epoxy	$217,798	$288,080	$242,616
- chrome			$724,891
- stainless steel			$8,976,000
Labor	$793,569	$519,680	
Misc	$321,182	$336,980	
ROW	$92,091	$21,516	
TOTAL	$1,424,640	$1,166,256	

10.3 Conclusions

Geomechanics Technologies has documented the top 20 CO_2 emission sources within the LA Basin. A southern California Carbon Atlas is produced by integrating known sinks, sources and pipelines. This interactive atlas can be viewed on our website: www.socalCARB.org. We also performed a feasibility study on the potential for converting existing oil or gas pipelines for CO_2 transport. There are virtually no un-used gas transmission or oil pipelines that can be converted for CO_2 usage. The cost for constructing a new pipeline is approximately about $1million per mile (labor material, labor and ROW).

11 Conclusion

Geomechanics Technologies has completed a detailed characterization study of the Wilmington Graben offshore Southern California for large-scale CO_2 storage. This effort has included evaluation of existing wells in both State and Federal waters, field acquisition of about 175 km (108 mi) of new seismic data, drilling 2 new wells drilling, deepening 1 existing well, and development of integrated 3D geologic, geomechanics, and fluid flow models for the area. The geologic analysis indicates that 796 MMt (P50) of storage capacity is available within Pliocene and Miocene formations in the Graben.

Integrated geologic, geomechanical, and fluid flow models have been developed with varying distributions of sand and shale sequences. Each of which are consistent with the limited well data, but likely span the range of sand and shale content. Numerical analysis of fluid migration indicates that injection into the Pliocene Formation at depths on the order of 1500 m (5000 ft) would lead to unacceptable vertical migration of the CO_2 plume, for the full range of reasonable lithology distributions. However, injecting into the deeper Miocene sands at > 2100 m (7000 ft) depth offers containment in the fluid migration modeling in 2 out of 4 scenarios ran.

The results of the fluid flow model were used as input in a geomechanical model established for two areas of the graben. The geomechanical model was developed to assess surface deformation, induced stresses, and fracture and fault activation risks associated with large scale CO_2 injection. No fault slips are observed, even with the most conservative fault properties inputs (cohesions and friction angles), for 30 years of CO_2 injection. Qualitative risk analysis and ranking indicates that large scale CO_2 injection into the Wilmington Graben presents relatively higher risk than other potential storage sites within the US primarily due to its geologic and geomechanical setting.

Based on our current analyses, we cannot recommend the shallow to mid-Pliocene formations be considered further for large scale CO_2 injection. Recent well drilling in 2014, however, indicates that deeper sands are available at depths exceeding 2100 m (7000 feet) which could be viable for large volume storage. The deep well DOE#2 also indicated the existence of a relatively thick shale interval that can serve as a strong barrier to vertical migration, which was confirmed by the deepening of SFI#1 well. More wells will need to be drilled to ascertain the lithology around the injection well.

For vertical containment, injection would need to be limited to about 250,000 metric tons per year per well, would need to be placed at depths greater than 7000ft, and would need to be placed in new wells located at least 1 mile from any existing offset wells. As a practical matter, this would likely limit storage operations in the Wilmington Graben to about 1 million tons per year or less.

Risks associated with CO_2 injection and sequestration have been evaluated. An interactive source, sink and pipeline map is produced. Existing gas and oil pipelines are not

capable or built to transport CO_2. The cost to build any CO_2 pipeline will be in excess of $1 million per mile.

12 Lessons learned

12.1 Lack of horizontally continuous caprock is usually insufficient

As discussed in *Geologic model development*, the offshore Wilmington Graben lies within a turbidite depositional environment and lithology is known to vary often, both vertically and laterally, over relatively small distances. A simple interpolation between the sparsely distributed wells (12 wells total for an area over 150 km^2 (60 mi^2)) would have created an overly simplified lithologic model. To account for such variation and uncertainty, therefore, strategic phantom wells were introduced to force the Rockworks software to create a heterogeneous lithology, honoring the general stratigraphic trend and turbidite depositional regime. Stochastic modeling approach for the geologic model could not be properly implemented, but the overall workflow established from the geologic model to gas migration model to geomechanical model work out well.

As discussed in the *CO2 injection and migration modeling* section above, this heterogeneous lithology model was used as a starting point for CO_2 migration and fluid flow simulation, and material properties were mapped from the geologic model grid onto the flow simulation model grid. Because lithologic heterogeneity, several models were constructed to capture geologic variations, with statistically appropriate varying proportions of shales and sands. For 8 of these scenarios, the horizontal migration of CO_2 was constrained, but two scenarios show vertical migration, no matter how convoluted the path was.

The lesson learned here is that a horizontally and vertically varied lithological environment, such as a turbidite depositional regime, without a vertically superseding, horizontally extensive caprock, will usually prove insufficiently confining for significant volumes of injected CO_2. However some of our models with injection at depths of 2135 m (7000 ft) and greater did indicate containment, even with no vertically superseding, horizontally extensive caprock. Safe injection requires limiting injection rates and volumes significantly. Ultimately the primary lesson here may be that more wells should be drilled in such environments to accurately ascertain the lithology and gas migration simulations run again to confirm no CO_2 leakage is possible at these greater depths.

12.2 Caprock Requirements

A thick and continuous caprock is necessary for a reduced risk CO_2 sequestration project. We have developed a Quantitative Risk & Decision Analysis Tool (QRDAT) for caprock integrity evaluation, to assess the potential for leakage during CO_2 injection. We consider three primary leakage mechanisms. These are tensile fracturing of the caprock, fault activation, and well damage.

12.2.1 Depth and caprock lateral extent/thickness

These parameters assess the lateral continuity of the caprock by normalizing it to a fixed value (formation depth and caprock thickness, respectively). Clearly, the more extensive a formation is in the lateral direction, the smaller the chance that CO_2 will reach a spill point and migrate upwards. Therefore, high ratio values for these parameters indicate low failure likelihood.

12.2.2 Caprock strength

A stronger caprock has a lower risk for caprock integrity loss, due to a lower risk for both tensile fracturing and the onset of new faults in the caprock. A fracture develops only when the compressive strength in a rock is overcome, so the higher the unconfined compressive strength the lower the risk for the development of fracture networks. Note that a stronger caprock may lead to higher pressure build-up, which may lead to overburden and surface heave (e.g., In Salah (Rutqvist et al. 2010)). Bending of the caprock during uplift may lead to the development of shear stresses at the top of the caprock (Vilarrassa et al. 2011), but no cases of caprock failure due to surface heave have been reported thus far.

12.2.3 Caprock permeability

Relatively permeable caprocks may lead to loss of CO_2 containment, simply because CO_2 can migrate through them under the influence of strong buoyancy forces. This can occur for caprocks with permeabilities as low as $k > 10^{-18}$ m^2 (Zhou et al. 2008). The permeability of the caprock mainly influences the potential pressure build-up in the caprock and so too the development of fractures. The higher the permeability of the caprock, the more fluid penetration can occur and the less pressure can build up, and, thus, a lower failure risk pertains.

12.2.4 Caprock dip

Caprock dip mainly influences the migration of CO_2 within the reservoir. Due to high buoyancy of the CO_2, the supercritical fluid will tend to move upward in the reservoir until structurally trapped. The greater the caprock dip, the further the CO_2 migrates upwards, with the risk of reaching a spill point or discontinuity in the caprock also increasing. Doughty (2010) demonstrates that dipping caprock-storage zone systems lead to preferred CO_2 migration in the up-dip direction. The greater the dip, and its extent, the more quickly, and further, the CO_2 may migrate laterally. Sub-horizontal reservoirs below anticlinal caprock structures, however, form structural traps and therefore securely contain CO_2.

12.2.5 Caprock thickness

As would be expected, thicker caprocks are lower risk for integrity loss, simply because fracture networks and faults can develop further into the caprock without fully transgressing it. For example, at In Salah a fracture network reaches 100-200 m into the caprock (Verdon et al.

2013), but since the caprock package is up to 950 m thick, this has no effect on the security of storage.

12.2.6 Caprock heterogeneity

Caprock heterogeneity increases the risk for integrity and containment loss for various reasons. First, in case of lateral heterogeneity (e.g. in turbidite settings), CO_2 may reach discontinuities in the caprock, which may allow upward migration. In very heterogeneous caprocks, connected fluid pathways to higher strata may be present. Second, heterogeneity of lithology within the caprock may lead to stress concentrations, rendering these interfaces prone to tensile and shear failure.

12.2.7 Number of sealing strata

The number of individual sealing strata within the general caprock package influences the integrity of the system simply by forming a baffled system of multiple storage locations with multiple caprocks which act as buffers if the primary seal below them fails. Rutqvist et al. (2008) assessed the risk for caprock failure in multilayered systems. Assessing stress developments in a storage system with three caprocks, of which the lower two have failed, they concluded that ensuing upward migration of CO_2 creates the highest shear and tensional failure risk at the interface of the shallowest storage zone and intact caprock. Thus existence of multiple caprocks is not a guarantee for CO_2 containment; however, in general the risk for integrity loss decreases with an increasing number of caprocks above the primary intended seal.

Table 44 gives the risk factor ranges for the various issues discussed above.

Table 44: Risk factor value ranges in current QRDAT version

Risk factor	Risk factor value ranges		
	High risk	**Moderate risk**	**Low risk**
Lateral extension of the storage zone/formation depth	<25	25-100	>100
Storage zone thickness/storage zone depth	> 0.5	0.1-0.5	< 0.1
Stress regime	Compressional	Transform	Extensional
Caprock strength	Weak	Moderate	Strong
Caprock thickness	≤ 3 m	3-30 m	≥ 30 m
Fault boundaries	Multiple	One	None
Natural seismicity	High	Moderate	Low
Number of caprocks	No	One	Multiple
Maximum formation pressure/formation depth	≥ 0.75	0.625-0.75	≤ 0.625
Desired maximum formation pressure/discovery pressure	≥ 1.5	1.25-1.5	≤ 1.25
Well density	> 15	5-15	< 5
Number of uncased wells/total number of wells	> 0.6	0.2-0.6	< 0.2
Temperature difference between the injected CO_2 and the ambient storage zone temperature	≥ 60 ◦C	30-60 ◦C	≤ 30 ◦C
Caprock heterogeneity	Significant	Moderate	Strong
Caprock permeability	> 10^{-15} m^2	10^{-18}-10^{-15} m^2	< 10^{-18} m^2
Caprock lateral extend/storage zone thickness	<25	25-100	>100
Caprock dip	≥ 8°	2°-8°	≤ 2°
Minimum horizontal stress/vertical stress (stress ratio)	<0.55	0.55-0.65	>0.65

13 References

Aliani, S., Bortoluzzi, G., Caramanna, G., and Raffa, F. (2010) Seawater dynamics and environmental settings after November 2002 gas eruption off Bottaro (Panarea, Aeolian Islands, Mediterranean Sea). *Cont. Shelf Res.* **30**: 1338-1348.

Anderson, E. M. (1951). The Dynamics of Faulting and Dyke Formation with Applications to Britain 206, Oliver and Boyd, London, ed.2:206.

American Petroleum Institute. (2010). Rheology and hydraulics of oil-well fluids, API recommended practice 13D, sixth edition.

BP Alaska Pipeline Fact Sheet. (2006). Available at: http://www.bp.com/liveassets/bp_internet/us/bp_us_english/STAGING/local_assets/downloads/a/PDFA04_trans_Alaska_Pipeline_fact_sheet_August06.pdf

Bachu, S., Hawkes, C., Lawton, D., Pooladi-Darvish, M., Perkins, E. (2009). IEAGHG R&D Programme: CCS Site Characterisation Criteria, Technical Study Report No. 2009/10.

Barrie, J., et al. (undated). Carbon Dioxide Pipelines: A Preliminary Review of Design and Risks. Available at: http://uregina.ca/ghgt7/pdf/papers/peer/126.pdf

Blanton, T. L., & Olson, J. E. (1999). Stress magnitudes from logs: effects of tectonic strains and temperature. *SPE Reservoir Evaluation & Engineering*, *2*(01), 62-68.

Bourgoyne, A. T., Millheim, K. K., Chenevert, M. E., & Young, F. S. (1986). Applied drilling engineering.

Bowes, C., & Procter, R. (1997). Drillers Stuck Pipe Handbook. *Ballater, Scotland: Procter & Collins Ltd*.

Bradshaw, J., Bradshaw, B.E., Allinson, G., Rigg, A.J., Nguyen, V. and Spencer, L., (2002). The potential for geological sequestration of CO_2 in Australia: preliminary findings and implications for new gas field development. *The APPEA Journal*, vol. 42 (1), pp. 25-46.

Brewer, P.G., "Progress in direct experiments on the ocean of fossil fuel CO_2," presented at the First National Conference on Carbon Sequestration, Washington, DC, May 14-17 (2001), available at http://www.netl.doe.gov/publications/proceedings/01/carbon_seq/5b1.pdf

Bruno, M. S., 2001, Geomechanical analysis and decision analysis for mitigating compaction related casing damage, Society of Petroleum Engineers Annual Technical Conference and Exhibition, 2001, SPE 71695, 13p.

Burton, Elizabeth A., Richard Myhre, Larry Myer, and Kelly Birkinshaw. *Geologic Carbon Sequestration Strategies for California, The Assembly Bill 1925 Report to the California Legislature*. California Energy Commission, Systems Office. CEC-500-2007-100-SD

CO_2CRC. (2008). Storage capacity estimation, site selection and characterisation for CO_2 storage projects. Cooperative Research Centre for Greenhouse Gas Technologies, Canberra. CO_2CRC report n RPT08-1001. 52pp.

Caldeira, K., H. Herzog, and M. Wickett, "Predicting and Evaluating the Effectiveness of Ocean Carbon Sequestration by Direct Injection," presented at the First National Conference on Carbon Sequestration, Washington, DC, May 14-17 (2001) , available at http://sequestration.mit.edu/pdf/Caldeira_et_al_NETL.pdf

California Carbon Capture and Storage Review Panel, 2010, Technical Advisory Committee Report, by Fish, Jerry and Martin, Eric

California Division of Oil, Gas and Geothermal Resources (DOGGR), 1992, *California Oil and Gas Fields, Volumes I, II and III*. Vol. I (1998), Vol. II (1992), Vol. III (1982). California Department of Conservation, Division of Oil, Gas, and Geothermal Resources (DOGGR). 1,472 pp. PDF file available on CD from www.consrv.ca.gov

California Division of Oil, Gas and Geothermal Resources (DOGGR), 2007, 2006 Annual Report of the State Oil & Gas Supervisor; Sacramento: California Department of Conservation, 270 p.

California Geological Survey (CGS), 2002. California fault parameters – Transverse Ranges and Los Angeles Basin, available at: http://www.consrv.ca.gov/cgs/rghm/psha/fault_parameters/htm/Pages/CA_flt_parameters_tr_la1.aspx#Palos%20Ve.HTM

Caramanna, G., Voltattorni, N., and Maroto-Valer, M.M. (2011) Is Panarea Island (Italy) a valid and cost-effective natural laboratory for the development of detection and monitoring techniques for submarine CO_2 seepage? *Greenhouse Gas. Sci. Technol.* **1**: 200-210.

Carman, P. C. (1997). Fluid flow through granular beds. *Chemical Engineering Research and Design, 75*, S32-S48.

Celia, M.A., Bachu, S., Nordbotten, J.M., Kavetski, D., Gasda, S.E. 2005. Modeling Critical Leakage Pathways in a Risk Assessment Framework: Representation of Abandoned Wells, Paper presented at Fourth Annual Conference on Carbon Capture and Sequestration DOE/NETL.

Chang, C. D. (2004). Empirical rock strength logging in boreholes penetrating sedimentary formations. *Geophysics and Geophysical Exploration*, *7*(3), 174-183.

Committee on Induced Seismicity Potential in Energy Technologies (CISPET); Committee on Earth Resources; Committee on Geological, Geotechnical Engineering; Committee on Seismology, Geodynamics; Board on Earth, Sciences, Resources; Division on Earth, Life, and Studies; National Research Council. Induced Seismicity Potential in Energy Technologies. 2012.

Cook, P. J. (2006). Site Characterization. *In*: *International Symposium on Site Characterization for* CO_2*Geological Storage*, 20-22 March 2006, Berkeley, California, USA. Lawrence Berkeley National Laboratory (LBNL), pp. 3-5.

Croucher, A. E., & O'Sullivan, M. J. (2013, November). Approaches to local grid refinement in Tough2 models. In *NZ Workshop*.

De Figueiredo, M.A. "The Hawaii Carbon Dioxide Ocean Sequestration Field Experiment: A Case Study in Public Perceptions and Institutional Effectiveness". M.S. thesis, Massachusetts Institute of Technology, 2003.

Det Norske Veritas (DNV). (2010) Design and Operation of CO_2 Pipelines, Recommended Practice, DNV-RP-J202

Doughty, C. (2010). Investigation of CO_2 plume behavior for a large-scale pilot test of geologic carbon storage in a saline formation. *Transport in porous media*, *82*(1), 49-76.

Drange, H., G. Alendal, and O. M. Johannessen (2001), Ocean release of fossil fuel CO_2: A case study, *Geophys. Res. Lett.*, 28(13), 2637–2640, doi:10.1029/2000GL012609.

Eaton, B. A. (1975). The equation for geopressure prediction from well logs. *paper SPE*, *5544*.

Element Energy (2010), CO_2 Pipeline Infrastructure: An Analysis of global challenges and opportunities, Final Report for International Energy Agency for Greenhouse for Greenhouse Gas Program,

http://www.ccsassociation.org/docs/2010/IEA%20Pipeline%20final%20report%202704100.pdf

Energy Almanac. "California Power Plants." California Energy Commission, <http://energyalmanac.ca.gov/powerplants/index.html>.

Evans DM, 1966, The Denver Area Earthquakes and the Rocky Mountain Arsenal Disposal Well, 3 The Mountain Geologist 23 [Reprinted in Engineering Case Histories No. 8, 25, Geological Society of America (1970)]

Fisher, M. A., Normark, W. R., Langenheim, V. E., Calvert, A. J., & Sliter, R. (2004). The Offshore Palos Verdes Fault Zone near San Pedro, Southern California. *Bulletin of the Seismological Society of America*, *94*(2), 506-530.

Fjar, E., Holt, R. M., Raaen, A. M., Risnes, R., & Horsrud, P. (2008). *Petroleum related rock mechanics* (Vol. 53). Elsevier.

Gibson-Poole, C.M. (2008). *Site Characterisation for Geological Storage of Carbon Dioxide: Examples of Potential Sites from Northwest Australia*. Thesis (PhD). The University of Adelaide.

Gibson-Poole, C.M. and Svendsen, L. (2005). *Reservoir Characterisation and Geological Model, Kingfish Field/Southern Oil Fields Area, Gippsland Basin, SE Australia: Implications for* CO_2 *Storage*. Australian School of Petroleum, The University of Adelaide, Adelaide. CO_2CRC Report No. RPT05-0041.

Hauksson, E., & Gross, S., 1991, Source parameters of the 1933 Long Beach earthquake, Bull. Seism. Soc. Am. 81, 81-98.

Healy, J.H., W.W. Rubey, D.T. Griggs, and C.B. Raliegh. 1968. The Denver Earthquakes. *Science*, vol.161, no. 3848, p. 1301-1310.

Heidbach, O., Tingay, M., Barth, A., Reinecker, J., Kurfeß, D., & Müller, B. (2001). World stress map. *Naturwissenschaften*, *88*, 357-371.

Herzog, H., K. Caldeira and E. Adams, Carbon Sequestration via Direct Injection. In J H Steele, S A Thorpe and K K Turekian (eds) Encyclopedia of Ocean Sciences Vol. 1, pp 408 - 414. London, UK: Academic Press, 2001.

Holasek, F. R. (2001). AAPG Memoir 76, Chapter 11: An Easily Derived Overburden Model Is Essential for the Prediction of Pore-Pressure Gradients and Fracture Gradients for Wildcat Exploration in the Gulf of Mexico.

Horsrud, P. (2001). Estimating mechanical properties of shale from empirical correlations. *SPE Drilling & Completion*, *16*(02), 68-73.

Ide, S.T., S.J. Fridemann , and H.J. Herzog, "CO_2 leakage through existing wells: current technology and regulations," presented at the 8th International Conference on Greenhouse Gas Control Technologies, Trondheim, Norway, June (2006), available at http://sequestration.mit.edu/pdf/GHGT8_Ide.pdf

Incropera, F. P., DeWitt, D.P. (1996). *Fundamentals of heat and mass transfer*. John Wiley & Sons, 4th Edition.

IPCC, 2005. Carbon Dioxide Capture and Storage: Summary for Policymakers and Technical Summary. Intergovernmental Panel on Climate Change, ISBN 92-9169-119-4.

Itasca Consulting Group. (2013). Flac3D Version 5.01 User's manual: Theory and Background, Section 2-Interfaces.

Kaldi, J.G., C.M. Gibson-Poole, and T.H.D. Payenberg. 2009. Geological input to selection an evaluation of CO_2 geosequestration sites. In M. Grobe, J.C. Pashin, and R.L. Dodge, eds. *Carbon Dioxide Sequestration In Geological Media-State of the Science*, AAPG Studies in Geology 59, pp. 5-16.

Klusman, R.W. 2003. Rate measurements and detection of gas microseepage to the atmosphere from an enhanced oil recovery/sequestration project, Rangely, Colorado, USA. App. Geochem., 18, 1825-1838.

Lal, R. (1999). Soil management and restoration for C sequestration to mitigate the accelerated greenhouse effect. *Progress in Environmental Science*, *1*(4), 307-326.

McNally, G. H. (1987). Estimation of coal measures rock strength using sonic and neutron logs. *Geoexploration*, *24*(4), 381-395.

MIT, 2006 (updated 2009), Carbon Management GIS: CO_2 Pipeline Transport Cost Estimation, for NETL, under contract DE-FC26-02NT41622, http://www.canadiancleanpowercoalition.com/pdf/CTS12%20-%20Transport.pdf

Matthews, W. R., & Kelly, J. (1967). How to predict formation pressure and fracture gradient. *Oil and Gas Journal*, *65*(8), 92-106.

Mitchell, J. (2009). *Stuck pipe prevention*. Drilbert Engineering.

National Energy Technology Laboratory (NETL, 2010). *Carbon Sequestration Atlas of the United States and Canada, 3rd Ed.* Available at http://www.netl.doe.gov/technologies/carbon_seq/refshelf/atlas/. Accessed September 1, 2012.

Parfomak, P. W., & Folger, P. (2007, April). Carbon dioxide (CO_2) pipelines for carbon sequestration: Emerging policy issues. Congressional Research Service, Library of Congress.

Petersen, M.D., Frankel, A.D., Harmsen, S.C., Mueller, C.S., Haller, K.M., Wheeler, R.L., Wesson, R.L., Zeng, Yuehua, Boyd, O.S., Perkins, D.M., Luco, Nicolas, Field, E.H., Wills, C.J., and Rukstales, K.S., 2011, Seismic-Hazard Maps for the Conterminous United States, 2008: U.S. Geological Survey Scientific Investigations Map 3195, 6 sheets, scale 1: 7,000,000.

Port of Los Angeles, *3.5 Geology*, Web. 5 December 2012. <http://www.portoflosangeles.org/EIR/PacificLAMarine/SEIR/3-5_Geology.pdf>

Pratt, W.E., and D.W. Johnson, Local subsidence of the Goose Creek oil field, *J. Geol.*, *34* (7), 577-590, 1926.

Price, P.N., McKone, T.E., and Sohn, M.D., 2008. Carbon Sequestration Risks and Risk Management. Lawrence Berkeley National Laboratory: LBNL-513E.

Pruess, K. (2010). Mathematical models as tools for probing long-term safety of CO_2 storage. *Lawrence Berkeley National Laboratory*. Lawrence Berkeley National Laboratory: Lawrence Berkeley National Laboratory. LBNL Paper LBNL-1587E. Retrieved from: http://escholarship.org/uc/item/04w053xn

Quantifying and Monitoring Potential Ecosystem Impacts of Geological Carbon Storage (QICS). 2012. *Scientific Summary*. Web. 26 September 2012. <http://www.bgs.ac.uk/qics/experiment.html>

Raleigh CB, Healy JH, and Bredehoeft JD, 1976, An experiment in earthquake control at Rangely, Colorado. Science 191:1230-37

Rutqvist J, Birkholzer JT, Tsang CF. Coupled reservoir–geomechanical analysis of the potential for tensile and shear failure associated with CO_2 injection in multilayered reservoir–caprock systems. International Journal of Rock Mechanics and Mining Sciences 2008; 45(2), 132-143.

Rutqvist J, Vasco DW, Myer L. Coupled reservoir-geomechanical analysis of CO_2 injection and ground deformations at In Salah, Algeria. International Journal of Greenhouse Gas Control 2010; 4(2), 225-230.

Shaw, J. H. (1999). *Seismic reflection transect and geologic cross section across the central Los Angeles basin and San Pedro Bay*. Annual Report to the Southern California Earthquake Center.

Shaw, J. H. (2007). *Subsurface geometry and segmentation of the Palos Verdes Fault and their implications for earthquake hazards in southern California*. Department of Earth and Planetary Sciences, Harvard University.

Singh, P. K., Agarwal, R. G., & Krase, L. D. (1987, January). Systematic design and analysis of step-rate tests to determine formation parting pressure. In *SPE Annual Technical Conference and Exhibition*. Society of Petroleum Engineers.

Southern California Earthquake Center (SCEC). Retrieved from: http://www.data.scec.org/significant/index.html

Taylor, D. W. (1948). Fundamentals of soil mechanics. *Soil Science*, *66*(2), 161.

Verdon JP, Kendall JM, Stork AL, Chadwick RA, White DJ, Bissell RC. Comparison of geomechanical deformation induced by megatonne-scale CO_2 storage at Sleipner, Weyburn, and In Salah. Proceedings of the National Academy of Sciences 2013; 110(30), E2762-E2771.

Vilarrasa V, Olivella S, Carrera J. Geomechanical stability of the caprock during CO_2 sequestration in deep saline aquifers. Energy Procedia 2011; 4, 5306-5313.

Wesson, R. L., and C. Nicholson. 1987. *Earthquake Hazard Associated with Deep Well Injection.* Prepared by the U.S. Geological Survey. Open-File Report 87-331.

Wilde, M., & Stock, J. (1997). Compression directions in southern California (from Santa Barbara to Los Angeles Basin) obtained from borehole breakouts. *Journal of Geophysical Research: Solid Earth (1978–2012)*, *102*(B3), 4969-4983.

Zhou Q, Birkholzer JT, Tsang CF, Rutqvist J. A method for quick assessment of CO_2 storage capacity in closed and semi-closed saline formations. International Journal of Greenhouse Gas Control 2008; 2(4), 626-639.

14 List of Acronyms and Abbreviations

BHA	bottom hole assembly
DOGGR	California Department of Oil, Gas, and Geothermal Resources
CCI	carrying capacity index
DOE	US Department of Energy
DOT	US Department of Transportation
FERC	US Federal Energy Regulatory Commission
MCS	multiple channel seismic
NETL	US DOE National Energy Technology Laboratories
KB	Kelly bushing
MD	measured depth
NCT	Normal Compaction Trend
OB	overburden
OPS	Office of Pipeline Safety
PV	Palos Verdes
PI	Pico Formation
PU	Puente Formation
QICS	Quantifying and Monitoring Potential Ecosystem Impacts of Geological Carbon Storage
QRDAT	Quantitative Risk & Decision Analysis Tool
RE	Repetto Formation
ROP	rate of penetration
RMS	root mean square
ROW	right-of-way
RW	RockWorks
SFI	Slurry Fracture Injection
SRT	step rate test
STB	surface transportation board
TD	total depth
TFA	total flow area
THB	Thums-Huntington Beach
TVD	total vertical depth
twtt	two-way travel time
USGS	US Geological Survey
WSM	World Stress Map

15 Appendices

15.1 Appendix 1: Wilmington Graben Site Characterization Plan

As has been exemplified by this report on our activities of the past five years, our site characterization plan for the Wilmington Graben involved these components:

1. **Seismic Data Analysis and Acquisition**: Improved evaluation and interpretation of existing 2D and 3D seismic data plus new seismic data acquisition within a "data gap" area.
2. **Well Data Review and Formation Evaluation**: Detailed log evaluation of existing exploration wells in the area.
3. **New Well Drilling, Logging, and Core Analysis**: Drilling and coring two new evaluation wells into the Graben (Pliocene and Miocene) and deepening of an existing well to test the Miocene sand continuity.
4. **3D Geological Model Development**: Development of 3D geologic models, geomechanical models, and CO_2 injection and migration models for the region – update with data from new DOE wells. Typical steps in site characterization are structural and stratigraphic interpretations based on available subsurface data, building of geologically constrained probabilistic models with realistic stratigraphic heterogeneity (Gibson-Poole et al., 2005; Gibson-Poole, 2008), in our case allowing for a range of shale-sand proportions found in a turbidite depositional environment.
5. **3D Gas Migration Modeling**: A typical step in site characterization is constructing numerical flow simulations to predict CO_2 plume migration (Gibson-Poole, 2008). This step should incorporate appropriate levels of uncertainty in interpretation, which should be reflected in the various outcomes of multiple flow simulation scenarios (CO_2CRC, 2008), in our case, again, allowing for a range of shale-sand proportions found in turbidite depositional environments.
6. **3D Geomechanical Model Development**: Geomechanical performance assessment is an integral part of site characterization (Bachu et al., 2009).
7. **Risk Analysis**: At the minimum review wellbore of surrounding wells to make sure the wells are properly abandoned.
8. **Infrastructure Assessment**: Engineering study of existing and new pipeline systems to transport CO_2 from significant local sources to sequestration sites, including an analysis of the top 20 industrial sources in the LA Basin.

15.2 Appendix 2: Best Practices for Characterizing CO_2 Storage Site

Site characterization consists of the collection, analysis and interpretation of subsurface data and the application of geologic and engineering knowledge to judge, with a degree of confidence, if an identified site will geologically store a specific quantity of CO_2 for a defined period of time (Cook, 2006). Characterization must demonstrate that it satisfies three fundamental requirements (Bachu et al., 2009):

1. capacity to store the intended volume of CO_2 over the lifetime of the operation,
2. injectivity, to accept/take CO_2 at the rate that it is supplied from the emitter(s), and
3. containment, to ensure that CO_2 will not migrate and/or leak out of the storage unit (safety and security of storage).

These three factors encompass the fundamental elements needed to characterize any potential CO_2 geological storage site (Bradshaw et al., 2002).

One of the main objectives of site characterization is to accurately predict CO_2 behavior in the subsurface, with respect to injectivity, containment, and storage capacity at a specific site. To do so certain data are necessary, as well as the application of certain tasks using this data (CO_2CRC, 2008).

The kinds of data necessary for characterization include the following (CO_2CRC, 2008):

- Maps:
  - Regional geology
  - Detailed/local geology
  - Structural contour
  - Reservoir geometry
  - Faults
  - Seismicity
  - Surface infrastructure
  - Pre-existing wells
- Seismic:
  - 2D
  - 3D
- Well logs:
  - Gamma ray
  - Porosity
  - Permeability
  - Density
  - Sonic
  - Image

- Cores
  - Porosity
  - Permeability
- Special core analysis
  - Ratio vertical/horizontal permeability
  - Relative permeability
  - Rock strength
- Subsurface history: Oil & Gas production
- Pore pressure:
  - Repeat formation tests; drill stem tests; step rate tests
  - Subsurface fluid properties
  - Leak-off tests; formation integrity tests
- Reservoir characterization:
  - Regional stress analyses
  - biostratigraphy

Geologic interpretation of map, seismic, well, and drilling data provides the first characterization of a potential injection site. The engineering, or performance, characterization phase carries on from this geologic characterization, using the data produced and integrating it with interpreted data from the gathered core, well, pore pressure, and reservoir data. Numerical simulation models of the injection phase are needed to provide data on the injection strategy required to achieve the desired injection rates (e.g. number of wells, well design and injection pattern) and to provide geomechanical models with pressure regimes. Post-injection phase numerical simulations evaluate the long-term storage behavior, modeling the likely migration, distribution and form of the CO_2 in the subsurface (CO_2CRC, 2008). Geomechanical models then evaluate the structural integrity of the reservoir-caprock system. Based on all three of these endeavors, a risk analysis can then be carried out to determine leakage and/or damage scenarios, as well as their likelihood and costs. Finally, an infrastructure assessment is necessary to determine avenues, existing or projected, for transporting the CO_2 from emission sources to storage reservoirs.

We also found an official peer review a little over halfway through to be extremely helpful in determining areas requiring our attention. Deeply involved in the project for years, focusing on our specific sub-projects, it was sometimes difficult to see the forest for our assigned trees. The disinterested eye of outside observers working on similar projects, but in different geological environments, could more easily see some trees we were missing in our project's forest. Their suggestions greatly enhanced our research program and led to more robust results and we heartily recommend such a review as a best practice.

Title: Characterization of Pliocene and Miocene Formations in the Wilmington Graben, Offshore Los Angeles, for Large-Scale Geologic Storage of CO_2

PI: Dr. Michael Bruno Final Report

As has been exemplified by this report on our activities of the past five years, we believe the ideal program for characterizing a CO_2 storage site such that these three requirements are fulfilled involves the following eight tasks:

1. Seismic Data Analysis and Acquisition;
2. Well Data Review and Formation Evaluation;
3. New Well Drilling, Logging, and Core Analysis;
4. 3D Geological Model Development;
5. 3D Gas Migration Modeling;
6. 3D Geomechanical Model Development;
7. Risk Analysis;
8. Infrastructure Assessment.

15.3 Appendix 3: Gridding Effect on Plume Migration

Since we observe gas migration potentially driven along cells with high aspect ratio in some of the simulation results, we investigated the so-called gridding effect. We applied a different mesh resolution for both locations and present the results & discussion in this appendix. Simulation results presented in this report are run with a mesh as shown in Figure 189 (right side), for the discussion of the gridding effect a mesh with regular cell spacing around the injection well has been set up for comparison - Figure 189 (left side).

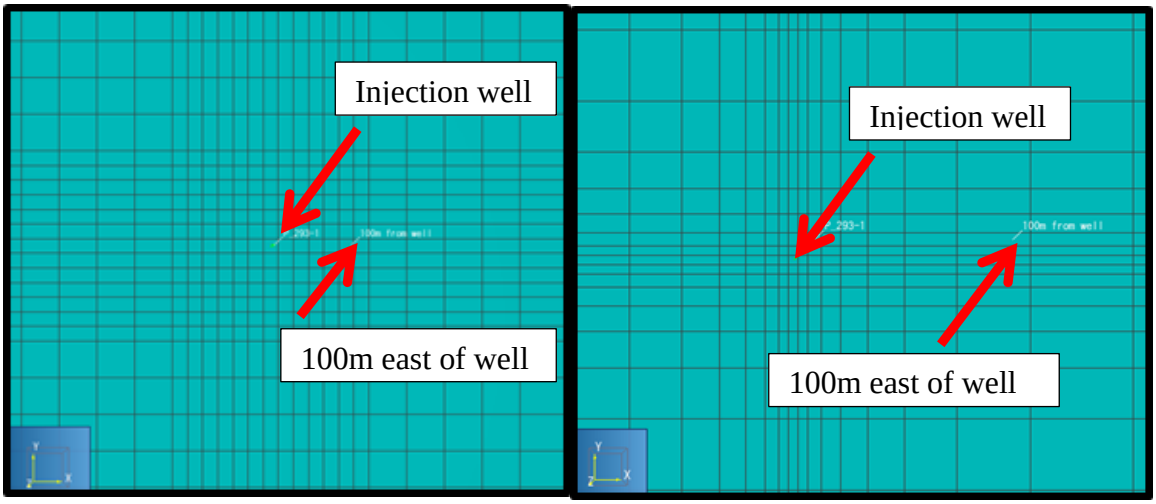

Figure 189: Compare grid refinement around well – regular (left), increasing (right)

Northern Graben: below we compare gas saturation after 30 years of injection in two locations (y=0 and y=120 m) for a model with regular refinement of cell dimensions around the injection wellbore, and a model with decreasing refinement (Figure 190 and Figure 191, respectively).

Title: Characterization of Pliocene and Miocene Formations in the Wilmington Graben, Offshore Los Angeles, for Large-Scale Geologic Storage of CO_2

PI: Dr. Michael Bruno Final Report

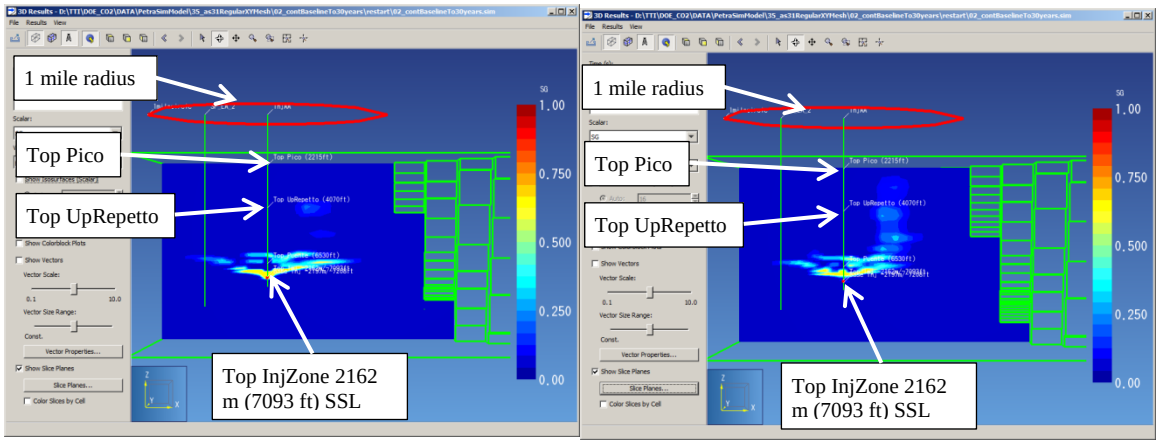

Figure 190: Regular grid around wellbore (13x13m) (17.4MMt – 95,935 cells)

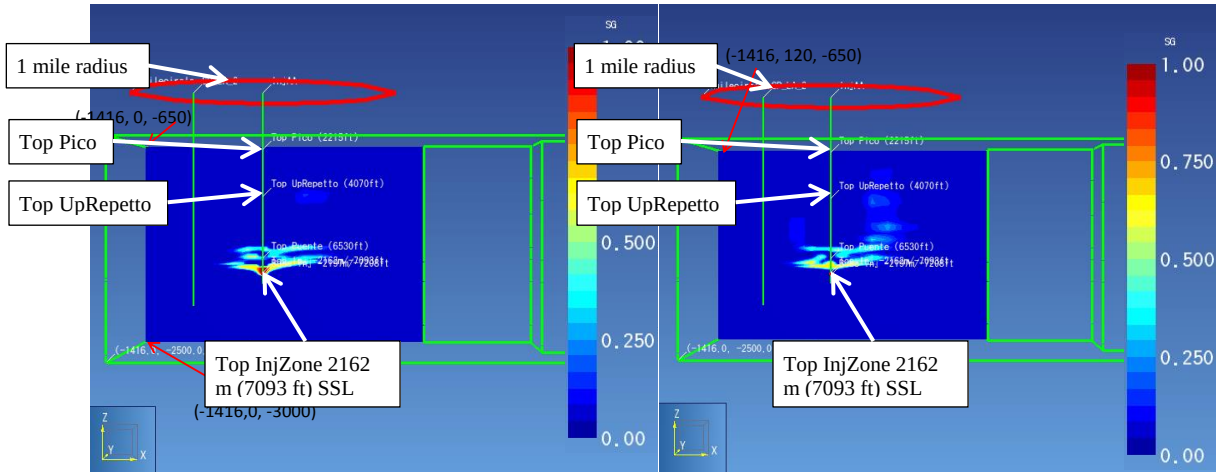

Figure 191: Decreasing horizontal mesh resolution, starting at 5x5 m near well (15.75 MMt – 61,244 cells)

Though we see differently shaped plumes from top views for these two runs (Figure 192), the general trend in vertical migration, i.e., how CO_2 finds a pathway into upper layers, looks similar (Figure 190 and Figure 191).

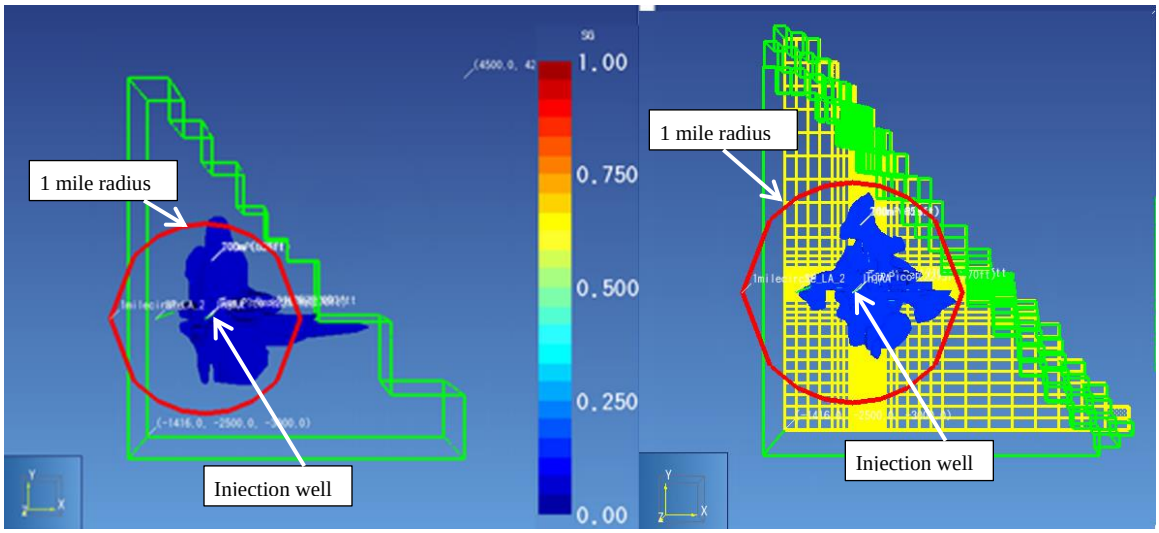

Figure 192**: CO_2 plume after 30 years of injection, top view – refining grid (left), regular grid (right)**

Central Graben: In the central Graben we compare two cross sections going through the injection well, one along the x-axis (Figure 193), the other one along the y-axis (Figure 194).

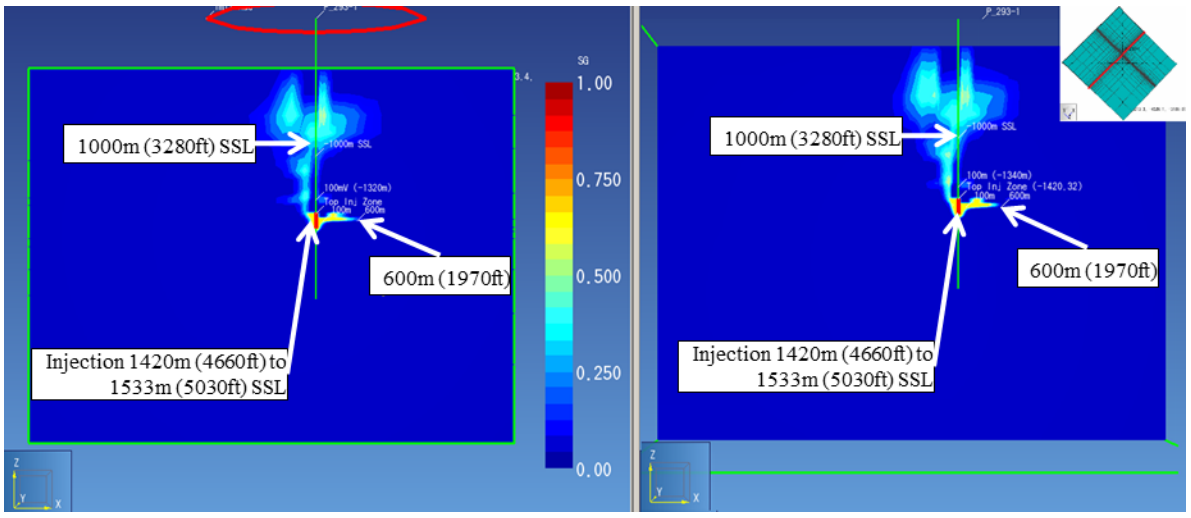

Figure 193: Refining grid (left), regular grid (right), around well bore, gas saturation after 30 years of injection – SW/NE

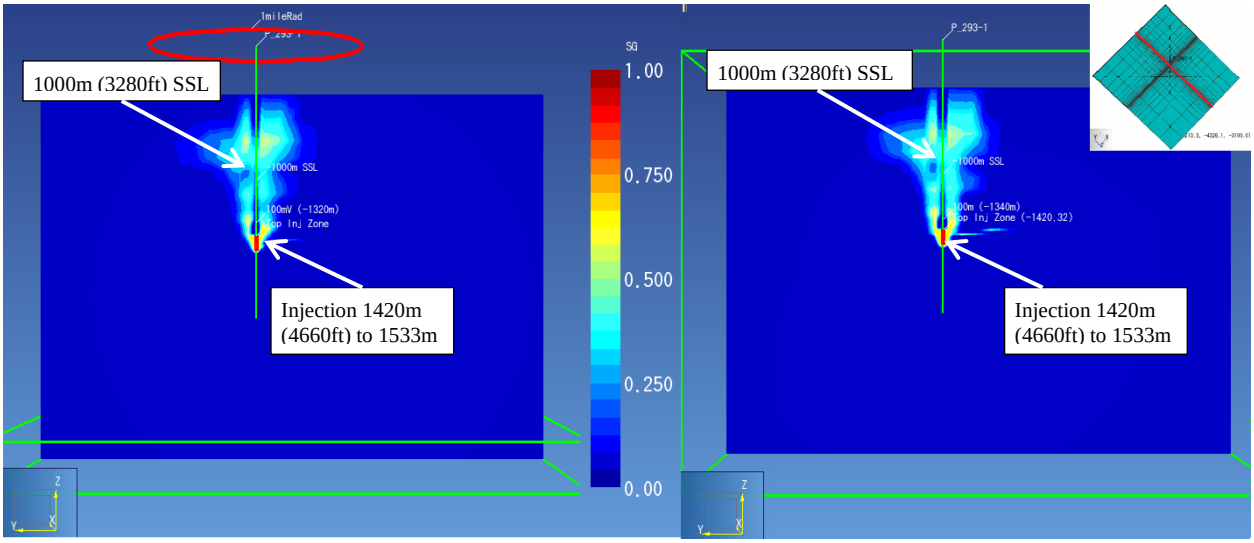

Figure 194: Refining grid (left), regular grid (right), around well bore, gas saturation after 30 years of injection – NW/SE

A top view of the plume is shown in Figure 195. Slight differences are seen in the shape, but extension looks similar, and no significant difference can be seen in the vertical plume migration cross sections above.

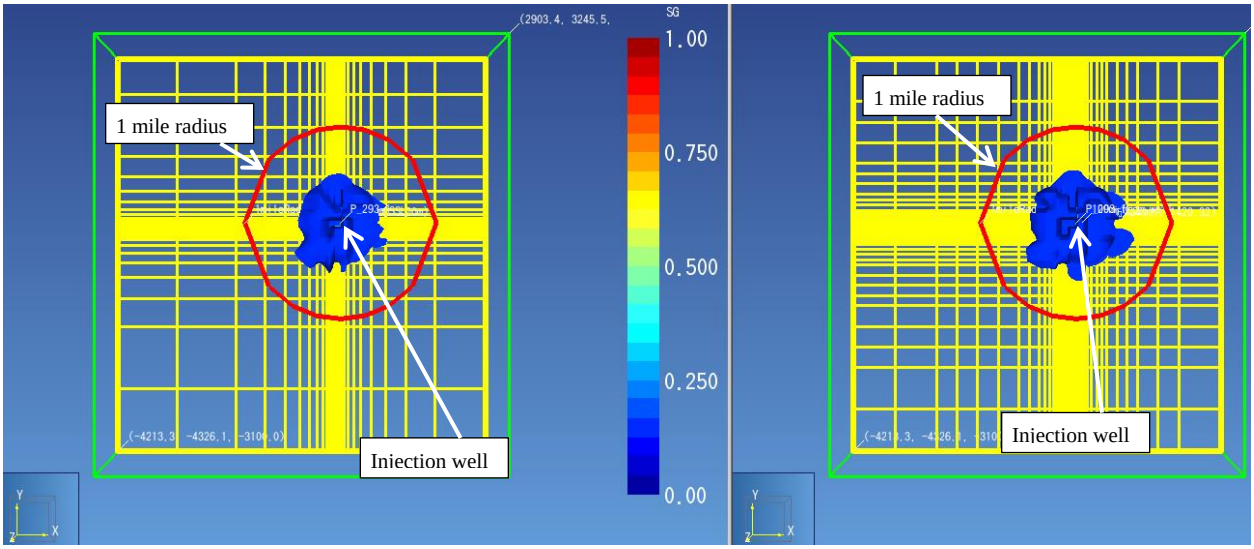

Figure 195: CO_2 plume after 30 years of injection – refining grid (left), regular grid (right)

Experiments with aligned meshes – in which cell boundaries follow the boundary of the structure - have been discarded, as even setting up natural state for such meshes was not successful. Additionally, it is not recommended to work with aligned meshes (Croucher & Sullivan, 2013) – tempting though it is, since pre-processor Petrasim allows such.

15.4 Appendix 4: Sensitivity Analysis for Northern Graben geomechanical model

For mesh resolution sensitivity analysis (Figure 196), one case with higher resolution mesh (123,750 elements) and other with lower resolution mesh (44,800 elements) were modeled (Table 45). No significant magnitude changes were observed in both cases with 0.00732 m (0.024 ft) and 0.00792 m (0,026 ft) as maximum surface uplift displacement for high resolution and low resolution case, respectively (Figure 196). Similar result can be seen in Figure 197. Meanwhile, for grid orientation sensitivity analysis (Figure 198), one case with elements parallel to THB fault and other with element parallel to PV fault were simulated. In Figure 199 and Figure 200, note that a small rotation in the center of the surface uplift displacement is seen, aligning the shape of the map contour parallel to the faults. Finally, a boundary conditions sensitivity analysis (Figure 201) was done. A shorter propagation on surface uplift area can be seen in Figure 202, Figure 203 and Figure 204 when boundary conditions are changed from roller to fix in x, y and z axis.

Table 45: Northern Graben Sensitivity Analysis

Cases		Results
Mesh Resolution	High (123750 elements)*	None significant magnitude changes
	Low (44800 elements)	
Grid Orientation	Elements parallel to THB fault*	None significant magnitude changes, but with a small rotation in the surface uplift area
	Elements parallel to PV fault	
Boundary Conditions	All faces roller*	None significant magnitude changes, but with a shorter Z-displacement area as boundaries are fixed
	Fixed X	
	Fixed XY	
	All faces fixed	
*Baseline		

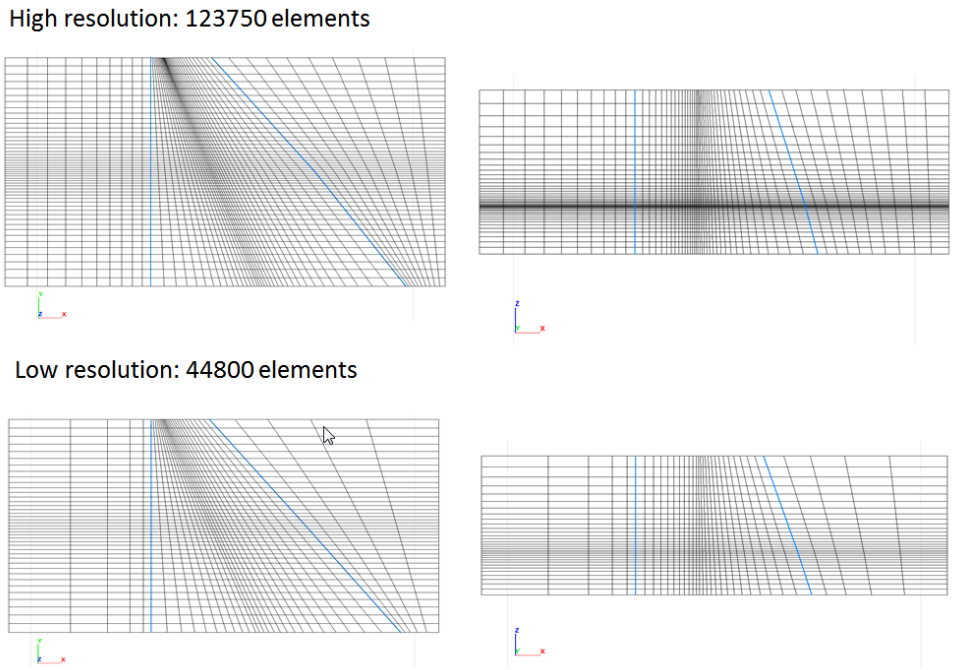

Figure 196: Mesh resolution – top left is 2D top view, top right is 2D cross section mesh, bottom left is 3D top view, bottom right is 3D view for surface uplift displacement across injection zone

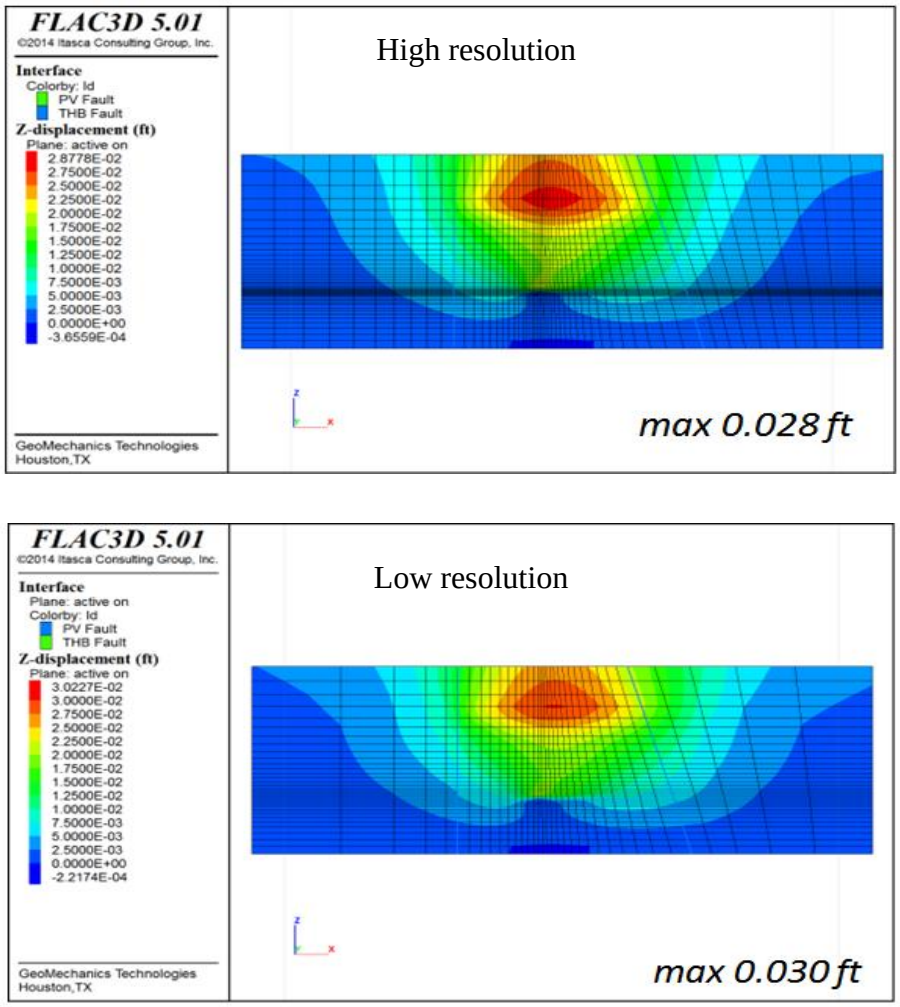

Figure 197: Mesh resolution - Cross section for vertical displacement across injection zone

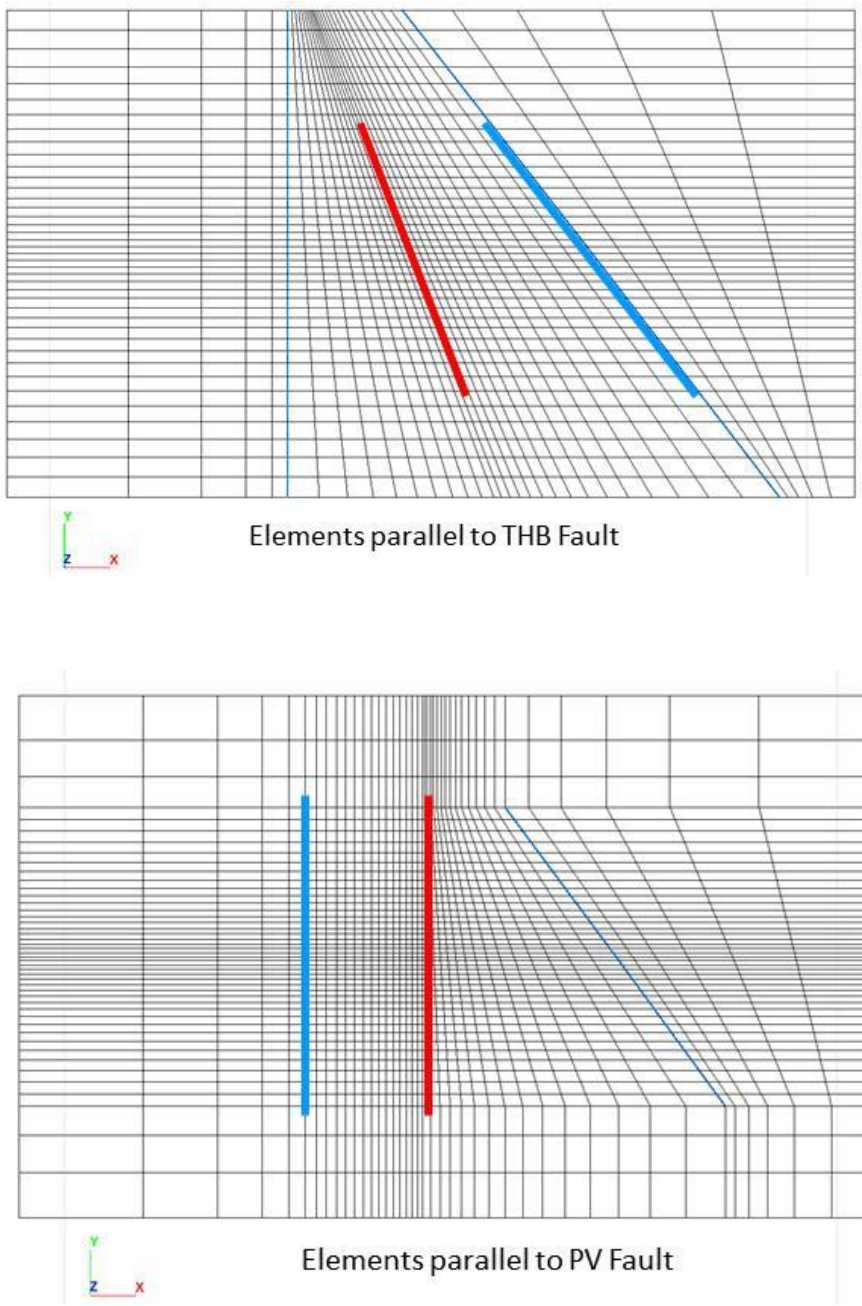

Figure 198: Gird orientation - Top view of elements parallel to THB fault and PV fault

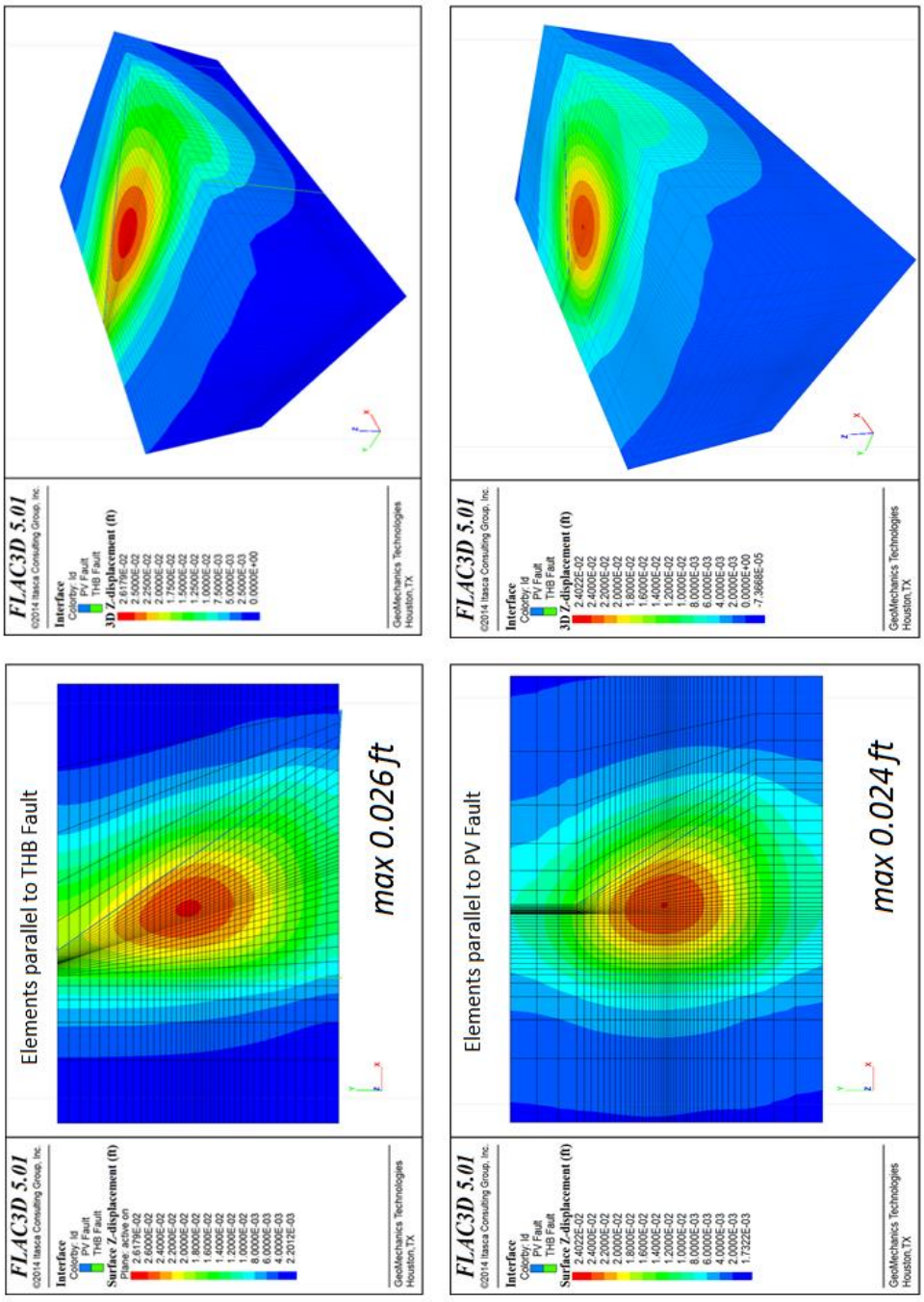

Figure 199: Grid orientation - Top view and 3D view for surface uplift displacement across injection zone

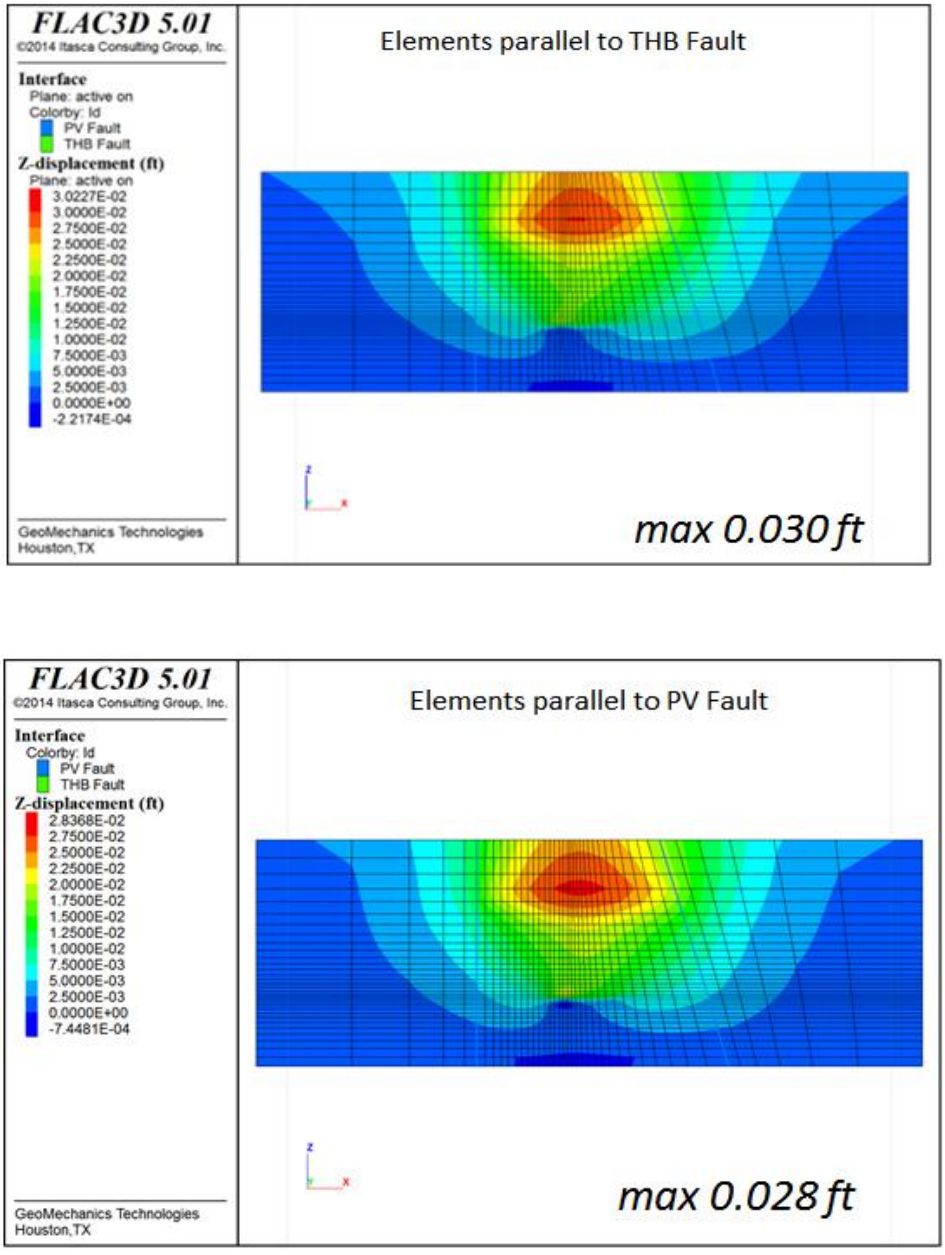

Figure 200: Grid orientation - Cross section for vertical displacement across injection zone

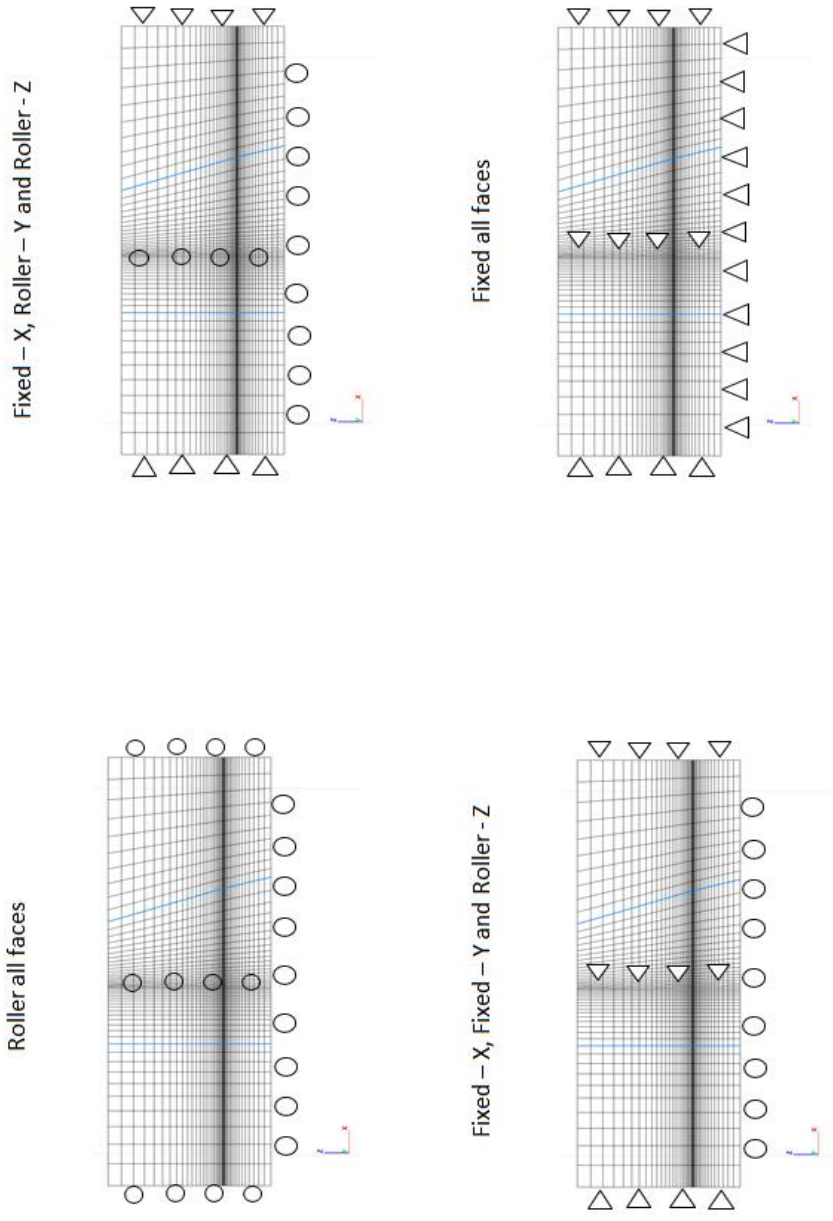

Figure 201: Boundary condition – Cross section schemes

Title: Characterization of Pliocene and Miocene Formations in the Wilmington Graben, Offshore Los Angeles, for Large-Scale Geologic Storage of CO_2

PI: Dr. Michael Bruno Final Report

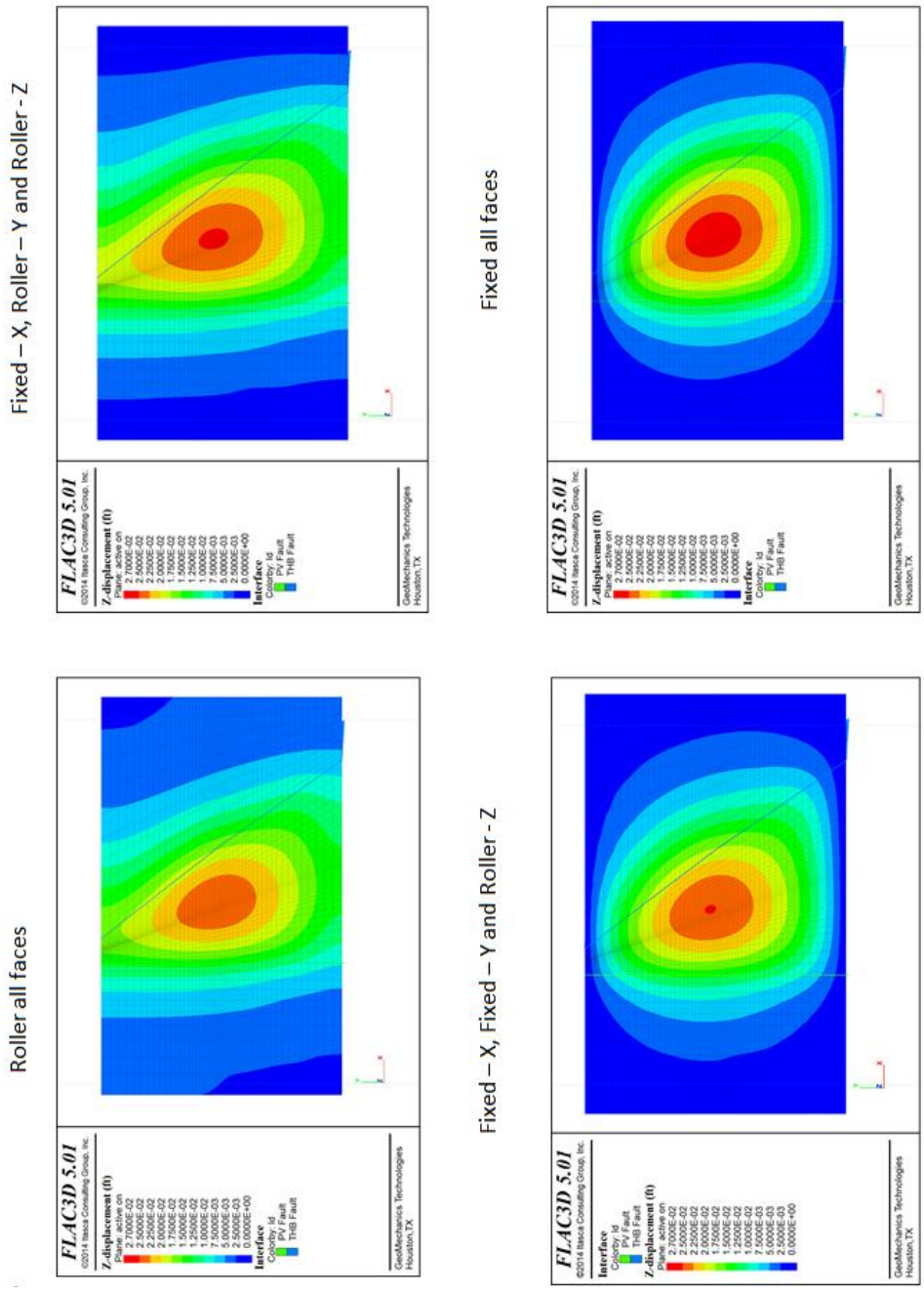

Figure 202: Boundary condition - Top view for surface uplift displacement across injection zone

Title: Characterization of Pliocene and Miocene Formations in the Wilmington Graben, Offshore Los Angeles, for Large-Scale Geologic Storage of CO_2

PI: Dr. Michael Bruno Final Report

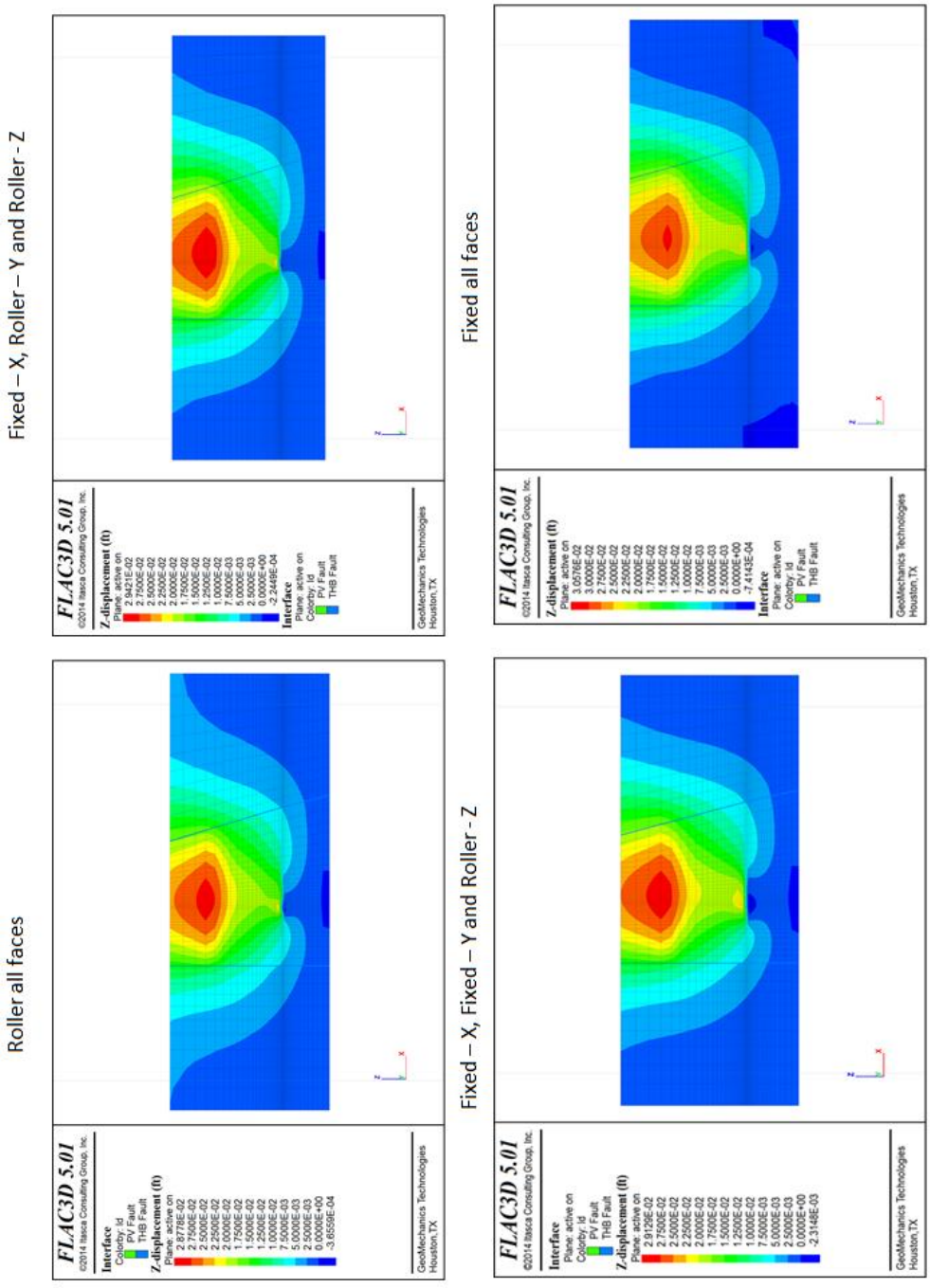

Figure 203: Boundary condition - Cross section for vertical displacement across injection zone

Title: Characterization of Pliocene and Miocene Formations in the Wilmington Graben, Offshore Los Angeles, for Large-Scale Geologic Storage of CO_2

PI: Dr. Michael Bruno Final Report

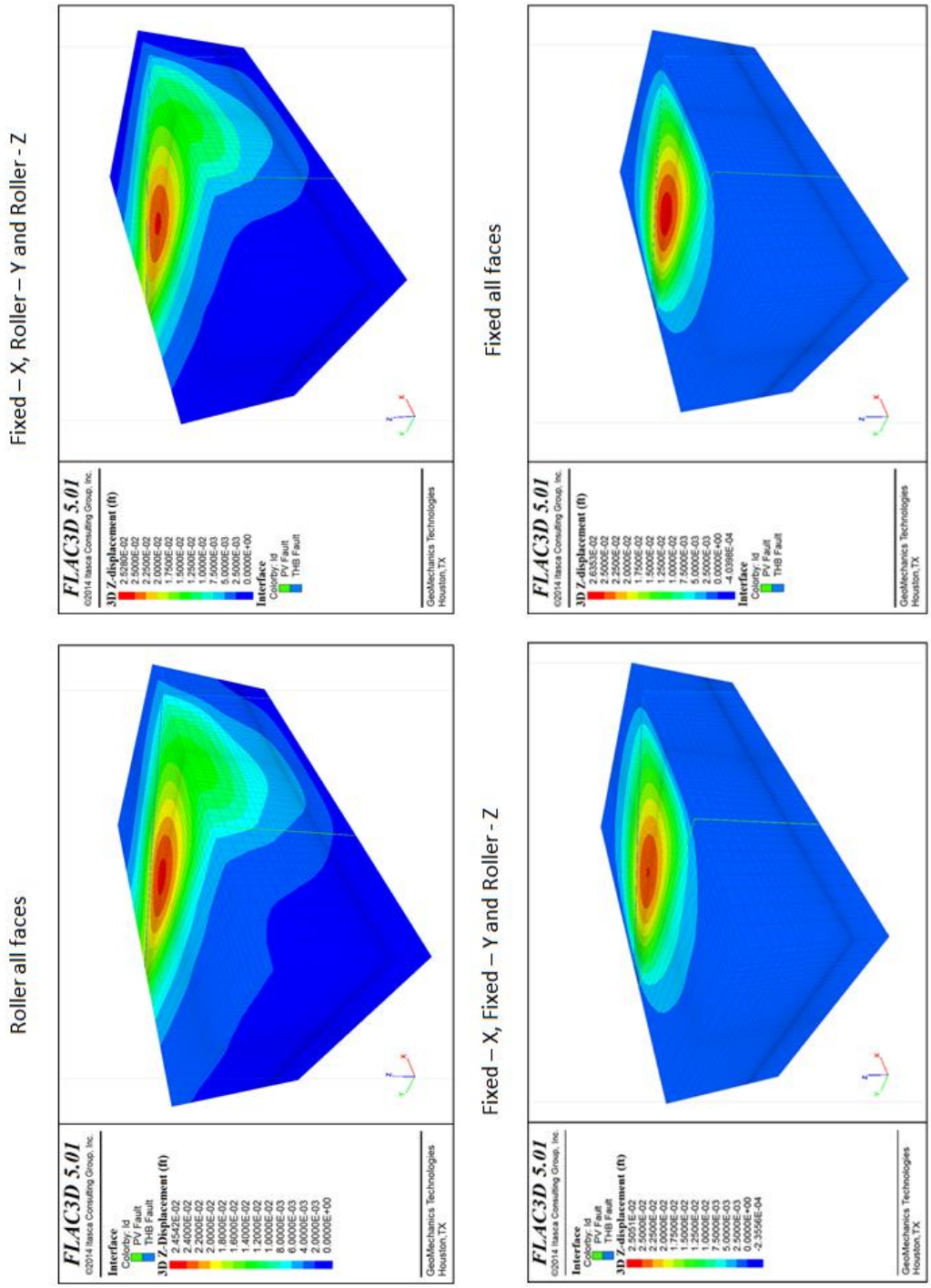

Figure 204: Boundary condition - 3D view for surface uplift displacement across injection zone